

Electrochemical imaging of metabolic activity in tissue and biofilms

Présentée le 11 février 2022

Faculté des sciences de base
Laboratoire d'électrochimie physique et analytique
Programme doctoral en chimie et génie chimique

pour l'obtention du grade de Docteur ès Sciences

par

Sorour DARVISHI

Acceptée sur proposition du jury

Prof. R. Beck, président du jury
Prof. H. Girault, Dr A. S. Lesch, directeurs de thèse
Prof. G. Wittstock, rapporteur
Dr M. Etienne, rapporteur
Dr R. Hovius, rapporteur

To my family ...
... تقدیم به خانواده ام

*If Simorgh unveils its face to you, you will find
that all the birds, be they thirty or forty or more,
are but the shadows cast by that unveiling.
What shadow is ever separated from its maker?
Do you see?
The shadow and its makers are one and the same,
so get over the surface and delve into mysteries*

Attar of Nishapur

Acknowledgment

My Ph.D. studies have been started at the same time as I have left my motherland, Iran. I had a brilliant time over the last four years. Getting through this incredible chapter of my life required more than academic support, and I have many, many people to thank.

First and foremost, I would like to express my sincere gratitude to my supervisor Prof. Hubert H. Girault for the continuous support of my Ph.D. study and related research, for his patience, motivation, and immense knowledge. His guidance helped me immensely in all the research and beyond that with my new young life in Switzerland. I could not have imagined having a better advisor and mentor for my Ph.D. study. Hubert has generously given me various great opportunities to promote myself as a scientist and human being. He has taught me to think from out of the box and not be biased, be precise and perfectly do things, and see life in all aspects.

I would like to thank Prof. Andreas Lesch, my co-supervisor significantly. We have worked close to each other in the first year of my Ph.D. I have had his incredible support over the last three years online. I have learned a lot from him. Andreas was always available whenever I needed to move forward, learn new concepts and skills, brainstorm, or share my thoughts. Andreas is so bright and patient and generously teaches these fantastic characters to his students. I am so lucky and grateful to have such a supportive and humble supervisor that was always by my side.

My sincere thanks also go to the Swiss National Science Foundation (SNSF), which secured my visiting experience at the University of Cambridge during six months of Doc. Mobility experience. Also, I would like to express my appreciation to my host supervisor, Prof. Clemens F Kaminski.

I would like to show gratitude to my Ph.D. exam committee, including Prof. Rainer Beck (president of the exam), Prof. Gunther Wittstock (examiner), Prof. Mathieu Etienne (examiner), and Prof. Ruud Hovius (examiner).

I would like to thank the people who came into my life during my Ph.D. studies as my new friends and became my chosen family. The list will be too long for this short acknowledgment. Here, I name only a few: Dominika Baster, Ioanna Mela, Seyed Mohamad Moosavi, Bardiya Valizadeh, Mehrdad Asgari, Fatemeh Rahimian, Samaneh Daviran, Zohreh Akbari, Maryam Asghari, Javad Shamsi, Sagnik Middya, Lucia Wunderlich, Luca Mascheroni, Nino Läubli, and Karsu İlksen Firat. I like to thank all the people I had a great time working with within the LEPA at EPFL and the LAG at Cambridge. I also would like to thank a lot Ms. Patricia Byron, Ms. Annick Évéquoz, Ms. Sandrine Jaussi, and Ms. Anne Lene Odegaard.

Most importantly, none of this could have happened without my family. I like to thank my great family, my parents “AbdolSamad and Monavar,” siblings “Setareh, Gholamreza, and Setayesh.” Even though we were geographically far apart, I had them close all the time. As I left my family for 12 years and got older, I realized how lucky I am for having such a fantastic family beside me that all they want is my happiness. I could not be thankful enough to my mom and dad. My mom is definitively my role model. Setayesh, my youngest sister, also has an extraordinary impact on my life. I also want to thank my cousin, Nemat, for the four last years. He has welcomed me when I have arrived in Europe. I always had a home that was warmly welcoming me in the Netherlands. I highly enjoyed the time we had brainstorming and talking while we were cooking Iranian food.

Abstract

Non-invasive or semi-invasive bioimaging is of great interest for diagnosis as it allows the mapping of the distribution and concentration of biomarkers in a biological sample. The as-obtained information can be used to design and define efficient treatments against cancer and pathogenic biological structures like biofilms. Electrochemical bioimaging is based on the local detection of redox reactions at local substrate sites, and its resolution can reach (sub)micrometers. Its tolerance to optical perturbations is a particular advantage over light-based detection methods. Electrochemical bioimaging can be applied to study electron transfer reactions and the metabolic activity of biological samples. By the implementation of immuno-affinity complexes, it can be made specific to proteins and other biomolecules. An electrochemical scanning probe platform can be used, such as Scanning Electrochemical Microscopy (SECM), in which a micrometric electrochemical probe is translated in close proximity to a surface. The active part of the tip senses electro-active species generated or consumed by an active site on the substrate. In terms of biological samples, SECM has in particular found applications for studying living cells, yeast, and bacteria.

This thesis looked at utilizing electrochemical bioimaging for sensing biomarkers of melanoma non- and semi-invasively and at developing new electrochemical strategies to study biofilms and the effects of biofilm treatments.

First, a non-invasive electrochemical melanoma detection approach is presented based on using adhesive tapes to collect and fix cells from a suspicious skin area and transfer them into an SECM for their analysis. The adhesive layer collects the cells from the *stratum corneum* and keeps them well adhered to the adhesive layer of the tape during experiments in an electrolyte solution. A melanoma biomarker, here the intracellular enzyme tyrosinase (TYR), was detected in the tape-collected cells, made permeable by the tape-stripping process. TYR-specific antibodies were used that were labeled with horseradish peroxidase (HRP). The HRP labels catalyzed the oxidation of a dissolved redox-active probe, which was detected at a soft microelectrode. The soft microelectrode was scanned over the sample in a gentle contact mode, which was essential for realizing and maintaining a constant working distance. The melanoma biomarker was first detected on tape-stripped samples with murine melanoma cells of different concentrations. After that, increasing levels of TYR were recorded in cells that were collected from the skin of melanoma mouse models representing three different stages of tumor growth. Additionally, SECM results of tape-stripped different human melanoma cell lines were in accordance with previous studies based on traditionally fixed and permeabilized melanoma cells.

The second study envisaged the semi-invasive direct electrochemical detection of melanoma biomarkers in non-treated skin. The enzyme tyrosinase was to be addressed with a microneedle electrochemical sensor. The microneedles were fabricated by polydimethylsiloxane (PDMS) casting with stable polymers. The as-prepared microneedles (MNs) were then coated by gold sputtering. The gold MNs were finally covered by alginate/catechol to provide a liquid electrolyte layer that contained electroactive species, such as catechol, whose redox state can be linked to the concentration of TYR in the skin. The sensor showed high sensitivity of $7.52 \mu\text{A} \cdot \text{mg}^{-1} \cdot \text{mL}$ TYR in dummy skin. A relative standard deviation (RSD) of 9% ($n=5$) demonstrated that the Catechol@alginate: gold MN electrode had an excellent reproducibility for continuous TYR detection. Also, five parallel Catechol@alginate: gold MN electrodes were fabricated using the same experimental setup and showed an RSD of 4% ($n=5$). These results suggest that the electrode fabrication process was reproducible, and Catechol@alginate: gold MN biosensors demonstrated high stability for the repetitive detection of TYR. Furthermore, the sensor has high selectivity against interfering components towards TYR screening.

The third study presents micrometric electrochemical imaging of *Escherichia coli* (*E. coli*) biofilms using Soft-Probe-SECM. The on-film reduction of an electro-active compound, here the oxidized form of ferrocene methanol, was used to create *in situ* biofilm metabolic activity maps by applying the feedback mode of SECM. SECM approach curves of identically grown biofilms suggest that the SECM-based detection of metabolic activity was surface-confined. The analysis could therefore be carried out on entire biofilms and tape-stripped biofilm surface layers. The method could distinguish between biofilms containing *E. coli* cells either with or without ampicillin resistance.

Finally, the SECM detection of the degradation of an *E. coli* biofilm in the presence of different gentamicin concentrations was studied.

In the fourth study, the direct effects of various antimicrobial agents, *i.e.*, sodium azide, silver nanoparticles, and flashlight, on the *E. coli* biofilms, were investigated using Soft-Probe-SECM. The degradation of *E. coli* biofilms was investigated by using the feedback mode of SECM. The recorded current depended on the redox activity of the biofilm to regenerate the redox mediator ferrocene methanol. SECM showed the possibility of recording the effect of antimicrobial agents, especially those with intracellular impact. Soft-Probe-SECM recorded the inhibitory effect of sodium azide on the plasma membrane of bacteria. The SECM feedback current decreased by 27% and 46% after 5 min and 15 min of incubation in sodium azide, respectively showing the decrease of the biofilm redox activity and its viability. The inhibitory effect of silver nanoparticles of different sizes and concentrations after one-day incubation were also recorded by SECM feedback mode. The result has shown a 90% reduction of the feedback current after incubation of the biofilm in silver nanoparticles for one day. The flashlight treatments reduced SECM feedback currents by 20%, 78%, and 88% after treating the biofilm with 550 V flashlight irradiations using one, three, and five shots. The flashlight treatment kills bacteria as well as leads to the eradication of the biofilm. Results were compared with complementary detection of live/dead and biomass staining and recording by using fluorescence microscopy. Biofilm viability was recorded based on the permeability of propidium iodide as a fluorescent intercalating agent. SECM was shown to be a sensitive and fast response technique to quantify the antimicrobial effects on the respiratory chain. It can be used as a complementary, for instance, optical microscopic technique, for recording the biofilm activity.

Finally, a novel antibiofilm material was developed based on DNA origami nanostructures loaded by Doxorubicin (DOX) to efficiently and selectively kill bacteria within a biofilm. The DNA origami nanostructures were utilized as nanocarriers to transport an antibiotic through the 3D structure of a biofilm and address one of the main challenges for treating biofilms, which is the efficient penetration of antibiofilm reagents through the extracellular polymeric matrix of the biofilm. The antimicrobial drug DOX, which inhibits bacteria growth, was loaded into DNA origami nanostructure. After that, a readout strategy was designed and developed to study the DOX/DNA origami treatment effects against biofilms using confocal laser scanning microscopy imaging and microelectrode arrays. The complementary readout showed that the DOX/DNA origami penetrated the biofilm efficiently. Furthermore, the treatment of DOX/DNA origami led to both the inhibition of biofilm formation and the eradication of the biofilm. The novel DOX/DNA origami could be a promising material for the selective treatment against biofilms thanks to their efficient penetration.

Keywords

Scanning electrochemical microscopy, Soft probe, Tyrosinase, Catechol, Melanoma, *E. coli* biofilm, Bioimaging, Antibiofilm treatments, silver nanoparticle, Sodium azide, microelectrode array, DNA origami, Doxorubicin, confocal laser scanning microscopy, Structured illumination microscopy.

Résumé

La bioimagerie non invasive ou semi-invasive est d'un grand intérêt pour le diagnostic car elle permet de cartographier la distribution et la concentration de biomarqueurs dans un échantillon biologique. Les informations obtenues peuvent être utilisées pour concevoir et définir des traitements efficaces contre le cancer et les structures biologiques pathogènes telles que les biofilms. La bioimagerie électrochimique est basée sur la détection locale de réactions d'oxydoréduction sur des sites de substrats locaux, et sa résolution peut atteindre des (sub)micromètres. Sa tolérance aux perturbations optiques est un avantage particulier par rapport aux méthodes de détection basées sur la lumière. La bioimagerie électrochimique peut être appliquée pour étudier les réactions de transfert d'électrons et l'activité métabolique d'échantillons biologiques. Par la mise en œuvre de complexes d'immuno-affinité, il peut être rendu spécifique de protéines et d'autres biomolécules. Une plate-forme de sonde à balayage électrochimique peut être utilisée, telle que la microscopie électrochimique à balayage (SECM), dans laquelle une sonde électrochimique micrométrique est traduite à proximité immédiate d'une surface. La partie active de la pointe détecte les espèces électro-actives générées ou consommées par un site actif sur le substrat. En matière d'échantillons biologiques, la SECM a notamment trouvé des applications pour l'étude des cellules vivantes, des levures et des bactéries.

Cette thèse portait sur l'utilisation de la bioimagerie électrochimique pour détecter les biomarqueurs du mélanome de manière non et semi-invasive et sur le développement de nouvelles stratégies électrochimiques pour étudier les biofilms et les effets des traitements par biofilm.

Tout d'abord, une approche de détection électrochimique non invasive du mélanome est présentée, basée sur l'utilisation de rubans adhésifs pour collecter et fixer les cellules d'une zone cutanée suspecte et les transférer dans un SECM pour leur analyse. La couche adhésive recueille les cellules de la couche cornée et les maintient bien collées à la couche adhésive du ruban pendant les expériences dans une solution d'électrolyte. Un biomarqueur de mélanome, ici l'enzyme intracellulaire tyrosinase (TYR), a été détecté dans les cellules collectées sur bande, rendues perméables par le processus de stripping. Des anticorps spécifiques de TYR ont été utilisés qui ont été marqués avec de la peroxydase de raifort (HRP). Les marqueurs HRP ont catalysé l'oxydation d'une sonde à activité redox dissoute, qui a été détectée au niveau d'une microélectrode souple. La microélectrode souple a été balayée sur l'échantillon dans un mode de contact doux, ce qui était essentiel pour réaliser et maintenir une distance de travail constante. Le biomarqueur du mélanome a été détecté pour la première fois sur des échantillons prélevés sur bande avec des cellules de mélanome murin de différentes concentrations. Après cela, des niveaux croissants de TYR ont été enregistrés dans des cellules prélevées sur la peau de modèles murins de mélanome représentant trois stades différents de croissance tumorale. De plus, les résultats SECM de différentes lignées cellulaires de mélanome humain dépouillées de bandes étaient conformes aux études précédentes basées sur des cellules de mélanome traditionnellement fixées et perméabilisées.

La deuxième étude envisageait la détection électrochimique directe semi-invasive de biomarqueurs de mélanome dans la peau non traitée. L'enzyme tyrosinase devait être traitée avec un capteur électrochimique à micro-aiguille. Les microaiguilles ont été fabriquées par coulée de polydiméthylsiloxane (PDMS) avec des polymères stables. Les micro-aiguilles (MN) telles que préparées ont ensuite été recouvertes par pulvérisation d'or. Les MN d'or ont finalement été recouverts d'alginate/catéchol pour fournir une couche d'électrolyte liquide contenant des espèces électroactives, telles que le catéchol, dont l'état redox peut être lié à la concentration de TYR dans la peau. Le capteur a montré une sensibilité élevée de $7,52 \mu\text{A} \cdot \text{mg}^{-1} \cdot \text{mL}^{-1}$ TYR dans une peau factice. Un écart type relatif (RSD) de 9 % ($n = 5$) a démontré que l'électrode catéchol@alginate : or MN avait une excellente reproductibilité pour la détection continue de TYR. De plus, cinq électrodes parallèles Catechol@alginate : or MN ont été fabriquées en utilisant la même configuration expérimentale et ont montré un RSD de 4 % ($n=5$). Ces résultats suggèrent que le processus de fabrication des électrodes était reproductible et que les biocapteurs Catechol@alginate: gold MN ont démontré une stabilité élevée pour la détection répétitive de TYR. De plus, le capteur a une sélectivité élevée contre les composants interférents vers le dépistage TYR.

La troisième étude présente l'imagerie électrochimique micrométrique des biofilms d'*Escherichia coli* (E. coli) à l'aide de Soft-Probe-SECM. La réduction sur film d'un composé

électroactif, ici la forme oxydée du ferrocène méthanol, a été utilisée pour créer des cartes d'activité métabolique du biofilm in situ en appliquant le mode de rétroaction de SECM. Les courbes d'approche SECM de biofilms cultivés de manière identique suggèrent que la détection de l'activité métabolique basée sur SECM était confinée à la surface. L'analyse pourrait donc être réalisée sur des biofilms entiers et des couches superficielles de biofilms striées. La méthode pourrait faire la distinction entre les biofilms contenant des cellules d'E. coli avec ou sans résistance à l'ampicilline. Enfin, la détection SECM de la dégradation d'un biofilm d'E. coli en présence de différentes concentrations de gentamicine a été étudiée.

Dans la quatrième étude, les effets directs de divers agents antimicrobiens, c'est-à-dire l'azoture de sodium, les nanoparticules d'argent et la lampe de poche, sur les biofilms d'E. coli, ont été étudiés à l'aide de Soft-Probe-SECM. La dégradation des biofilms d'E. coli a été étudiée en utilisant le mode de rétroaction de SECM. Le courant enregistré dépendait de l'activité redox du biofilm pour régénérer le médiateur redox ferrocène méthanol. SECM a montré la possibilité d'enregistrer l'effet des agents antimicrobiens, en particulier ceux à impact intracellulaire. Soft-Probe-SECM a enregistré l'effet inhibiteur de l'azoture de sodium sur la membrane plasmique des bactéries. Le courant de rétroaction SECM a diminué de 27% et 46% après 5 min et 15 min d'incubation dans l'azoture de sodium, montrant respectivement la diminution de l'activité redox du biofilm et sa viabilité. L'effet inhibiteur des nanoparticules d'argent de différentes tailles et concentrations après une journée d'incubation a également été enregistré par le mode de rétroaction SECM. Le résultat a montré une réduction de 90 % du courant de rétroaction après incubation du biofilm dans des nanoparticules d'argent pendant une journée. Les traitements à la lampe de poche ont réduit les courants de rétroaction SECM de 20 %, 78 % et 88 % après avoir traité le biofilm avec des irradiations de lampe de poche de 550 V en utilisant un, trois et cinq coups. Le traitement à la lampe de poche tue les bactéries et conduit à l'éradication du biofilm. Les résultats ont été comparés à la détection complémentaire de la coloration et de l'enregistrement des vivants/morts et de la biomasse en utilisant la microscopie à fluorescence. La viabilité du biofilm a été enregistrée sur la base de la perméabilité de l'iodure de propidium en tant qu'agent d'intercalation fluorescent. La SECM s'est avérée être une technique de réponse sensible et rapide pour quantifier les effets antimicrobiens sur la chaîne respiratoire. Elle peut être utilisée comme technique complémentaire, par exemple en microscopie optique, pour enregistrer l'activité du biofilm.

Enfin, un nouveau matériau antibiofilm a été développé sur la base de nanostructures d'origami d'ADN chargées par la doxorubicine (DOX) pour tuer efficacement et sélectivement les bactéries dans un biofilm. Les nanostructures d'origami d'ADN ont été utilisées comme nanosupports pour transporter un antibiotique à travers la structure 3D d'un biofilm et relever l'un des principaux défis du traitement des biofilms, à savoir la pénétration efficace des réactifs antibiofilm à travers la matrice polymérique extracellulaire du biofilm. Le médicament antimicrobien DOX, qui inhibe la croissance des bactéries, a été chargé dans la nanostructure de l'origami d'ADN. Après cela, une stratégie de lecture a été conçue et développée pour étudier les effets du traitement origami DOX/ADN contre les biofilms en utilisant l'imagerie confocale par microscopie à balayage laser et des matrices de microélectrodes. La lecture complémentaire a montré que l'origami DOX/ADN a pénétré efficacement le biofilm. De plus, le traitement de l'origami DOX/ADN a conduit à la fois à l'inhibition de la formation de biofilm et à l'éradication du biofilm. Le nouvel origami DOX/ADN pourrait être un matériau prometteur pour le traitement sélectif contre les biofilms grâce à leur pénétration efficace.

Mots-clés

Microscopie électrochimique à balayage, Sonde souple, Tyrosinase, Catéchol, Mélanome, Biofilm E. coli, Bioimagerie, Traitements antibiofilm, nanoparticule d'argent, Azoture de sodium, barrette de microélectrodes, Origami DNA, Doxorubicine, Microscopie confocale à balayage laser, Microscopie à illumination structurée.

List of abbreviations

Abbreviation	Full form of a word or phrase
ABNC	Active but nonculturable
AgNP	Silver nanoparticle
2D	Two dimensional
3D	Three dimensional
Ab	Antibody
AC	Approach curve
AFM	Atomic force microscopy
AgNP	Silver nanoparticle
BSA	Bovine serum albumin
CV	Cyclic voltammograms
CV	Crystal violet
CFU	Colony-forming unit
CLSM	Confocal laser scanning microscopy
DMSO	Dimethylsulphoxide
DOX	Doxorubicin
E. coli	Escherichia coli
EcN	E. coli Nissle
EPS	Extracellular polymeric substances
EMA	Ethidium monoazide
ETC	Electron transport chain
EDTA	Ethylenediaminetetraacetic acid
FACS	Fluorescent activated cell sorting
FCM	Flow cytometry
FNA	Fine needle aspiration
HRP	Horse radish peroxidase
IHC	Immunohistochemistry
ISF	interstitial fluid
LCMM	Laser capture microdissection microscopy
LSM	Laser scanning micrograph
LPS	lipopolysaccharides
MN	Microneedle
MEA	Microelectrode array
MS	Multispectral
NASBA	Nucleic acid sequence-based amplification
NP	Nanoparticle
O	Oxidized form of the redox active species
OCTA	Optical coherence tomography
PBS	Phosphate buffered saline
PCA	Phenazine-1-carboxylic acid
PCR	Polymerase chain reaction
PET	Polyethylene terephthalate
PGA	Poly-glycolic acid
PI	Propidium iodide
PIA	Polysaccharide intercellular adhesin
PLA	Poly-L-lactic acid
PLGA	Poly-lactic-co-glycolic acid
PMA	propidium monoazide
PMM	Poly (methyl methacrylate)
P. aeruginosa	Pseudomonas aeruginosa
PVP	Polyvinylpyrrolidone

PYO	Phenazine pyocyanin
qPCR	quantitative PCR
QRE	quasi-reference electrode
R	Reduced form of the redox active species
RC	Redox competition
RE	Reference electrode
RT	Reverse transcription
RT-PCR	Reverse transcriptase PCR
RT-qPCT	Real time-quantitative polymerase chain reaction
RT-SDA	reverse transcriptase-strand displacement amplification
RIERT-SDA	Reactive ion etchingreverse transcriptase-strand displacement amplification
RGP	Radial growth phase
RNA	Ribonucleic acid
rms	Root mean square
rRNA	Ribosomal ribonucleic acid
[Ru(NH ₃) ₆] ³⁺	Ruthenium (III) hexaamine ion
<i>S. aureus</i>	<i>Staphylococcus aureus</i>
<i>S. epidermidis</i>	<i>Staphylococcus epidermidis</i>
SECM	Scanning electrochemical microscopy
SECCM	Scanning electrochemical cell microscopy
SEMS	Scanning electron microscopy
SG/TC	Substrate generation/tip collection
SICM	Scanning ion-conductive microscopy
SOB	Super Optimal Broth
SOC	Standard of care
SPD	Surfactant polymer dressing
SWV	Square-wave-voltammetry
T	Tip
TiO	Titanium oxide
TG/SG	Tip generation/substrate collection
TyR	Tyrosinase
UME	Ultramicroelectrode
UV	Ultraviolet
VGP	Vertical growth phase
WE	Working electrode

List of symbols

Symbol	Meaning	Units
c	Concentration	$\text{mol} \cdot \text{cm}^{-3}$
c_0	Maximum concentration	$\text{mol} \cdot \text{cm}^{-3}$
c_{Bulk}	Bulk concentration	mol cm^{-3}
D	Diffusion coefficient	$\text{cm}^2 \cdot \text{s}^{-1}$
d	Probe-substrate distance in SECM	μm
E_{T}	Probe (tip "T") potential	V
F	Faraday constant	C
h_{p}	Height of probe, plastic probe body-substrate distance for plastic microelectrode in Soft-Probe-SECM	μm
i	Current	nA
I	Normalized current	dimensionless
i_{s}	Substrate current in SECM	nA
i_{T}	Tip ("t") current recorded at the microelectrode in SECM	nA
I_{T}	Normalized current recorded at each point steady-state diffusion	dimensionless
$i_{\text{T},\infty}$	current recorded at the SECM tip in the solution bulk	nA
t	Time	s
v_{T}	Translation rate of the tip in SECM	$\mu\text{m} \cdot \text{s}^{-1}$

Content

Acknowledgment	4
Abstract	5
Résumé	7
List of abbreviations	9
List of symbols	11
CHAPTER 1 INTRODUCTION	16
1.1 Electrochemical imaging.....	16
1.1.1 Scanning electrochemical microscopy (SECM).....	17
Major SECM constraints	21
SECM applied to biological samples	22
Soft-Probe-SECM electrochemical microscopy.....	22
Instrumentation of Soft-Probe-SECM	25
1.1.2 2D chips with microelectrode arrays.....	26
Design of a Microelectrode Array (MEA)	27
1.2 Melanoma	28
1.2.1 Characteristics of Melanoma	28
1.2.2 Conventional detection methods	29
1.2.3 Electrochemical biosensors for the detection of the Melanoma biomarkers	30
1.2.3.1 Tyrosinase	30
1.2.3.2 Electrochemical detection and microneedle-based biosensors	31
1.3 Bacterial biofilms.....	33
1.3.1 Detection methods for biofilms viability	35
1.3.1.1 Colony forming units (CFU).....	35
1.3.1.2 Polymerase chain reaction (PCR)	37
Ethidium monoazide (EMA)- and propidium monoazide (PMA)- PCR.....	37
Reverse transcriptase PCR (RT-PCR)	38
Real time quantitative polymerase chain reaction (RT-qPCT or qPCR)	39
1.3.1.3 Flow cytometry (FC)/fluorescent activated cell sorting (FACS).....	39
1.3.1.4 Microscopy methods.....	40
Electrochemical bio-imaging.....	41
1.3.2 Methods for the treatment of biofilm	43
1.3.2.1 Antibiotics	44
1.3.2.2 Biofilm eradication	44
1.3.2.2.1 Ultrasound debridement	45
1.3.2.2.2 Mechanical / sharp debridement	45

1.3.2.2.3 Chemical debridement.....	46
1.3.2.3 Nanotechnology.....	46
1.3.2.3.1 Antibiofilm Mechanism of Nanoparticles.....	46
1.3.2.3.2 Metal/ metal oxide-based nanoparticles.....	47
1.3.2.3.3 Polymeric nanoparticles.....	47
1.4 Thesis outline.....	48
CHAPTER 2 EXPERIMENTAL PART	49
2.1. Sample preparations.....	49
2.1.1 <i>In vitro</i> cell culture methods on adhesive tape	49
2.1.2 Melanoma mouse model and tape stripping of melanoma samples	50
2.1.3 TYR Immunoassay for melanoma detection	51
2.1.4 Colorimetric visualization of TYR immunoassays for melanoma detection.....	52
2.1.5 Ampicillin resistant <i>E. coli</i> DH5 α cells.....	52
2.1.6 Preparation of <i>E. coli</i> DH5 α and ampicillin-resistant <i>E. coli</i> DH5 α cell cultures.....	52
2.1.7 <i>E. coli</i> DH5 α biofilm culture	52
2.1.8 <i>E. coli</i> BL21 biofilm culture	52
2.1.9 Biofilm tape stripping procedure and sample preparation	53
2.1.10 Antibiotic treatments for biofilm degradation	53
Gentamicin treatment	53
Sodium azide	53
Silver nanoparticles in three methods	53
2.1.11 Reactions of silver NPs with biofilms.....	54
2.1.12 Flashlight irradiation for treating biofilms	54
2.1.13 Synthesis of DNA origami nanostructures for biofilm studies.....	54
2.1.14 Loading of DOX to DNA origami for biofilm treatments.....	55
2.1.15 Filtering of DOX loaded to DNA origami for DOX loading efficiency studies	55
2.1.16 <i>In vitro</i> release profiles of Doxorubicin for biofilm studies	55
2.2. Characterization methods.....	55
2.2.1 Soft-Probe-SECM measurements for melanoma and biofilm studies.....	55
2.2.2 Electrochemical characterization of the Gold MN electrode for melanoma studies.....	57
2.2.3 Optical microscopy of melanoma and biofilm samples	57
2.2.4 Electroanalytical measurements with the MN electrode for tyrosinase detection	57
2.2.5 Confocal laser scanning microscopy (CLSM) for biofilm characterization	57
2.2.6 Crystal violet staining of biofilms	58
2.2.7 Scanning electron microscopy (SEM) of biofilms	58
2.2.8 Statistical analysis	58
2.2.9 Characterization of AgNPs, Ag/PVP nanocomposites	58
2.2.10 Atomic Force Microscopy (AFM) of DNA origami for biofilm treatments.....	59
2.2.11 Structured Illumination Microscopy (SIM) for bacteria studies	59
2.2.12 SIM images of <i>E. coli</i> treated by DNA origami	59

2.2.13 SIM images of <i>E. coli</i> treated by DOX	59
2.2.14 Fabrication of 2D microelectrode arrays (MEAs) for biofilm analysis	59
2.2.15 Electrochemical characterization of the MEAs for biofilm analysis	60
CHAPTER 3 Tape-stripping electrochemical detection of melanoma	64
3.1 Introduction	65
3.2 Results and discussion	67
3.3 Conclusions	81
CHAPTER 4 Toward <i>ex vivo</i> performance evaluation of a transdermal gold injectable microneedle for tyrosinase sensing	83
4.1 Introduction	84
4.2 Results and discussion	85
4.2.1 Fabrication of the polymeric base of MNs	85
4.2.2 Gold coating	89
4.2.3 Mechanical behavior of gold-coated MNs	90
4.2.4 Definition of the active areas of the gold microneedles	92
4.2.5 Hydrogel coating of the microneedles	93
4.2.6 Electrochemical properties of hydrogel coated gold MNs	93
4.3 Conclusion	97
CHAPTER 5 Soft-Probe-Scanning Electrochemical Microscopy reveals electrochemical surface reactivity of <i>E. coli</i> biofilms	99
5.1 Introduction	100
5.2 Results and discussion	100
5.2.1 Optical characterization of biofilm surfaces	100
5.2.2 SECM feedback mode characterization of <i>E. coli</i> biofilms surfaces	105
5.2.3 Feedback mode imaging of biofilm formation with ampicillin resistant or susceptible DH5 α <i>E. coli</i> cells	110
5.2.4 SECM imaging of <i>E. coli</i> biofilm during antibiotic treatment	116
5.3 Conclusions	117
CHAPTER 6 Revealing the effects of four different antimicrobial agents on <i>E. coli</i> biofilms by using Soft-Probe Scanning Electrochemical Microscopy	119
6.1 Introduction	120
6.2. Results and discussion	121
6.2.1 Selection of redox mediator for feedback mode imaging of native <i>E. coli</i> biofilms	121
6.2.2 SECM investigation of biofilm degradation induced with azide	127
6.3.3 SECM investigation of biofilm degradation by silver nanoparticles	133
6.3.4 SECM investigation of biofilm treatment by flashlight	140
6.3 Conclusions	144
CHAPTER 7 Destruction of <i>E. coli</i> biofilms with DNA nanostructures loaded Doxorubicin	146
7.1 Introduction	147
7.2 Results and discussion	149

7.2.1 Doxorubicin loaded DNA origami	149
7.2.2 DOX/DNA origami against E.coli planktonic bacteria	153
7.2.3 DOX/DNA origami against E.coli biofilm.....	157
7.3 Conclusion	170
CHAPTER 8 General conclusions and future perspectives	171
References	179
Curriculum vitae: Sorour Darvishi	199

CHAPTER 1 INTRODUCTION

This thesis proposes and implements complementary detection based on electrochemical and fluorescence bioimaging for early and non-invasive detection. The thesis is divided into two main targets, melanoma and bacteria biofilms.

A non-invasive method has been developed to collect sample surfaces, such as cutaneous cells from suspicious areas of skin that was followed by the detection of the expression of tyrosinase, a melanoma protein marker. In the second part of the thesis, the surface activity of a bacteria biofilm was studied based on Soft-Probe-Scanning electrochemical microscopy (SECM). Finally, several complementary studies were performed to investigate the impact of antibiofilm reagents.

1.1 Electrochemical imaging

Taking high-resolution images of electrochemical reactions is important for many applications in various fields that include material science, energy research, life sciences, (electro-) and (photo-) catalysis, transport phenomena studies, and neurochemistry [1]. It is possible to divide electrochemical imaging platforms into two groups. First, an electrical probe records data at defined raster points over a biological sample using a nano- or micrometric probe (called a tip) whose position is controlled with nano-resolved motoric positioners. Secondly, the biological sample is deposited onto a microchip, consisting of an array of individually addressable microelectrodes (MEs) or nanoelectrodes. The imaging resolution depends on for instance on the microelectrode size, working distance, the active region under the ME and the relationships thereof. Most electrochemical imaging methods developed to date have been scanning probe microscope (SPM) techniques, such as scanning electrochemical microscopy (SECM) [2]. Still, microelectrode arrays with increasing numbers of individually addressable MEs, increasing resolution, and faster data acquisition rates get increasingly into the focus.

Furthermore, the hyphenation of SPMs with an optical microscope enables accurate probe positioning and complementary optical detection methods of biological samples such as living cell cultures on glass or in plastic dishes. This thesis reports several studies using Soft-Probe SECM for electrochemical bioimaging, complementary with optical and fluorescence microscopy, of a range of complex biological samples, such as biofilms and skin samples. Complex in this context relates to

the sample morphology, the addressability of a target analyte, and potential interferences to the signal (e.g., presence of interfering compounds and sample porosity).

1.1.1 Scanning electrochemical microscopy (SECM)

SECM was used in this thesis as the major tool for detecting the expression of cancer biomarkers in skin samples and investigating biofilms. SECM is a scanning probe microscopy technique that exploits for instance faradaic currents (in case of amperometric microelectrodes) to obtain topographical and microelectrochemical information of a substrate surface. Potentiometric SECM tips record local distributions of ions or local pH values. Considering Engstrom *et al.* [3], the first measurement that was later considered as the SECM experiment, was made in 1986 using a microelectrode to measure the concentration profile of a redox species, thus the diffusion layer, above a biased macroscopic electrode. In another work at about the same time, Bard and co-workers observed surprisingly large currents recorded at the tip of an electrochemical scanning tunneling microscope (ECSTM) when it was positioned near a conductive substrate outside the tunneling distance [4]. The authors realized that the current was caused by a flux of redox-active species from the substrate and not by tunneling currents. Based on these discoveries, Bard and colleagues developed a quantitative description of the diffusion-limited current at a ME as a function of the working distance above a macroscopic planar sample and called it "scanning electrochemical microscopy (SECM)" [5-8].

In SECM, a tiny electrode tip generally called an ultramicroelectrode (UME) or simply microelectrode ME, with a disc-shaped active part with a diameter of $\leq 25\ \mu\text{m}$ is positioned near a conductive, semiconductive, or insulating substrate. It is also denoted as tip "T". The substrate and the UME are immersed in an electrolyte solution. The type of probe electrode used in SECM depends on the particular process under investigation. A diversity of probes is available for amperometry and potentiometry. An amperometric UME is fabricated by sealing a metal wire or carbon fibre into a glass capillary, making an electrical connection, and polishing the end of the sealed tip flat to obtain the disk shape; **Fig.1.1a** and **Fig.1.1b** show illustrations of such a UME. Pt, Au, and C UMEs have been successfully fabricated in this way. For most SECM studies, the ratio of the radius of the entire tip (electrode plus surrounding insulator, r_{total}) to that of the active part, a , $\text{RG} = r_{\text{total}}/a$ is typically around 10. Still, it can be larger and smaller depending on the purpose of use. Larger RG values minimize the effects of diffusion from behind the probe and make the electrode response more sensitive to the surface process [9]. Still, it is often more challenging to approach them as close as possible to a sample, as most of the time, the tip and sample are not positioned 90° to each other. In that case, the tip corner can touch the substrate while the active part of the microelectrode is still far. Smaller tips can be easier approached very close to a sample, but, as mentioned, diffusion from the back of the tip can contribute substantially to the tip response.

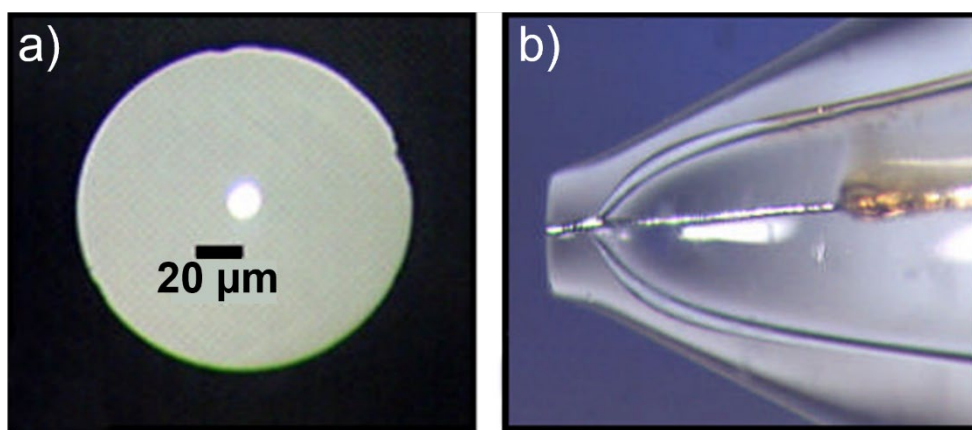


Fig.1.1 Optical microscope images: (a) disc-shaped UME (top view), (b) disc-shaped UME (side view). Adapted with permission from ref. [9]. Copyright 2018 Springer.

SECM is used to characterize processes and structural features at the surface of a substrate while the tip is translated near the surface. Microelectrodes have several typical attributes, including small currents, steady-state responses, and short response times [10]. The tip can be translated from the bulk solution towards the surface (z-direction, for instance, to probe the diffusion layer), or the tip can be scanned at constant height (z constant) along the surface (the x and y directions). The tip and substrate are part of an electrochemical cell that usually contains an auxiliary and a reference electrode. For amperometric microelectrodes, the tip current results from electron transfer reactions at the tip and the substrate and is controlled by the electron transfer kinetics at the interfaces and mass transfer processes in solution.

Other similar scanning electrochemical probe techniques, such as scanning ion conductance microscopy (SICM) [11], scanning electrochemical cell microscopy (SECCM) [12], SECM-atomic force microscopy [13], and combinations of them, such as SECM-SICM [14, 15], have been developed and were used for a variety of electrochemical imaging-based studies. Together, these scanning electrochemical probe techniques make a very useful suite of electrochemical imaging methods. They have been applied for the imaging of a variety of subjects, including living cells [16], electrocatalyst arrays [17], surface corrosion [18], nanopore transport [19], and single nanoparticles [20].

SECM can be used to image the reactivity and topography of biological specimens and detect electrochemically metabolites for mapping localized biochemical activity [21-25]. Several SECM modes of operation have been developed, including the feedback mode, the tip generation/substrate collection (TG/SC) mode, the substrate generation/tip collection mode (SG/TC), the redox competition (RC) mode, the penetration mode, and the ion transfer mode. However, the feedback and generation/collection modes are the most widely used ones for SECM imaging.

Feedback mode

The feedback mode is widely used to investigate electron transfer kinetics [26]. In this mode, a UME is immersed in a solution containing a so-called redox mediator, for example, in its reduced form R. When a suitably positive potential is applied at the tip, R is oxidized to its oxidized form O according to (Equation 1.1):



Usually, the system selected (electrode material and redox mediator) demonstrates fast electrode kinetics. The current at the UME is determined by the diffusion of R to the UME tip surface. When the tip is positioned far from the substrate ($d > 10a$, where d is the distance between tip and substrate and a is the radius of the active part of a disk-shaped electrode), the steady-state current in bulk solution $i_{T,\infty}$ is:

$$i_{T,\infty} = 4nFDca \quad (\text{Equation 1.2})$$

Where F is the Faraday constant, n is the number of electrons exchanged in the redox reaction, D is the diffusion coefficient of R, and c_∞ is the bulk concentration of R. The number 4 is a factor related to the geometry of the UME and is valid for disc-shaped active parts with an infinitely large RG value. When the tip is brought very close to a conducting substrate (*i.e.*, within few tip radii), the species O that was generated at the UME and that diffused to the substrate can be reduced back to R based on the reaction:



This process causes the production of an additional flux of R to the tip, defined as “positive feedback” if the reaction at the sample is very fast. The resulting current is $i_T > i_{T,\infty}$. In contrast, when the substrate is inert, the diffusion of R to the active part of the UME is physically hindered by the presence of the substrate, and therefore $i_T < i_{T,\infty}$ (“negative feedback”) (**Fig.1.2**). On the one hand, the feedback currents depend on the working distance and recording tip current-working distance relationships, so called approach curves, results in very characteristic graphs, in which positive feedback represents the limiting case of fast sample reaction kinetics and negative feedback of a purely insulating surface. On the other hand, the feedback currents depend on the kinetics of the electrode reactions at the substrate. Electrode reactions of finite kinetics result in a reduced flux of regenerated redox mediator to the SECM tip and the obtained feedback currents are lower than for the limiting case of positive feedback but higher than for negative feedback. Indeed, approach curves can be used to extract the rates of heterogeneous reactions at the sample by fitting experimentally obtained approach curve data to analytical approximations using software. What can be obtained are heterogeneous reaction rate constants. However, in this thesis no quantitative analysis of approach curve data was made and the theory is therefore not discussed in detail.

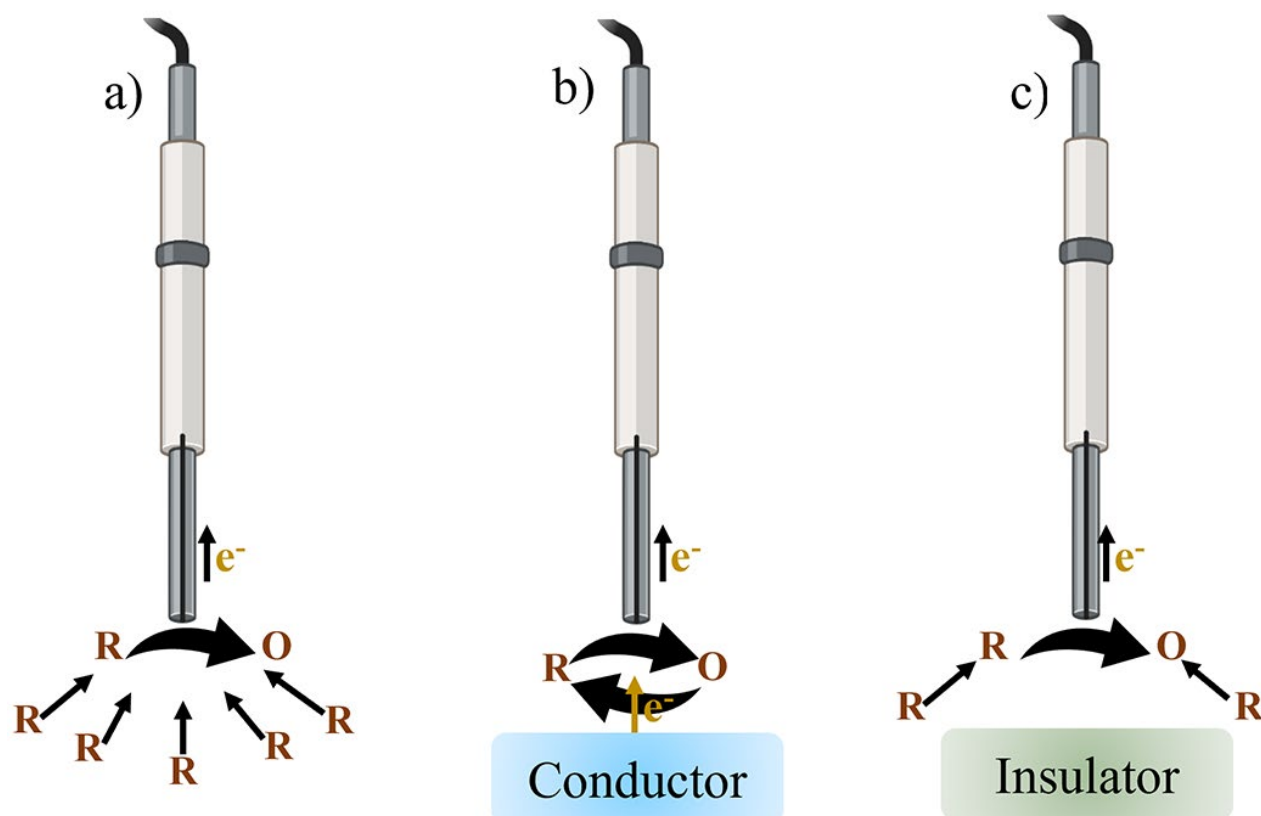


Fig.1.2 Schematic representation of the SECM operation in feedback mode: (a) UME tip far from the substrate. (b) Positive feedback: the species R is regenerated at the substrate. (c) Negative feedback: the diffusion of R to the UME tip is hindered by the substrate.

Tip generation/substrate collection (TG/SC) and substrate generation/tip collection (SG/TC) modes

A schematic of generation/collection modes is shown in **Fig.1.3**. In this SECM mode, both the tip and the substrate can be used as working electrodes, for instance, to generate an electro-active species at one electrode electrochemically and to collect the product at the other electrode. Simultaneous measurements of the tip current, i_T , and substrate current, i_S , are performed and a collection efficiency i_S/i_T for the TG/SC mode can be expressed. For realizing the SG/TC mode, the substrate can be made of an immunoassay with an HRP label, which catalyzes the oxidation of a redox-active species like ferrocene methanol that is collected by the SECM tip. This is often applied in biotechnology applications, for instance, to study and optimize biosensors.

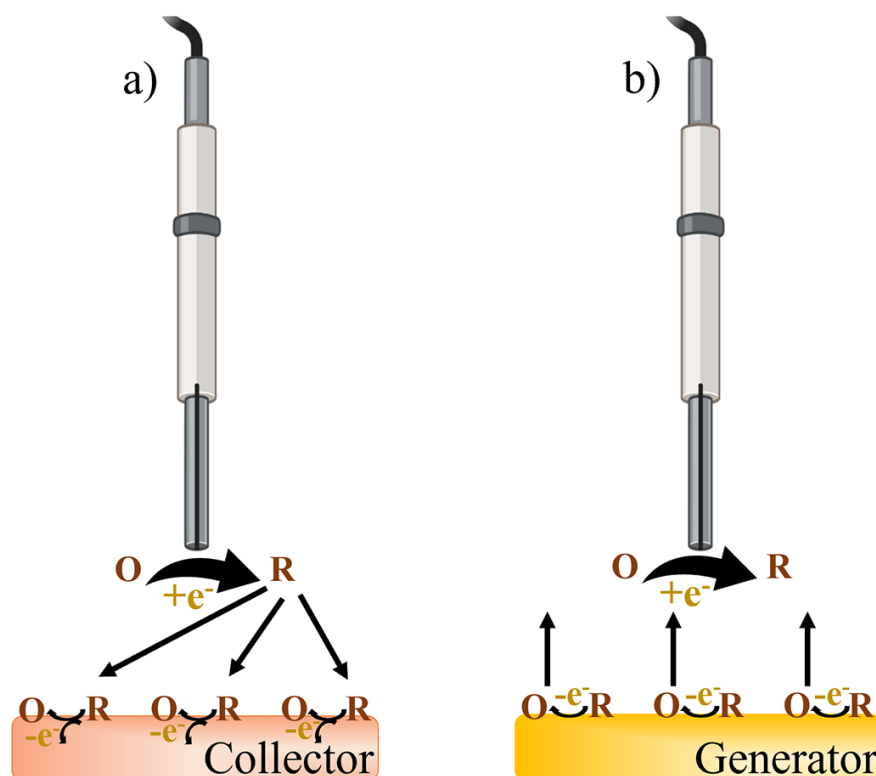


Fig.1.3 Schematic representation of the SECM operation in (a) TG/SC mode and (b) SG/TC mode. The UME tip generates the species R by reduction of O in solution. R diffuses to the substrate and is re-oxidized to O (a). O is electrogenerated at the substrate and collected at the UME. Both tip and substrate currents are recorded.

Redox competition mode

The redox competition mode (RC-SECM), in which the UME and the sample compete for the same analyte in solution, often oxygen, was introduced by Schuhmann and coworkers [27]. During the experiment, the oxygen reduction current recorded at a UME remained constant unless the UME approached an oxygen-consuming feature on a substrate, *e.g.*, an electrocatalyst, as the oxygen concentration in the gap between UME and substrate is depleted. For this mode, both the UME and a conductive substrate must be held at the oxygen reduction potential [28, 29].

Major SECM constraints

The study of real samples requires overcoming several drawbacks encountered in SECM, such as the probe response dependence on both the chemical reactivity of the sample surface and the working distance. Consequently, it is required to maintain a constant d during scanning to avoid topographic artifacts (*e.g.*, with tilted or rough samples). Furthermore, when scanning large area samples (*e.g.*, $> 1 \text{ cm}^2$), experimental times could be as long as 24 h, because rather slow probe translations in the range of micrometers per second must be realized as faster tip movements cause convective disturbances of the diffusion and thus limit resolution.

SECM applied to biological samples

SECM can be used to image the topography and reactivity of biological specimens and detect electrochemically metabolites for mapping localized biochemical activity. SECM analysis of biological samples can require less extensive sample preparation times compared to traditional fluorescence and colorimetric assays [30]. Fluorescence assays could be invasive and can adversely affect cell health due to labeling and intense illumination required for those measurements [31, 32]. In contrast, SECM measurements of living cells can be non-invasive (when analytes in the cell's microenvironment are investigated) or semi-invasive (when intracellular measurements are performed with nanoelectrodes penetrate the cells). Electrochemical measurements, also when applying the immunoaffinity concept for specific detections of proteins, do not suffer from light-interfering issues, such as photobleaching. SECM has been successfully used to investigate various biological systems because a localized chemical reaction under physiological conditions can be quantitatively characterized *in situ* in a non-invasive manner [33-38]. Interestingly, SECM can detect changes in cellular activity more rapidly than conventional live/dead stains [39]. Further examples of SECM of cells include intracellular measurements of the cell redox activity [40, 41] and assays to evaluate the differentiation status of embryonic stem cells using an indirect enzymatic assay [42, 43].

Constant-height mode cellular scanning electrochemical microscopy has been used for cell visualization. In a first general approach using the feedback mode, a redox mediator was used that did not penetrate through the cell membrane sensing the surface of a living cell like it is a three-dimensional insulator. Scanning in constant height in feedback mode over the cells will reduce the feedback current above the cells as the working distance decreases. Therefore, lower feedback currents compared to the bare substrate surface, usually, a glass slide, indicate the presence of a live cell underneath the UME. The as-obtained SECM line scan or imaging data can approximate the cell shape and height using mathematical functions. The RC mode of SECM can be used to study the oxygen consumption rates of living cells. However, in the latter case, the challenge is to separate the topographic contribution of the SECM signal (hindered diffusion due to the live cell topography) from the oxygen consumption by the cell [44], as both reduce the SECM feedback current.

Soft-Probe-SECM electrochemical microscopy

Conventional SECM experiments are carried out in constant height mode, which has limitations regarding the required constant working distance d if substrates are tilted or uneven. As shown in **Fig.1.4**, scanning over tilted or topographic samples leads to a change of d , which affects i_T . In this case, reactivity and topography contribute both to the signal making it challenging to extract just the reactivity component of the measured signal. In addition, the probe and the sample can be damaged and or contaminated during a mechanical probe-sample contact.

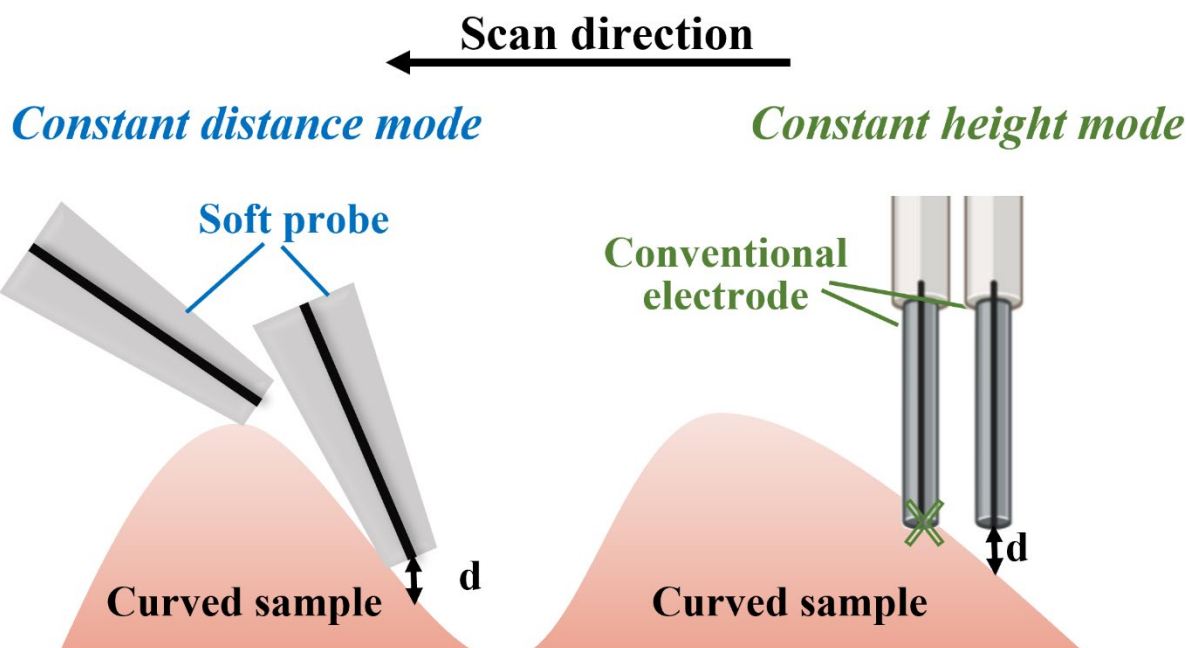


Fig.1.4 Schematic representation of lateral SECM scanning over a curved sample with a conventional microelectrode (right) and a soft probe (left).

So-called soft SECM probes represent an attractive alternative. They are made of thin, flexible materials and were jointly introduced in 2009 by the groups of Girault and Wittstock [45]. Upon mechanical contact with a substrate, the probes bend and are brushed in contact mode over irregularly curved and tilted substrates (**Fig.1.4**). The setup itself operates in standard constant height mode configuration and does not require additional constant distance accessories. For fabricating a soft probe, a microchannel is drilled by UV laser ablation into a thin PET sheet. Then, the channel is filled with a graphite paste, followed by thermal curing at 80°C. Finally, the channels, filled with a conductive carbon track, are covered and sealed with a Parylene C coating of a few micrometer thicknesses. The soft probe production steps are shown in **Fig.1.5**. These thin and flexible probes can be used for scanning biological samples, which often have irregular morphology. For instance, Lin *et al.* [46] [47] reported Soft-Probe-SECM for mapping the distribution of biomarkers and injected nanomaterials in animal and human tissues.

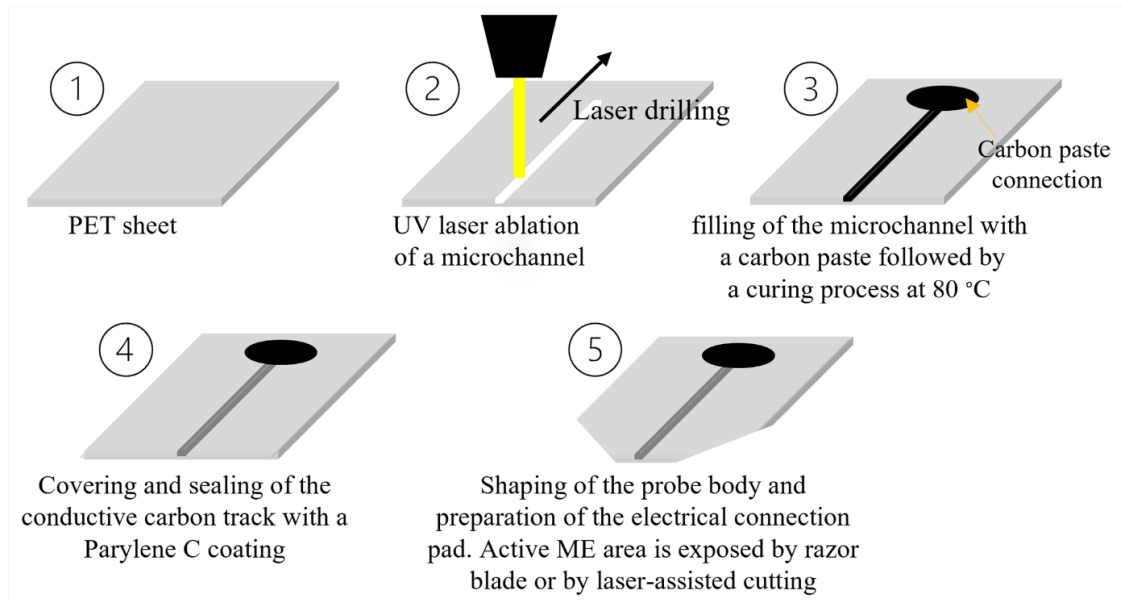


Fig.1.5 Soft probe fabrication: (1) the base of the probe is PET. (2) UV laser ablation of a microchannel in a PET sheet. (3) filling the microchannel with a carbon paste followed by a curing process at 80 °C. (4) Cover and seal the conductive carbon track with a Parylene C coating. (5) Shape the probe body and prepare the electrical connection pad. A razor blade or laser-assisted cutting exposes the active microelectrode area.

These soft probes also known as Soft Stylus Probes, allow SECM imaging in contact mode of tilted and curved substrates since the flexibility of the soft probes allows the probe body to follow the topography of the sample surface. As a result, a nearly constant working distance is achieved, avoiding changes in the recorded current related to different topographic artifacts. This is true as long as the soft probe scans surface artifacts that are larger than the soft probe width. Furthermore, the soft stylus probe concept can be multiplexed into an array format [46] so that a larger sample area can be scanned in a shorter time than a single microelectrode [48-50]. In order to achieve this, multichannel potentiostats or multiplexers need to be integrated into the SECM setup.

For plotting approach curves that include the touching of the sample and bending/sliding of the soft probe on the surface, a vertical coordinate h_p (height of the probe) is applied (**Fig.1.6**). It describes the difference $h_p = h_A - l_T$ between the height of the attachment point above the sample h_A and the vertical extension l_T of the unbent probe. Thus, the effective working distance d is defined as where α is the angle between the cross-sectional plane of the probe and the sample surface and t_L is the thickness of an insulating film, such as a Parylene C film, that covers the carbon tracks. In Eq. 1.4, the working distance depends on h_p , while in Eq. 1.5, the working distances change only if α changes, which happens only slightly.

$$d = h_p + t_L \sin(\alpha); (h_p > 0, \text{non-contact region}) \quad (\text{Equation 1.4})$$

$$d = t_L \sin(\alpha); (h_p < 0, \text{contact region}) \quad (\text{Equation 1.5})$$

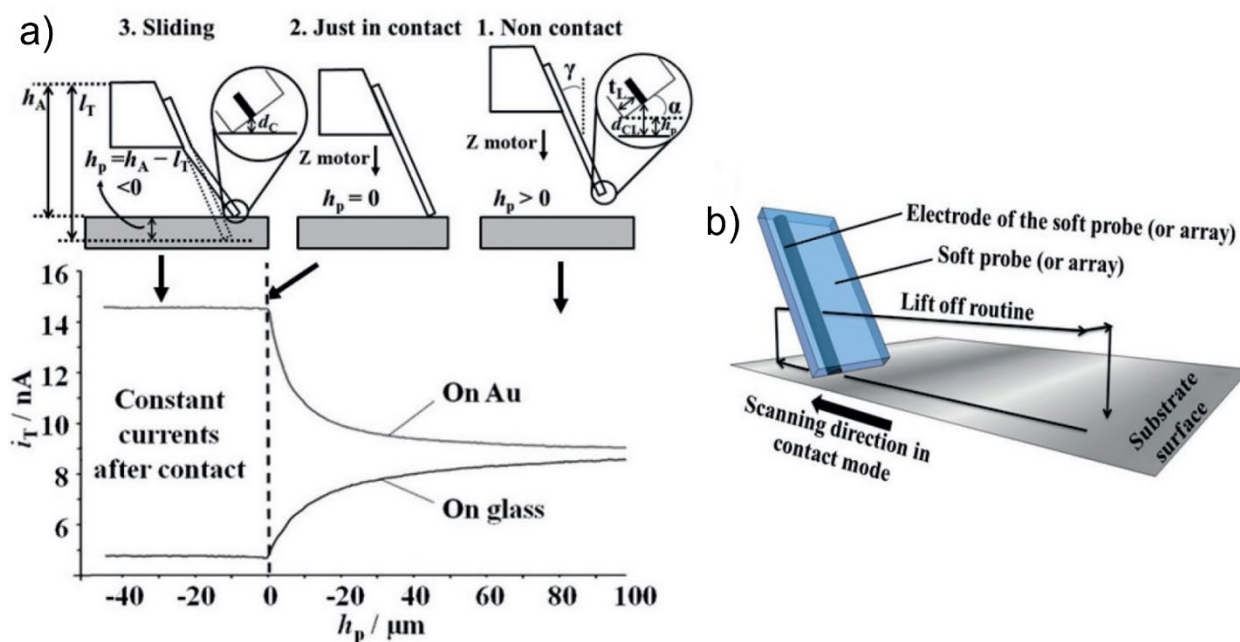


Fig.1.6 (a) Recording current-distance curves with a soft probe on gold and glass surfaces. (b) Schematic representation of soft probe translations during SECM imaging. (a-b) Adapted with permission from ref. [51]. Copyright 2018 Springer.

During Soft-Probe-SECM imaging, the soft probe is translated in an x-y plane and the SECM currents are recorded at defined grid points. With soft probes, the scanning mode is different from typical SECMs, where the probe is moved forward and backward identically. Soft probes must be retracted properly from the substrate surface using a lift-off mode after a contact mode line scan has been completed. Consequently, there is no overbending or mechanical stress on the probe or the substrate. After repositioning the probe with a small displacement perpendicular to the scanning direction, the probe is reapproached and the following line scan started. As the soft probe is bent, the bending direction when being in contact is predefined (**Fig.1.6b**). This brings advantages for scanning stability.

Instrumentation of Soft-Probe-SECM

The basic SECM setup consists of hardware components to precisely position and translate a soft probe vertically and horizontally over a sample surface (**Fig.1.7**). The soft probe is attached to a fine x,y,z positioning system composed of piezoelectric, stepper, or hybrid motor to control the probe position. Additionally, a (bi)potentiostat is required to control the applied potential at the tip and/or the substrate and measure the current produced at the substrate and/or the tip. Since low current values (*i.e.*, pA to nA) are measured and high precision probe positioning (*i.e.*, μm range) is required, electromagnetic noise and mechanical vibrations should be avoided by isolating the SECM setup inside a Faraday cage by placing it on top of an anti-vibration table. However, rapid tip movements can cause convection in the solution around the microelectrode, which perturbs the diffusion of redox-active species and thus influences the measurement results, especially for high-resolution experiments. As a result, experiments with translation speeds higher than $10 \mu\text{m s}^{-1}$ could already affect the obtained results [52]. A delay time, which is the time between probe translation and data

acquisition, is typically applied to let the electrode rest for a short moment after a translation step in order to avoid interference from convection. Convection is affecting the diffusion of the redox species being detected or generated at the SECM tip. Soft-Probe SECM was used in Chapters 3-6.

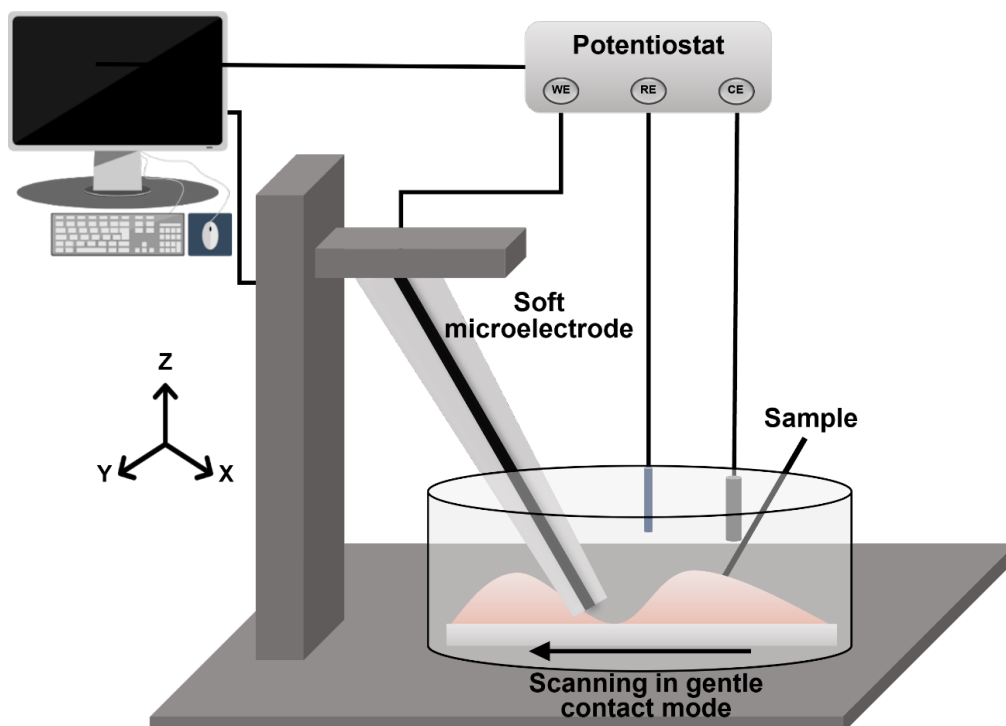


Fig.1.7 The basic setup of Soft-Probe-SECM consisting of a soft microelectrode probe, a potentiostat, that controls a three-electrode cell (*i.e.*, working electrode (WE), reference electrode (RE) and counter electrode (CE)). The positioning system allows the probe to move in x,y,z directions.

1.1.2 2D chips with microelectrode arrays

Microelectrode arrays (MEAs, **Fig.1.8**) are widely used in electro-analytical chemistry due to their numerous advantages over conventional electrodes. (i) Their miniaturized size and compact design allow experiments to perform measurements in tiny sample volumes. (ii) MEAs provide an increased signal-to-noise ratio that scales with the square root of the number of implemented microelectrodes [53-55]. (iii) The magnitude of current produced by MEAs is minimal and less destructive to the samples being analyzed, making them very useful for *in vivo* electrochemistry applications [53]. (iv) MEAs exhibit increased rates of mass transport to the surface of the electrode, which facilitates steady-state electrochemistry, and reduces the iR (ohmic) drop, enabling analysis in highly resistive solutions, such as organic solvents [53]. An MEA was used in Chapter 7 of this thesis.

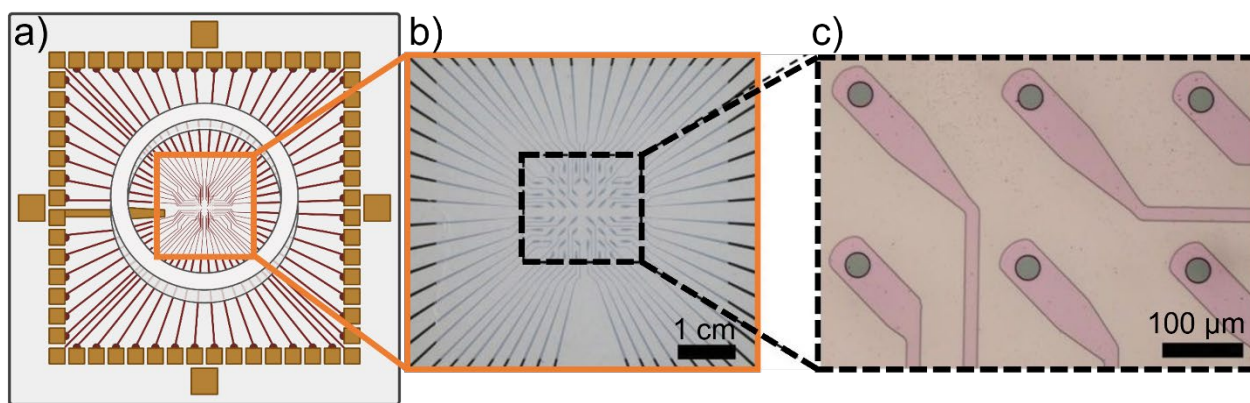


Fig.1.8 (a) Schematic of a microelectrode array. (b) Optical image of close-up view of the transparent recording region (middle), and (c) optical micrograph of the recording electrodes (right) [56]. The MEs are located in the center, hardly visible due to their small size. They are located in the round small volume cell whose cell walls are indicated by a cylinder. The larger squares at the lateral sizes of the MEA chip are the electrical connections.

Design of a Microelectrode Array (MEA)

The geometric characteristics of a MEA play a critical role, for instance, in cyclic voltammetry (CV) because there are different possible diffusion profiles around each electrode. MEAs are classified into two categories based on diffusion: radial diffusion (nonlinear diffusion) and planar diffusion (linear diffusion). As shown in **Fig.1.9a** for an array of microband electrodes, for radial diffusion, the diffusion zone around each microband electrode should be independent, *i.e.*, the diffusion layers of adjacent microband electrodes should not overlap. Radial diffusion will yield the highest ratio of faradic current to background current [55]. If radial diffusion occurs at the array, the response of the MEA is equivalent to the individual responses of each electrode times the total number of electrodes [55]. MEAs operating under radial diffusion can produce steady-state currents as shown in the I - V curve in **Fig.1.9a**. **Fig.1.9b** shows how MEAs, made of microband electrodes, can have diffusional overlap between microband electrodes, resulting in planar diffusion and a CV with redox peaks at the maximum mass transport rate.

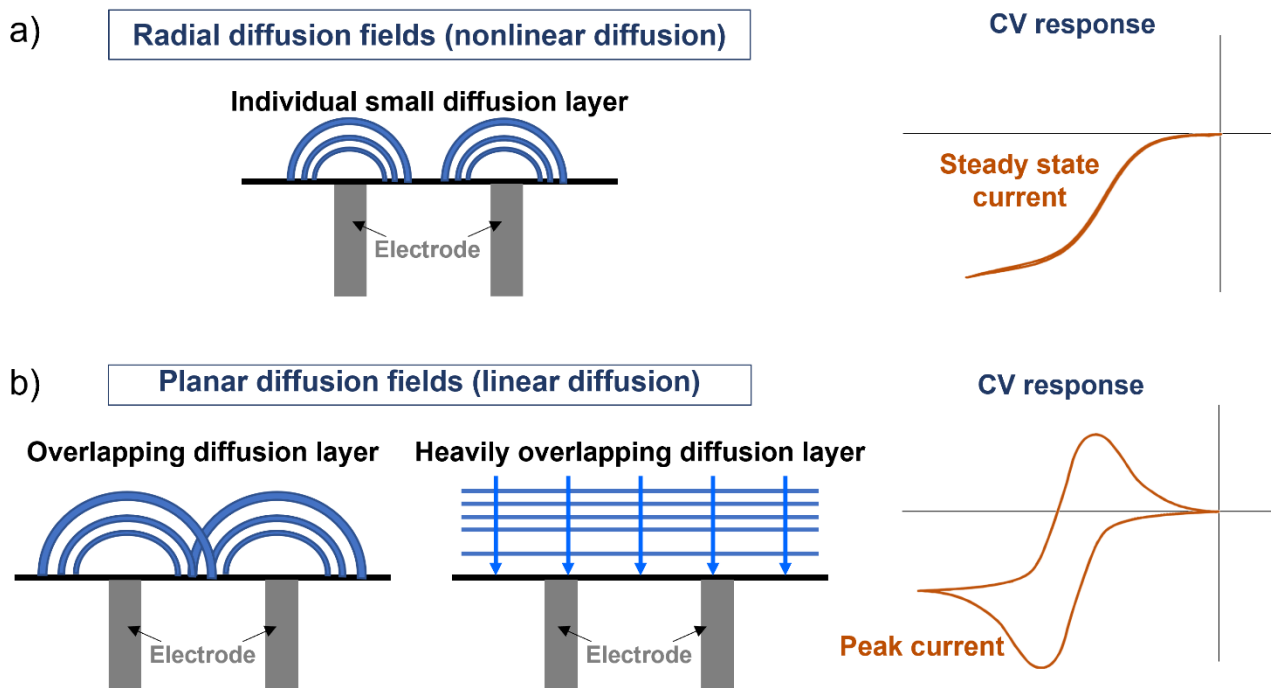


Fig.1.9 Diffusion field (left) and voltammetric response (right, drawn manually) for different MEA designs. a) Independent diffusion layers of microbands. b) overlapping diffusion layers of microbands.

1.2 Melanoma

1.2.1 Characteristics of Melanoma

Melanoma is cancer typically occurring in the skin. It is the most dangerous skin cancer. When it is still superficial, detecting melanoma at its early stage enables curing by minor surgery. Melanoma occurs in the top layer of skin, *i.e.*, the epidermis. At later stages, the penetration of melanoma from the upper layers of the skin to lower levels, *i.e.*, the dermis, can result in a distribution of melanoma cells in the body reaching the bloodstream. The result is the formation of global metastases. Melanoma and nonmelanoma (*i.e.*, basal and squamous cell carcinomas) skin cancers are now the most common types of cancer in white populations [57]. Both tumor entities show an increasing incidence rate worldwide [57, 58].

Many risk factors for melanoma have been identified, such as exposure to ultraviolet (UV) light, including sunlight and tanning beds. Still, it is not always obvious how they exactly cause this cancer. Melanoma cells originate from melanocytes, which are generally located near the basal layer of the epidermis [59]. The melanocytes produce the skin pigment melanin in small organelles called melanosomes, which are then transferred into surrounding keratinocytes [60]. Keratinocytes migrate within a few weeks towards the outer part of the skin, where they transform into flattened, stratified corneocytes constructing the outermost skin protection layer called *stratum corneum* [61]. This skin layer is generally less than 20 μm thick [62] but contains important information due to its continuous growth from the depth. Melanoma grows first radially, *i.e.*, horizontal spreading, and then vertically reaching on the one hand upper skin layers and on the other hand blood vessels and the lymphatic system in the dermis underneath, facilitating metastasis [63].

The classification of malignant melanoma can be done as follows: superficial spreading melanoma, nodular melanoma, lentigo malignant melanoma, acral lentiginous melanoma, desmoplastic melanoma (uncommon), miscellaneous group (rare).

Melanoma presents three clinically and histomorphological discernable steps in tumor progression [64] (**Fig.1.10**).

1. Malignant melanoma is confined to the epidermis (melanoma *in situ*) called Radial Growth Phase- (RGP) determined melanoma.
2. Radial Growth Phase (RGP)-confined microinvasive shows some malignant cells present in the superficial papillary dermis.
3. Vertical Growth Phase (VGP), which means melanoma, has entered the tumorigenic and/or mitogenic phase.

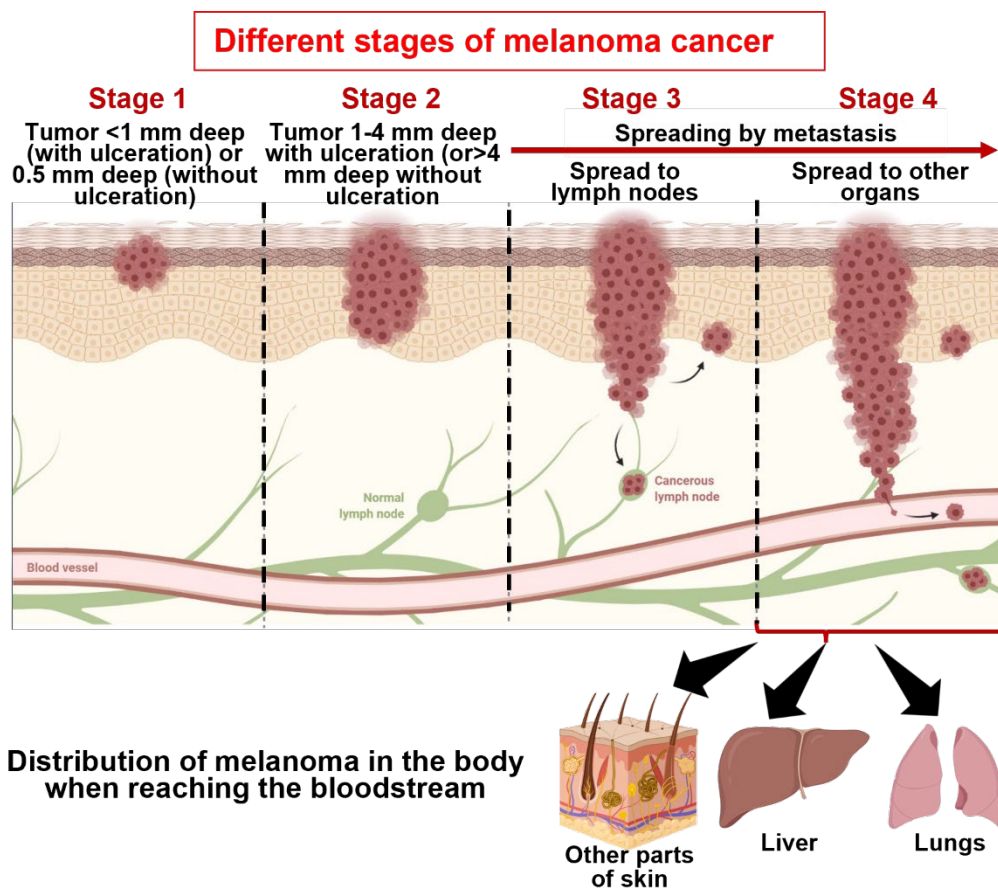


Fig.1.10 Different stages of melanoma [64]. The scheme was created on the Biorender website with a license.

1.2.2 Conventional detection methods

Most melanomas are brought to a doctor's attention because of signs or symptoms in the skin. There is a suspicious area that might be skin cancer. In that case, a doctor will examine it and organize further tests to determine whether it is a melanoma, another type of skin cancer, or another skin condition. If a melanoma is found, other tests may be done to determine already metastatic. Briefly, these methods are based on the patient's physical examination and medical history at the beginning.

If melanoma cancer is diagnosed, the dermatologist uses skin biopsy. Different kinds of biopsy can be performed, such as shave (tangential) biopsy, punch biopsy, incisional and excisional biopsies, optical biopsies, fine needle aspiration (FNA) biopsy, surgical (excisional) lymph node biopsy, and sentinel lymph node biopsy.

All those methods are invasive, causing discomfort for patients. One of the critical barriers in early skin cancer detection is the lack of reliable non-invasive techniques [65]. It needs a high detection probability (*i.e.*, the probability of correctly detecting a malignant lesion) and low false-alarm likelihood (*i.e.*, declaring a benign lesion as malignant) to detect cancer early.

Non-invasive techniques for skin-cancer detection include multispectral (MS) imaging [66-68], digital dermatoscopy and videodermoscopy (sequential digital dermatoscopy) [69, 70], reflectance-mode confocal microscopy [71], ultrasound [72, 73], laser Doppler perfusion imaging [74], and optical coherence tomography (OCT) [75, 76]. Each technology presents some restrictions and limitations to non-invasively detect skin cancer with high detection probability and low false-alarm probability. Electrochemical biosensors for melanoma biomarker detection carry a considerable potential for melanoma diagnosis. An effective and low-cost diagnostic tool for detecting functional biomarkers may provide a reliable diagnosis of melanoma, substantially improving sensitivity and specificity.

1.2.3 Electrochemical biosensors for the detection of the Melanoma biomarkers

The main application of biosensors is the quantification of biological or biochemical processes. This provides quantitative or semi-quantitative analytical information by using a biological recognition element. This qualification is of outmost importance for medical, biological, and biotechnological applications. Electrochemical biosensors are attractive to analyze the content of a biological sample due to the conversion of a biological event to an electronic signal.

Recently, the electrochemical detection of melanoma has been demonstrated by addressing the enzyme tyrosinase (TYR), a known skin cancer biomarker over-expressed in melanoma [46, 77]. Studies have shown tyrosinase to be a highly selective marker for melanoma, not cross-reacting with other tumors or normal tissues.

1.2.3.1 Tyrosinase

Tyrosinase, a typical polyphenol oxidase, is a copper-containing enzyme widely distributed in all kinds of organisms, such as plants, animal tissues, and fungi [78, 79]. It can catalyze the hydroxylation of phenolic substrates to catechol derivatives, further oxidized to orthoquinone [80]. These reactions have been recognized as critical processes in the biosynthetic pathway of some natural pigments [78]. TYR is considered a targeting enzyme to establish treatments for several hypopigmentation-related problems [81]. More importantly, the disruption of tyrosinase will lead to severe skin diseases such as oculocutaneous albinism type I [82]. Accumulated tyrosinase is a biomarker of melanoma cancer cells [83]. Literature also indicates that tyrosinase is a more sensitive

marker than other markers such as HMB-45 and MART-1 [84]. Therefore, sensitive detection of tyrosinase activity is of great importance for melanoma diagnosis [85].

1.2.3.2 Electrochemical detection and microneedle-based biosensors

There is an interest in non-invasive and painless electrochemical methods using microneedle-type electrodes to penetrate the epidermis and detect TYR inside the skin cells.

Skin can be divided into three regions: (1) the outermost cellular layer, the epidermis, which contains the stratum corneum, (2) the middle layer, the dermis, and (3) the innermost layer, hypodermis (**Fig.1.11**) [86]. The epidermis layer is 150–200 μm thick and consists of viable cells without a vascular network. This layer obtains its nutritional needs by passive diffusion through interstitial fluid [87]. The outermost layer of the epidermis (10–20 μm) contains dead cells and is known as the stratum corneum [88]. The dermis, an integrated fibro-elastic structure, provides mechanical strength to the skin. This layer contains an extensive nervous and vascular network. TYR-based biosensors should be inserted into the epidermis layer and not the dermis to detect TYR for early-stage detection of melanoma. So, the biosensor should be thin enough to insert in the stratum corneum. Microneedle devices are generally known for transdermal drug delivery. They can insert in the skin with low injury, pass the hydrophobic stratum corneum and release hydrophilic drugs.

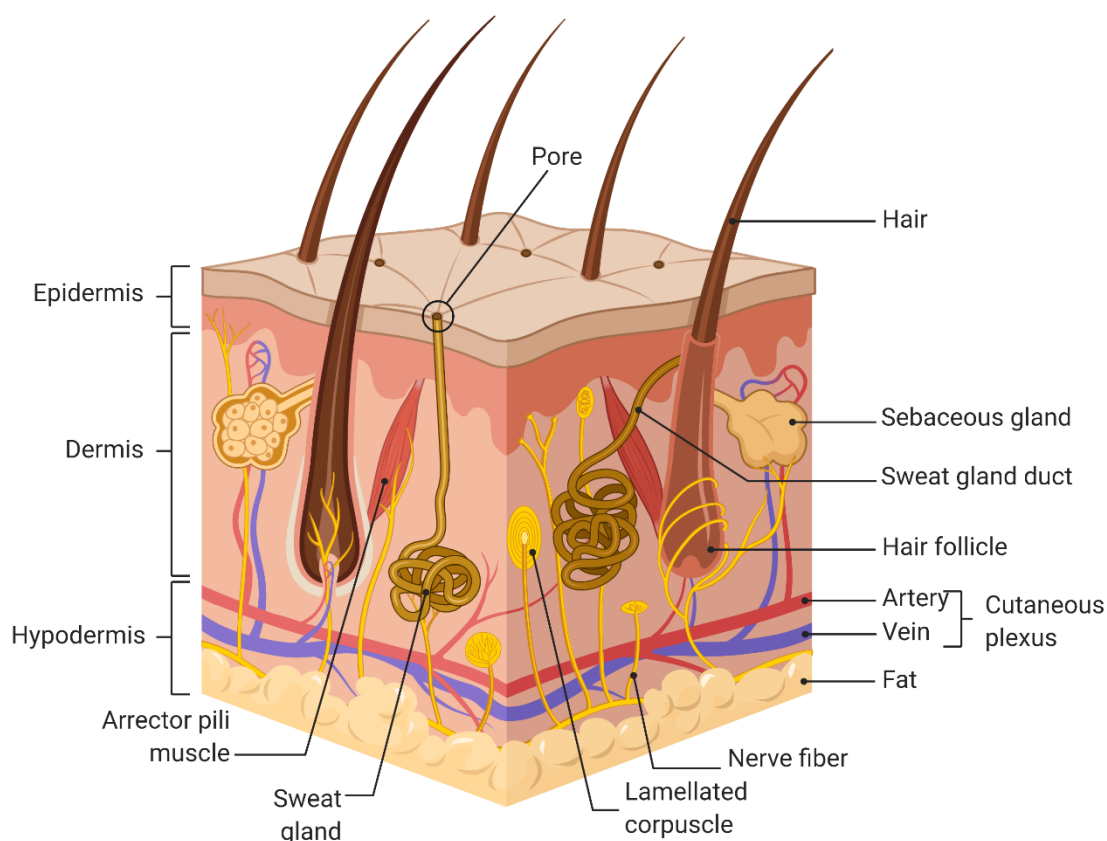


Fig.1.11 Skin structure shows three major regions: epidermis, dermis, and hypodermis [86]. The scheme was created on the Biorender website with a license.

Microneedles (MNs) can be defined as a solid or hollow cannula with an approximate length of 50–900 μm and an external diameter of not more than 300 μm [89]. Microneedles were first proposed in 1976 [90]. Microneedles are thin and short and do not penetrate the dermis layer with their nerves; hence, the painless application can penetrate through the epidermis up to 200 μm in-depth [91, 92]. There are a lot of advantages for microneedles as biosensors besides their painlessness, which includes faster healing at the injection site than with a hypodermic needle, no fear of needle and biopsy by the patient, ease of application, decreased microbial penetration as compared with a hypodermic needle and a specific skin area can be targeted for the suspected spot of cancer.

Microneedles (MN) can be broadly divided into solid, degradable/dissolvable, and hollow. The material selection for the microneedle fabrication should be based on sufficient mechanical strength for insertion into the skin, and they should be made of biocompatible materials.

The first MN devices were fabricated from silicon [93, 94]. Still, many other materials have also been used in MN fabrication, such as stainless steel [95], dextrin [96], glass [97], ceramic [98], maltose [99], galactose [100], and various polymers [101–103]. In the first published study, solid silicon MN arrays were fabricated using a reactive ion etching (RIE) process, a chromium mask, a dry-etch process [94]. Although silicon is attractive, as a common microelectronic substrate with extensive processing experience for more than 30 years, it is relatively expensive and requires cleanroom processing [104]. In contrast, metal and glass MNs are equally effective in skin penetration and can be produced at lower costs than silicon MNs.

Polymeric MNs are gaining importance due to various properties, such as biocompatibility, biodegradability, strength, toughness, and optical clarity [105, 106]. Polymeric materials which have been efficiently fabricated into MNs include; poly (methyl methacrylate) (PMMA), poly-L-lactic acid (PLA), poly-glycolic acid (PGA), and poly-lactic-co-glycolic acid (PLGA), cyclic-olefin copolymer, poly (vinyl pyrrolidone), and sodium carboxymethyl cellulose [107].

MNs should demonstrate sufficient strength to penetrate the skin or other biological tissues without breaking or bending before or during insertion [108]. Major factors accountable for MN performance are the type of material, needle height, tip radius, base diameter, needle geometry, needle thickness, and needle density, which, in turn, determine the overall insertion and fracture force of the MN [109]. The importance of the experimental testing of MN failure forces can only be assessed appropriately compared with the equivalent insertion forces [102]. Human or animal skin tissue is required to measure the insertion forces. In most studies, researchers evaluate the ability of the MNs to pierce the skin using techniques such as microscopy or histological analysis.

The microneedles must be coated with a suitable electrode material and *in vivo* monitoring of TYR requires biocompatible coatings, such as hydrogels. It provides (a) a liquid electrolyte layer and (b) contains electroactive species whose redox state can be linked to the concentration of TYR in the skin [110].

1.3 Bacterial biofilms

Bacterial biofilms are 3D structures consisting of extracellular polymeric substances (EPSs) and single or multiple bacteria species forming clusters and adhering to surfaces [111, 112]. Biofilms are micro-organisms in which microbes produce EPS. EPS include proteins (<1-2%, including enzymes), DNA (<1%), polysaccharides (1-2%) and RNA (<1%). Water (up to 97%) is the major part enabling the transport of nutrients inside the biofilm matrix [113]. Compared to planktonic bacteria, bacteria in biofilms survive better harsh environmental conditions, and consequently, biofilm bacteria show a 10–1'000 times higher resistance towards antibiotics than planktonic bacteria [114]. Indeed, culture media provide nutrients to planktonic organisms unnaturally, which is why they multiply rapidly and are highly motile. This makes planktonic bacteria more susceptible to antibiotics, environmental factors, and host factors [115]. The bacteria embedded in biofilms, on the other hand, are able to resist or evade such destructive factors by forming aggregates, altering their physiology, and taking advantage of a host's inability to clear them [115]. This has become a significant healthcare concern for treating harmful biofilms. The antibiotic resistance of bacteria in a biofilm has been attributed to the EPS matrix, acting as a protective barrier [116] and preventing nutrients from penetrating the deeper layers of biofilms. The metabolic degradation further limits the availability of nutrients in deeper biofilm layers by organisms residing in the upper layers, leaving bacteria in the deeper layers of a biofilm in a dormant state [117-120]. Multiple factors contribute to the resistance character of biofilms, including physical and chemical diffusion barriers [121], reduced sensitivity towards antibiotics due to the slow growth rate of bacteria in biofilms [119, 122], as well as the structural heterogeneity within biofilms and development of biofilm-specific biocides-resistant bacteria phenotypes [114, 123].

The viability of bacteria in biofilm, or at least a relative reduction in viable bacteria due to the treatment, should be assessed to determine antibiotic susceptibility or the effectiveness of other bactericidal treatments. The ideal scenario for most microbial diagnostic applications is to detect only viable cells. Pathogens only threaten humans, animals, and plants when they are alive. Several methods are available for quantifying bacterial viability, but these are generally better suited to assessing planktonic cultures. There is no way to transfer tests performed on planktonic bacteria to tests done on biofilm bacteria since it is known, for example, that biofilm bacteria are less susceptible to antibiotics than planktonic bacteria of the same species. The term 'viability' refers to the ability of cells to replicate themselves and has been the subject of many discussions. There are different physiological states between "live" and "dead". **Fig.1.12** illustrates four of these states and illustrates the wide spectrum of opinions concerning viability (**Table 1.1**). There are three viability criteria (**Fig.1.12**): culturability, metabolic activity, and membrane integrity. According to this simplified scheme, viable cells would fulfill all three viability criteria. "Active but nonculturable" (ABNC) refers to active and intact cells but cannot be cultured on a standard medium. On the other hand, intact

cells that no longer exhibit respiration or metabolic activity are called 'ghosts'. In membrane-compromised cells, none of these three viability characteristics would be present.

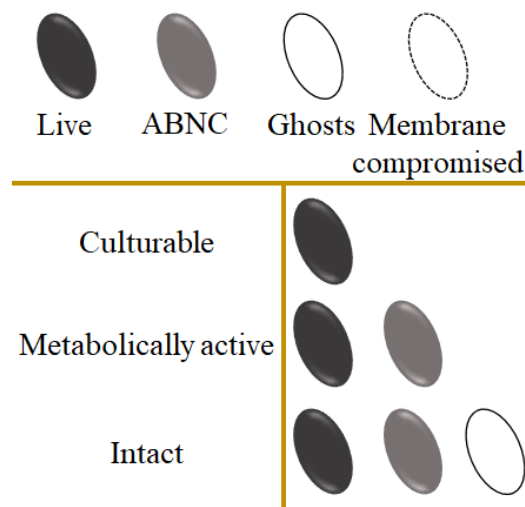


Fig.1.12 Schematic representation of selected viability states and their main characteristics [124]

Table 1.1 Major physiological states of bacteria cells.

Physiological state	Phenotype	Reference
Viable (live)	Intact cytoplasmic membrane, functional synthesis of protein and other cell components (nucleic acids, polysaccharides, etc.), and energy production necessary to maintain cellular metabolism and, eventually, growth and multiplication.	[125]
Non-replicating (in stationary phase; inhospitable conditions for replication; or injured)	Will not form a colony on an agar plate nor proliferate observably in a liquid medium but may have active physiologic activity and intact cytoplasmic membrane. Cells may be inhibited by the medium or injured but capable of repair	[126]
Starving	Cells undergo dramatic decreases in metabolism but remain fully culturable	[127]
Dormant (viable but not culturable)	In a low metabolic activity and unable to divide or form a colony on an agar plate without a preceding resuscitation phase. A protective response. Also seen in "post-acidification."	[128, 129]
Irreparably damaged cells	Will not grow with vigor under any conditions due to progressive metabolic decline. These cells may be irreparably injured	[126]
Non-viable (dead)	No metabolic activity.	[126, 128]

As the viable ability of microorganisms can typically not be determined directly in their natural environment, different techniques to assess viability are used, including traditional cultivation on artificial substrates, detection of RNA, detection of the metabolic activity or substrate responsiveness, and the determination of membrane integrity, briefly shows in **Fig.1.13** [130].

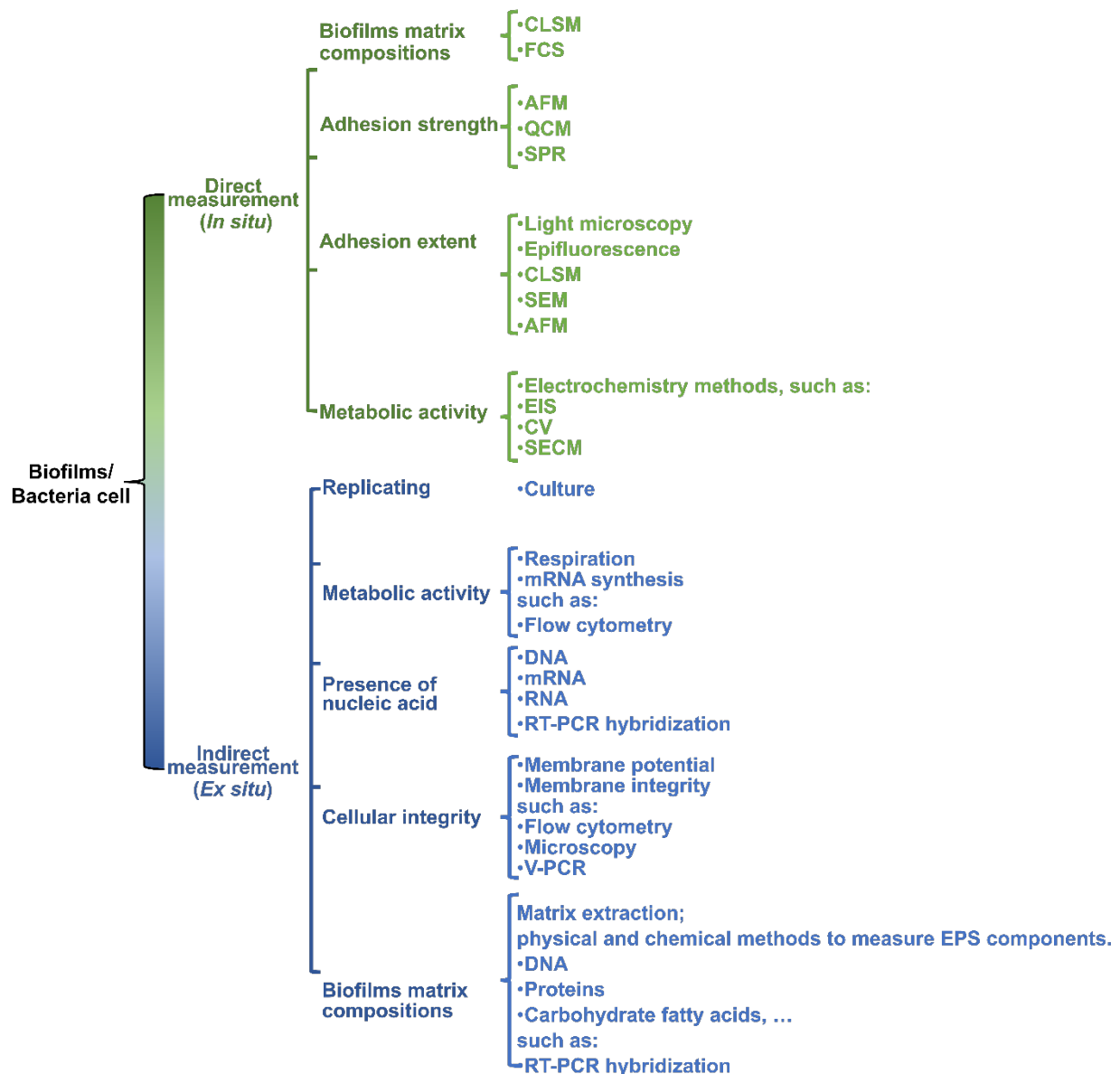


Fig.1.13 Summary of the facets of a biofilm/ bacterial that may be probed via various direct and indirect-based techniques to assess biofilm/ bacteria viability [131].

1.3.1 Detection methods for biofilms viability

1.3.1.1 Colony forming units (CFU)

An aerobic plate count, or viable cell enumeration, is a standard quantification method that determines how many viable cells are in culture [132-134]. This assay involves growing colonies from cells on an agar plate so one can distinguish between living and dead cells and quantify the live cells without using dyes or instruments. The starting point is liquid planktonic cultures or mature biofilms that are scraped, vortexed, or sonicated in a liquid medium. Plated biofilm is removed by

aseptically removing small amounts, followed by serial dilution, and then plated onto nutrient-containing agar. Colonies are counted after incubation (usually 24–72 hours). Based on the number of colony forming units per milliliter (CFU/mL) and the volume of culture plated on the plate, the number of CFU/mL in the original culture can be calculated (**Fig.1.14a**). To assess the population dynamics with *E. coli* (*E. coli* Nissle 1917 (EcN)) in dual-species biofilms, Hong *et al.* [135] examined molecular interactions between *E. coli* (*E. coli* Nissle 1917 (EcN)) biofilms and four other bacteria species. EcN has been examined for its influence on the formation of dual-species biofilms by CFU. The authors did not find an effect of EcN or commensal *E. coli* BW25113 (BW) on the formation of *Pseudomonas aeruginosa* (*P. Aeruginosa*) PAO1 (PA) (**Fig.1.14b**), suggesting that the biofilm formation of PA is unaffected by the presence of *E. coli* strains. Dual-species biofilms formed with EcN showed a substantial decrease in biofilm formation by 1'100-times and 8'300-times compared to their single-species biofilms (**Fig.1.14b**). In contrast, when non-probiotic *E. coli* was added to *Staphylococcus aureus* (*S. Aureus*) JE2 (SA) and *Staphylococcus epidermidis* (*S. Epidermidis*) RP62A (SE), their biofilm formation did not decrease.

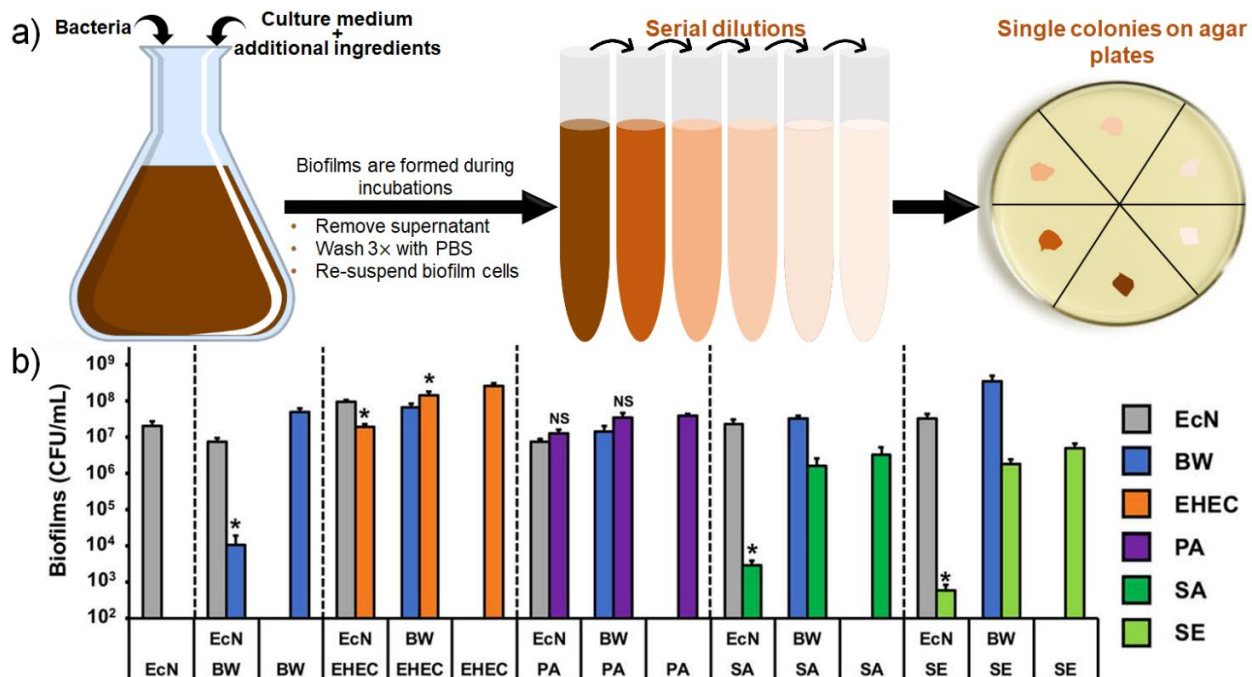


Fig.1.14 Viability test of biofilms with CFU method: (a) Scheme represents the CFU method's basis. (b) Single- and dual-species biofilms were formed in polypropylene culture tubes, and CFU quantified viable biofilm cells. Probiotics EcN, BW, enterohemorrhagic *E. coli* EDL933 (EHEC), PA, SA, and SE were tested to determine the effect of EcN on biofilm formation in other bacteria. (b) Adapted with permission from ref. [135] Copyright 2018 Nature.

Counting the number of colony forming units after plating cultures is the classical method for determining bacterial viability. Since the presence of the biofilm matrix can result in high levels of aggregation, using the CFU method to assess biofilm viability can lead to significant errors. It is possible to remove bacteria from the matrix or surface to which they are attached using techniques

such as sonication or matrix-degrading enzymes. Still, such methods may negatively impact the bacteria's viability. To perform CFU counting, the bacteria should also be re-suspended.

1.3.1.2 Polymerase chain reaction (PCR)

Viability is determined by enumerating the definitive and relative composition of treated biofilms using PCR, a technique that has been shown to distinguish viable and dead bacteria from various bacteria biofilms [136-138]. In recent publications, PCR has been used for a variety of purposes. For instance, PCR analysis was used to investigate the mechanism of water-soluble surfactant polymer dressings (SPD) on inhibition of bacterial biofilm development [139]. There are different types of PCR techniques that could be used. They are briefly explained below.

Ethidium monoazide (EMA)- and propidium monoazide (PMA)- PCR

Nogva *et al.* [140] introduced the idea of (ethidium monoazide) EMA PCR, a diagnostic method that relies on membrane integrity as a determinant of viability in the DNA-based detection of bacteria. Viability is determined by membrane integrity in this approach. DNA-intercalating dye, EMA, has an azide group attached to it. There is a theory that EMA can enter only membrane-compromised ('dead') cells, whereas intact membranes of 'live' cells act as a barrier. Within membrane-compromised cells, EMA intercalates into DNA (**Fig.1.15a**). After exposure to bright visible light, such samples are subsequently covalently linked to DNA (photolysis of EMA converts the azide group into a highly reactive radicals that forms covalent bonds). In the covalent crosslinking of EMA to DNA, PCR amplification of the modified DNA is strongly inhibited. Only DNA that has not been crosslinked with EMA and was not modified by EMA can be amplified during treatment. Contrary to this, DNA modified in membrane-compromised cells is efficiently suppressed from amplification. The analysis results might be changed if cells with damaged membranes are excluded after treatment [141, 142]. As a result, only live cells can be detected in quantitative PCR (qPCR) due to covalent bonding. For instance, **Fig. 1.15b** shows the design of a novel three-dimensional inter-kingdom wound biofilm model conducted by Townsend *et al.* [143]. The viability of the biofilms was evaluated using live-dead qPCR at a molecular level. A triadic biofilm composed of *Candida albicans*, *Pseudomonas aeruginosa*, and *Staphylococcus aureus* was characterized using complex hydrogel-derived cellulose substrates to evaluate frequently used topical wound treatments. PCR was performed on samples modified with PMA, which prevented DNA from cells with compromised membranes from being detected.

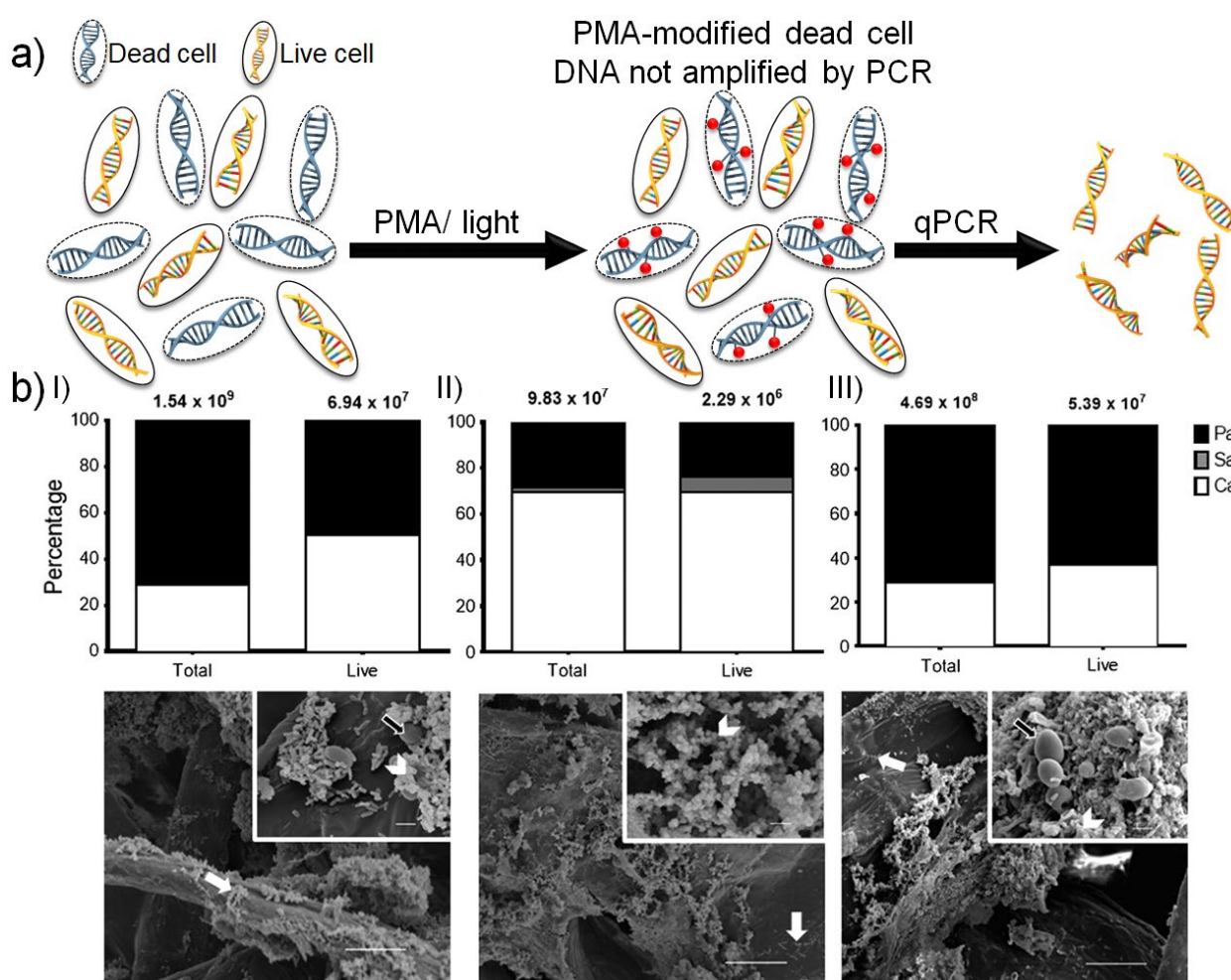


Fig.1.15 (a) Scheme representing the basis of the PMA PCR method. (b) Data represent percentage composition calculated from CFE values from triplicates carried out on three separate occasions. SEM, shown in lower panels, was conducted as described in the methods. Note: *P. aeruginosa* indicated by a solid white arrow, *S. aureus* by white arrowhead, *C. albicans* by a black arrow. *C. albicans* is present in predominantly hyphal form; the bacteria can be seen attached to the hyphae. (b) Adapted with permission from ref. [143]. Copyright 2016 Taylor & Francis.

EMA has also been shown to penetrate intact membranes in later studies [144-146]. Intact cells absorb EMA to varying degrees depending on the species of bacteria [144]. As a result, EMA's use is severely restricted. As a result, PMA was assessed using EMA [144]. It was shown that PMA, as opposed to EMA, is efficiently excluded from intact cells, perhaps because of its higher positive charge [147].

Reverse transcriptase PCR (RT-PCR)

RT-PCR allows the amplification of multiple copies of a particular sequence and is one of many PCR variants. Reverse transcriptase is used to convert ribonucleic acid (RNA) into its DNA complement. mRNA has been used as a viability marker. Markers like this are highly labile molecules with a very short half-life (seconds). As a result, detecting mRNA transcription rather than DNA synthesis should be a more reliable viability indicator. RT-PCR and nucleic acid sequence-based amplification (NASBA) [154] are the two most common methods for detecting mRNA [148]. Both methods have been used to determine bacterial viability to varying degrees of success. A more recent technique

for measuring bacterial viability is reverse transcriptase-strand displacement amplification (RT-SDA) [149]. In some bacterial conditions, ribosomal ribonucleic acid (rRNA) can also be used to measure viability, and it can be correlated positively with viability [150].

Real time quantitative polymerase chain reaction (RT-qPCR or qPCR)

The genes expressed by biofilm-forming bacteria are often different than those expressed by planktonic strains. Real-time quantitative reverse transcription PCR (qRT-PCR) is an effective method for quantifying the amount of RNA transcripts from specific genes in bacteria growing in biofilms. The RT-qPCR method offers a wide dynamic range and may be used to verify the results of gene expression microarrays. In addition, qRT-PCR is highly sensitive. So, it can be used to quantitate gene expression from biofilm samples that contain only a small amount of biological material, such as those obtained by laser capture microdissection microscopy (LCMM). Methods commonly used for qRT-PCR include SYBR Green and dual-labeled probes (Taqman). In both methods, reverse transcription converts mRNA to cDNA followed by PCR amplifying the cDNA [151].

1.3.1.3 Flow cytometry (FC)/fluorescent activated cell sorting (FACS)

Multiparametric flow cytometry allows simultaneous analysis of physical and chemical properties of large numbers of particles in real time. A fluorescent dye must first be applied to the cell surface. Monodisperse suspensions (single, unclamped cells) are aligned in a laser beam so that each labeled cell can pass through the laser beam. Fluorescent molecules are excited by laser light, which causes them to emit light at different wavelengths. Different cell types or cell components are present in the sample (**Fig.1.16**).

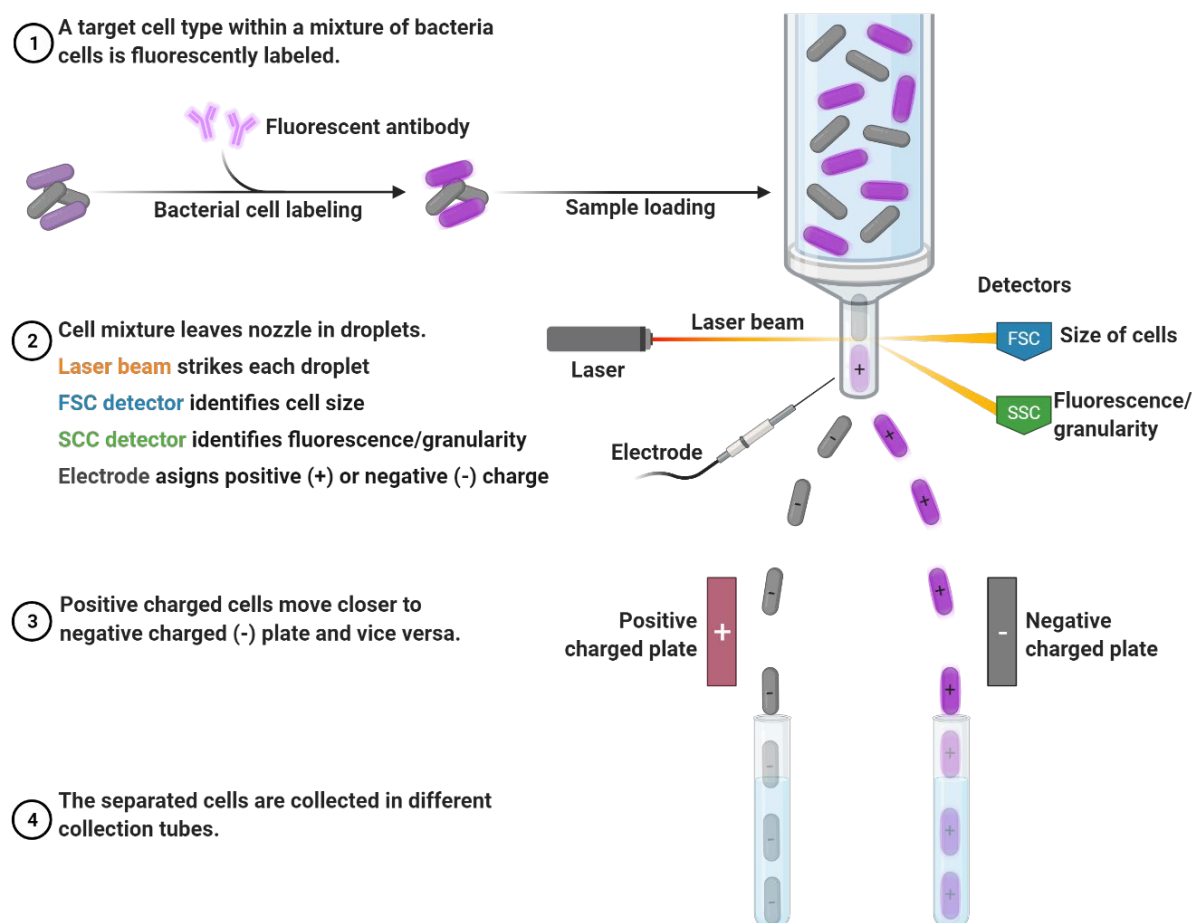


Fig.1.16 Schematic representing the main steps in flow cytometry. The scheme was created on the Biorender website with a license.

The FC can examine many cells at once (200 to 2000 cells per second), recording several parameters for each cell that can be later correlated with a wide variety of cell characteristics [152]. Fluorescent probes can be used to measure the viability criteria of living cells, including cytoplasmic pH, intracellular enzyme activity, and membrane potential [153]. The Fluorescent Activated Cell Sorting (FACS) technique is a type of flow cytometry that sorts a heterogeneous mixture of biological cells according to their fluorescent characteristics and light scattering characteristics. The fast and powerful cell-sorting techniques could reduce the time required to determine bacteria abundance, size, and metabolic activity. The use of fluorescent DNA stains, nucleic acid probes, and immunofluorescence probes targeting cell proteins increase the technique's capabilities, distinguishing cells based on their nucleic acid amount and type, respiratory enzyme content, and membrane integrity.

1.3.1.4 Microscopy methods

Staining techniques such as crystal violet and live/dead staining [154] offer valuable information but also have inherent limitations. For visualizing biofilm formation quantitatively *in vitro*, i.e., the total biofilm biomass, crystal violet staining is the gold standard [155]. However, this method does not

measure the viability of biofilms. In addition to the bacteria, it also stains the extracellular polymeric matrix [156]. This method has some further limitations, including the possibility that parts of the biofilm could be washed away during sample washing [157].

A live/dead stain is used to quantify planktonic bacteria in conjunction with flow cytometry [154] and for imaging biofilms. Despite this, it is not ideal for high-throughput quantification of biofilm viability since it requires a laser scanning confocal microscope in a time-consuming process where only a small section of the biofilm can be assessed at a time. Metabolic assays are excellent candidates for quantifying bacterial viability in biofilms. It is an indirect method that relies on detecting metabolic products produced by bacteria and offers the advantage of determining viability without undergoing sample manipulation since biofilms are generally not removed from adherent surfaces. Bacterial metabolic activity can be detected using several different indicators. For example, reducing resazurin is the basis for the resazurin assay (also known as the Alamar Blue assay). Metabolically active cells can reduce the blue dye to pink resorufin, a fluorescent dye, within the respiratory electron transport chain [158]. As a result, fluorescent measurements of a biofilm with resazurin assay can be used to quantify the viability of the biofilm [134, 159]. The variety of metabolic assays is partly due to the fact that some of the assays are strain-specific or work well with certain types of bacteria [160-164]. There is, however, one significant limitation of these metabolic assays that have not been adequately addressed: bacteria in biofilms do not have the same metabolic activity as planktonic, *i.e.*, free-floating, bacteria. Biofilm assays are usually calibrated based on their planktonic cultures, assuming their metabolic rates are similar. Since planktonic bacteria and biofilm bacteria may have significant metabolic rates that differ from each other [114, 117, 165], this introduces significant errors. In the resazurin metabolic assay, for instance, it has been demonstrated that *S. aureus* planktonic bacterial suspensions generate a higher signal than the same concentration of corresponding biofilm bacteria [166].

Electrochemical bio-imaging

Biofilms can be investigated with electrochemical methods. These methods are increasingly used for monitoring biofilms at an early stage of development [167]. Various ways can be used to detect biofilm formation, including electrochemical impedance spectroscopy [168], cyclic voltammetry [169], and chronoamperometry [170]. Single bacterial cells and bacterial cell aggregates have been studied using electrochemical methods [171-174]. Quorum sensing, for instance, is an important mechanism that identifies a stimuli-response mechanism of bacteria aggregates that monitors their population density and enhances gene transcription when a certain number of bacteria is reached. Researchers have electrochemically imaged the release of quorum-sensing molecules from aggregates of *P. aeruginosa*, such as pyocyanin (PYO, the blue phenazine) [174-176]. SECM imaging revealed that a single aggregate of 500 cells produced PYO (**Fig.1.17**) [174].

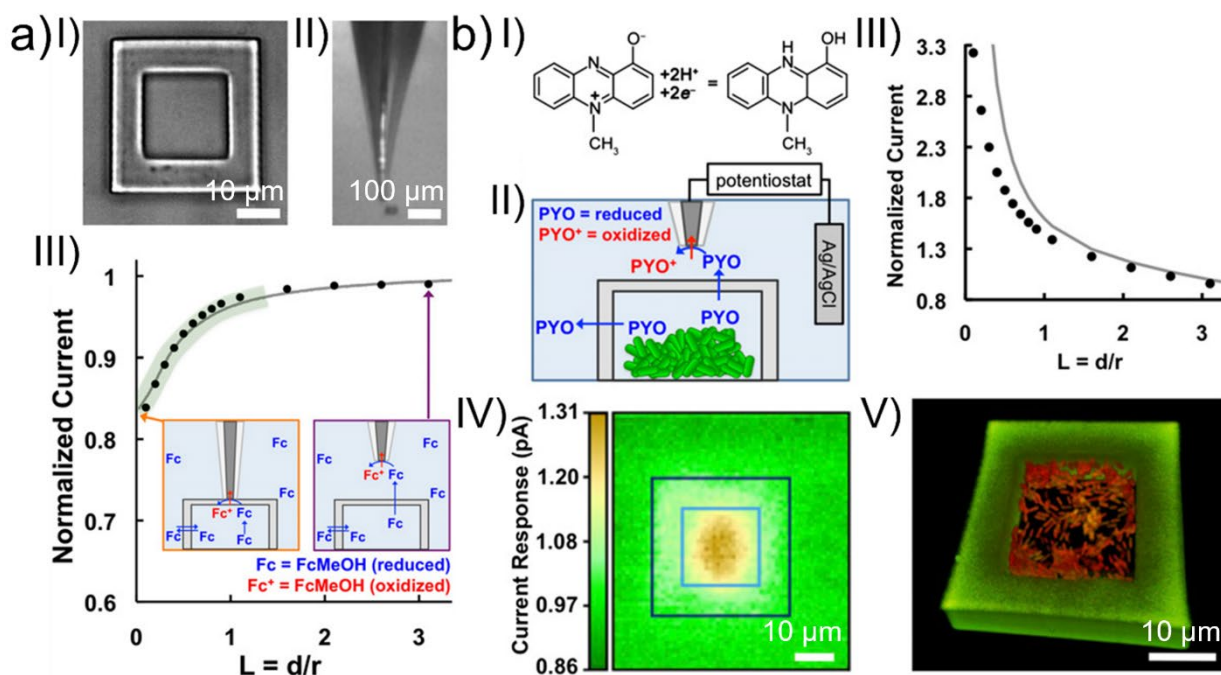


Fig.1.17 (a) (I) Bright-field image of microtrap. (II) Microscope image of SECM probe (III) SECM feedback approach curve (solid line). The experimental curve (gray line) fit a simulated negative feedback approach curve (black circles). (b) (I) PYO redox reaction. (II) Schematic of the microtrap-SECM system for measuring PYO in real-time. (III) Simulated approach curve (points). The solid line represents the theoretical diffusion-limited response. (IV) An SECM reactive image for PYO. (V) A 3D confocal reconstruction. (a-b) Adapted with permission from ref. [174]. Copyright 2014 Proceedings of the National Academy of Sciences.

Electrochemical methods have the benefit of being able to reach high sensitivities while operating in small liquid volumes. Depending on the detection strategy, it is possible to analyze biofilms and bacterial cells without fixing them. Portable and small electrochemical hardware is possible. To study the electron transfer and metabolic activity of biofilms, electrochemical bio-imaging can use (sub)micrometric electrodes [177]. In close proximity to a sample, a micrometric electrochemical probe is translated on an electrochemical scanning probe platform, such as SECM. Particularly, it has been used to study living cells [178, 179], yeast [180], and bacteria, as well as biofilms [181-184]. SECM has diverse applications in terms of analytes to detect and types of bacteria to be investigated [177, 185]. SECM may also be combined with other techniques, including atomic force microscopy [186], fluorescence microscopy [187, 188], or used alone, such as scanning ion conductance microscopy (SICM), for bacterial and biofilm studies [189]. Due to the redox-active compounds that produced or consumed by bacteria cell, the SECM signal can be as the result of an amperometric current [175, 185, 190, 191]. SECM has demonstrated and studied the reduction of ferricyanide to ferrocyanide by the respiratory activity of *E. coli* cells [191, 192]. In addition, SECM was used to detect hydrogen peroxide at *Streptococcus gordonii* biofilms to determine glucose metabolism and catalase activity [193]. Researchers have used amperometric glucose micro-sensors to detect metabolites selectively in *Streptococcus mutans* biofilms [194]. Alternatively, a two-dimensional microelectrode array chip can be used to achieve micrometer-resolved electrochemical imaging of biofilms [176, 195]. To detect multiple metabolites, Bellin *et al.* [176] used

square-wave-voltammetry (SWV) (**Fig.1.18**). Voltammetric peaks at specific potentials may be linked to specific redox-active phenazines. In less than 7 minutes, large biofilms were measured onto a chip with 1'824 MEs using track-etched, agar-soaked membranes [176]. Phenazine production was correlated with specific locations and oxygenation time inside the bacterial colony.

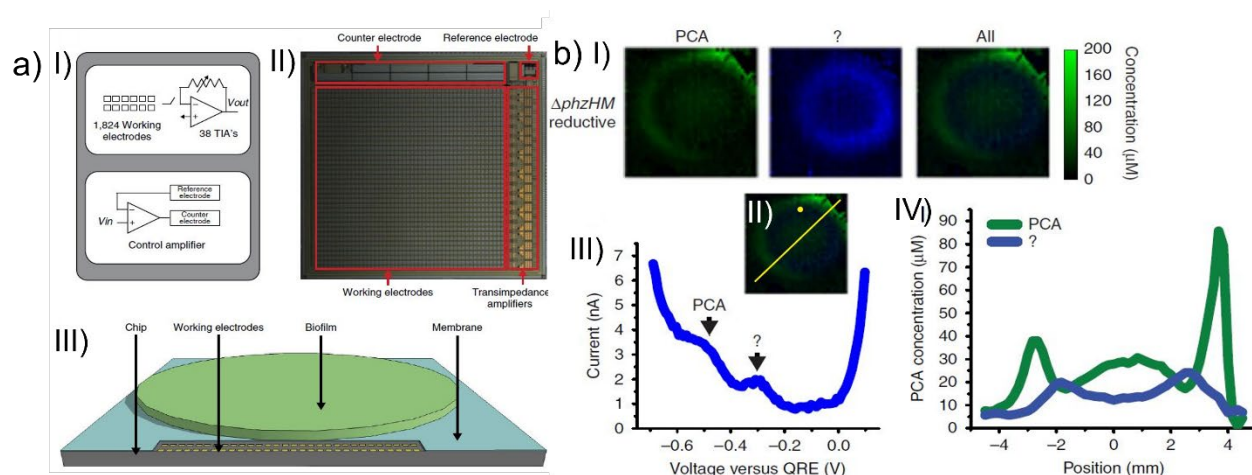


Fig.1.18 (a) (I) Block diagram of the electrochemical camera chip. (II) Optical micrograph of the electrochemical camera chip. (III) Diagram of the imaging platform. (b) (I) Electrochemical imaging, based on reductive SWV, of a DphzHM biofilm after two days of development. (II) Locations of example squarewave voltammogram and cross-section. (III) Example SWV from a single electrode. (IV) Example cross-section from the electrochemical image. (a-b) Adapted with permission from ref. [176]. Copyright 2016 Nature.

1.3.2 Methods for the treatment of biofilm

It can become difficult to treat mature biofilms once they have been established. Biofilms can be treated in several ways. Biofilm eradication through conventional treatment is currently the Standard Of Care (SOC) for biofilms. In the treatment of biofilms, physical and chemical debridement and topical and systemic antimicrobials are applied (**Fig.1.19**) [196, 197]. Antimicrobial agents, disinfectants, and the host's immune system cannot treat mature biofilms with high efficiency. It is important to note that biofilm biology extends beyond biofilms alone. Biofilms are defined by the dynamic exchange of microbial biofilms and host responses [198]. Thus, nanomaterials and ultrasonic treatments have led to new methods and reagents (**Fig.1.19**).

Methods for biofilm therapy

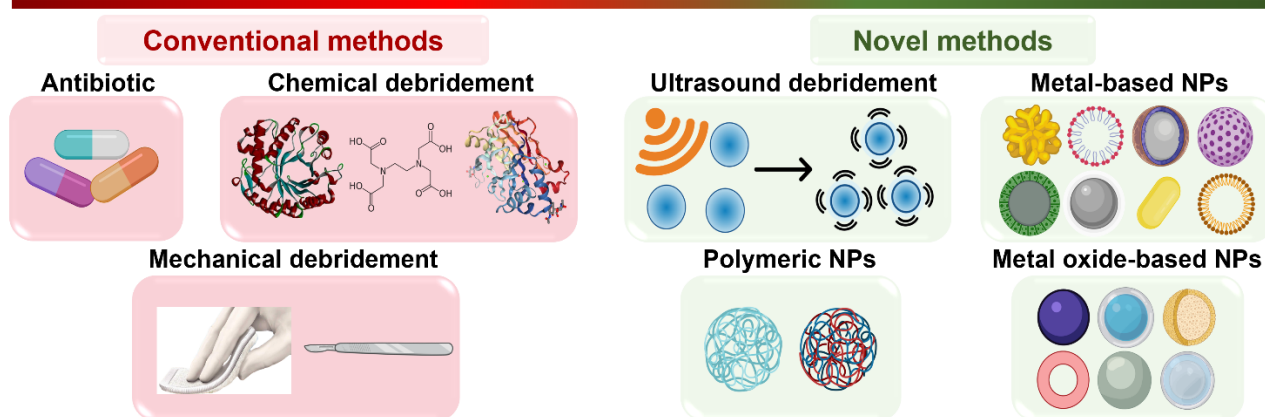


Fig.1.19 Methods for biofilm therapy: Conventional methods and novel methods. The scheme was created on the Biorender website with a license.

By containing EPS in the biofilm, the residing microorganisms are protected from antibiotic therapies and the host's innate immune responses. A biofilm may also develop oxygen gradients and/or anoxic environments, leading to anaerobic conditions deep within the structure [146, 147]. As these cells are located within the biofilm, they have reduced metabolism, making them less susceptible to antibiotics. Since clinicians have limited options for treating biofilm infections, there is an urgent need for a non-toxic antimicrobial treatment that disrupts biofilms rapidly and efficiently.

1.3.2.1 Antibiotics

Chronic biofilm infections can be treated only minimally with topical or systemic antibiotics currently available [199]. Due to the protective barrier formed by EPS, the penetration of antimicrobials to bacteria is slowed or incomplete [200]. Aside from this, antibacterial agents may chemically bind to the extracellular components of the biofilm or attach to the anionic polysaccharides without affecting the target bacterial cells [121]. There is a growing trend to replace antibiotics in healing applications with alternative materials due to the increased concern about antibiotic overuse leading to drug-resistant bacteria. The biofilms in implanted devices remain resistant to antibiotics, making their treatment challenging, especially when they are infected by bacteria [201, 202].

1.3.2.2 Biofilm eradication

There are two main types of biofilm eradication: physical (e.g., ultrasound, mechanical) debridement and chemical debridement. [203-205] (**Fig.1.20**).

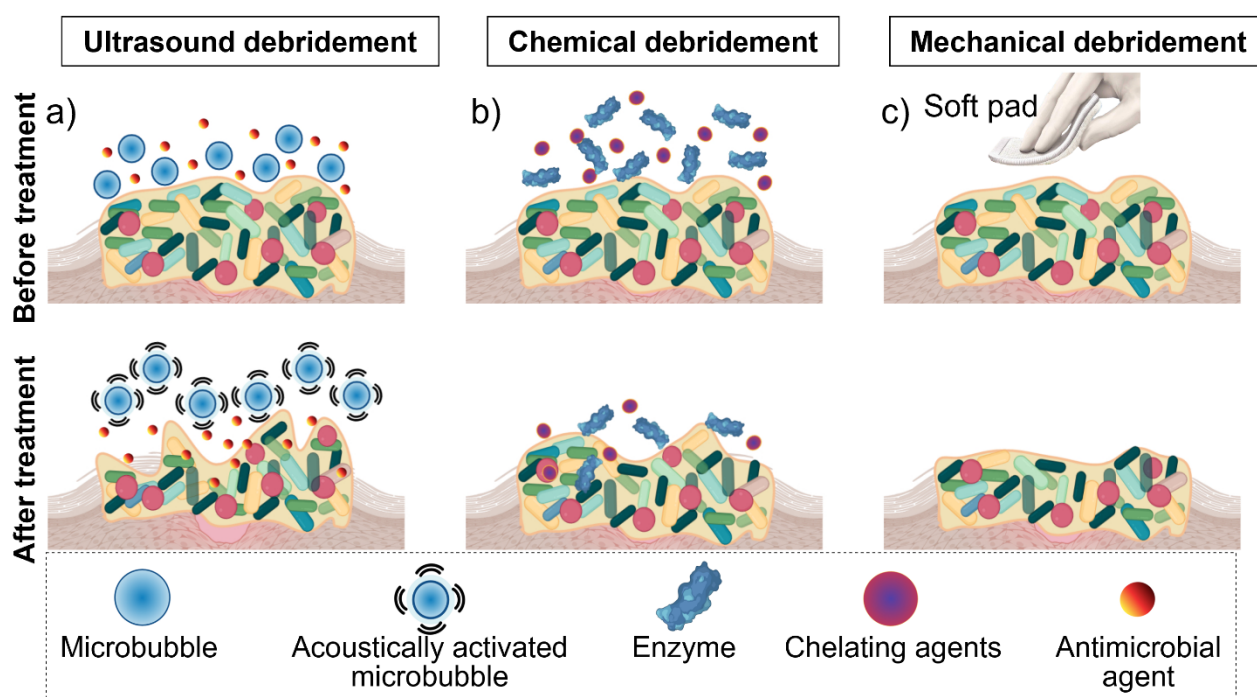


Fig.1.20 Principle of different types of debridement. (a) Conceptualization of ultrasound-mediated microbubble treatment. After delivering nano/microbubbles and antimicrobials to the biofilm-infected site (before treatment), the nano/microbubbles are acoustically activated to disrupt the biofilm and allow the antibiotics to penetrate (after treatment).

1.3.2.2.1 Ultrasound debridement

In addition to treating biofilm-infected wounds, ultrasound debridement has been shown to enhance antibiotic efficacy and promote healing [206-209]. The advantages of ultrasound debridement over mechanical debridement include that ultrasound is less painful for patients [210]. Furthermore, ultrasound may be useful in treating implanted biofilm infections and increasing their antibiotic efficacy [211]. More clinical research is needed for the large-scale implementation of ultrasound-based treatment in a healthcare setting. Ultrasound-based therapies may be used to treat wounds and implants infected with biofilms. Moreover, nano/microbubbles have gaseous cores surrounded by stabilizing shells that can be acoustically activated to deliver drugs and mechanically disrupt biofilms [212]. Researchers have recently emphasized their adaptable composition, size, and fabrication and their ability to control their reactivity in the body [212-214]. In the past few years, nano/microbubble research has focused on cancer therapies; however, there has been increasing interest in its application to biofilms.

1.3.2.2.2 Mechanical / sharp debridement

Sharp or mechanical debridement will primarily eliminate biofilm by scraping off bacteria and necrotic tissues. There are some disadvantages to the current SOC since treatments often do not remove all bacterial colonies. Biofilms have been shown to regain antibiotic resistance 72 h after debridement, reducing treatment efficacy [215]. In addition, sharp debridement is a painful and uncomfortable procedure, affecting patient compliance and treatment effectiveness.

1.3.2.2.3 Chemical debridement

Using a corrosive material to sterilize surfaces is one of the most effective and basic techniques [216]. It is also possible to chemically degrade biofilm EPS. Polysaccharide cross-linking within EPS is carried out by divalent cations such as calcium and magnesium, and manganese and iron contribute to bacteria's cell membrane and metabolic functions [217]. As a result, biofilm formation and strength are affected by competition for these ions or their removal (chelation). There is a wide variety of metal chelating agents. However, the consideration of biocompatibility and safety criteria is still limited. In terms of anti-biofilm agents and with the best affinity for calcium and magnesium cations, the most commonly discussed is ethylenediaminetetraacetic acid (EDTA). *In vitro* and *in vivo* anti-biofilm activity has been demonstrated with an anti-biofilm gel containing a surfactant and calcium chelator. Even though the gel is not yet commercially available, it has shown to be superior to standard care and synergistic effects [218].

1.3.2.3 Nanotechnology

Nanoparticle-based technologies offer new and promising opportunities for effectively defending against infections associated with biofilms. Nanoparticle-based approaches against biofilm infection increasingly focus on developing nanoparticles with specific chemical properties and properties that inhibit biofilm growth. **Fig.1.21** illustrates the mechanism of action of different nanoparticle-based anti-biofilm systems. In some studies, nanoparticle-coated surfaces have been shown to inhibit biofilm formation [219, 220]. The small size of nanoparticles allows them to penetrate cell walls and biofilm layers, causing irreversible damage to cell membranes and DNA. They make effective drug loading and targeting agents due to their long plasma half-life and the high surface-to-volume ratio [221].

1.3.2.3.1 Antibiofilm Mechanism of Nanoparticles

The exact mechanism by which nanoparticles prevent biofilm formation is still unknown. Damage can be caused by DNA damage, oxidative damage, or the generation of free radicals. Below are a few of the properties associated with nanoparticles and their antibiofilm capabilities. Nanoparticles may develop antibiofilm properties by altering the cell membrane, causing impairment of respiratory activity, membrane lipid peroxidation, ROS generation, inducing DNA unwinding, or disrupting metabolic pathways by releasing nitric oxide [222]. According to research, smaller diameters have greater antimicrobial properties. In other words, nanoparticles that are smaller in size would be more effective at penetrating bacterial membranes. It decreases the viability of cells, therefore, inhibiting biofilm formation [223]. Transmission electron microscopy analysis showed significant changes in the cell membrane upon treatment with different shapes of nanoparticles, causing cell death.

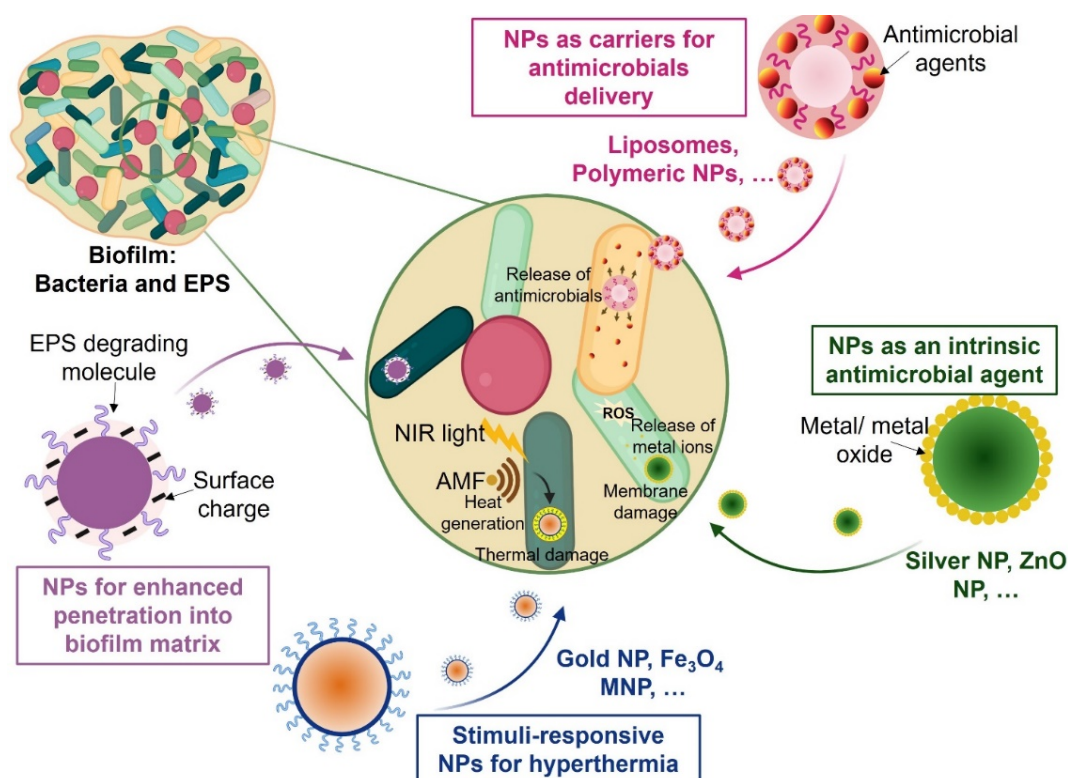


Fig.1.21 Schematic on the mechanism of actions for various nanoparticle (NP)-based approaches for treating biofilm infections. The scheme was created on the Biorender website with a license.

1.3.2.3.2 Metal/ metal oxide-based nanoparticles

Silver, copper, gold, titanium, and zinc are among the nanoparticles showing antimicrobial properties against biofilms. Particular attention has been paid to nanoparticles based on silver. Silver ions require interactions with thiol groups [224, 225]. Thus, bacteria's membrane, respiratory chain, and enzyme activity are disrupted [226]. Silver compromises the intermolecular forces and destabilizes biofilms' matrix as a result. [227, 228]. By decreasing the particle size to nanometers, the surface area, as well as its antibacterial property hasnd its antibacterial property, have been increased [229]. Several metal oxide nanoparticles have been studied for their antibacterial and antibiofilm properties, including titanium oxide, copper oxide, zinc oxide, iron oxide, magnesium oxide, aluminum oxide, and cerium oxide [230].

1.3.2.3.3 Polymeric nanoparticles

The use of polymer-based nanoparticles to deliver antibacterial properties can be achieved in various ways, such as the controlled release of antimicrobial agents, antibiotics or modifying their surfaces with quaternary ammonium compounds. The ion exchange interaction between polycationic polymers and bacterial membranes causes the polymers to interact with the membrane. The result is a disruption of bacterial membranes that causes cell death and damage [231]. Biodegradable hydrogels are another class of emerging antibacterial products [232]. These

polycarbonate hydrogel nanoparticles were also shown to remove planktonic and sessile organisms from biofilms, providing an effective method of preventing biofilm-mediated infections. [232].

1.4 Thesis outline

This thesis aimed at applying Soft-Probe-SECM for bioimaging of melanoma markers in skin-related specimens and bacterial biofilms. The information from the SECM images can be used to identify cancer and biofilm activity. The experimental part presents the chemicals used in this thesis and gives a detailed overview of the experimental procedures developed and used at the EPFL and in Cambridge. In Chapter 3, a tape-stripping method for collecting skin cells and an electrochemical method for detecting melanoma biomarkers in the tape-collected cells are presented. In Chapter 4, the design, fabrication and initial electrochemical characterization of transdermal gold injectable microneedle electrodes with catechol-containing hydrogel coating are introduced for tyrosinase sensing in skin dummies. In Chapter 5, Soft-Probe-SECM was used to detect the electrochemical surface reactivity of *E.coli* biofilms. Chapter 6 presents a non-invasive electrochemical strategy for detecting with Soft-Probe-SECM the effect of an antibiofilm treatment. Finally, in Chapter 7, the novel antibiofilm reagent is developed based on DNA origami, penetrating efficiently through the EPS barrier. In this chapter, the complementary device has also been designed for correlative fluorescence and electrochemical readout.

CHAPTER 2 EXPERIMENTAL PART

All chemicals were of analytical grade and used as received. They are listed in Annexe 2.1. The phosphate buffer (PB) was prepared with monopotassium phosphate (KH_2PO_4 , 99%) and sodium hydroxide (NaOH, 98%). Phosphate buffered saline (PBS, 10 mM, pH 7.4) was prepared with disodium phosphate (Na_2HPO_4 , 99.5%), monosodium phosphate (NaH_2PO_4 , 99.5%) and sodium chloride (NaCl, 99.5%).

2.1. Sample preparations

2.1.1 *In vitro cell culture methods on adhesive tape*

Melanoma cell lines B16, WM239, WM115, and SBcl2 were purchased from the American Type Culture Collection (ATCC) and kept in medium containing ~9.9% v/v newborn calf serum (heat inactivated, Life Technologies), ~89.1% v/v Dulbecco's modified Eagle's medium (DMEM)/Nutrient Mixture F-12 with GlutaMAX Supplement (Life Technologies), and ~1% v/v penicillin-streptomycin (10'000 U/mL, Life Technologies). The cells were cultured in cell culture dishes 60 (growth area 22.1 cm^2) within an incubator (37 °C, humidified atmosphere, 5% CO_2). Cell counting was done by taking a representative image (area 0.26 mm^2) of the adhered cells in the Petri dish by using a Axio Observer inverted microscope (Zeiss) and extrapolating the cell number (obtained with ImageJ software, W. Rasband, National Institutes of Health, USA) to the entire dish surface area. All cells were assumed to be transferred into the DMEM mixture of known volume following the above-described protocol. Solutions with B16 cells were diluted to obtain cell dropping solutions of 240 cells/ μL (for 4x samples), 120 cells/ μL (for 2x samples), and 60 cells/ μL (for 1x samples). For human melanoma, cells solutions contained 2200 WM115 cells/ μL , 1200 WM239 cells/ μL , and 2000 SBcl2 cells/ μL . Then, 10 μL of the cells suspensions were pipetted on the adhesive layer as a single spot and incubated overnight (37 °C, humidified atmosphere, 5% CO_2) to settle the cells and further growth on the tape. Afterward, the culture medium was removed, and the tape was washed with water three times, while in-between the washing steps, the tape was incubated in water for 5 min. The tape was dried for 30 min, and then the cells were tightly pressed with a non-adhesive plastic film to fix and compress the cells. The cells were well adhered, as rinsing with water and bending the tape did not remove them. The samples were stored in a refrigerator at 4 °C. In order to provide samples with tape-collected cells from the mouse skin, the adhesive layer was first non-invasively

applied to the real skin of mice. Then, circular adhesive pads were placed on top for the growth of B16 melanoma cells from dropped cell suspensions (**Fig.2.1**).

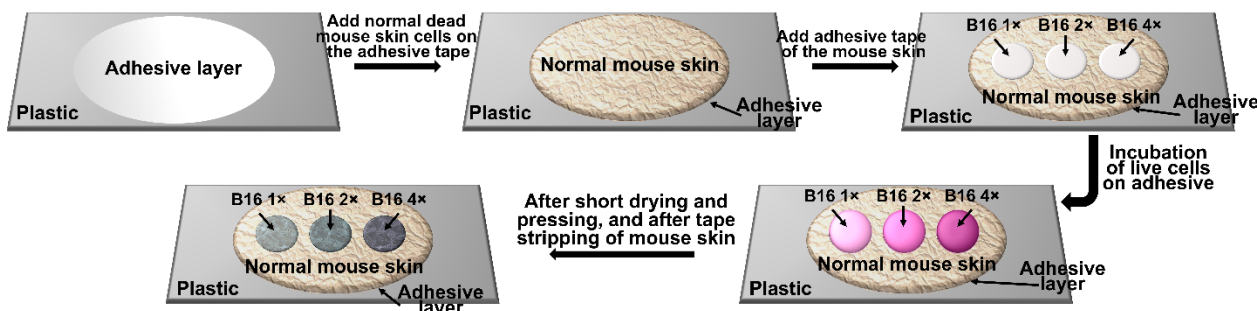


Fig.2.1 Schematic of exemplary sample preparation of a tape sample with B16 melanoma cells, previously grown in Petri dishes and dropped on the adhesive layers; normal mouse skin was collected from the melanoma-free back of mice.

2.1.2 Melanoma mouse model and tape stripping of melanoma samples

All experiments with mice followed ethical guidelines. The murine $\text{Braf}^{\text{CA}}; \text{Tyr}::\text{CreER}; \text{Pten}^{\text{lox4-5}}$ (Braf/Pten) melanoma mouse model was used and prepared following previous reports in the literature [233]. For local tumor induction, 3-week-old Braf/Pten mice were administered $1.5 \mu\text{L}$ 4-hydroxytamoxifen (4-HT; 50 mg/mL in dimethylsulphoxide (DMSO)) typically on the back skin and examined every week for melanoma growth. Mutation of the BRAF gene and deactivation of the tumor suppression gene PTEN resulted in tumor growth. The transgene $\text{Tyr}::\text{CreER}$ encodes CreER^{T2} to avoid lethality by the embryonic expression of $\text{Braf}^{\text{V600E}}$. Indeed, $\text{BRAF}^{\text{V600E}}$, a protein serine kinase, is often mutated in melanoma and enhances the growth and spread of this type of cancer. As the oncogenic activation of $\text{BRAF}^{\text{V600E}}$ alone is insufficient for transforming melanocytes into melanoma cells, the tumor suppressor gene PTEN has been deactivated in the mice used herein. After sacrificing, the part of the back of the mice, where the tumor had been induced, was shaved with a razor blade and disinfected with a wipe containing 70% ethanol solution to provide hairless and clean skin. The adhesive tape from DermTech was then pressed firmly onto the skin under slight lateral movements for several seconds to provide good adhesion before the tape was gently removed. The successful collection of cells could be verified by microscopy. As both the adhesive layer and the plastic support of the tape are transparent, the melanoma region on the sample was conveniently marked with a dark pen on the backside of the tape (**Fig.2.2**). Tape stripping of three mice at 3, 4.5, and 6 weeks following the tumor induction, respectively, was carried out, and each of the three samples was analyzed (*vide infra*).

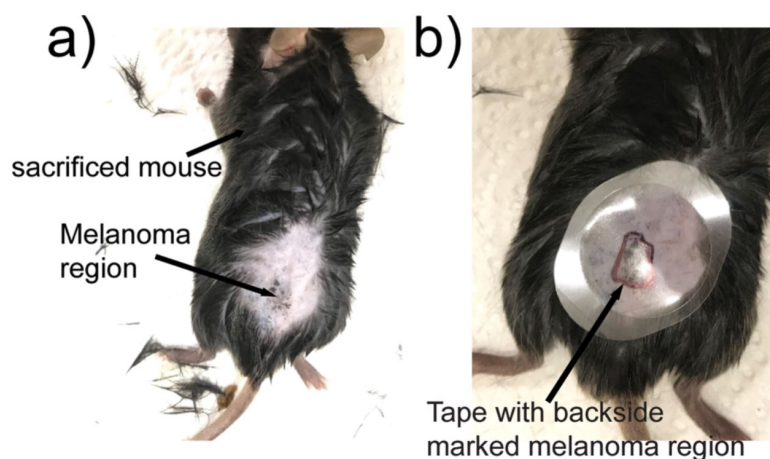


Fig.2.2 Photographs showing the tape-stripping procedure on a melanoma mouse model. (a) Melanoma region on shaved skin region. (b) Transparent adhesive tape placed on the melanoma region with a black mark on the backside of the tape to locate the melanoma region in SECM experiments.

2.1.3 TYR Immunoassay for melanoma detection

A solution of 1% bovine serum albumin (BSA) in 50 mM phosphate buffer was applied to the sample to block the non-specific binding of antibodies to the tissue. Afterward, the BSA solution was removed and a 10 μ L solution of the primary antibody against TYR in 1 mL PBS was added and followed by 30 min of incubation (**Fig.2.3**). Then, the sample was washed three times with PBS, each time for 5 min. Afterward, a 10 μ L solution of the secondary antibody labeled with horse radish peroxidase (HRP) in 1 mL PBS against the primary antibody was added and incubated at room temperature for another 30 min. Finally, the sample was washed three times with PBS for 5 min. The steps of immunostaining of cells and the adhesive layer are shown in **Fig.2.3**.

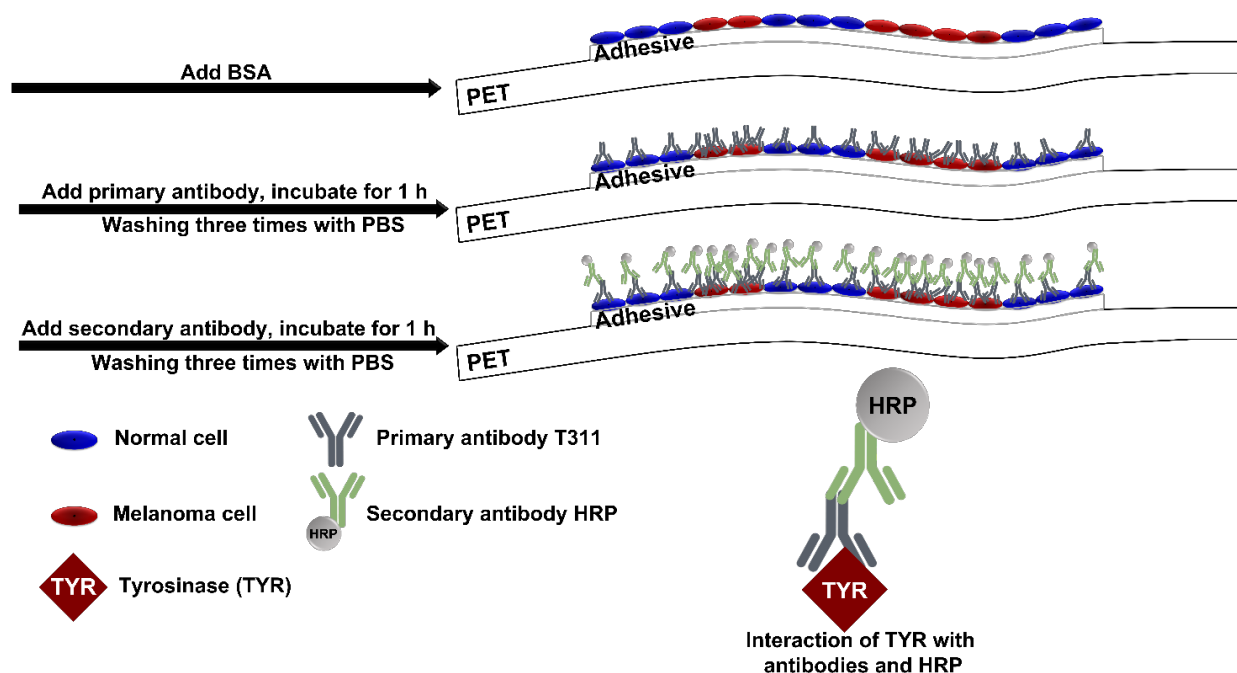


Fig.2.3 Schematic of immunostaining of cells on and adhesive layer.

2.1.4 Colorimetric visualization of TYR immunoassays for melanoma detection

For the colorimetric visualization, immuno-labeled samples were incubated in 2 μL solution of TMB_{red} and H_2O_2 for 2 min. The HRP-catalyzed oxidation of TMB_{red} to TMB_{ox} resulted in a blue coloration of the solution.

2.1.5 Ampicillin resistant *E. coli* DH5 α cells

E. coli DH5 α cells were transformed with pBluescript SK II (+), conferring resistance to ampicillin. 50 μL of a solution with competent *E. coli* DH5 α cells were incubated on ice with 10 ng of pBluescript plasmid DNA. After that, a heat shock at 42 °C was applied for 45 seconds with subsequent incubation on ice for 2 min. The outgrowth of transformed bacteria was performed in LB by shaking (200 rpm) at 37 °C for 30 min. The cells were then distributed on LB agar plates containing 100 $\mu\text{g/mL}$ ampicillin and incubated for 16 h at 37 °C. Finally, single bacterial colonies were picked to start suspension cultures and were grown for 12-16 h at 37 °C in LB containing 100 $\mu\text{g/mL}$ ampicillin. This treatment affected all non-ampicillin-resistant bacteria and avoided cross-contamination of *E. coli* with other bacteria in the environment.

2.1.6 Preparation of *E. coli* DH5 α and ampicillin-resistant *E. coli* DH5 α cell cultures

E. coli strain DH5 α was grown as pre-cultures in LB at 37°C for 6 h with continuous shaking at 200 rpm. 100 μL of each pre-culture was added into 900 μL of 2xYT and incubated overnight at 37 °C with constant shaking at 150 rpm. *E. coli* strain DH5 α with resistance to ampicillin was also cultured in the same way as native *E. coli*, but the culture medium was enriched with a solution of 100 $\mu\text{g/mL}$ ampicillin during all incubation steps. The obtained fresh cultures were then used for measurements of ampicillin-resistant *E. coli*.

2.1.7 *E. coli* DH5 α biofilm culture

4 mL of 5 mM MgSO_4 in 2xYT was added to the solution of *E. coli* DH5 α cells (prepared in section 2.1.6), which was incubated for 2 h under continuous shaking at 150 rpm. Glass slides were placed in the culture dish 60 (Thermo fisher scientific, Switzerland) and incubated overnight at 37 °C and 50% humidity. The biofilm formed at the interface between the glass substrate surface and air and/or culture medium. The presence of Mg^{2+} in the medium positively affects the initial attachment of bacterial cells fostering biofilm formation [234] and the biofilms' mechanical strengts [235].

2.1.8 *E. coli* BL21biofilm culture

E. coli strain the BL21(DE3) was grown as pre-cultures in LB at 37 °C for 24 h with continuous shaking at 200 rpm. 100 μL of each pre-culture was added into 900 μL of 5 mM MgSO_4 2xYT and incubated overnight at 37 °C with constant shaking at 150 rpm. Further, *E.coli* cells had been

transformed with pUC19GFP plasmid and express GFP, meaning no additional staining is required for this strain. Biofilm was cultured as in the previous study [25]. Briefly, cultured *E. coli* BL21 cells after adding 4 mL fresh 5 mM MgSO₄ 2xYT were incubated for 2 h under continuous shaking at 150 rpm. Glass slides were placed in culture dishes 60 (Thermo fisher scientific) and incubated overnight at 37 °C and 50% humidity.

2.1.9 Biofilm tape stripping procedure and sample preparation

The biofilm-coated glass slides were removed from the culture dishes and air-dried. An adhesive tape was then pressed firmly onto the biofilms under slight lateral movements for several seconds to provide good adhesion before the tape was gently removed and further air-dried. This procedure removes the surface layer of the biofilm and fixes it on the adhesive (*vide infra*). The adhesive tape with the collected biofilm top layer was fixed with double-side tape on a glass slide.

2.1.10 Antibiotic treatments for biofilm degradation

Gentamicin treatment

Antibiotic treatments were carried out for 1 h or 24 h of incubation in aqueous solutions with 32 µg/mL and 640 µg/mL of gentamicin. The biofilms were collected from the glass slides with adhesive tapes and transferred and fixed to the bottom of an SECM cell. Antibiotic treatments with gentamicin were made on the tape-collected biofilms. After each antibiotic treatment and before each SECM measurement, *i.e.*, the SECM cell was washed three times with DI water when the solutions were changed.

Sodium azide

Sodium azide was prepared in 4 mM solution in DI water at room temperature. One-day-old biofilms on the glass slides were incubated at room temperature for 5 min and 15 min in the sodium azide-containing solution. After that, the sodium azide solution was washed away gently three times with DI water.

Silver nanoparticles in three methods

Silver nanoparticles were synthesized using three different methods:

Synthesis 1. Silver nanoparticles were prepared by reducing dissolved silver nitrate using citrate [236]. An aqueous solution of 17 mg of AgNO₃ in 100 mL water was heated under reflux and vigorous stirring for two minutes. After that, 10 mL of a 35 mM aqueous sodium citrate solution was rapidly added. The solution gradually turned yellow within a few minutes, indicating the formation of Ag

nanoparticles. The solution was heated under reflux for 6 minutes. After that, the solution was cooled down to room temperature.

Synthesis 2. 50 mg AgNO₃ (29.4 mmol) was first dissolved in 0.15 mL deionized water, then 40 mL acetone was added, and the resulting solution was mixed under magnetic agitation for 20 min. In this solution, 1.6 g PVP powder was added, and the agitation was continued for another 35 min. After 30 min stirring, PVP was observed to agglomerate and stick on the beaker's bottom and wall. The remaining acetone was decanted at the end of the mixing period. At the end of the experiment, the solid PVP (initially white) turned into a light brown and then dark brown paste, indicating silver nanoparticles' formation embedded in the polymer matrix. The final solid was then allowed to dry in the air for 48 h. The Ag/PVP colloid powder was dissolved in 50 ml water under magnetic agitation and kept stirring for 10 days, giving the colloidal dispersions of PVP-protected silver in water [237].

Synthesis 3. In this synthesis, in the final steps, instead of dissolving in water (Synthesis 2), the Ag/PVP colloid was dissolved in 50 ml ethylene glycol to make a colloidal dispersion of PVP-protected silver in ethylene glycol for 10 days [237].

2.1.11 Reactions of silver NPs with biofilms

0.1 µg·mL⁻¹ and 1 µg·mL⁻¹ of AgNPs were added to the one-day-old biofilms on the glass slides and incubated at 37 °C with 50% humidity for one day. Afterward, the sample was thoroughly rinsed with water three times to wash away the silver nanoparticles.

For both azide and silver treatments, the samples were air-dried and were used for complementary detections of live/dead fluorescence microscopy measurements and soft-probe-SECM.

2.1.12 Flashlight irradiation for treating biofilms

The PulseForge 1300 photonic curing system (Novacentrix) was utilized for the irradiation of biofilms. Flashlight irradiation has been done with a Xenon flashlight by pre-charging the capacitors of the lamp control units at 550 V for one, three, and five consecutive shots.

2.1.13 Synthesis of DNA origami nanostructures for biofilm studies

DNA Origami design is based on the work of Yoshidome *et al.* [238] and DNA origami functionalities as in the work of Mela *et al.* [239]. In an origami buffer, staples and scaffold were mixed together to 50 nM and 10 nM, respectively [239]. The assembly was completed by decreasing the temperature

from 85 °C to 25 °C at a rate of –1.0 °C/min. The designs incorporated two functionalities: Alexa-Fluor 647 for fluorescence analysis and aptamers for targeting *E. coli* [240].

2.1.14 Loading of DOX to DNA origami for biofilm treatments

A mixture of different concentrations of DOX (20 µM, 40 µM, and 60 µM) and DNA origami at two temperatures (23 °C and 37 °C) was shaken up to 60 h at 100 rpm to evaluate drug loading efficiency. The loading efficiency was calculated by measuring the absorption of doxorubicin at 480 nm.

2.1.15 Filtering of DOX loaded to DNA origami for DOX loading efficiency studies

After loading DOX to DNA origami, the excess DOX, which were not fully loaded, were removed using a Micro Biospin column (Bio-Rad) packed with Sephacryl S-300 (GE Healthcare). Micro Bio-Spin columns clean up DNA and protein samples quickly. First, Sephacryl S-300 was washed three times with 1× DNA origami at 3000 rpm for 3 min. Then DOX-loaded DNA origami was washed at 1000 rpm for 3 min three times with Sephacryl S-300 and one time with DNA origami.

2.1.16 In vitro release profiles of Doxorubicin for biofilm studies

Five conditions of PBS (pH 7.4), PBS (pH 5.5), DNA origami (pH 7.2), DNase I, and extracellular polymeric matrix that mimic intracellular and physiological conditions and demonstrate pH influence on the release of DOX from DNA origami were evaluated. Generally, normal cells show an extracellular pH value around 7.4 which contrasts with the pH of cancer cells, typically varying between 6.7-7.1 [241]. Further, biofilm has a variant pH that is influenced by environmental conditions. Drug-loaded origami was incubated for 0, 5, 10, 15, 20, 40, and 60 hours at 37 °C and then centrifuged at 10000 rpm at room temperature for 10 min. After centrifuging, the released doxorubicin in the supernatant was collected and quantified by measuring doxorubicin's emission (480nm).

2.2. Characterization methods

2.2.1 Soft-Probe-SECM measurements for melanoma and biofilm studies.

SECM measurements were carried out in a three-electrode configuration using a homemade SECM setup running under SECMx software (G. Wittstock, University of Oldenburg) and comprising an Ivium Compactstat (Ivium Technologies). A soft SECM probe containing a carbon paste microelectrode (ME, active electrode area ~100 µm²) acted as a working electrode, a silver wire was used as a quasi-reference electrode (QRE), and a platinum wire as a counter electrode (CE). All potentials noted herein for SECM measurements were referred to the QRE. The soft SECM probe (VersaScan (VS) Stylus probes obtained from Princeton Applied Research – Ametek) was made of a thin and flexible PET sheet of 100 µm thickness where the ME (electrode area ~100 µm²) was

embedded into a laser-drilled microchannel and sealed with a 2 μm thin Parylene C layer. Soft SECM probes are brushed over the samples in a gentle contact mode with the Parylene C side touching the substrate. Prior to each experiment, the tip of the soft SECM probe was cut with a razor blade to provide a clean active electrode surface (**Fig.2.4**).

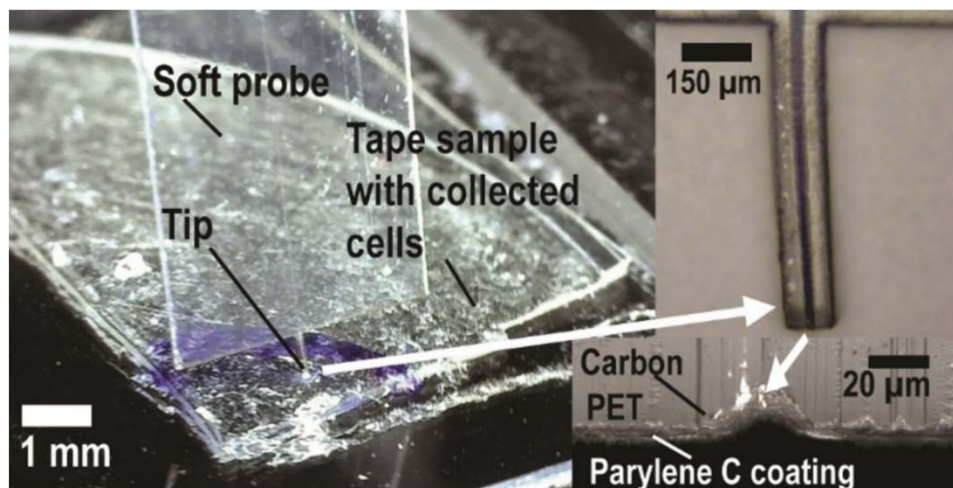


Fig.2.4 Optical micrographs of a soft SECM probe on an adhesive tape with collected sample (insets show the side and cross-sectional view of the tip). Note: blue marks are guides to the eye on the backside of the tapes.

The soft SECM probe was brushed over the samples in a gentle contact mode with the Parylene C side touching the substrate. The probe was tilted by 20° with respect to the surface normal. All experiments were performed at room temperature ($23 \pm 2^\circ\text{C}$).

For chapter 3, all the SECM experiments were performed at room temperature ($23 \pm 2^\circ\text{C}$) in 2 mM FcMeOH and 1 mM H_2O_2 in 50 mM PB with pH 6. Adhesive tapes were fixed with the collected sample facing upwards onto a microscope glass slide for stabilization and placed on the bottom of an electrochemical cell. HRP catalyzed the oxidation of FcMeOH to FcMeOH^+ . Lateral SECM probe translations were carried out with a working electrode potential $E_T = -0.2\text{ V}$ for the reduction of FcMeOH^+ , probe translation speed = $50\text{ }\mu\text{m/s}$, step size = $25\text{ }\mu\text{m}$ and delay time between probe movement and current reading = 0.1 s. SECM soft probe translation experiments were carried out in an alternating probe translation and probe resting period. After a translation step, the soft probe rested for data acquisition and digitization. In order to bring the SECM probe into contact with the substrate, a vertical probe movement was made until the soft probe touched the substrate. The SECM data were analyzed using statistical significance tests. Variance (ANOVA) and t-tests were applied (details vide infra). For all analyzes, $p < 0.05$ was considered statistically different.

For Chapters 5 and 6, lateral SECM probe translations were carried out with a working electrode potential $E_T = 0.5\text{ V}$ for the oxidation of FcMeOH and FcCOOH, $E_T = -0.4\text{ V}$ for the reduction of $[\text{Ru}(\text{NH}_3)_6]^{3+}$ with probe translation speed = $25\text{ }\mu\text{m/s}$, step size = $10\text{ }\mu\text{m}$ and delay time between

probe movement and current reading = 0.1 s. The experimental solution contained 2.5 mM FcMeOH in 100 mM PBS with pH 7.4.

2.2.2 Electrochemical characterization of the Gold MN electrode for melanoma studies

In Chapter 4, cyclic voltammetry of a gold microneedle electrode in 2 mM FcMeOH and 0.1 M KNO₃ solution was performed. The potential scan rate was 10 mV/s.

2.2.3 Optical microscopy of melanoma and biofilm samples

The collected cells from culture and mice were observed either under a Keyence VK-8700 laser scanning microscope, Axio Observer (Zeiss), or by a Dino-Lite camera AM4013MT (1.3 M Pixels).

2.2.4 Electroanalytical measurements with the MN electrode for tyrosinase detection

The analytical performance of the Catechol@alginate: gold MN sensor toward melanoma detection was tested with samples that mimicked human skin using a TYR-dosed agarose dummy skin. Dummy gels are commonly employed in diagnosis *in vitro* research due to their skin-like properties and reproducible behavior. Therefore, a flexible 1 × 1 cm², 500 μm high PDMS platform to confine 1% w/v agarose-based dummy skin for SECM imaging was designed. The dummy gel was injected with different concentrations of TYR, ranging from 0.1 to 0.5 mg·mL⁻¹ that were allowed to diffuse into the gel before applying the MN sensor. A new skin phantom platform was used for each TYR screening test because the immobilized catechol, reacting with the target TYR, is oxidized to benzoquinone (BQ), as indicated by the yellow color of the gel.

2.2.5 Confocal laser scanning microscopy (CLSM) for biofilm characterization

CLSM was applied for biofilm studies. A 20 μM solution of SYTO 9 was prepared from a 5 mM stock solution in DMSO by dilution with PBS. 300 μL of the solution was dropped on a biofilm-coated glass coverslip and incubated for 30 min at room temperature. The absorption wavelength and emission wavelength of SYTO 9 are 485 nm and 500 nm, respectively. Then, a 500 nM solution of PI was prepared by diluting a 1 mg/mL 1.5 mM stock solution in LB. 300 μL of the solution was dropped on the biofilm-coated glass coverslip and incubated for 5 min at room temperature. The absorption and emission wavelengths of PI are 535 nm and 617 nm, respectively. A solution of 50 mM CTC was prepared in PBS for CTC staining. 20 μL were dropped on the biofilm-coated glass coverslip and incubated for 2 h at 37 °C. CTC's absorption wavelength and emission wavelength are 480 nm and 630 nm, respectively. For DAPI staining, 1 μg/mL of DAPI in DMSO was prepared. 300 μL of the solution was dropped on the biofilm-coated glass coverslip and incubated for 10 min at room

temperature. The absorption wavelength and emission wavelength of DAPI are 358 nm and 461 nm, respectively.

The Leica TCS SP8 white light laser (WLL) confocal microscope was used to visualize fluorescent markers.

2.2.6 Crystal violet staining of biofilms

Biofilm-coated glass coverslips were washed three times with PBS and then dried at 60 °C for 15 min. Afterward, the coverslips were incubated in 2 mL of 0.1 wt% crystal violet staining solution for 15 min. After that, the coverslips were washed with PBS three times and dried at 60°C for 15 min. Afterward, the stained biofilm was immersed in 30% acetic acid for 15 min to detach the stained biofilm from the glass slide. The solution was then analyzed with a Lambda 950S UV-Vis spectrophotometer (PerkinElmer), and the results are given as optical density at 630 nm (OD₆₃₀).

2.2.7 Scanning electron microscopy (SEM) of biofilms

Gold was sputtered with a 6 nm thickness on chromium pre-treated glass slide using a DP650 sputtering machine (Alliance-Concept). A bacterial biofilm was grown on a gold-coated glass slide in the culture medium for one day. Then, the Au-coated glass slide with biofilm on top was dried for 1 h in an incubator at 60 °C. The SEM images were acquired with a Thermo Scientific Teneo SEM at 5 kV accelerating voltage and a beam current of 13 pA.

For SEM analysis of gold-coated MNs, the samples were fixed on the stand with double-sided tape.

2.2.8 Statistical analysis

Statistically significant differences for Chapter 3 and Chapter 6 were determined using the *t*-test, one-way ANOVA, and two-way ANOVA. Tukey-Kramer posthoc analysis was used when the ANOVA rejected the null hypothesis. All data were presented as the average \pm standard deviation, and comparisons with $p < 0.05$ were considered statistically different.

For statistical analysis of Chapter 3, the SECM data from the study of the patterns of the normal mouse skin and the B16 melanoma cell line and simulated skin sample (WM239, WM115, SBcl2 cells, normal skin, and plastic) were analyzed with one-way ANOVA. The null hypothesis for all statistical analyses was that two sample means were identical.

2.2.9 Characterization of AgNPs, Ag/PVP nanocomposites

The synthesized AgNPs and Ag/PVP nanocomposites were characterized by using Ultraviolet-visible spectroscopy (UV/Vis) (Lambda 950S UV-Vis spectrophotometer (PerkinElmer)). Colloidal Ag/PVP of 0.05 mL was added to 5 mL water in a quartz cell. For syntheses 1 and 2, the blank test was the corresponding water-PVP solution. In the case of ethylene glycol (Synthesis 3), the blank

solution was the corresponding ethylene glycol-PVP solution, and the chosen volume is the same as the sample preparation for Syntheses 1 and 2.

Furthermore, AgNPs and nanocomposites' size was measured using dynamic light scattering (DLS) (Nano series, Malvern, UK).

2.2.10 Atomic Force Microscopy (AFM) of DNA origami for biofilm treatments

The formation of DNA origami was verified using atomic force microscopy (AFM). For AFM, the DNA nanostructures were diluted 10 times in Origami Buffer (OB). 20 μ L was deposited on mica and incubated for 15 minutes at room temperature before washing three times with 1 mL of OB. The Bioscope Resolve BioAFM was used with SCANASYST-FLUID+ tips (Bruker). Stability assessment for storage at 4 °C was done using weekly AFM images and calculating the percentages of correctly formed structures. Nanoscope 1.9 (Bruker) software was used to analyze dimensions and structure features.

2.2.11 Structured Illumination Microscopy (SIM) for bacteria studies

SIM images of planktonic bacteria were collected using 3-color SIM for optical sectioning.[242] The same lense of A \times 60/1.2 NA water immersion lens (UPLSAPO 60XW, Olympus) focused on the structured illumination pattern and captured the fluorescence emission light before imaging onto an sCMOS camera (C11440, Hamamatsu). The wavelengths for excitation were 488 nm (iBEAM-SMART-488, Toptica), 561 nm (OBIS 561, Coherent), and 640 nm (MLD 640, Cobolt). Images were acquired using custom SIM software [243]. The images were processed with an automated analysis which was written in MatLab. For each SIM imaging, 3 μ L of the sample were deposited on a glass coverslip, and an agarose pad was positioned over the sample to prevent the bacteria from moving during imaging. Another coverslip was positioned on top to minimize drying of the agarose pads.

2.2.12 SIM images of E.coli treated by DNA origami

10 μ L of bacterial suspension (OD_{600} of \sim 1) were mixed with 10 μ L of DNA origami (final concentration \sim 10 nM) and incubated with shaking at room temperature for 15 min.

2.2.13 SIM images of E.coli treated by DOX

Bacterial suspensions (OD_{600} of \sim 1) in solutions with different concentrations of DOX, such as 20 μ M, 40 μ M, and 60 μ M, were incubated either at room temperature (23 °C) or body temperature (37 °C).

2.2.14 Fabrication of 2D microelectrode arrays (MEAs) for biofilm analysis

PEDOT:PSS coated Au MEAs were fabricated by lithography as reported in [56]. Briefly, a 10 nm Ti/100 nm Au layer was first patterned by lift-off. Next, PEDOT:PSS dispersion (Clevios PH 1000,

Heraeus, Germany) containing 5% (v/v) ethylene glycol, ~0.0015% (v/v) of dodecyl benzene sulfonic acid (DBSA) and 1% (v/v) 3-Glycidyloxypropyltrimethoxysilane (GOPS) (Sigma Aldrich, UK) was spin-coated to a thickness of around 380 nm. The film was baked at 110 °C for 1 hr and soaked in de-ionised (DI) water overnight. It was subsequently patterned by photolithography and reactive ion etching. An insulating Parylene C layer was deposited by chemical vapor deposition (SCS Labcoater, Speciality Coating Systems, USA). The openings for the electrodes and contact pads were defined in the PaC layer by lithography followed by reactive ion etching. Since the PaC surface is hydrophobic, the MEAs were treated with O₂ plasma prior to culturing biofilms on them.

2.2.15 Electrochemical characterization of the MEAs for biofilm analysis

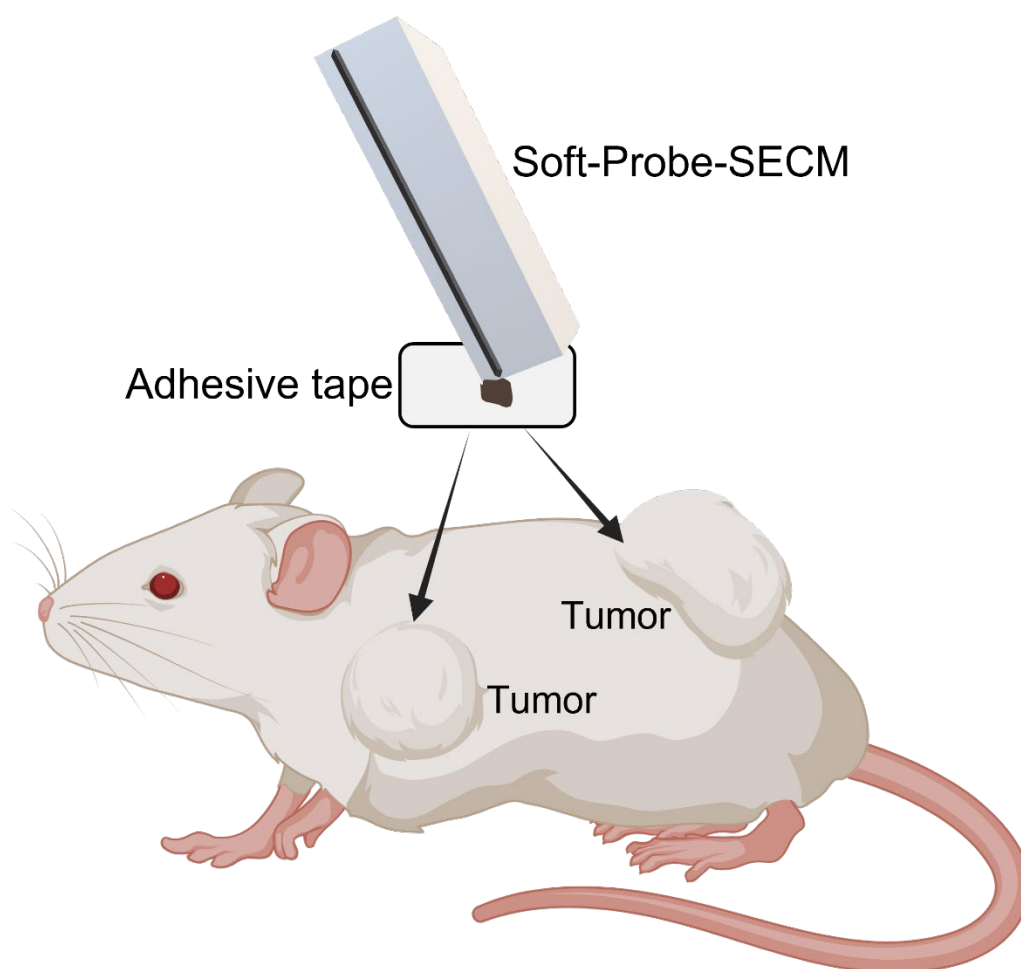
EIS measurements were conducted with an Ivium Compactstat (Ivium Technologies), and the data were fitted by the “impedance.py” package from python. The measured frequency range was from 1 Hz to 100 kHz with an amplitude of ±10 mV at the open-circuit voltage. All experiments were performed at room temperature.

Annex 2.1

Chemical	Supplier	Formula	Chapter
Anti-tyrosinase monoclonal antibody (Ab) T311	Bio Medical (USA)		3
Bovine serum albumin (BSA)	Sigma–Aldrich (Switzerland)		3
Catechol	Fluka (Switzerland)	$C_6H_4(OH)_2$	3
Commercial 3,3',5,5'-tetramethylbenzidine (TMBred) solution	ABRAXIS (USA)		3
Deionized water Milli-Q plus 185 model (produced on site)	Millipore (Switzerland)	H_2O	3,4,5,6
Dipotassium monohydrogen phosphate	Sigma–Aldrich (Switzerland)	K_2HPO_4	3,4,5,6
Ethanol	Sigma–Aldrich (Switzerland)	CH_3CH_2OH	3,4,5,6
Hydrogen peroxide (3%)	Sigma–Aldrich (Switzerland)	H_2O_2	3
Hydrogen peroxide, 60%	Fisher Chemicals (Switzerland)	H_2O_2	3
Ferrocenemethanol 97%	Sigma-Aldrich (Switzerland)	$FcMeOH$	3,4,6
Polydimethylsiloxane	Biesterfeld, Germany	PDMS	3
UV curable resins (EMD6415)	Sun chemical, USA		3
Calcium chloride	Sigma Aldrich (Switzerland)	$CaCl_2$	3
Alginic acid sodium salt	Sigma Aldrich (Switzerland)	$NaAlg$	3
Glycerol	Sigma Aldrich (Switzerland)		3
Lysogeny broth	Sigma-Aldrich (Switzerland)	LB	5,6
2xYT microbial growth medium	Sigma-Aldrich (Switzerland)	2YT	5,6

Ampicillin	Sigma-Aldrich (Switzerland)		5
Gentamicin	Sigma-Aldrich (Switzerland)		5
Propidium iodide	Thermo Fisher Scientific company (USA)	PI	5,6
Polyvinylpyrrolidone	Sigma-Aldrich (Switzerland)	PVP	6
SYTO™ 9 Green Fluorescent Nucleic Acid Stain	Thermo Fisher Scientific company (USA)	SYTO 9	5,6
D-Squame adhesive sampling discs	Clinical and Derm (USA)		5,6
<i>E. coli</i> strain DH5α	Invitrogen (USA)		5,6
<i>E.coli</i> strain BL21	Invitrogen (USA)		7
pBluescript SK II (+)	Stratagene (USA)		5
Ferrocenecarboxylic, 97%	Sigma-Aldrich (Switzerland)	FcCOOH	6
Silver nitrate (>99%)	Sigma-Aldrich (Switzerland)	AgNO ₃	6
Sodium Azid	Sigma-Aldrich (Switzerland)	NaN ₃	6
Trisodium citrate dihydrate (99.0%)	Sigma-Aldrich (Switzerland)		6
L-3,4- dihydroxyphenylalanine (L-DOPA, 99%)	Sigma–Aldrich (Switzerland)	C ₉ H ₁₁ NO ₄	3
Monopotassium dihydrogen phosphate	Sigma–Aldrich (Switzerland)	KH ₂ PO ₄	3,4,5,6
Secondary anti-mouse Abs conjugated with horse radish peroxidase (Abs- HRP)	Abcam (UK)		3
Disodium phosphate (99.5%)	Sigma–Aldrich (Switzerland)	Na ₂ HPO ₄	3,4,5,6
Monosodium phosphate (99.5%)	Sigma–Aldrich (Switzerland)	NaH ₂ PO ₄	3,4,5,6
Sodium chloride (99.5%)	Fluka (Switzerland)	NaCl	3,4,5,6
Sodium hydroxide	J.T. Baker (USA)	NaOH	3,4,5,6

Tris base, 3,3',5,5'-tetramethylbenzidine (TMB) powder	Sigma–Aldrich (Switzerland)	$C_{16}H_{20}N_2$	3
Tyrosinase (from mushroom, lyophilized powder, ≥ 1000 unit/mg solid)	Sigma–Aldrich (Switzerland)		3
Hexaammineruthenium (III) chloride (99%)	abcr	$[Ru(NH_3)_6]Cl_3$	6
Doxorubicin	Sigma–Aldrich (United Kingdom)	$C_{27}H_{29}NO_{11}$	7



¹ Adapted from: Sorour Darvishi, Horst Pick, Tzu-En Lin, Yingdi Zhu, Xiaoyun Li, Ping-Chih Ho, Hubert H Girault, Andreas Lesch, *Analytical Chemistry* 2019, 91, 12900-12908.

3.1 Introduction

The identification and surgical removal of melanoma at early stages, *i.e.*, when it is still superficial, show higher survival rates. The gold standard for diagnosing melanoma is histopathology, where dermatologists, after visual inspection of a suspicious skin area, excise a piece of skin, and pathologists examine immuno-stained slices of it for the confirmation of melanoma. A major issue is that 20-25 biopsies are needed to identify one melanoma correctly [244]. A high rate of false positives on the dermatologic level leads to a large number of unnecessary excisions. To assist dermatologists in decision making for or against an excision, several non- and semi-invasive technologies, including multispectral imaging, Raman spectroscopy, and electrical impedance spectroscopy with microneedles, have been proposed [245]. These methods generally aim to detect microstructural changes inside the different skin layers due to the presence of a tumor. As a straightforward and rapid alternative, tape-stripping with adhesive films on thin plastic foils has been proposed to remove cells from the *stratum corneum* to diagnose various skin diseases, *e.g.*, by applying genomic and protein analyses [244, 246-248]. The *stratum corneum* has limited functions, apart from being a hydrophobic protection layer, and its superficial removal is considered as a non-invasive or semi-invasive process. Sampling with tapes is particularly attractive for melanoma and other skin cancers, such as squamous cell carcinoma [249, 250], as it provides an elegant and painless way of collecting, preparing (also with harsh post-collection treatments) and analyzing cutaneous samples. However, genomic methods require a large genetic profile for differentiating melanoma from benign lesions. It is important to note that non-invasive methods are not supposed to replace histopathology, but only positive test results lead to an excision reducing the false positive rate. On the other hand, negative results lead to follow-up medical visits with higher frequency for visual inspection and possible excision at a later stage. Liquid biopsy on the contrary, *i.e.*, the non-invasive detection of circulating tumor cells or melanoma cell-derived free DNA or exosomes in blood, requires usually complex sample preparation steps and is limited to later melanoma stages (tumor components reaching the bloodstream). However, the detection of blood circulating methods is currently under evaluation for being potentially used for personalized therapy and prognosis [251-254].

Non-invasive melanoma detection aims to address the point-of-care testing (POCT) market, which finds growing attention in various diagnostic areas [255]. In particular, compact electrochemical platforms have been demonstrated to be reliable, affordable, and time-saving [256-258]. Electrochemical methods have the advantage of being unaffected by optical interferences or opaque sample matrices. Various groups have recently applied electrochemical approaches to excised melanoma tissue to detect tyrosinase (TYR) [77, 259]. TYR is a transmembrane, Cu-containing monooxygenase inside the melanosomes where it catalyzes mono- and di-phenols oxidation, such as L-tyrosine and L-3,4-dihydroxyphenylalanine (L-DOPA) [260]. The follow-up cyclization products are derivatives of melanin. Histopathologic TYR assays show high sensitivity (>90%) and specificity

(>97%) for primary melanoma [261]. They can also be electrochemically read out by applying immunoassays with enzymatic labels that generate electroactive species [262, 263] or by employing electro-active TYR substrates and di-phenol derivatives, such as L-DOPA [259, 262] and catechol [264]. In the first case, peroxidase-labeled antibodies can be used to catalyze the generation of colored or electroactive species, while in the latter case, TYR oxidizes diphenols directly into detectable quinones. Besides the overall TYR activity, the micrometric distribution of TYR in tumor tissue provides important information for melanoma staging, as recently demonstrated by TYR mapping using scanning electrochemical microscopy (SECM) [77]. Electrochemical scanning probe microscopies [265] have been applied to investigate the metabolic activity of a broad range of live cells [266, 267], the redox activity of cancer cells [268-270], enzymatic activity on cell membranes [271], and cellular responses to toxins [272]. Nanometric tips, including nanopipettes measuring the ion conductance, provide enhanced sensitivity and lateral resolution on the single-cell level by damage-free tip insertion into single cells [273-275].

Herein, an electrochemical tape-stripping approach is presented. It is based on removing and collecting outermost cellular layers from a patient's skin (here a mouse) with an adhesive tape (**Fig.3.1a**) and analyzing the sample in an SECM. The well-characterized method of using a TYR antibody with an HRP label has been adopted for immunolabeling and detection. In contrast to measuring excised and fixed samples, the tape-stripping approach is operated without further cell lysing.

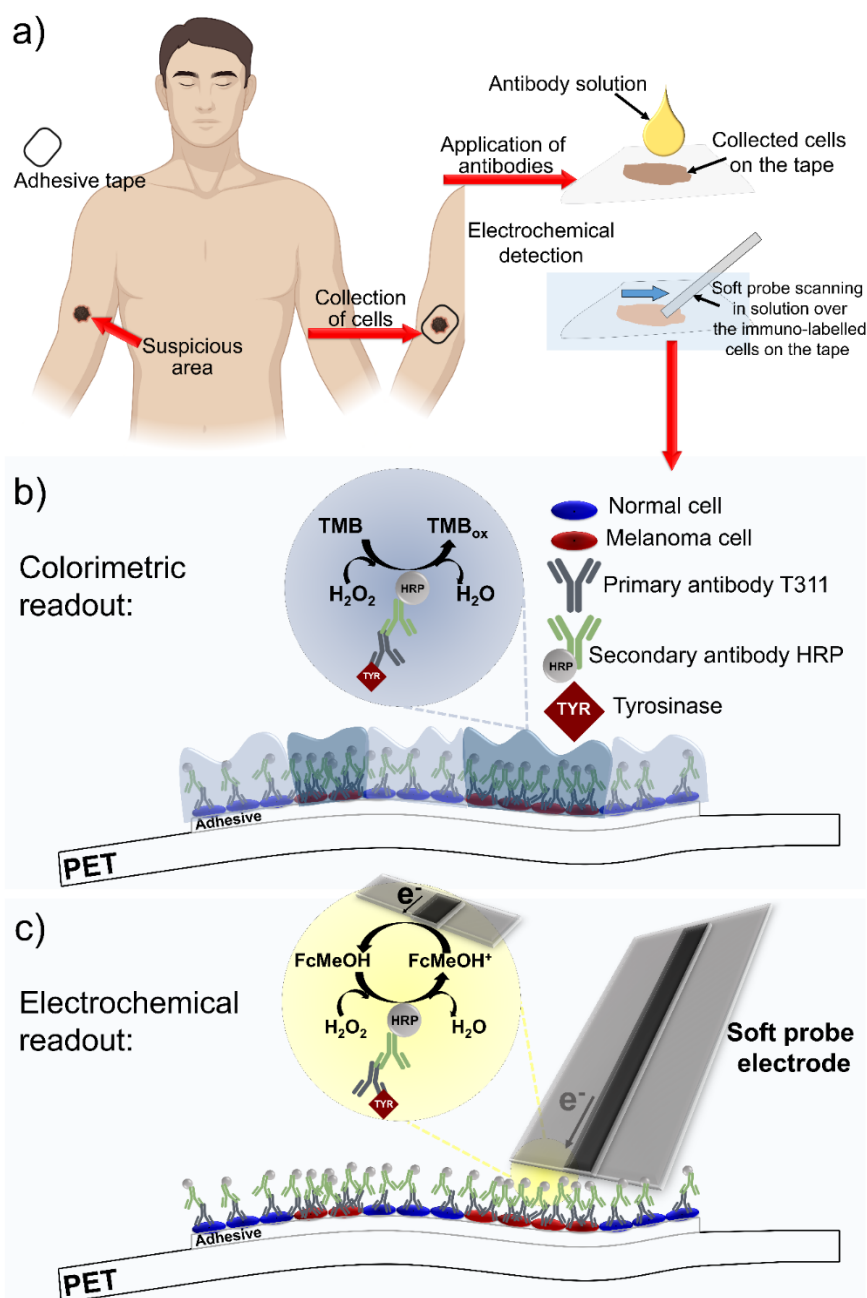


Fig.3.1 Tape-Stripping-SECM. (a) Workflow: (i) collection of skin cells from the skin with an adhesive layer, (ii) staining melanoma antigens with antibodies and (iii) micro-electrochemical imaging. (b) Colorimetric readout (visualizes antigen accessibility). (c) Electrochemical readout (micrometric antigen detection).

A low-resolution colorimetric visualization (**Fig.3.1b**), e.g., with 3,3',5,5'-tetramethylbenzidine (TMB) as substrate, with its oxidation catalyzed by HRP presence of H_2O_2 , provides a rapid proof-of-concept test to visualize the accessibility of the intracellular TYR activity. The electrochemical readout (**Fig.3.1c**) with ferrocene methanol (FcMeOH) as a substrate for HRP measures local TYR activity with high resolution. Soft microelectrodes are ideal probes for contact mode scanning of flexible and bent substrates, such as the tapes, with a constant working distance.

3.2 Results and discussion

A photograph of intact B-16 cells grown in a Petri dish is shown in **Fig.3.2**.

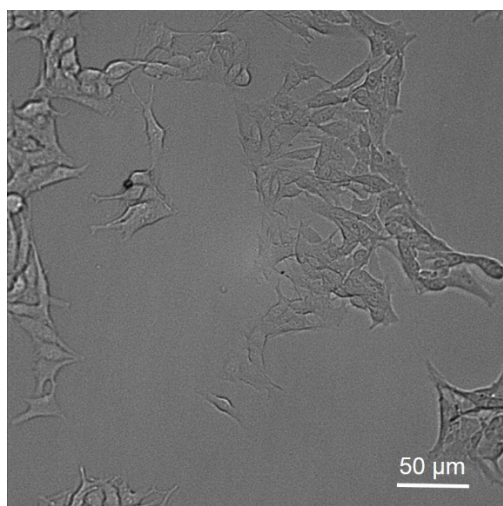


Fig.3.2 Microscopic image of B16 melanoma cell culture in Petri dish.

Cultured B-16 cells (**Fig.3.2**) were cultured and then placed on three different circular bare spots of adhesive (**Fig3.3a**) that was surrounding by previously collected normal mouse skin cells. Cell suspensions with decreasing concentrations of B16 melanoma cells (murine tumor cell line) [276], with the highest relative cell number (4x), two times dilution (2x), and four times dilution (1x) were grown on the three adhesive spots. After culturing, washing, and drying, the cells were pressed with a plastic film onto the adhesive layer to imitate tape-stripping of melanoma cells from the skin. This resulted in flattened and deliberately damaged cells (**Fig3.3b**). Normal skin cells appeared flat and stratified (**Fig3.3b**). **Fig3.3c** shows macroscopic images of the individual cell patterns before and after the colorimetric TYR visualization (2 min). A bluish color in the tape area indicated the presence of TYR activity as a result of the HRP-catalyzed oxidation of TMB_{red} into its cation-free-radical TMB_{ox} (a blue-colored charge transfer complex) [277]. The solution droplets on the tape above the pattern with melanoma cells turned stronger to blue than the droplet over the normal skin pattern indicating higher TYR activity in B16-containing sample regions. Indeed, the compression of the cells affected the integrity of the cell membrane, allowing the TYR antibody to access the TYR without prior chemical membrane permeabilization [278].

Furthermore, a more significant cell density colored the solution stronger. Notably, the colorimetric approach serves as a rapid and straightforward visual tool to verify the success of immuno-labeling. Different cell concentrations and locations in a real skin sample can result in a mixed-colored droplet (optical disturbances). Furthermore, droplets can spread differently on such samples affecting the color intensity for the inspector. Therefore, alternative readouts are necessary when melanoma staging is aimed.

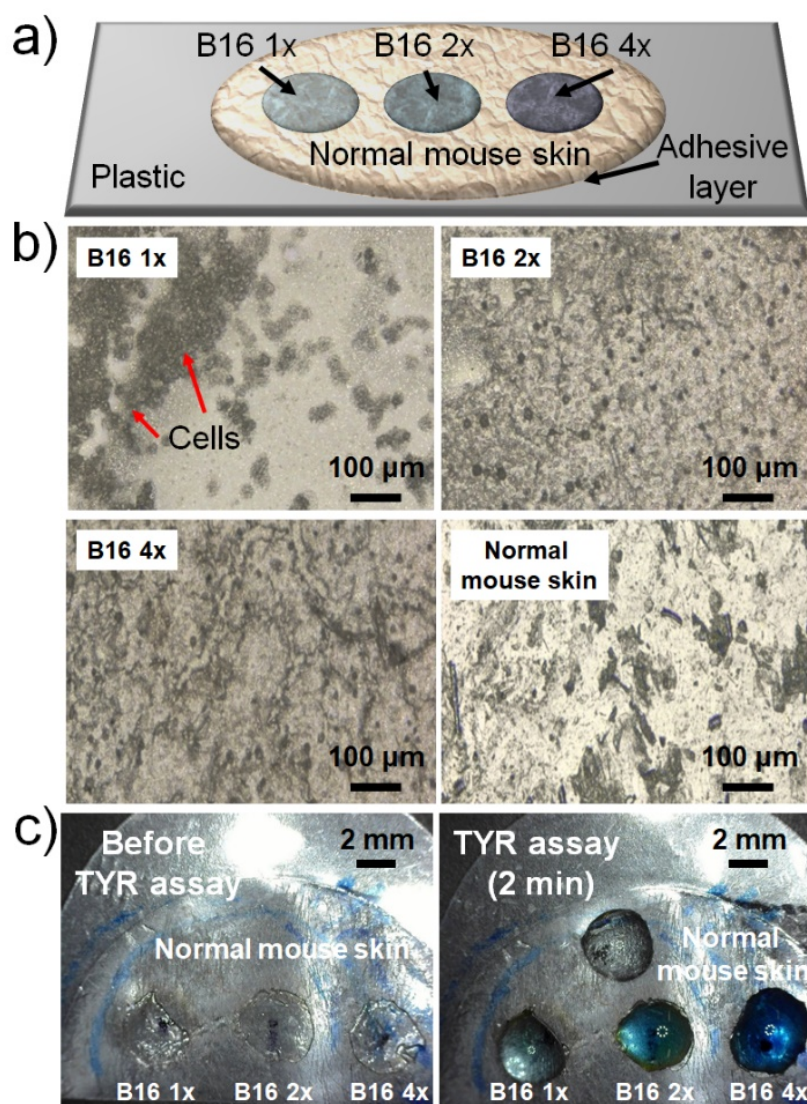


Fig.3.3 (a) Schematic of the sample composition with different relative B16 melanoma cell concentrations. (b) Laser scanning micrographs of cells collected and pressed on the adhesive layer. (c) Colorimetric TYR visualization. Note: blue marks are guides to the eye on the backside of the tapes.

For the localized electrochemical detection, an identically prepared tape with B16 murine melanoma cells was placed after immunostaining into an electrochemical cell and covered with FcMeOH containing solution. A soft microelectrode (**Fig.3.4**) was brushed linearly in contact mode five times along the circular cell patterns with step sizes $\Delta x = 25 \mu\text{m}$ and line displacement $\Delta y = 200 \mu\text{m}$.

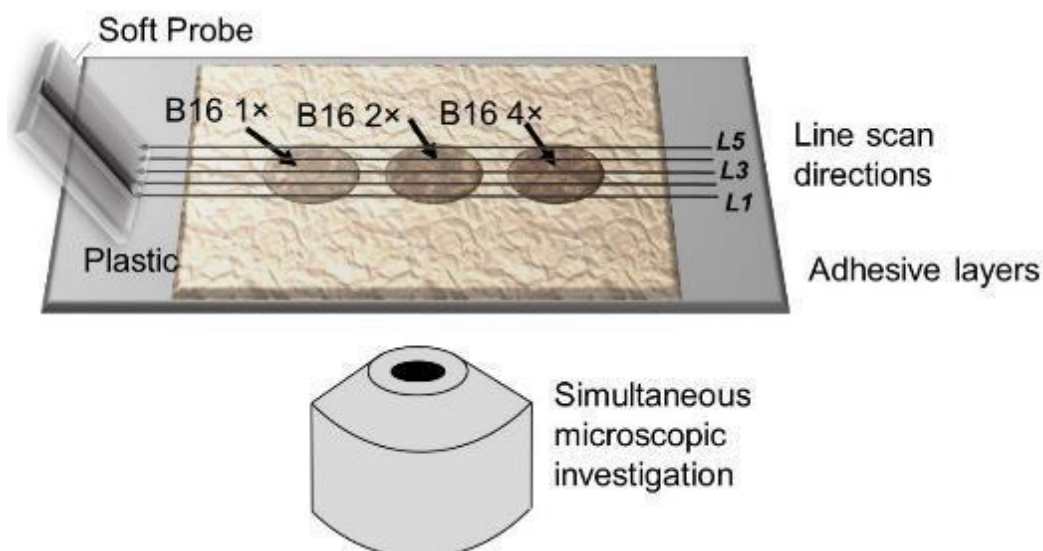


Fig.3.4 Schematic of Soft-Probe-SECM line scan directions on a sample with normal mouse skin and B16 cells of different relative concentrations. The number of line-scans L were either 1-5 or 1-10. The scanning direction was from right to left, and line-scan 3 ($L3$) and line-scans 5-6 ($L5$, $L6$) were located near the center of all patterns for experiments with 5 and 10 line-scans, respectively.

FcMeOH^+ , generated by the HRP labels in the sample, was electrochemically reduced at the soft SECM probe. Higher SECM currents refer to higher concentrations of the immuno-labelled TYR, *i.e.*, a larger coverage with B16 cells, in close vicinity of the soft microelectrode (**Fig.3.5**). Lower SECM currents were recorded over the normal skin patterns. The position of the soft SECM probe on the tape was simultaneously observed with optical microscopy in transmission mode thanks to the transparency of the cellular layer, adhesive and plastic support. SECM signals were precisely correlated with the sample regions of interest (labeled with a blue marker on the backside of the samples). However, the position of all cells on the tape cannot match exactly the grid points of the SECM scanning parameters (step sizes in x - and y -directions).

Moreover, regions with higher cell density or fewer cells (*e.g.*, multi-layers versus incomplete coverage) could be present. In addition, variations in sample roughness, porosity, and permeability for electro-active species can affect the measured current. It is essential to define a sustainable procedure for tape stripping and data collection and data treatment to consider these effects.

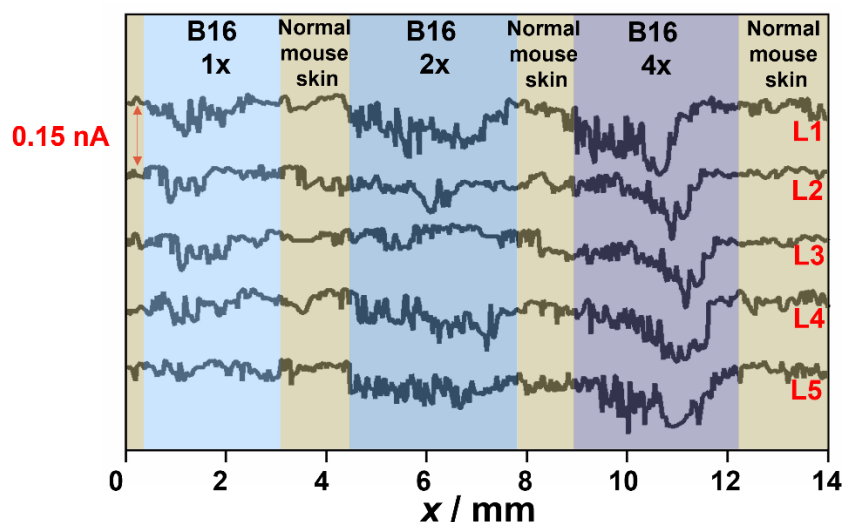


Fig.3.5 SECM line scans over B16 melanoma cells on the adhesive tape. Working potential $E_T = -0.2$ V, probe translation speed = $50 \mu\text{m s}^{-1}$, step size = $25 \mu\text{m}$. 2 mM FcMeOH and 1 mM H_2O_2 in PB (pH 6).

Therefore, the mean currents and standard deviations from each of the four sample regions for the five line scans were calculated (**Fig.3.6** and **Table 3.1**). A constant background current was recorded over bare plastic, which resulted from the diffusion of redox-active species from the solution bulk into the gap between insulating plastic and the soft microelectrode. Partially air-oxidized FcMeOH could already be present in the solution or accumulated over time from its conversion by catalytically active sites spread all over the sample.

Table 3.1 Details about SECM data of B16 melanoma mouse cell samples (**Fig.3.6**):

Pattern	Mean current / nA	Std. Dev./ nA	No. of data points
Normal mouse skin	-0.073	0.019	910
B16 1x	-0.076	0.021	435
B16 2x	-0.099	0.021	595
B16 4x	-0.105	0.034	614

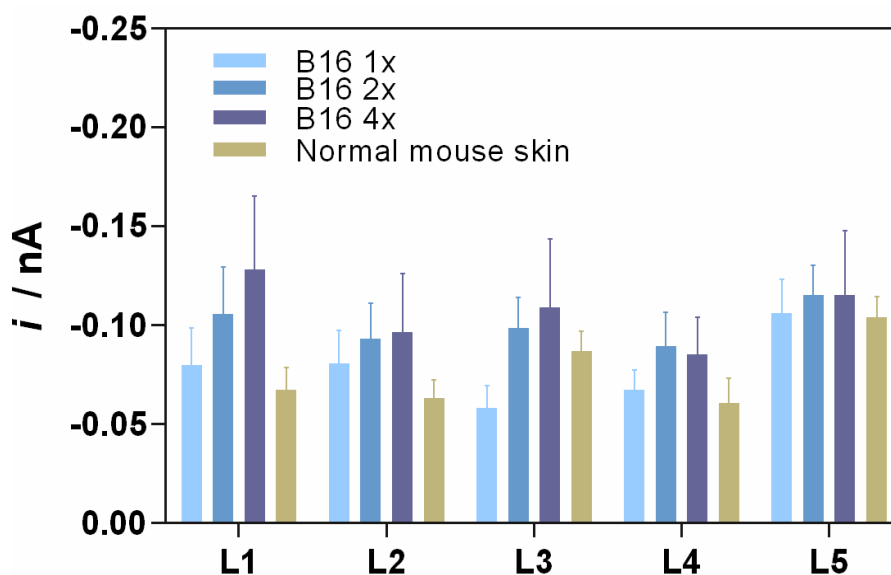


Fig.3.6 Mean values \pm the standard deviation of all data points recorded for each of the five line scans of Fig.3.6 - B16 melanoma mouse cell samples.

The background currents varied slightly between experiments due to minor variations of the soft microelectrode dimensions and microelectrode angle [279]. The bar plot of the region-separated mean currents shows increasing SECM currents with increasing B16 cell numbers. Also, the murine corneocytes (normal mouse skin) gave a small signal, which on the one hand can be explained by low TYR activity in these cells and on the other hand by other proteins than TYR that are present in the sample. While the SECM signals over the 2× and 4× concentrated B16 samples increased significantly, the SECM currents over the B16 1× sample were only slightly higher than the SECM signal over the normal mouse skin sample, which served as a reference for the detection of TYR in the melanoma cells. This was most likely due to the relatively low coverage with B16 cells leading to a non-linear trend in the SECM signals. The increase of the mean SECM currents with B16 cell concentration was confirmed by one-way ANOVA using as N here the number of data points per sample region of one analyzed sample (Fig.3.7). It was consistent with the rise of color intensity observed with the colorimetric visualization.

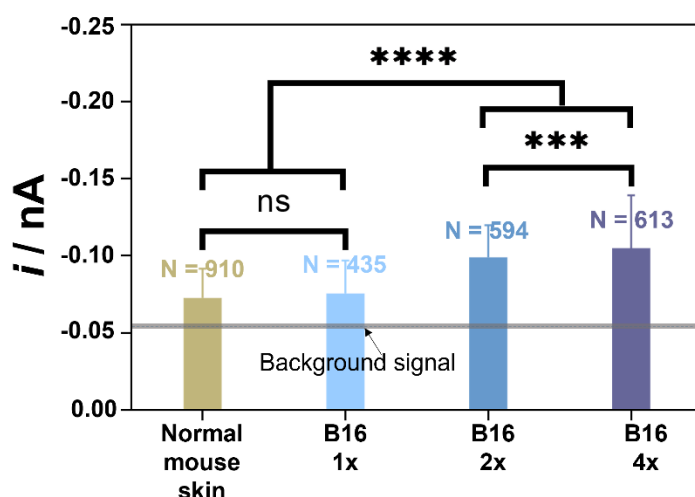


Fig.3.7 Mean currents \pm the standard deviation from the five line-scans of Figure 2 and background current on bare plastic. N corresponds to the number of data points for each sample region in this experiment. One sample with different regions was analyzed. Meanings: n.s. not significant, *** $p < 0.001$ and **** $p < 0.0001$. For all analyzes, $p < 0.05$ was considered statistically different.

However, these artificial melanoma samples were homogeneous and pure in their composition, while melanoma samples from the skin are complex and heterogeneous. Micrometer-resolved SECM detection represents, therefore, a significant advantage to detect both the TYR global activity and local heterogeneity. Both characteristics can be linked to disease progression as previously demonstrated on excised and sliced tissues [77]. Importantly, electrode fouling and contamination of the solution with the glue from the adhesive layer were not observed thanks to the quality of the materials employed. In addition, due to the preset angle of the soft probe (generally 20° *versus* the surface normal), the active part of the microelectrode was never in physical contact with the glue.

Tape-stripping SECM was then applied to the skin of melanoma mouse models with mutated BRAF gene and deletion of tumor suppression gene PTEN at weeks 3, 4.5, and 6 after tumor induction. Both the BRAF and PTEN gens mutations are often found in melanoma [233]. The mouse melanoma model has been designed and applied for the fast development of metastasis in less than seven

weeks, as confirmed by using the gold standard IHC [233]. The melanoma regions of the mice, which were visible by the eye as small pigmented spots, were marked on the backside of the tape (**Fig.3.8a,b**). It must be noted that the adhesive tapes used herein were commercial products routinely used as skin sampling kits for genomic melanoma detection [280]. The tapes are composed of a strong adhesive layer, specifically designed and fabricated for reproducible cell collection from the skin [62, 246]. Furthermore, non-invasiveness has been demonstrated in the literature [250].

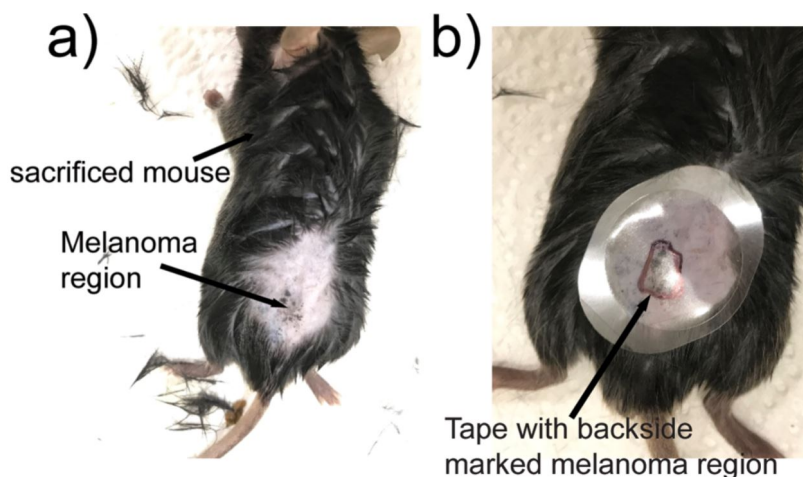


Fig.3.8 Photographs of the tape-stripping procedure on a melanoma mouse model. (a) Melanoma region on shaved skin region. (b) Transparent adhesive tape was placed on the melanoma region with a black mark on the backside of the location of the melanoma region in SECM experiments.

After the tapes were removed from the mouse skin, the TYR assay was applied to the entire collected material. The signals from the electrochemical measurements inside the marked area ("melanoma region") were compared with those outside the mark ("normal skin region"). The normal skin region served as a reference. The confluence of the cells in both areas was considered equal. Few hairs, which remained after shaving and collected together with the cells, were equally distributed over both sample regions and present in all specimens. To verify the accessibility of TYR in the skin samples, collected by tape-stripping and not treated by cell lysing, first, the rapid colorimetric TYR test was applied to the skin samples from all three weeks (photographs in **Fig.3.9**).

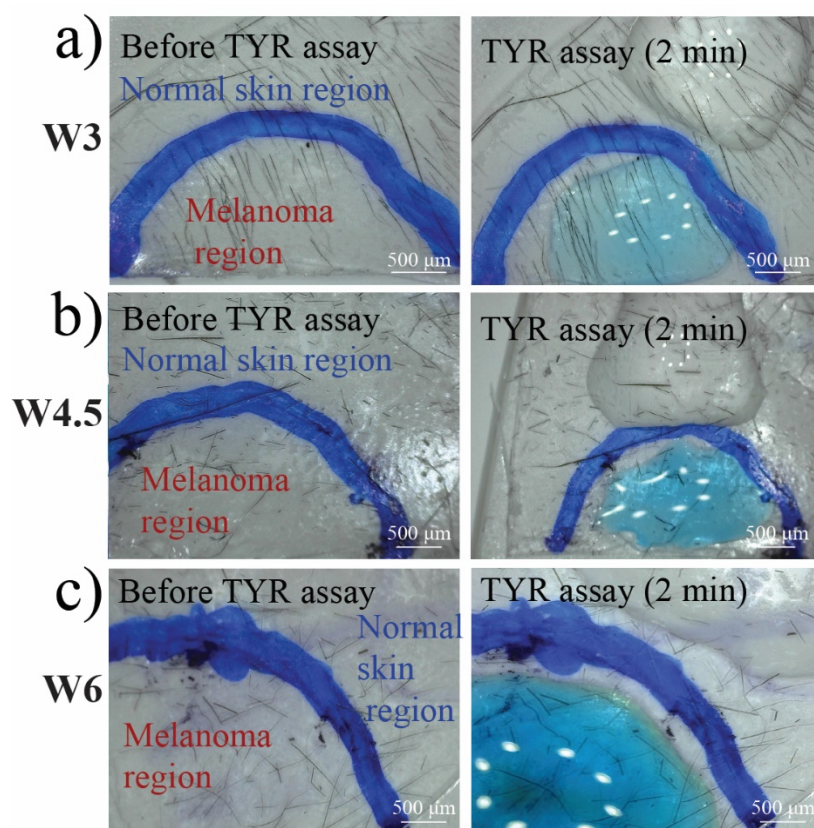


Fig.3.9 Colorimetric detection of TYR in tape-stripped mouse melanoma model skin at different periods after melanoma induction: (a) 3 weeks, (b) 4.5 weeks and (c) 6 weeks.

Indeed, the solution over the melanoma regions turned blue, demonstrating that tape-stripping of the cells from the stratum corneum provided direct access to TYR. In addition, the solution over the normal skin region remained colorless, which confirmed a higher TYR activity in the melanoma region. After that, ten SECM line-scans were performed over an identically prepared sample, and the mean current values inside and outside the marks for each line-scan L1 - L10 ($\Delta x = 25 \mu\text{m}$ and $\Delta y = 200 \mu\text{m}$) and for all ten-line scans together are shown in the bar plots in **Fig.3.10** and **Table 3.2**.

Table 3.2 Details about SECM data of the mice skin samples (**Fig.3.10**):

Time / weeks	Normal skin region			Melanoma region		
	Mean current / nA	Std. Dev. / nA	No. of data points	Mean current / nA	Std. Dev. / nA	No. of data points
3	-0.078	0.012	635	-0.089	0.034	1067
4.5	-0.094	0.051	954	-0.124	0.055	1434
6	-0.089	0.048	1105	-0.193	0.082	1794

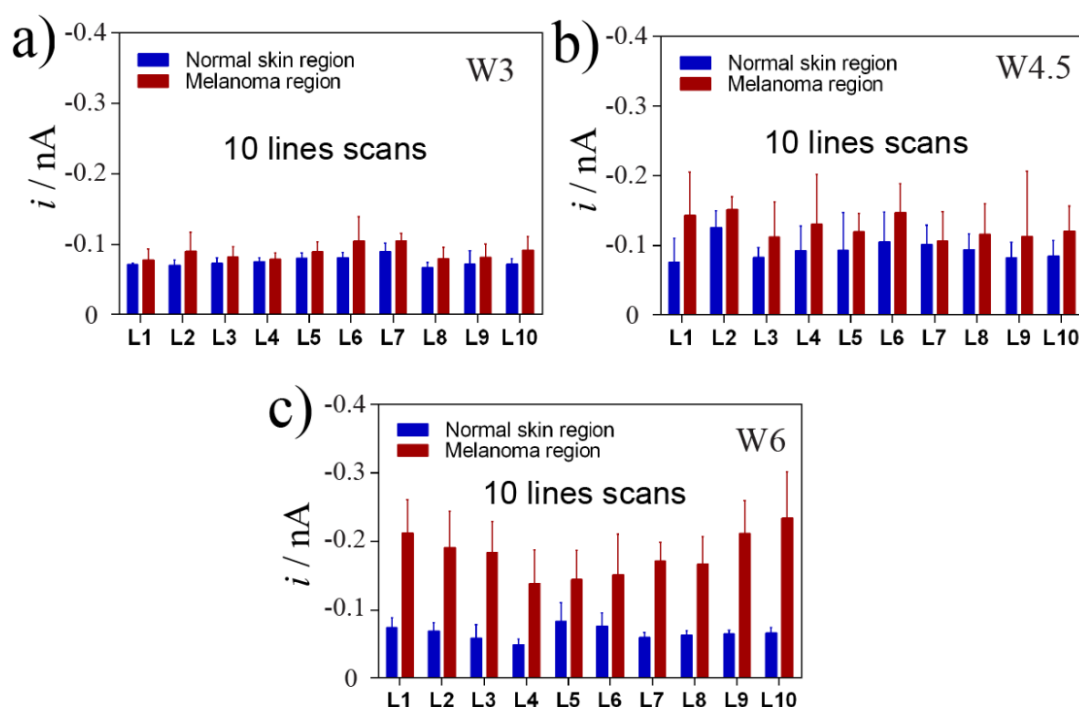


Fig.3.10 Electrochemical detection at different time periods after melanoma induction: (a) 3 weeks, (b) 4.5 weeks and (c) 6 weeks with mean currents \pm standard deviation for each out of ten performed SECM line-scans. Experimental details: One mouse for each week, working potential $E_T = -0.2$ V, probe translation speed = $50 \mu\text{m s}^{-1}$, step size = $25 \mu\text{m}$, 2 mM FcMeOH and 1 mM H_2O_2 PB (pH 6).

Comparing first the individual line scans for each week, it becomes directly clear that variations between the line-scan regions for both the normal skin and melanoma region can be significant (e.g., for week 4.5). This demonstrates the importance of recording sufficient data points from the entire sample area, which here was at least 635 for one sample region. Comparing the mean values from **Fig.3.11**, it is clear that the recorded currents over the melanoma region of week 3 were just slightly higher (-10 pA) compared to the normal skin region. For week 4.5, the difference between the melanoma region and normal skin cell region became more significant (absolute current difference was -30 pA), which can be associated with higher TYR activity as a direct result of progressed tumor growth. This effect became even more pronounced after 6 weeks (-100 pA absolute current difference between normal skin region and melanoma region), indicating further melanoma progression. Between different experiments, the SECM currents can vary due to slight variations in electrode area and soft probe angle due to the mechanical cutting of the SECM tip [279]. Tape-stripping removes a cellular layer of single or strongly connected cells. The electrochemical and colorimetric readout results represent the biomarker concentration in that particular layer. Subsequent tape-stripping removes the next layer of cells. By analyzing the samples with profilometry can provide information about the depth of this sample [62]. Consequently, a layer-by-layer depth profile could be envisaged in future studies.

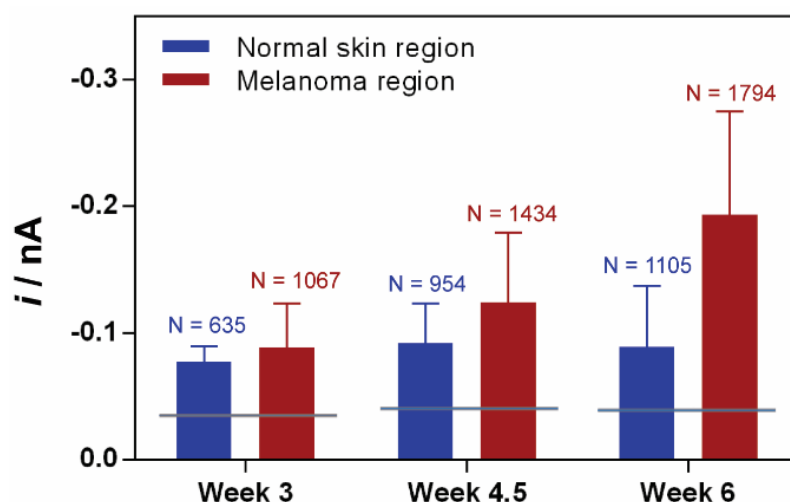


Fig.3.11 Mean current \pm standard deviation of the electrochemical detection at different periods after melanoma induction (3, 4.5, and 6 weeks) with the data from **Fig.3.11**. N indicates the number of data points per sample region. For each week, the melanoma region and normal skin region of one mouse were investigated (1 sample per week, three samples in total). Grey horizontal lines indicate the background SECM current on bare plastic.

A statistical analysis has been performed for **Table 3.3** and **Fig.3.12** and showed the differences after cancer development between TYR expression from normal skin vs. the melanoma part. With tumor progression, the probability that the mean currents of the melanoma region and normal skin sample were not different decreased drastically.

Table 3.3 t-tests of SECM currents over melanoma region vs. normal skin for each week of tumor progression. Comment: The p values are that extremely small because of the large N values used in this case (N = number of data points per sample area = line scan coordinate)

Test	p value
Week 3: normal mouse skin vs. melanoma	$1.4 \cdot 10^{-24}$
Week 4.5: normal mouse skin vs. melanoma	$9.8 \cdot 10^{-42}$
Week 6: normal mouse skin vs melanoma	0

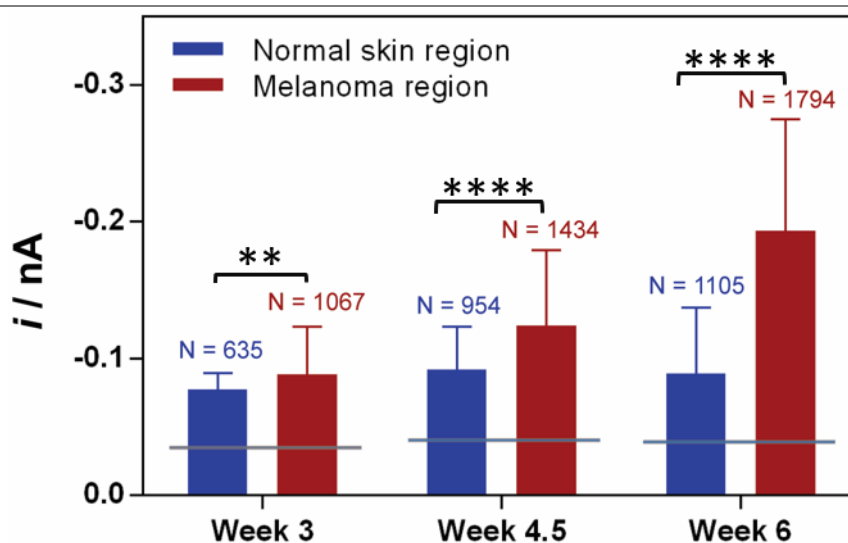


Fig.3.12 Mean current \pm the standard deviation of electrochemical detection at different periods after melanoma induction (3, 4.5, and 6 weeks). N indicates the data points on the normal skin region and melanoma region of the same tapped skin. For each week, the melanoma region and normal skin region of one mouse were investigated. Grey horizontal lines indicate the background SECM current in bare plastic. Meanings: **p < 0.01, ***p < 0.001, and ****p < 0.0001.

The tape-stripping concept was further applied to human melanoma cell lines, which have recently been studied using fixation and cell membrane permeabilization approaches [278]. Herein, an adhesive tape with three patterns of the human melanoma cell lines SBcl2 (radial growth phase of melanoma, RGP, earliest stage between the three investigated ones), WM115 (vertical growth phase of melanoma, VGP), and WM239 (metastatic melanoma, the latest stage of the three investigated human melanoma cell lines) was prepared. **Fig.3.13** shows the photograph of the cells on the petri dish.

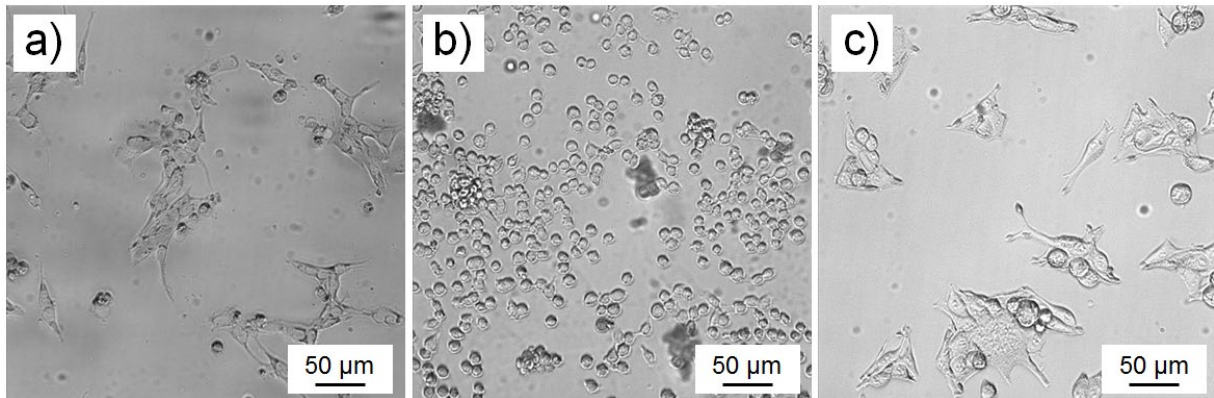
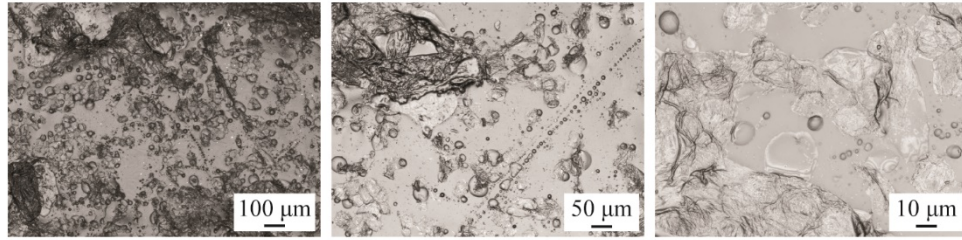


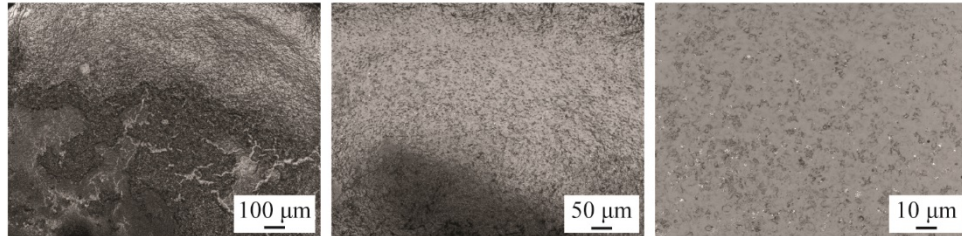
Fig.3.13 Microscopic images of cell culture in Petri dishes of live and intact (a) WM115, (b) SBcl2, and (c) WM239 cells.

As indicated, the melanoma cell lines can be attributed to different melanoma stages. The cell suspensions were dropped on the bare adhesive layer and incubated. The cells were let dry and then compressed to imitate the tape stripping procedure (**Fig.3.14**).

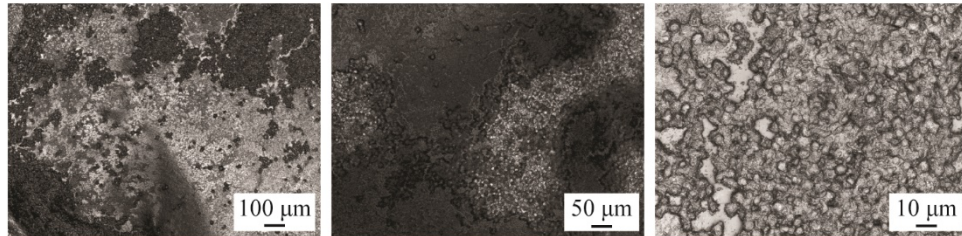
Tape-collected corneocytes



WM115



WM239



SBcl2

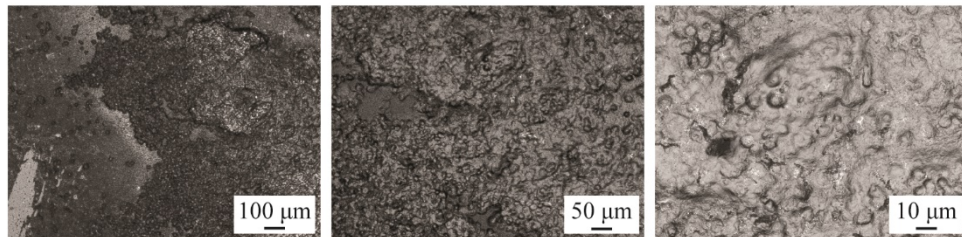


Fig.3.14 Laser scanning micrographs of WM115, SBcl2, WM239, and cells collected from the stratum corneum after tape collection and pressing.

The colorimetric TYR immunoassay was first applied to intact cells. The schematic in **Fig.3.15a** shows the design of the sample with WM115, WM239, and SBcl2 melanoma cells, dead normal skin cells, and a bare adhesive layer on a PET foil. The macroscopic image of the adhesive tapes before and 2 min after covering the cell patterns with TMB solution are shown in **Fig.3.15b,c**. The solution above non-pressed cell patterns did not turn blue, confirming that the antibodies did not access the TYR inside the cells without damaging the cell membranes. In addition, the immunoassay test on the bare adhesive layer confirmed that non-specific binding of the antibodies to the adhesive layer was excluded (no color change).

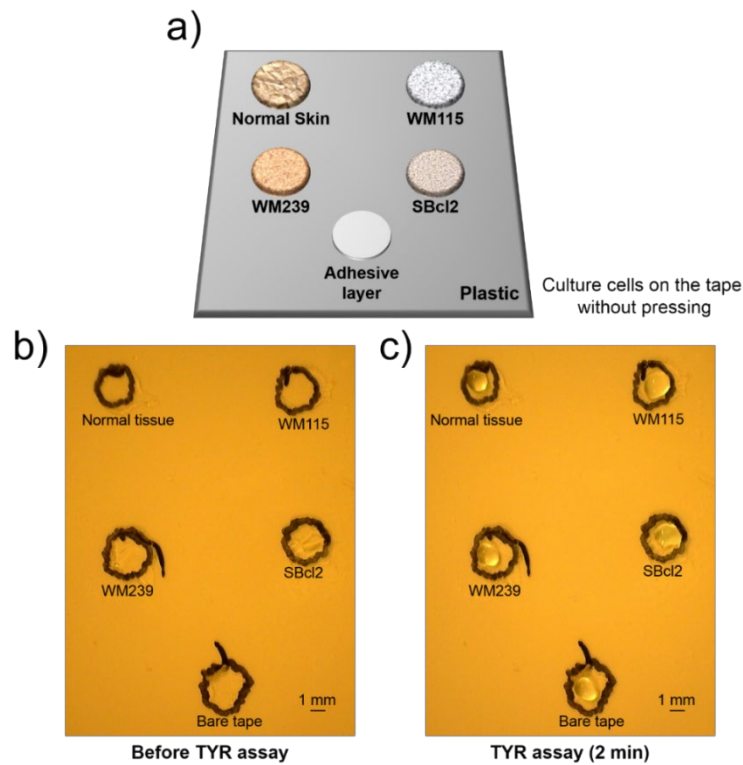


Fig.3.15 Colorimetric visualization of three melanoma cell lines on adhesive tape without mechanical pressing of the cells. a) Schematic of the sample design. b) Before and c) after 2 min of the colorimetric TYR assay using TMB as a reagent. Note: black lines in (b) and (c) were drawn on the back of the tape as guides to the eye to indicate the location of the cell patterns.

Thereafter, the cells were pressed after culturing to imitate cell membrane rupture as for tape stripping. **Fig.3.16** shows that after pressing the solution above the cell patterns turned blue confirming that the antibodies got access to the TYR inside the cells.

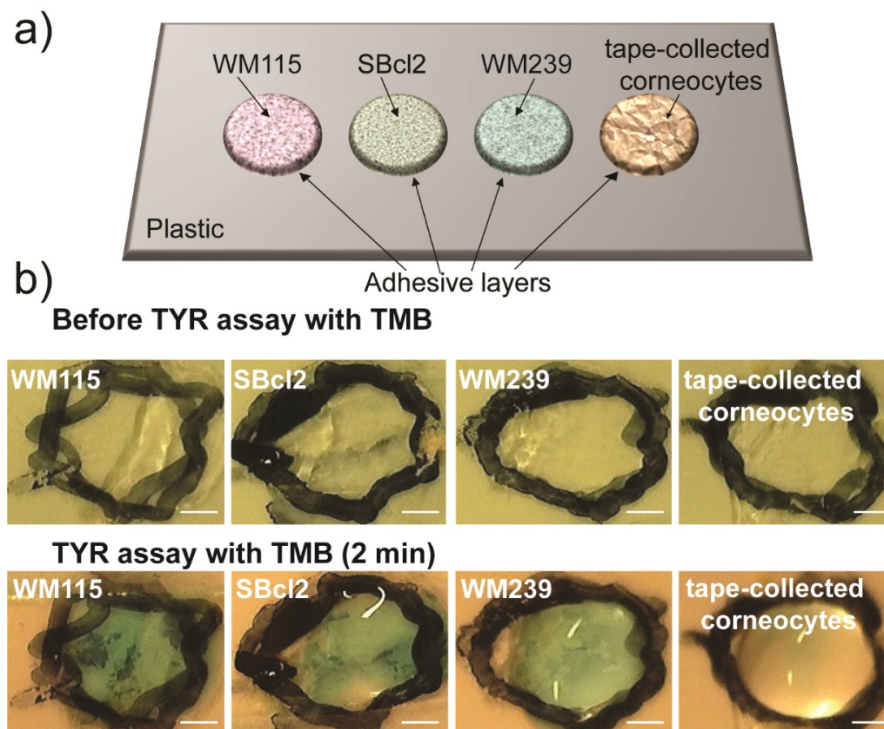


Fig.3.16 Exemplary sample with human melanoma cells lines WM115, SBcl2, and WM239, and tape-collected corneocytes cells after tape collection and pressing. (a) Schematic representation of sample design. (b) Colorimetric visualization. Note: Black marks are on the back of the tape as guides to the eye.

The analysis by SECM after immuno-labeling is shown in **Fig.3.17a,b**. Five line scans were performed with $\Delta x = 25 \mu\text{m}$ and $\Delta y = 200 \mu\text{m}$.

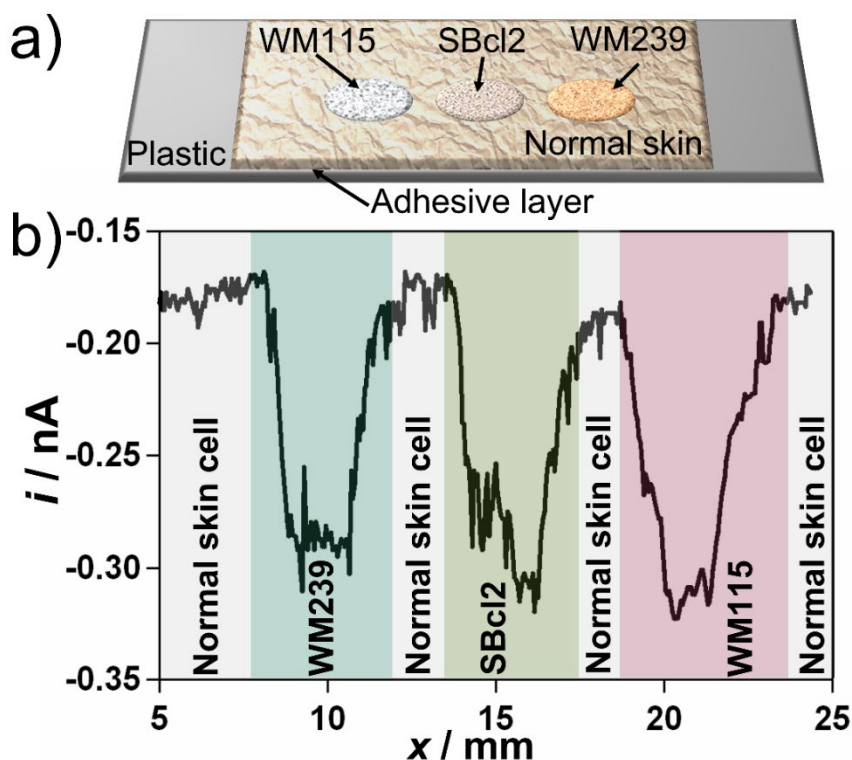


Fig.3.17 (a) Sample design with WM115, SBcl2, WM239 human melanoma cell lines and tape-collected cells from the stratum corneum. (b) SECM line scan with $E_T = -0.2 \text{ V}$, probe translation speed = $50 \mu\text{m s}^{-1}$, step size = $25 \mu\text{m}$. 2 mM FcMeOH and 1 mM H_2O_2 in PB (pH 6).

In the mean currents, it can be seen that the pattern with WM115 (VGP) cells showed the highest TYR activity among the investigated human cell lines, which is confirmed by previous literature reports [278]. Cells of the RGP (earlier melanoma stage than VGP) and metastatic phase (later melanoma stage than VGP) presented both lower mean activity of TYR, being not significantly different from each other (**Fig.3.18**).

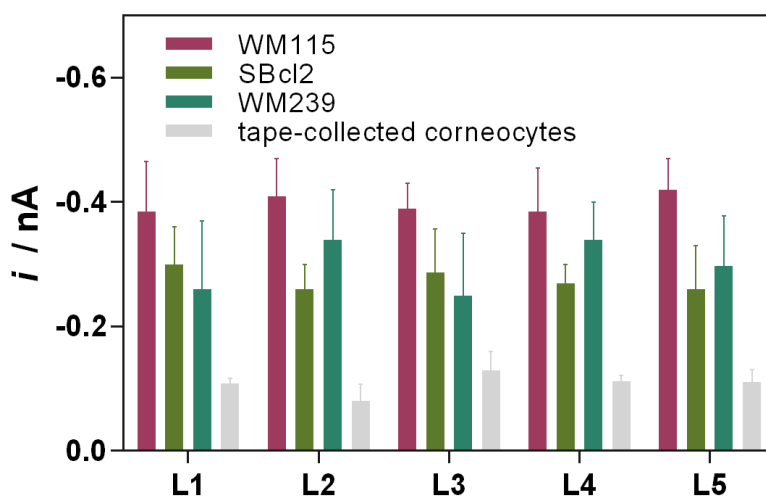


Fig.3.18 Mean current values \pm the standard deviation of all data points of each of the five line scans of human melanoma cell lines. $E_T = -0.2 \text{ V}$, probe translation speed = $50 \mu\text{m s}^{-1}$, step size = $25 \mu\text{m}$. 2 mM FcMeOH and 1 mM H_2O_2 in PB (pH 6).

This was confirmed by one-way ANOVA (**Table 3.4** and **Fig.3.19**). Tumors have developed strategies to become invisible to the immune system. Therefore, although TYR expression increases with cancer progression, enzyme degradation at advanced melanoma stages occurs [281, 282]. This leads, besides a decrease of the global TYR activity, to a heterogeneous antigen expression. Hence, both information, from which heterogeneity can be correlated to the more considerable variation of the mean current, are essential parameters. Compared to a previous study on fixed and permeabilized melanoma cells, the data recorded herein over the WM-239 cell pattern on tape gave the same trends [77].

Table 3.4 Details about SECM data of human melanoma cell lines (**Fig.3.19**):

Pattern	Mean current / nA	Std. Dev./ nA	No. of data points
WM115	-0.400	0.061	361
SBcl2	-0.287	0.050	344
WM239	-0.292	0.082	365
Tape-collected corneocytes	-0.108	0.019	728

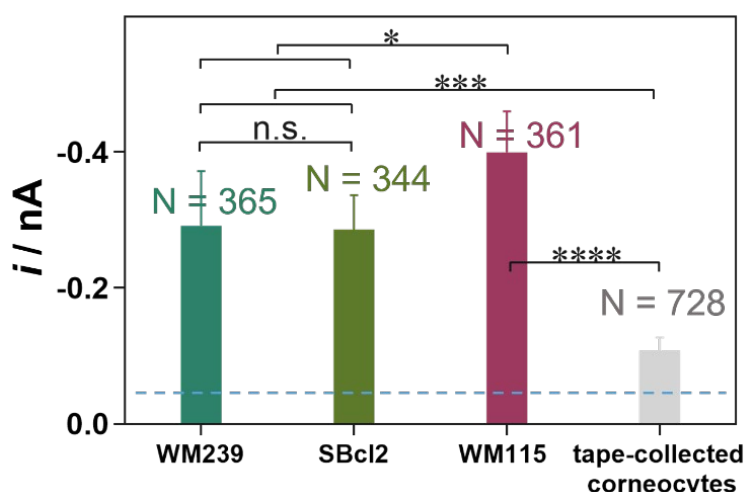


Fig.3.19 Mean currents \pm the standard deviation from five line scans of Figure 6. N indicates the number of data points for each sample region in one experiment. Blue horizontal lines indicate the background SECM current on bare plastic. Meanings: n.s. not significant, * $p < 0.05$, *** $p < 0.001$ and **** $p < 0.0001$.

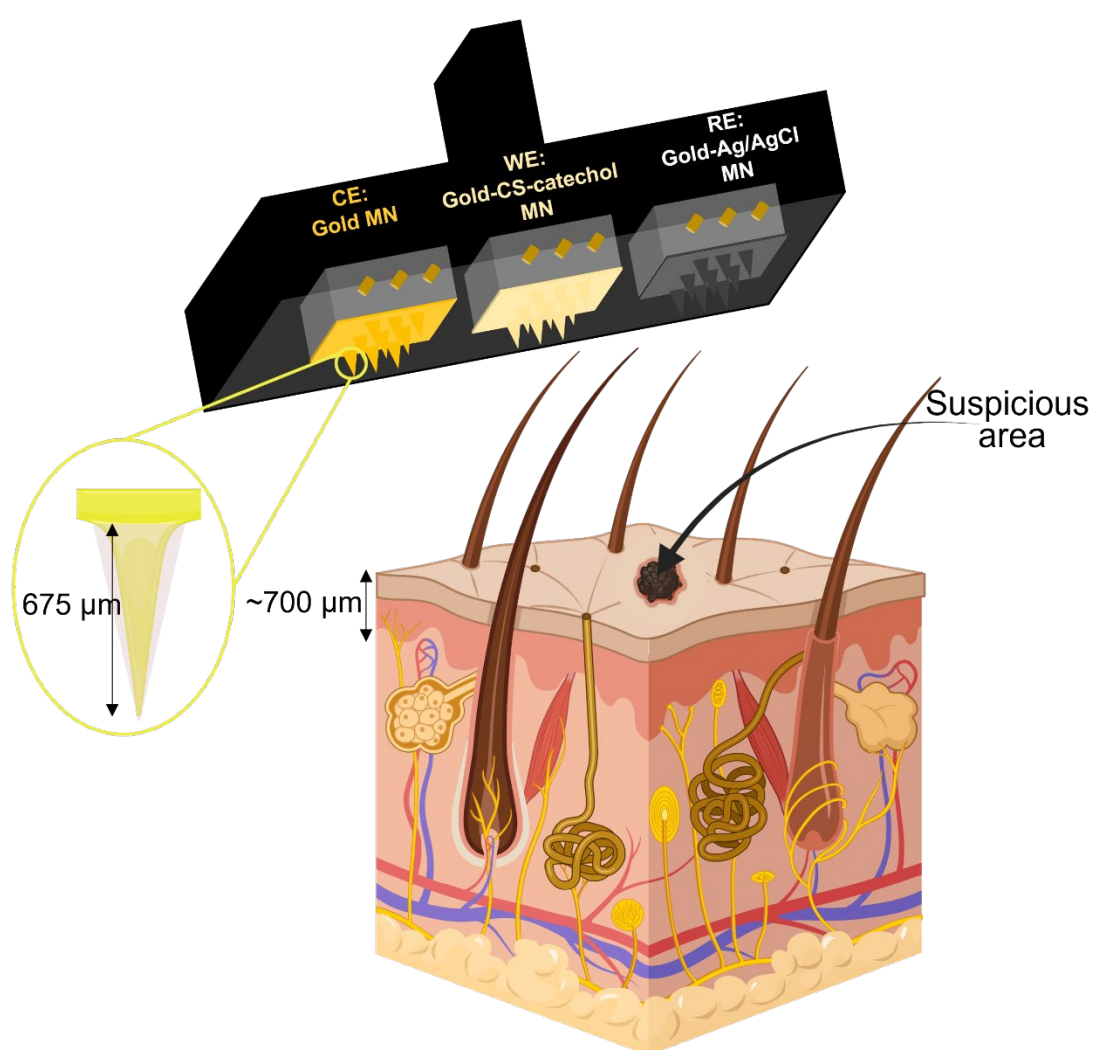
The number of human melanoma cells on the tape samples before incubation were by a factor of about ten higher than for the murine melanoma cells (*vide supra*) resulting consequently in higher SECM signals in **Fig.3.19** compared to **Fig.3.6**. The SECM signals of human corneocytes were slightly higher than for murine corneocytes, which could be explained by the higher content of TYR in human skin due to sunlight exposure.

3.3 Conclusions

Tape-Stripping-SECM was used to collect and analyze biological samples with micrometric electrodes. *In vitro* grown skin cancer cells and cells from the stratum corneum of melanoma mouse models were investigated for the presence of the melanoma biomarker TYR. The quality of the tapes

ensured reproducible cell collection. Removing the stratum corneum with the tape damaged cell membranes sufficiently for enzyme labeling with antibodies. Increased TYR levels were recorded following melanoma progression. The colorimetric visualization of immuno-labeled TYR confirmed the accessibility of intracellular proteins by the tape stripping method. Immunostaining of intact viable adherent melanoma cells did not give a TYR signal, showing the importance of cell membrane damage during tape-stripping. Further studies are ongoing on developing imaging protocols towards melanoma staging based on global and local protein activity. Three-dimensional information about melanoma biomarker distribution can be obtained by analyzing cells from the stratum corneum of different depths, subsequently taken with various adhesive tapes from the same skin area. This sample collection method combined with electrochemical analysis can be further developed as a skin screening tool for skin disease diagnostics on a broader range. This will require studies on more samples, but the method may also be applicable to organoids and 3D micro-tissues, increasingly applied for cancer research. Also, in the recent study based on laser desorption ionization mass spectrometry is coordinated to record skin surface molecular mass in minutes [283]. The samples are collected also by adhesive tape and automated result interpretation is achieved by data learning, using similarity scoring and machine learning algorithms. Furthermore, the progression of malignancy and also prediction of skin disorder progression have been developed. Furthermore, the time of SECM analysis could be drastically reduced by using linear arrays of microelectrodes [279]. By placing a taped sample onto a flat microchip with implemented microelectrode array (MEA), the MEs are arranged in a grid format [284], the presented electrochemical TYR detection approach can potentially be integrated into Point-Of-Care Testing (POCT) devices. SECM scanning parameters, such as ME size and step size, can be used to determine the best design experimentally before fabricating MEA prototypes.

CHAPTER 4 Toward *ex vivo* performance evaluation of a transdermal gold injectable microneedle for tyrosinase sensing¹



¹ Adapted from: Sorour Darvishi and Hubert H Girault, *ChemRxiv* 2021. (<https://doi.org/10.26434/chemrxiv-2021-g6rj2>).

4.1 Introduction

Diagnostic devices, including dermal biosensors, are becoming increasingly popular due to their high potential in the laboratory and their potential for personal health observations. Dermal biosensors, *i.e.*, sensors applied to detect analytes selectively in the skin are principally divided into wearable sensors, including skin-worn surface electrodes, and needle-type skin-penetrable biosensors. These classes of devices were broadly developed to analyze a wide range of analytes in skin tissue and fluids, including sweat [285] and interstitial fluid (ISF) [286], to detect biomarkers for diseases and cancer, such as melanoma [264]. One of the most promising skin-diagnostic devices is the skin-penetrating microneedle array biosensor. At the same time, and if well-designed in terms of materials and geometries, they enable access to the dermal layers without or only with minimal pain or bleeding while providing robust information [287]. Apart from the potentially pain or bleeding, penetrating needles should not provoke the spread of for instance cancer cells to other body parts when hitting blood vessels.

The sensitive and reliable detection of tumor markers, particularly at the early stage of cancer, is currently the subject of many intensive studies, particularly melanoma. In general, a wide range of label-free immunosensing methods has been reported for the detection of cancers, which includes the use of optical techniques, such as surface plasmon resonance [288], ellipsometry [289], and electrochemical methods [290, 291]. The electrochemical methods have many theoretical advantages such as fast operation, ease of use, inexpensiveness, portability, tolerance to sample turbidity, and often ultrasensitivity for identifying target analytes in complex biological samples [292, 293].

Melanoma can be electrochemically read out by employing electro-active TYR substrates and derivatives, such as L-3,4-dihydroxyphenylalanine (L-DOPA) [294]. Although histopathologic analysis of biopsied skin samples will remain the gold standard for confirming melanoma, there is also an interest in non-invasive and painless screening methods that support dermatologists in deciding whether a suspicious skin region should be excised for pathology or whether it can be inspected over a more extended period without invasive intervention. Electrochemical sensing in this sense can be realized by using microneedle-type electrodes penetrating the epidermis. The microneedles must be coated with or made of suitable electrode material that is non-toxic, stable, and provides a sensitive response. *In vivo* electrochemical detection of TYR requires further biocompatible needle electrode coatings, such as solid electrolytes or hydrogels, to provide a liquid electrolyte layer between the electrodes (including a counter and optionally a reference electrode) and the skin. This electrolyte layer must contain an electroactive species, which diffuses inside the electrolyte layer and can react with one or more analytes in the skin, such as with the protein TYR. TYR is an intracellular protein, and addressing it sufficiently might require permeabilizing or rupturing the cell membrane. The permeabilization step removes more cellular membrane lipids to allow large

molecules like antibodies to get inside the cell [295]. This might be achievable directly by using the needles. So far, only a few works have been published on wearable TYR electrochemical sensors for the screening of melanoma on the skin, from which one example is the work of Wang and co-workers [264].

This chapter presents the fabrication and electrochemical characterization of nine gold coated microneedles on one base as a working electrode with external reference electrode and counter electrode. This work shows preliminary data, but the strategy could be further developed in the future and applied for *in vivo* skin measurements. The active electrode area at the cone of the gold needle was defined by insulating the base part of the MNs with a photo-curable polymer. An *ex vivo* study has been done herein with dummy skin composed of an agarose gel with controllable concentrations and distribution patterns of TYR. The gold MNs were coated with an alginate-based hydrogel loaded with an electrolyte and catechol. TYR catalyzes the oxidation of catechol in the presence of oxygen, and the main product of the reaction, o-benzoquinone, is electrochemically detectable at the gold electrodes. This concept principally enables the use of electrochemical catechol redox cycling as a measure for the presence and expression of TYR in the immediate environment of the MN, similar to the work from Wang and co-workers [264]. The microneedle chip was mounted to the z-motor of an SECM to enable the precise penetration of the MNs into a dummy skin. Depending on the penetration depth, this principally allows the recording of the lateral and vertical distribution of TYR, which is important for the electrochemical identification of the progression stage of melanoma and for studying the MN performance in general.

4.2 Results and discussion

4.2.1 Fabrication of the polymeric base of MNs

The microneedle (MN) chip was fabricated as positive mold from a stainless steel MN template. This stainless steel MN template was fabricated by using electrical discharge machining, which uses electrical discharges (sparks) generated between a workpiece (anode) and a shaping piece (cathode). Material is anodically removed from the workpiece in a three-dimensional manner by a series of rapidly recurring current discharges between the two electrodes. The gap between the two is filled with a dielectric liquid due to an applied electric voltage [296]. **Fig.4.1(a-d)** shows the different steps of electrical discharge machining to fabricate stainless steel MN of the machine, which was carried out in collaboration with the mechanical workshop of the EPFL site in Sion. A very thin copper wire (**Fig.4.1a**) is guided near to the stainless steel block (*i.e.*, the workpiece) into which the MNs were to be fabricated (**Fig.4.1b**). The block stand on the holder and the wire were translated relative to each other in the directions shown in **Fig.4.1e**. The result was a three-dimensional steel template containing nine needles in the shape of equal pyramids (**Fig.4.1f**). In order to get the pyramide-shaped needles, the electrical discharge machining process was carried out twice with intermediate rotation of the workpiece by 90 °.

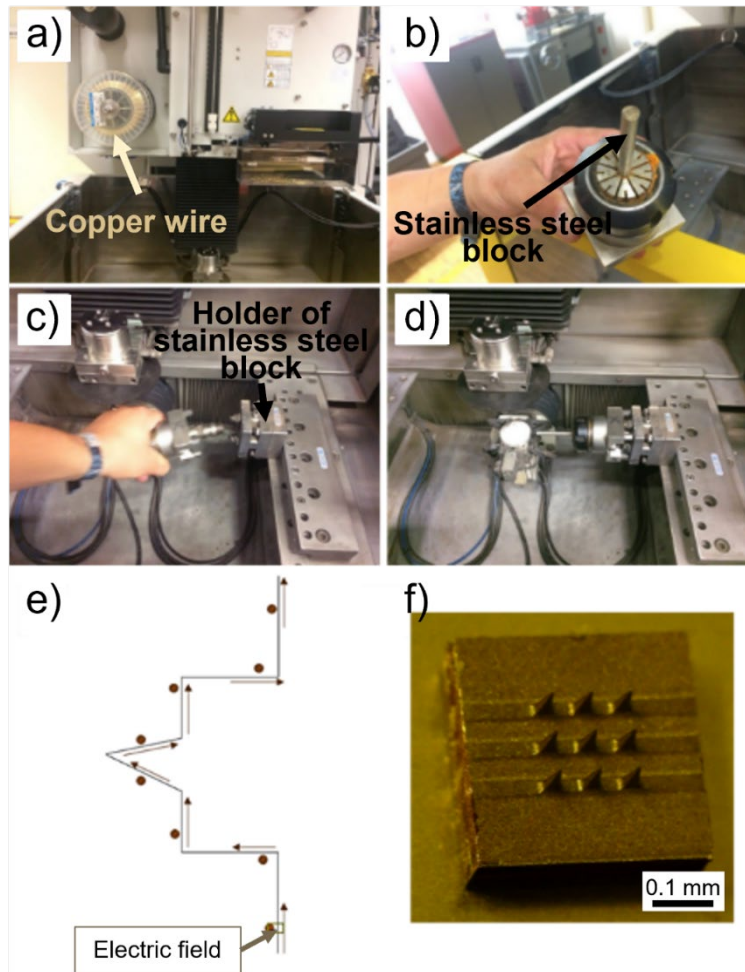
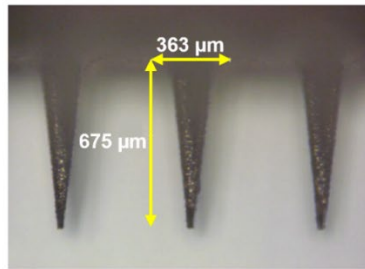


Fig.4.1 (a) Copper wire for electrosparking. (b) Stainless steel block. (c) Holders of the stainless steel block. (d) The whole system of electrosparking. (e) The direction of movement of copper wire. (f) Stainless steel microneedle.

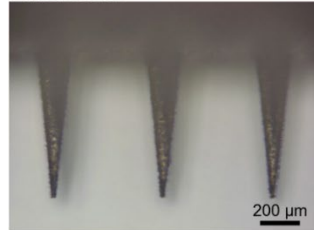
Laser scanning microscopy (LSM) was used to characterize the dimensions of the microneedles. LSM images of one example of the as-obtained stainless steel microneedle template is shown in **Fig.4.2**. Four side views of the MN template are presented. As it can be seen in **Fig.4.2**, the MNs have the same shape and size on all four sides. The MNs have a further height of $\sim 675 \mu\text{m}$ and a base width of $\sim 363 \mu\text{m}$, which are dimensions suitable for insertion into the skin, in which the epidermis that includes the proteins of interest of this work has a thickness of up to $700 \mu\text{m}$. However, the applied MN template fabrication method is flexible in terms of the design of the MN template so that geometry adjustments are facile by modifying the digital process parameters.

Dimension

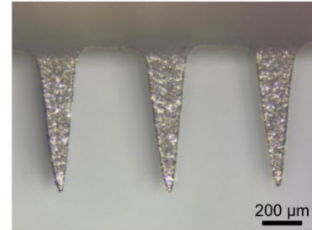


Different view

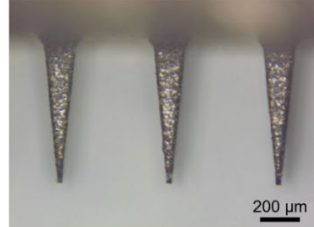
First side



Second side



Third side



Forth side

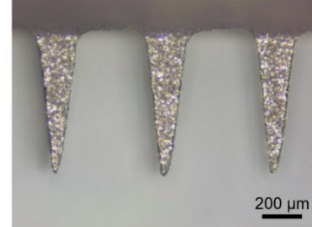


Fig.4.2 Laser microscopy images of stainless steel MNs of the template from the four lateral sides of the template.

After that, a polydimethylsiloxane (PDMS) negative mold of the MNs was made from the stainless steel template. The mold's replicate was created by casting the PDMS precursor mixture with a 10:1 weight ratio of elastomer to curing agent. The PDMS precursor mixture was degassed and subsequently cured in an oven at 80 °C for 4 h to generate the negative mold of the stainless steel master. The solid PDMS negative mold was detached from the steel template and, afterward, its surface was treated with oxygen plasma to make the surface hydrophilic. This will enable an easier removable of the pieces fabricated after that. The cross-section of a PDMS negative mold is shown in **Fig.4.3**.

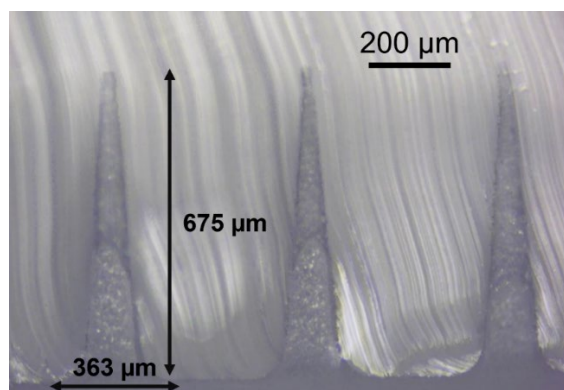


Fig.4.3 Laser microscopy image of PDMS negative mold for the production of a MN chip; side view.

The PDMS negative mold contained MN negatives of a depth of $\sim 650\ \mu\text{m}$ and a maximum width of $\sim 278\ \mu\text{m}$. PDMS molds are suitable for casting many kinds of polymers. In this thesis, polystyrene (PS) was first cast into the PDMS negative mold. **Fig.4.4a** shows the LSM image of the entire PS MN plate, and **Fig.4.4b** shows the LSM of three adjacent PS microneedles with dimensions. Although having the desired dimensions, the PS MNs were mechanically very fragile. As it is shown in **Fig.4.4a**, the tips of certain MNs have partially bent already after the removal from the PDMS mold. The mechanical strength of MNs is one of the key parameters to insert them into matrixes like skin successfully. Therefore, the casting polymer for MN production was changed to a commercial methacrylate-based UV photopolymerizable ink (EMD6415 from SunChemical).

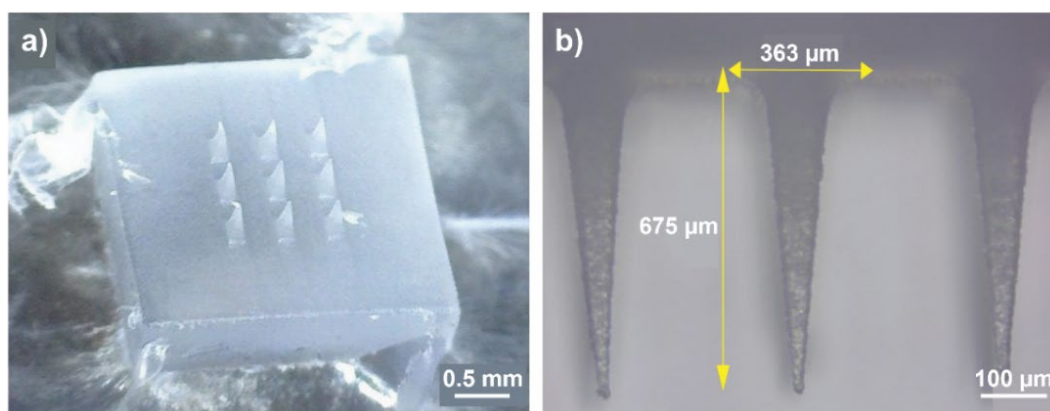


Fig.4.4 (a) Macroscopic image of PS microneedle chip. (b) Laser microscopy image of PS microneedles with dimensions.

The procedure for the fabrication of the EMD6415-based MN chip was rather facile. The UV-photo-curable ink was poured into the PDMS mold and cured under UV light irradiation for 48 hours. A solid and rigid polymer was obtained after 4 hours. It is known that methacrylates are rather toxic. Therefore, it must be guaranteed that the polymerization was complete before using the MN chips further. Indeed, the ink was photochemically cured until the yellowish color of the initial EMD6415

ink changed to nearly completely transparent. **Fig.4.5** shows a microscopic image of an MN chip based on the EMD6415-based polymer.

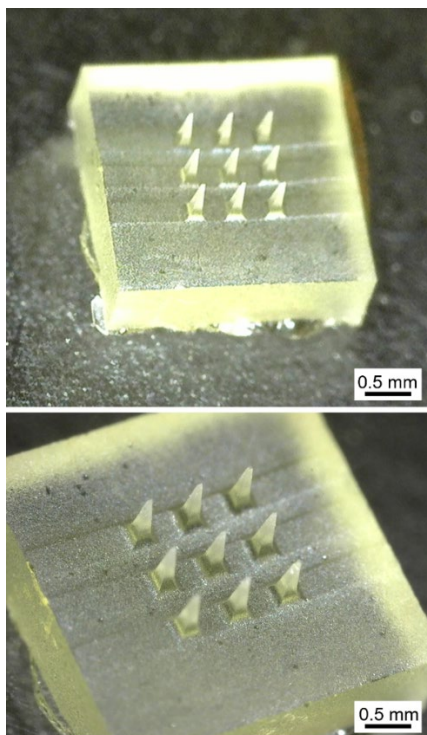


Fig.4.5 Macroscopic image of an EMD6415-based MN chip.

Furthermore, the MNs were characterized by scanning electron microscopy (SEM, **Fig. 4.6**). The tip of the MN contained a quasi-plateau with a length of about 8 μm and a width of about 500 nm. Ideally, a sharp tip would have been desired, but the accuracy of the template fabrication was limited.

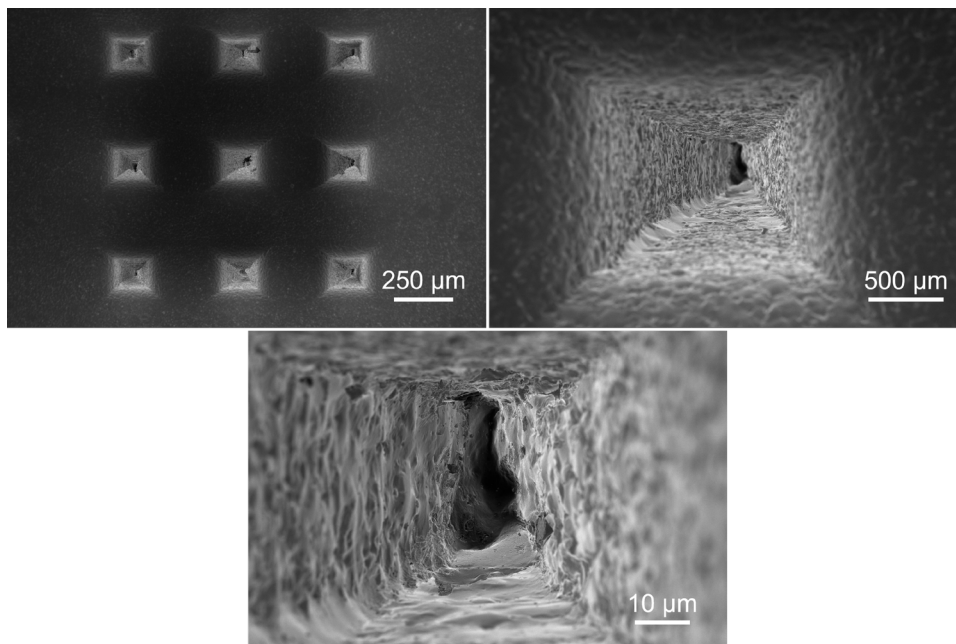


Fig.4.6 SEM images of the EMD6415-based MN base plate (top views with different magnifications).

4.2.2 Gold coating

A gold layer was deposited as a conductive electrode layer onto the polymeric EMD6415 MN base plate by thermally subliming gold particles at around 0.185 A/s (1 hour evaporation procedure) using

a DP650 sputtering machine (Alliance-Concept). **Fig.4.7** shows a microscopic photo of an Au-coated MN electrode (a) and an LSM of the cross-section of a single microneedle (b).

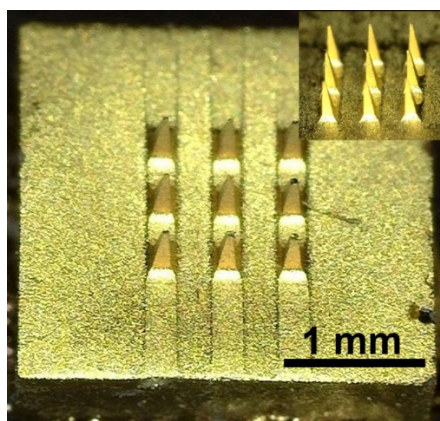


Fig.4.7 Microscopic image of a gold-coated MN chip.

Fig.4.8 shows the XRD pattern of the thin gold layer on the EMD6415 MN chip. Gold nanocrystals exhibited four distinct peaks at $2\theta = 38.1, 44.3, 64.5,$ and 77.7 . All the four peaks corresponded to standard Bragg reflections (111), (200), (220), and (311) of face center cubic (fcc) lattice [297], indicating the successful gold coating on the EMD6415 MN base plate. XRD was used instead of XPS or EDS just because it was immediately available.

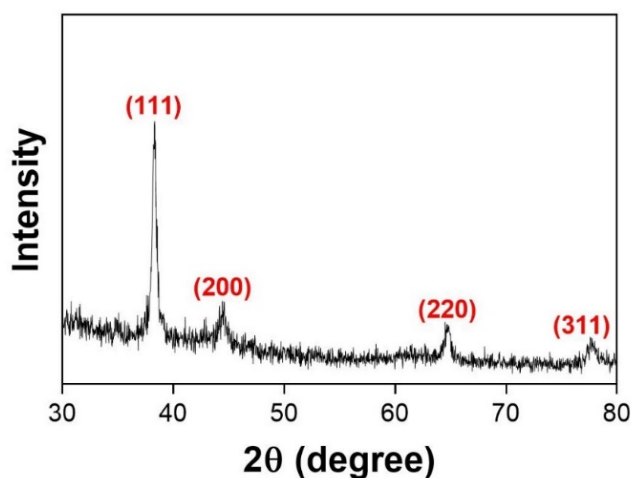


Fig.4.8 XRD pattern of the gold layer on the MN chip.

4.2.3 Mechanical behavior of gold-coated MNs

An important requirement for using MNs is the effective and reproducibly penetration of the MNs into the skin. For establishing designs allowing effective and repeatable MN punctures, a good understanding of the mechanical characteristics of the MNs is essential. The mechanical behavior of the MNs was evaluated by gently applying a force from the top of the needles until they fail, *i.e.* their breaking. The force loading system for assessing the mechanical properties of the MNs is shown schematically in **Fig.4.9**.

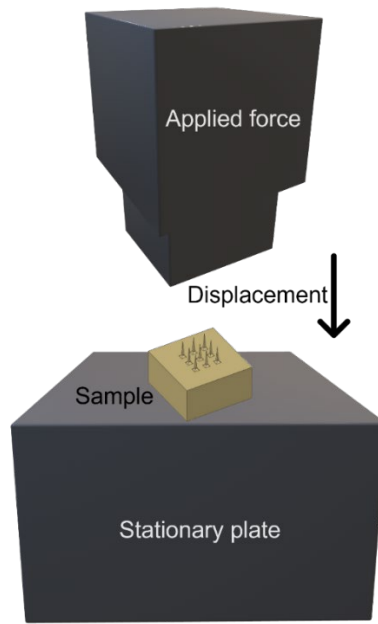


Fig.4.9 Machine for characterization the mechanical behavior of MNs.

Fig.4.10 shows the mechanical behavior of the gold-coated EMD6415 MN chip. **Fig.4.10a** shows the load-displacement curves recorded with the speed of $50 \mu\text{m}\cdot\text{s}^{-1}$. The failure of the microneedle chip occurred at 0.22 mm with an applied force of 0.7 N. The results show that the MNs showed a 2.5-3 times higher strength compared to many other values reported in the literature [298]. The stress-strain curve of the MN chip was also plotted, in which the stress is defined as force per area of the applied force. The total area of the MN chip was 1 mm^2 , as shown in **Fig.4.10b**. The mechanical strain is defined as the displacement per the whole length, which for the microneedles on average is $675 \mu\text{m}$. **Fig.4.10c** shows the stress-strain plot of the EMD6415 MN chip. The Young's Modulus data collected in this study at low levels of deformation in the elastic part is shown in **Fig.4.10d**. The elasticity of the MN is $0.78 \text{ N}\cdot\text{mm}^{-2}$, which demonstrates a value that is suitable for initial insertion into a material like skin [299].

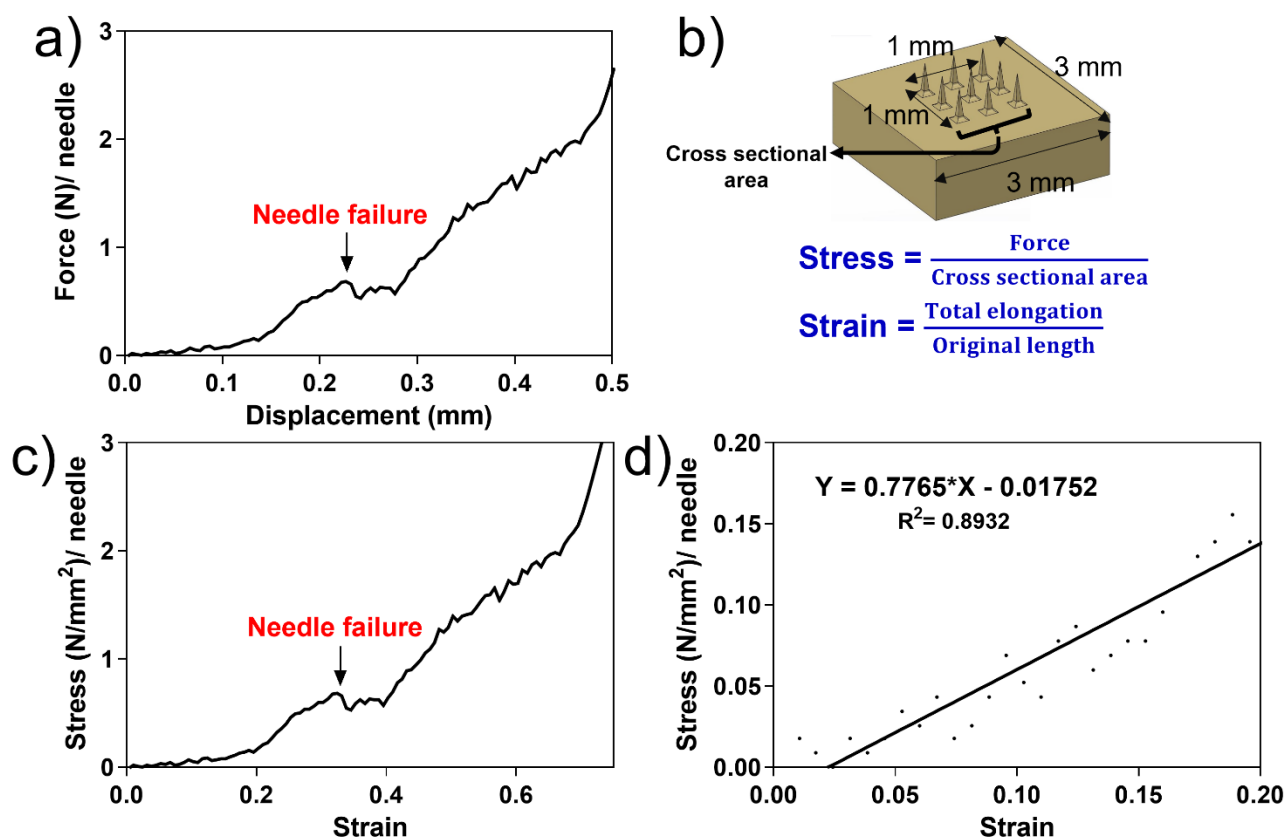


Fig.4.10 Analysis of the mechanical strength of the EMD6415 MN chip. (a) Load- displacement plot. (b) The scheme of the top view of MN shows the dimensions used for calculations for creating **Fig.4.10c** and **Fig.4.10d**. (c) The stress-strain plot, and (d) the stress-strain plot zooms into the elastic part.

4.2.4 Definition of the active areas of the gold microneedles

The base of the gold MN chip was insulated using the UV-curable dielectric ink EMD6415, as shown in **Fig. 4.11**.

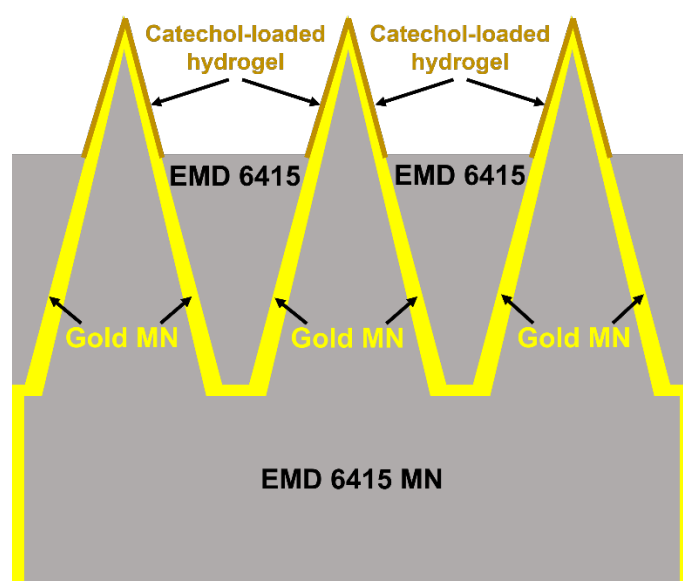


Fig.4.11 Scheme illustrating all layers of the final MN sensor (cross-sectional view).

4.2.5 Hydrogel coating of the microneedles

For electrochemical measurements in skin the MN electrodes must be coated with a solid or highly viscous, stable electrolyte layer. Herein, a calcium alginate hydrogel was deposited on the needles after cross-linking sodium alginate with Ca^{2+} (added as CaCl_2) in the presence of glycol according to the scheme shown in **Fig.4.12**. The deposition of the hydrogel on the MNs was realized by dip-coating the MNs into the freshly-prepared hydrogel. After that, the gel-coated MNs were immersed in a solution containing catechol to load the sensor with that electro-active compound.

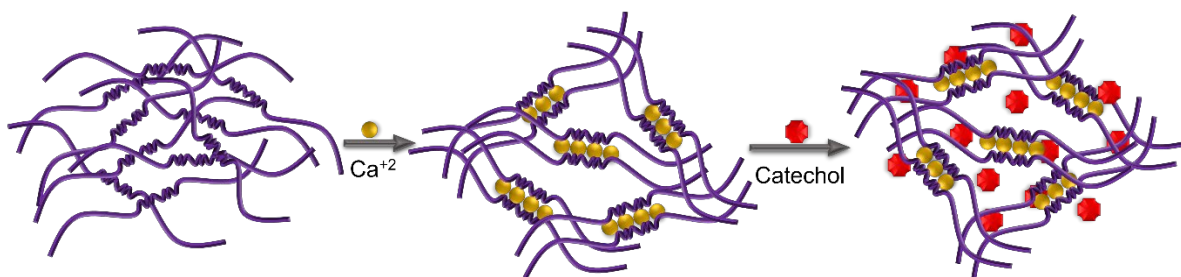


Fig.4.12 Schematic representation of alginate hydrogel formation and subsequent loading with catechol.

The thickness of Ca-alginate/glycerol hydrogels on the sensor was estimated for different times of dip-coating (5 min - 180 min) using a flat gold-coated sample and measuring the hydrogel thickness with a laser microscope. The plot in **Fig.4.13** shows the thickness obtained by dip-coating as a function of the dipping time. As shown, after 50 min, the thickness of the hydrogel coating approached a plateau, and after about 1 hr, the thickness of hydrogel reached 90 μm . It was assumed that the thickness of the hydrogel coating on the microneedle surface was similar.

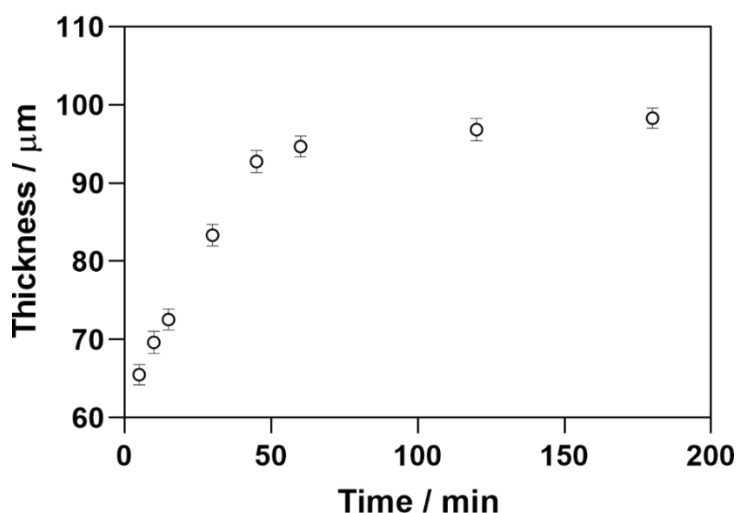


Fig.4.13 Thickness of CaAlg/glycerol hydrogel layer on gold as a function of the time of immersion.

4.2.6 Electrochemical properties of hydrogel coated gold MNs

Electrochemical measurements have been carried out by mounting an MN chip holder, produced in-house, to the Z motor of the Märzhäuser SECM system (**Fig.4.14(a-c)**). One needle plate was used

as WE (consisting of nine electrically connected Au MNs), one needle plate of Au MN as CE, and one needle plate of Ag MN as a QRE. First, cyclic voltammetry measurements were performed for the bare, alginate, and catechol/alginate coated gold MN electrode, from which some examples are shown in (**Fig.4.14d**). The sensor was immersed in PBS that contained in all cases FcMeOH. The redox peaks for FcMeOH are clearly observed in all cases. Comparing the response of the gold MN electrode with and without hydrogel, it can be clearly seen that the presence of the alginate gel reduced the active area of the WE as the redox peaks for the oxidation and reduction of FcMeOH were substantially reduced. However, this result demonstrates that a redox species like FcMeOH diffused from the sample solution through the alginate gel to the MN electrode. When the gel had been loaded with catechol, the redox peaks in the CV were increased, most likely due to the presence of the two redox-active species (FcMeOH plus catechol). In all of the cases, the supporting electrolyte was PBS. In order to investigate the sensitivity of the sensor for TYR, first solutions with different concentrations of TYR in PBS were prepared, and the catechol-loaded hydrogel MN chip was inserted. The detection principle was the following: the oxidation of catechol was catalyzed by TYR, and the as-generated o-benzoquinone was electrochemically reduced at the Au-MN electrode. The concept is based on the assumption that the higher the TYR concentration in the environment of the gel-coated MN chip, the higher the reduction current of o-benzoquinone. The sensitivity for TYR of the sensor was determined as $47.04 \mu\text{A mg}^{-1}\text{mL}$ (**Fig.4.14e**). To obtain this value, chronoamperometry was carried out in an unstirred solution, and the current values at 100s were taken.

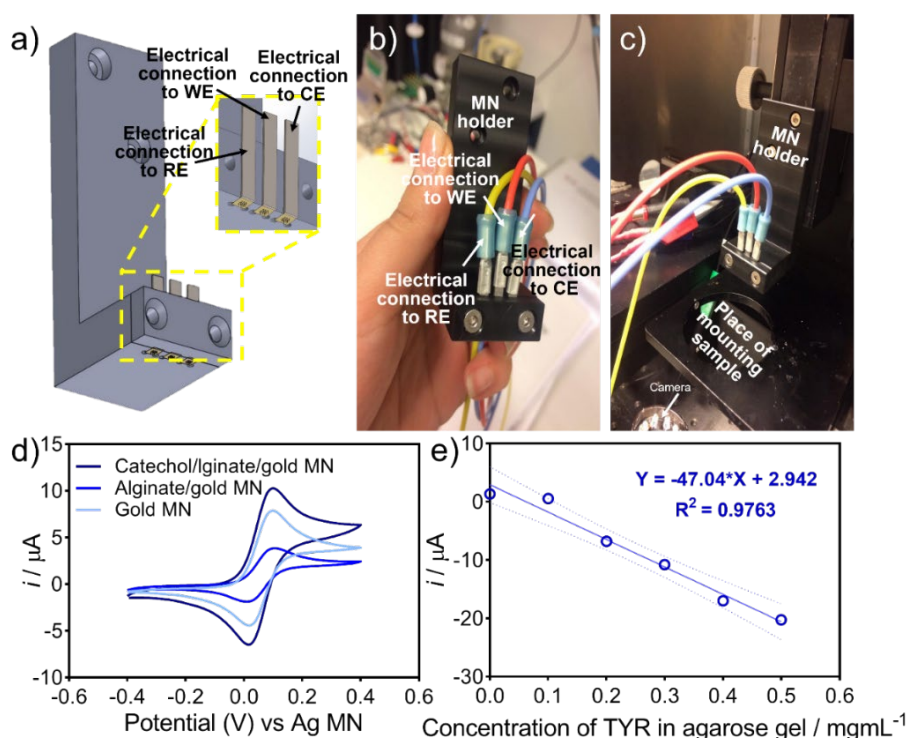


Fig.4.14 (a) Schematic representation of the three-electrode setup connected to the z-motor of an SECM. (b) Photograph of the holder. (c) Photograph of the holder mounted to the z-motor. (d) Cyclic voltammogram of Gold MN, Alginate/gold MN, and Catechol@alginate: gold MN biosensors in 5 mM FcMeOH in 0.1 M PBS. Scan rate= 50 mV/s. (e) Calibration curve extracted from chronoamperometry curves of Catechol@alginate: gold MN biosensor for different concentrations of TYR in PBS. Applied potential = -0.115 V , time = 100 s.

The final measurements of this part of the thesis were done in dummy skin made of an agarose gel (**Fig.4.15a**). TYR of different concentrations was injected locally into the dummy skin generating a simplified model with TYR-containing features. **Fig.4.15b** demonstrates the electrochemical detection principle discussed *vide supra*. **Fig.4.15(c,d)** show the electrochemical behavior of the catechol-loaded gel MN electrodes that were fully inserted into the dummy skin to detect TYR. Compared to the sensor response in the solution, the concentration of TYR in the gel is an assumption due to the practical difficulties in preparing a skin model accurately. The sensitivity for TYR of the MN sensor in dummy skin, obtained from reading the MN reduction current at 100s with an applied potential of -0.115 V, was about $7.52 \mu\text{A} \cdot \text{mg}^{-1} \cdot \text{mL}$. This relatively long time of 100s was selected as the current signals reached quasi-plateaus. The enzymatic oxidation of catechol requires oxygen. Whether the availability of oxygen during this extended time was constant was not experimentally verified. This should be done in follow up studies.

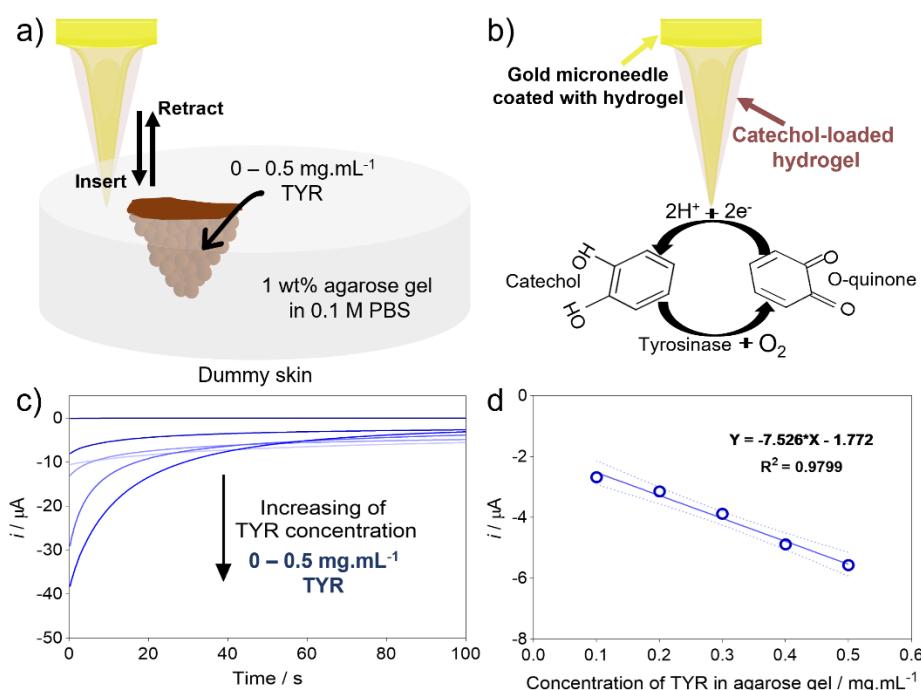


Fig.4.15 (a) Schematic representing the electrochemical readout strategy of the gel-based MN sensor for TYR. (b) Schematic is representing the detection principle for TYR based on the recycling of catechol. (c) Electrochemical detection of TYR using chronoamperometry of 0.1–0.5 mg/mL TYR in agarose gel. (d) Calibration curve extracted from chronoamperometry curves (c). Applied potential = -0.115 V, time = 100 s.

Selectivity is an important factor in analytical measurements to determine the performance of a designed sensor. Catechol@alginate: gold MN shows a low negative potential of about -0.115 V vs Ag/AgCl for the detection of benzoquinone, and the probability of catechol oxidation with a variety of components in skin or sweat is low. Several electroactive skin components include glucose [300], ascorbic acid [301], uric acid [302], histidine [303], cysteamine [304], and glutathione [305] were examined by inserting 1 mM of each component in the dummy skin. However, as most of these compounds are reducing agents, they are not suspected of oxidizing catechol. However, they could reduce o-benzoquinone. The current signals in **Fig.4.16** in the bare 1 wt% agarose (black line, "blank") and in the presence of other constituents such as 1 mM glutathione (**Fig.4.16a**), 1 mM uric

acid (**Fig.4.16b**), 1 mM glucose (**Fig.4.16c**), 1 mM ascorbic acid (**Fig.4.16d**), 1 mM histidine (**Fig.4.16e**), 1 mM cysteamine (**Fig.4.16f**), and 1 mg·mL⁻¹ TYR (**Fig.4.16g**) were evaluated. The current signal in the presence of TYR demonstrated a clear difference compared to all other components. The relative current values corresponding to different compounds in dummy skin are shown in **Fig.4.16h**. Such differences in the responses between TYR and other components suggest a high selectivity of the MN sensor toward TYR screening, however not considering that competing compounds in the skin could reduce o-benzoquinone and thus compete with the electrode for this electro-active species.

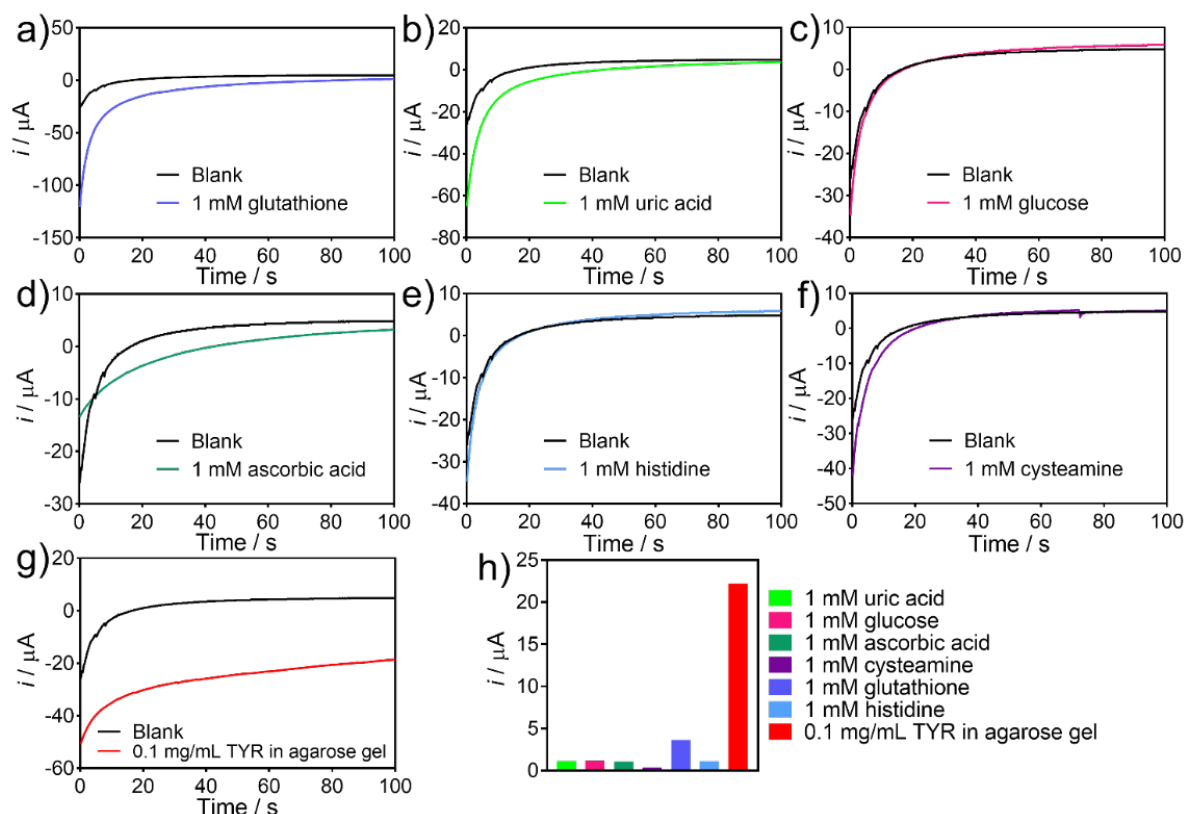


Fig.4.16 Sensor selectivity in the presence of potential interferences. Amperometric response of the microneedle sensor before (black) and after (red) contact with dummy skin, (a) 1 mM glutathione, (b) 1 mM uric acid, (c) 1 mM glucose, (d) 1 mM ascorbic acid, (e) 1 mM histidine, (f) 1 mM cysteamine, (g) 0.1 mg/mL TYR. (h) Relative current values corresponding to different compounds in phantom tissue (a–g). Applied potential = -0.115 V, time = 100 s.

To investigate the reproducibility and stability of catechol@alginate:gold MN biosensors, five continuous measurements for the detection of o-benzoquinone were carried out in 1 wt% agarose gel containing 0.1 mg·mL⁻¹ TYR. Differential pulse voltammetry (DPV) was applied from 0.1 V to -0.8 V. The reduction of o-benzoquinone, which was produced by the oxidation of catechol at the electrode as well as by TYR, was carried out at the Au MN electrode leading to a reduction peak at -0.15 V. A relative standard deviation (RSD) was calculated by dividing the standard deviation by the average of currents. An RSD of 9% (n 5 measurements with the same electrode) confirmed that the catechol@alginate: gold MN shows a reproducible performance for continuous TYR detection (**Fig.4.17(a,b)**). With experiment number, the current increased, which could probably be linked to slight continuous degradation of the hydrogel increasing the active Au electrode surfaces. In another set of experiments, five catechol@alginate: gold MN electrodes were fabricated and measured. An

RSD of 4% (n 5 electrodes) was obtained (**Fig.4.17(c,d)**). These results suggest that the electrode fabrication process was reproducible, and Catechol@alginate: gold MN biosensors demonstrated high stability for the repetitive detection of TYR.

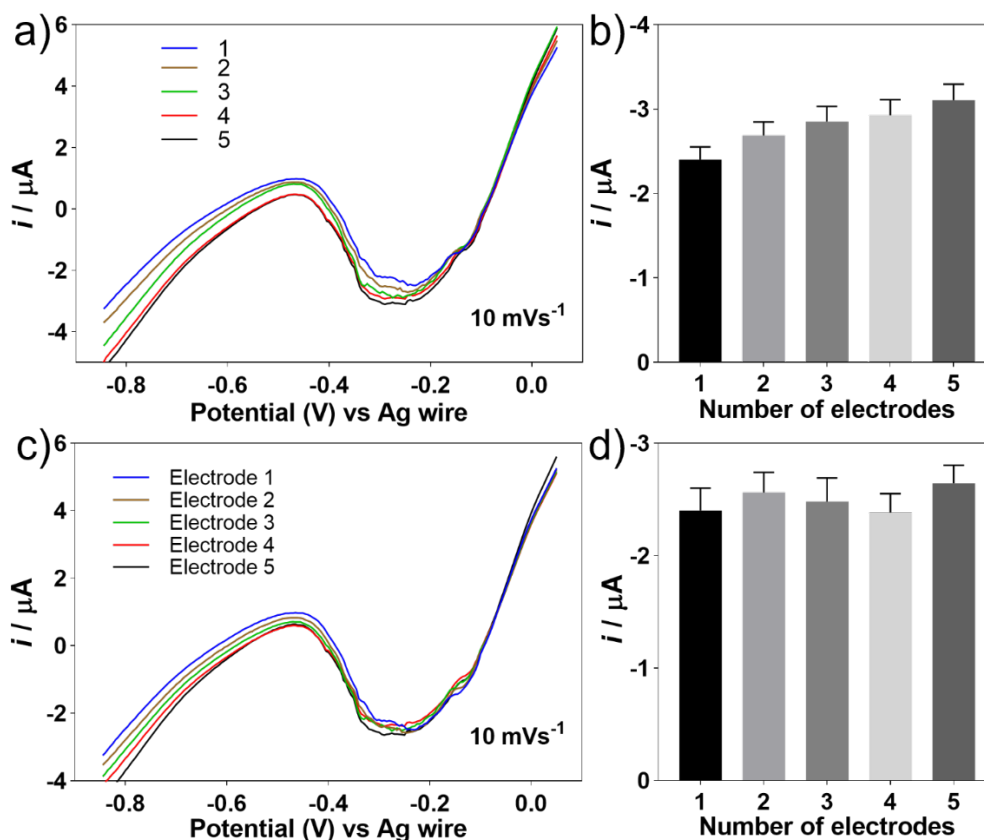


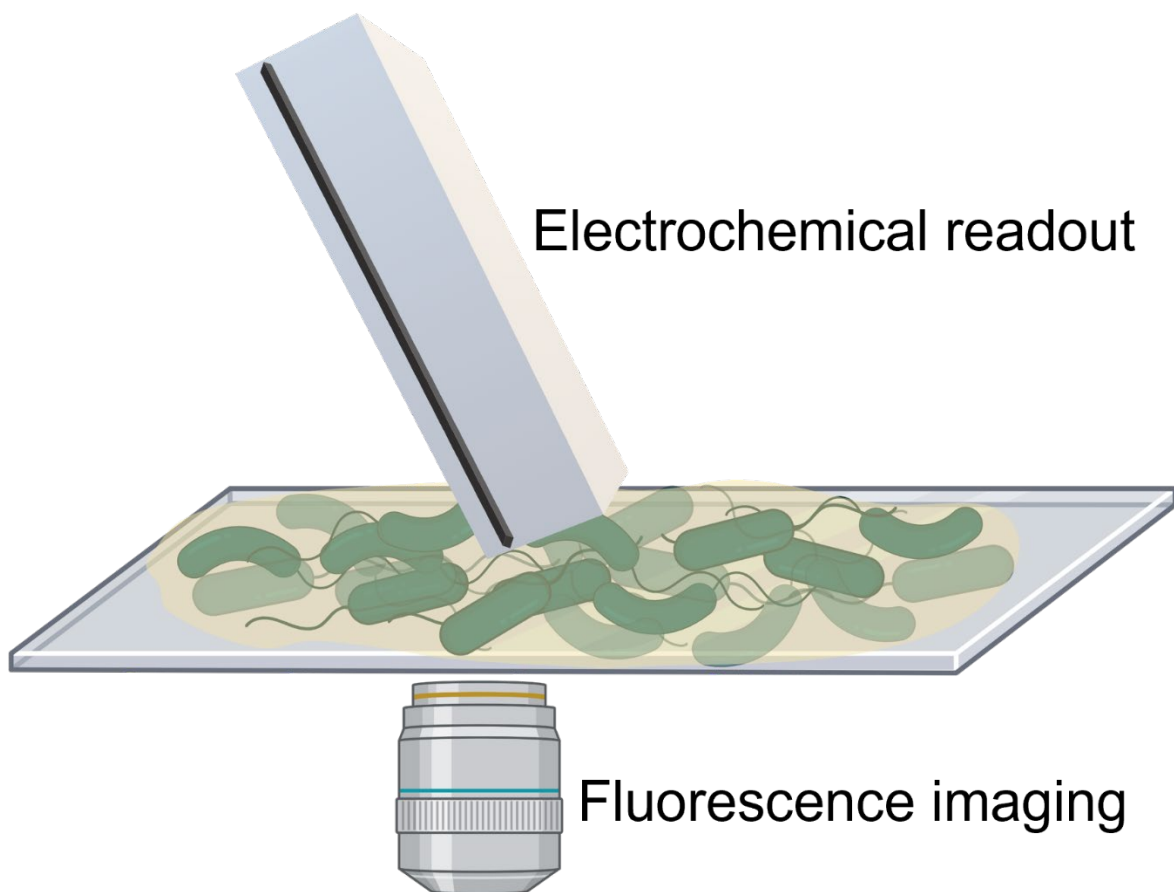
Fig.4.17 (a) and (b) Current response of Catechol@alginate: gold MN for detecting 0.1 mg/mL of TYR with five continuous measurements using the same electrode. (c) and (d) Current response Catechol@alginate: gold MN for detecting 0.1 mg/mL of TYR with five identically made electrodes. The scan rate = 10 mV/s, and the scan is from -0.8 V to 0.1 V.

4.3 Conclusion

This study proposed a fabrication protocol of an MN electrode chip that could be used for the large-scale fabrication of transdermal TYR sensors. The preliminary results in dummy skin showed promising properties of the MNs for sensing the TYR expression present in the matrix where the MNs are inserted. The microneedles were fabricated via PDMS casting to fabricate a polymer needle support. After that, the plastic microneedles were coated with a gold film by sputtering to produce an Au MN electrode. The gold MNs were then covered with an alginate gel loaded with catechol and PBS to provide a liquid electrolyte layer that contained an electroactive species, which is sensitive to oxidation that TYR catalyzes. The sensor showed high sensitivity of $7.52 \mu\text{Amg}^{-1}\text{mL}$ TYR in dummy skin using chronoamperometry (readout time 100s). A relative standard deviation (RSD) of 9% (n 5 measurements with the same electrode) confirmed that Catechol@alginate: gold MN is reproducible, allowing for continuous TYR detection. Also, five parallel Catechol@alginate: gold MN electrodes were fabricated using the same experimental setup and showed an RSD of 4% (n 5 electrodes). These results suggest that the electrode fabrication process was reproducible, and Catechol@alginate: gold MN biosensors demonstrated high stability for repetitive detection of TYR.

Furthermore, the sensor showed reasonable selectivity in potentially interfering compounds; here reducing agents were tested. Considering that this work was preliminary, it can be envisaged to continue this approach by a) addressing the MNs individually for electrochemical bioimaging and c) to fabricate a more robust solid electrolyte layer, for instance, with a conductive polymer as catechol derivate to improve the sensing further and to approach *in vivo* sensing.

CHAPTER 5 Soft-Probe-Scanning Electrochemical Microscopy reveals electrochemical surface reactivity of *E. coli* biofilms¹



¹ Adapted from: Sorour Darvishi, Horst Pick, Emad Oveisi, Hubert H Girault, Andreas Lesch. *Sensors and Actuators B: Chemical* 2021, 91, 12900-12908.

5.1 Introduction

Although much progress has been made in recent years, little is still known about biofilm growth and the development of its defense mechanisms against antimicrobials [306]. This is often linked to the limited information that can be obtained by using state-of-the-art analytical methods, which include for instance the tissue culture plate method [307], tube adherence method [308], congo red agar method [309], bioluminescent assays [310], and fluorescent microscopic examination [311]. Scanning electron microscopy is applied to visualize the morphology of biofilms, but it cannot measure the viability of bacteria. Fluorescence microscopy relies on dyes and might require bacterial cell fixation [312]. High-resolution techniques, such as electron and fluorescence microscopies, are generally used for micrometric sample regions at certain time points of biofilm development. *In situ* methods for the long-term monitoring of larger areas during biofilm formation and growth are therefore of high relevance in order to complement the state-of-the-art methods towards a deeper understanding of the processes involved. One approach to simplify the experimental procedures is the application of soft contact mode microelectrodes (MEs) that were developed for Soft-Probe-SECM imaging of extremely delicate targets with irregular topographic features [46, 77]. Using soft probes in contact mode, the working distance is kept nearly constant without implementing specific hardware and software, which is required for many other constant distant SECM probes and modes.

This chapter presents approach curves and electrochemical imaging of *E. coli* strain DH5 α biofilms over square millimeter-sized biofilm regions using soft microelectrodes. Biofilms were grown and analyzed on different substrates and at different periods of the biofilm development. The concept of detection was to visualize biofilms by their bacterial metabolic activity that was most likely based on the ability of the biofilm surface to reduce the oxidized form of ferrocene methanol. Nevertheless, as biofilms represent complex samples, alternative signal origins are also discussed. Soft-Probe-SECM electrochemical imaging was specifically utilized to analyze various biofilm samples with and without ampicillin resistance as well as after gentamicin treatments. The number of samples and measurements was elevated to approach size data sets that allow the statistical verification of the results.

5.2 Results and discussion

5.2.1 Optical characterization of biofilm surfaces

Biofilms of *E. coli* strain DH5 α were grown *in vitro* on glass under static conditions. An alternative would be the growth of biofilms under flow conditions. The presence of a biofilm on the glass slide was confirmed by using state-of-the-art microscopic techniques, *i.e.*, SEM, LSM, and CLSM. **Fig.5.1** shows an exemplary biofilm of several square millimeters in lateral size. As the varying intensity can be seen in the white color, the biofilm contained regions with higher and lower density. Crystal violet staining visualized the presence of bacterial cells and extracellular polymeric substances (EPS) by turning the color of the biofilm violet (inset in **Fig.5.1**).

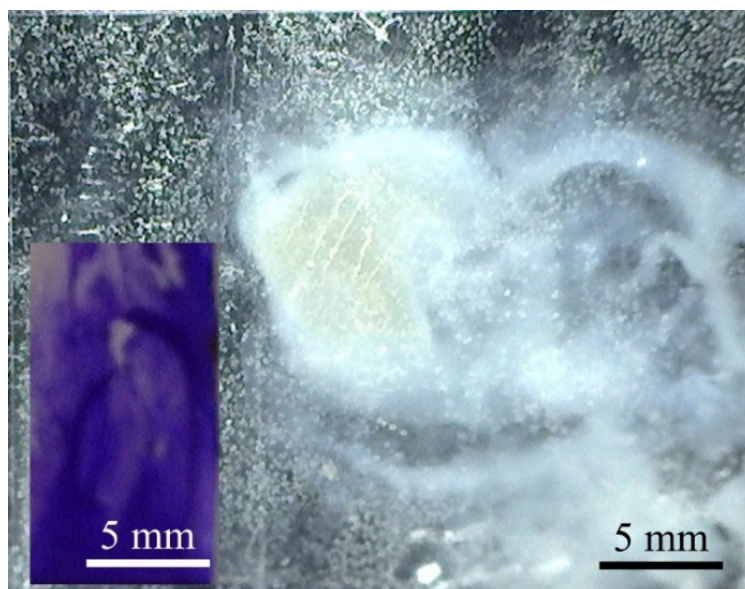


Fig.5.1 *E. coli* biofilm that was grown for one day on a glass slide was investigated by using optical microscopy. Light micrographs using crystal violet staining before (main figure) and after (inset) biomass testing. (Note: two different samples).

CLSM of the biofilm was used to investigate the viability of *E. coli* cells in the biofilm. The continuous z-stack confocal bright-field image demonstrated the presence of a three-dimensional biofilm structure (**Fig.5.2a**). Only a few bacterial cells moved within and near the biofilm, demonstrating that the major part of the bacterial cells was fixed in a matrix. SYTO 9/PI co-staining of nucleic acids was applied to distinguish live from dead bacterial cells (**Fig.5.2b,c**). SYTO 9 is a green fluorescing, intercalating and membrane-permeable molecule that initially stains all bacterial cells, *i.e.*, live and dead cells. In contrast, PI is a red intercalating stain for which the membranes of intact bacterial cells is impermeable. PI stains, therefore, only dead bacterial cells with the damaged and porous cell membrane. As a result, green stains indicate all the bacterial cells (**Fig.5.2b**), and red (here shown in yellow) stains indicate dead bacterial cells (**Fig.5.2c**). The images suggest that the number of living bacterial cells was clearly higher than for dead bacterial cells indicating an intact biofilm. CTC/DAPI staining confirmed the results (**Fig.5.2d,e**). CTC and DAPI offer a fast, facile, and reliable method for metabolic investigation of bacteria in both suspension and attached to surfaces [313]. DAPI labels nucleic acids of cells. DAPI does not penetrate living bacterial cells and shows, therefore, only the extracellular DNA (eDNA) of bacterial cells within a biofilm (**Fig.5.2d**) [314]. CTC is a monotetrazolium redox stain that produces a red fluorescent formazan. Red formazan forms when CTC is chemically or biologically reduced (**Fig.5.2e**) [315]. It is a marker for respiratory activity, thus of viable bacterial cells.

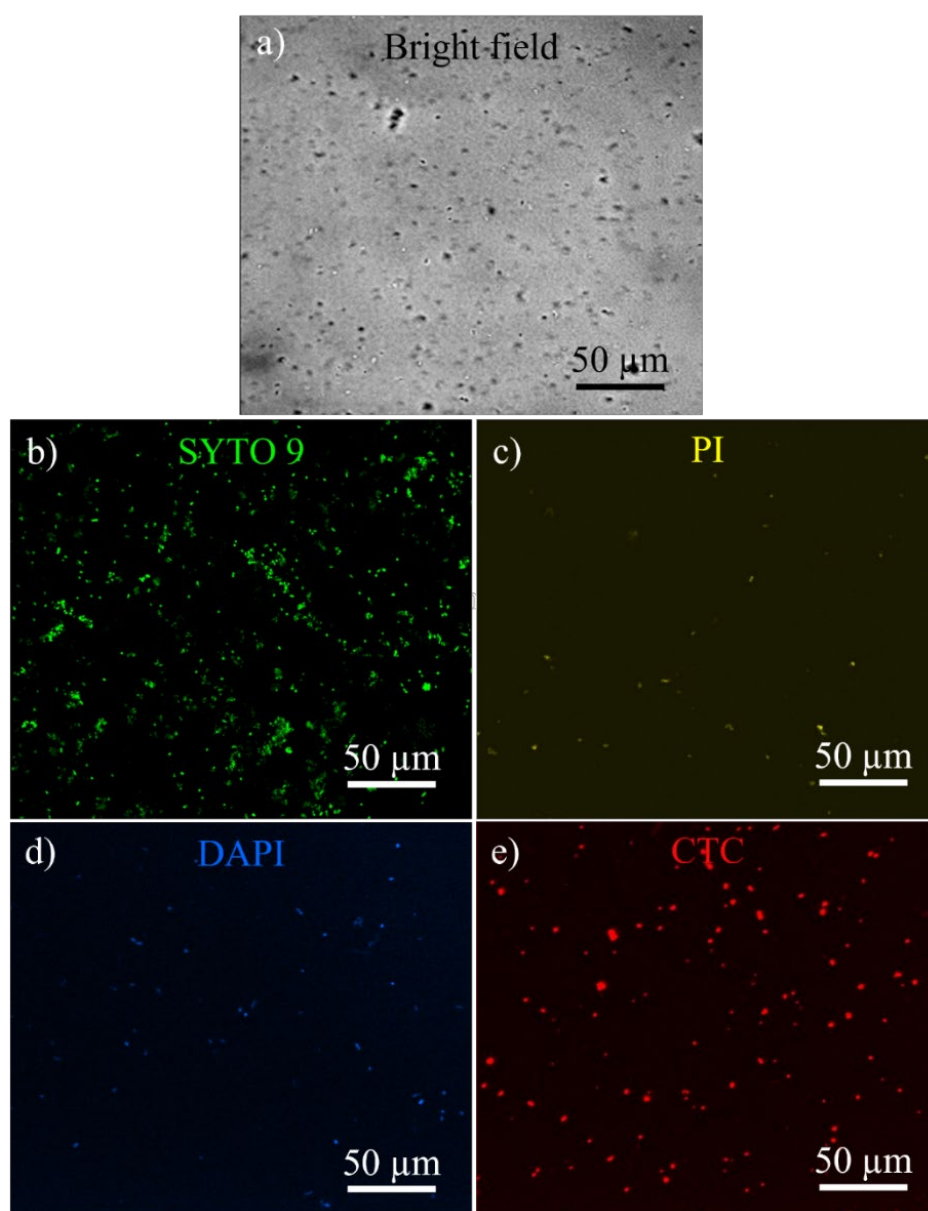


Fig.5.2 Confocal laser scanning fluorescence microscope images of one-day-old biofilm. (a) Bright field, (b) SYTO 9 staining, (c) PI staining, (d) DAPI staining, and (e) CTC staining. Confocal fluorescence images (a), (b), and (c) were in the same area of the sample. Confocal fluorescence images (d) and (e) were in the same area of the sample.

Analyzing the morphology of the biofilms, SEM showed densely packed, multi-layered bacterial cells (**Fig.5.3**). A thin layer of the EPS matrix covered and connected individual bacterial cells and confirmed the presence of a biofilm.

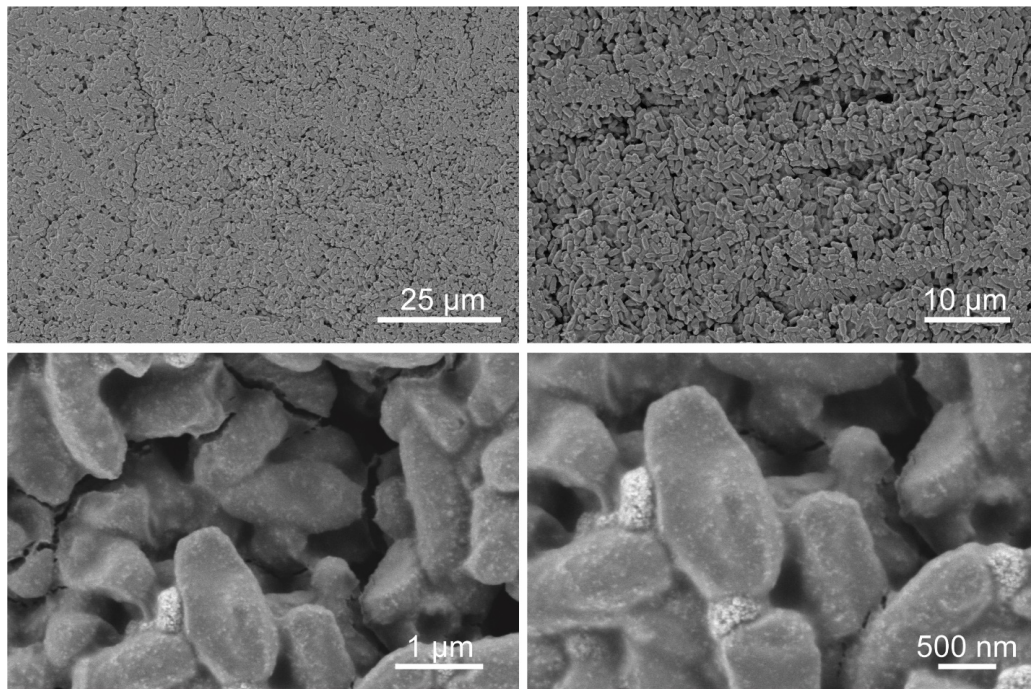


Fig.5.3 Scanning electron microscopy images of one-day-old *E. coli* biofilm with four different magnifications.

Fig.5.4 shows EPS-covered *E. coli* cells. The bacterial cell in the center is dividing while coated with EPS. This makes the EPS layer very clear.

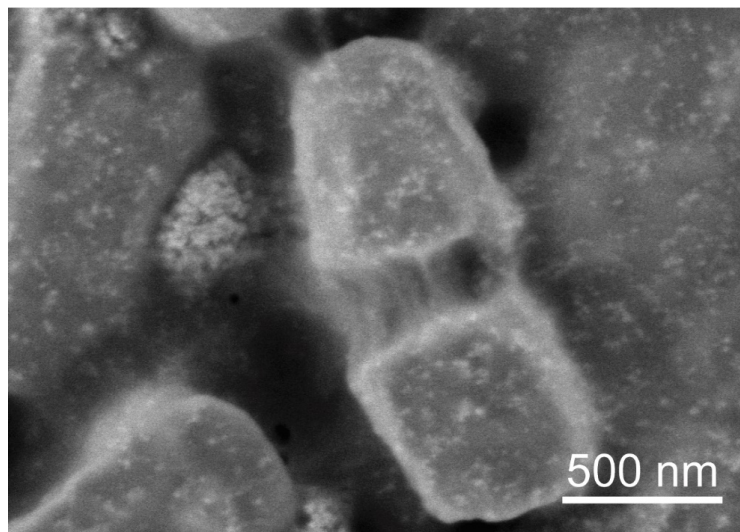


Fig.5.4 Scanning electron microscopy image of a dividing *E. coli* cell. *E. coli* cells are clearly covered by a connecting EPS layer.

The EPS layer is shown in the SEM of **Fig.5.5**. The EPS layer divided, maybe due to mechanical stress during drying under the ultra-high vacuum conditions of the SEM or because bacterial cells of the biofilm started the process of detaching [316]. This is one of the processes in the growth cycle of biofilms, which includes the attachment of bacterial cells to a surface, the formation of a monolayer of bacterial cells that initiate the production of the EPS, colony, and multilayer growth, matured heterogeneous biofilm with a detachment of planktonic bacterial cells for attaching to a new surface.

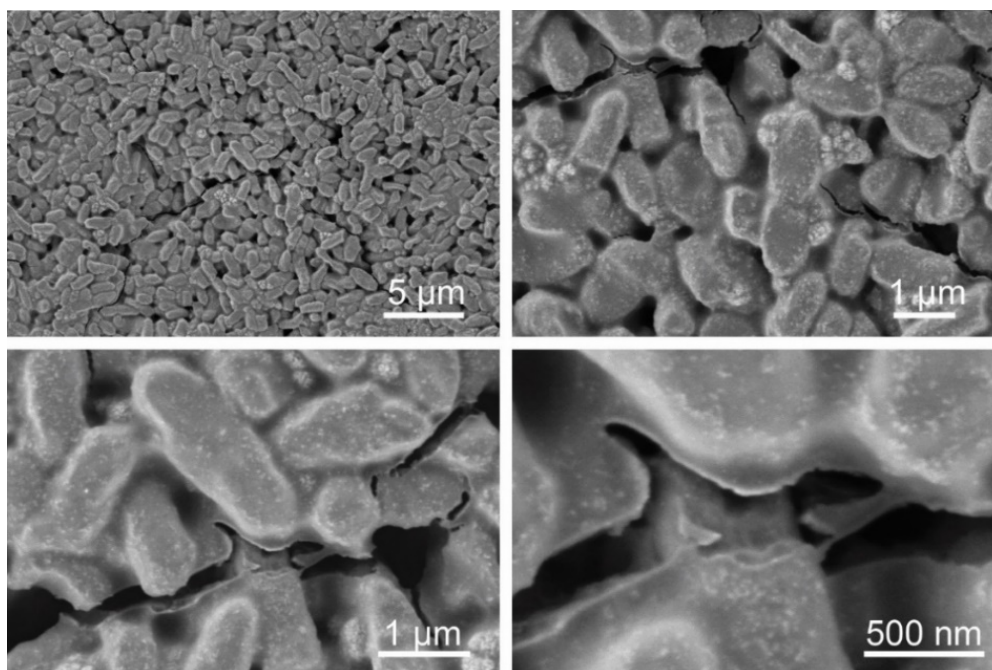


Fig.5.5 Scanning electron microscopy images of a biofilm with a cracked EPS layer demonstrating its presence.

A laser scanning micrograph determined the thickness of a one-day-old biofilm on a glass slide as shown in **Fig.5.6**. The biofilm thickness was extracted from the 2D profile created by the microscope software and resulted in being up to 10 μm from the biofilm edge, *i.e.* the bare glass surface.

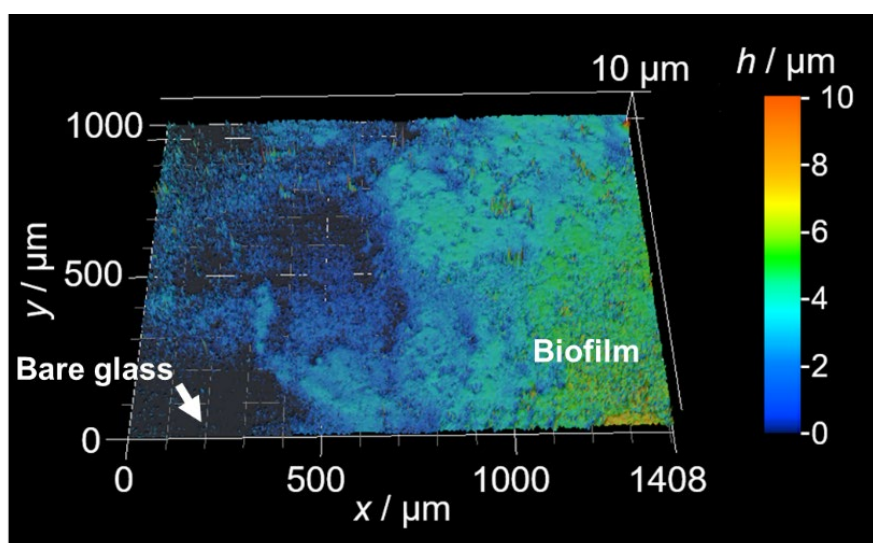


Fig.5.6 Laser scanning micrograph of one-day-old biofilm grown on the glass slide.

The thickness of the top layer of a one-day-old biofilm, which was removed from the glass slide with an adhesive tape of high quality (medical scotch tape for skin cell sampling), was estimated from SEM images that were taken from a cross-section of the adhesive tape (**Fig.5.7a**). ImageJ (1.52a, USA) software was used to measure the biofilm layer's thickness from the high magnification SEM image in **Fig.5.7b**. Due to the limited resolution of the tape-stripped biofilms as a result of the exposure of large areas of plastic to the electron beam, individual bacterial cells cannot be seen. The thickness of the vacuum-dried biofilm on tape in ten different places (separated by 2 μm) was determined. The diameter of living individual *E. coli* cells is ~1 μm. Therefore, some of the following values indicate that several parts of the collected biofilm on the adhesive tape were most likely not

covered by bacterial cells. The following values were measured: 1.15 μm , 1 μm , 0.06 μm (no bacterial cells), 1.43 μm , 3.35 μm , 0.213 μm (no bacterial cells), 3.17 μm , 2.98 μm , 0.54 μm (no bacterial cells), and 0.03 μm (no bacterial cells). The average and standard deviations were 2.18 μm and 1.1 μm , respectively.

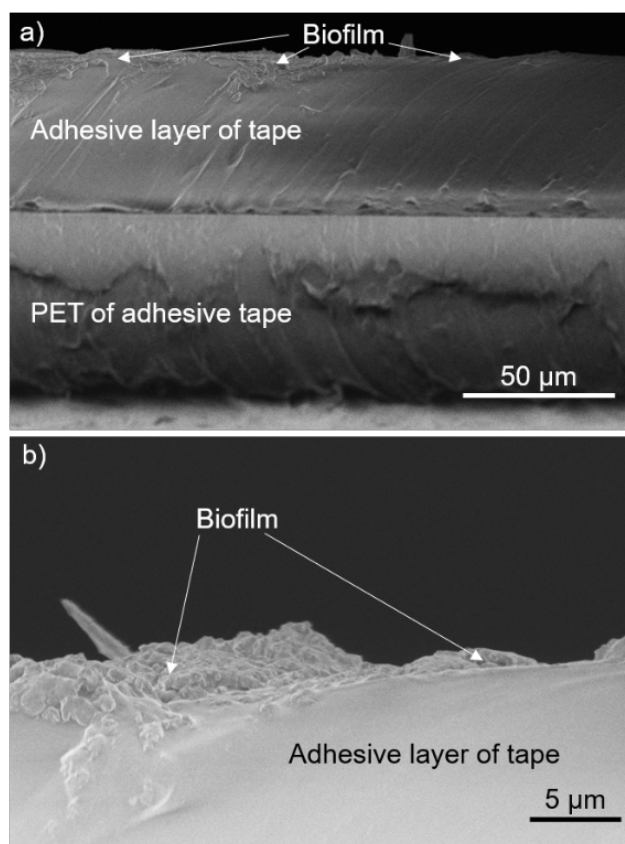


Fig.5.7 Scanning electron microscopy images of the cross-section of adhesive tape covered with the surface layer of a one-day-old biofilm taken from a biofilm on glass. (a) and (b) are images with two different magnifications.

5.2.2 SECM feedback mode characterization of *E. coli* biofilms surfaces

Soft-Probe-SECM in feedback mode was carried out in 100 mM PBS (pH 7.4) using 2.5 mM FcMeOH as a redox mediator in order to investigate the electrochemical surface reactivity of a biofilm and the possibility of electrochemical biofilm imaging. During approach curves, the soft probe was tilted with an angle of 20° respect to the surface normal and controlled by the SECM probe holder. The probe height h_P is considered for approach curve analysis instead of the working distance d . h_P is positive when the soft probe is in solution, and it becomes zero when the deepest part of the soft probe touches the sample ($d > 0$) and negative when it is pressed against the substrate ($d > 0$) (**Fig.5.8**).

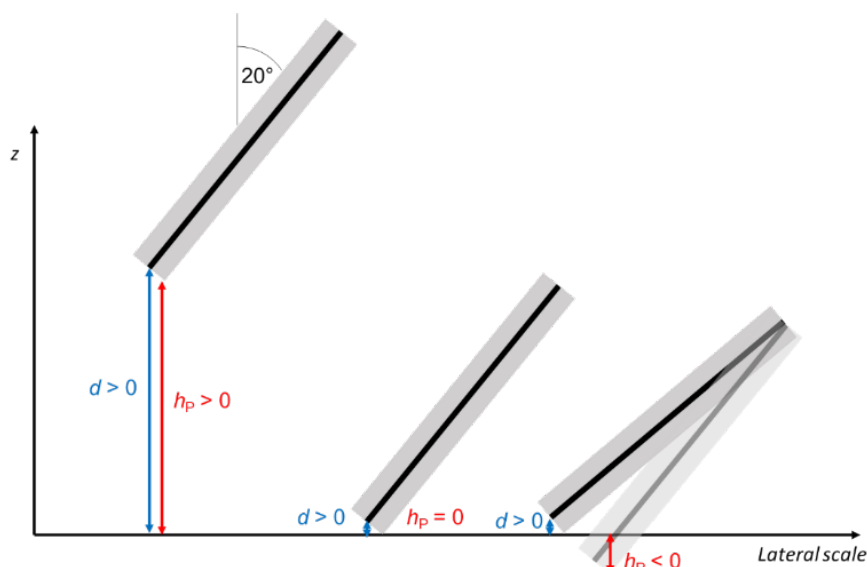


Fig.5.8 Schematic representation of the meaning of the probe height h_P and the relation to the working distance d between active part of the soft probe and the sample surface as already explained in **Fig.1.6**.

Once the probe touched the substrate surface, slight bending of the SECM probe on the plastic sets in while the SECM current remains nearly constant, demonstrating the constant working distance. The probe during that period is pressed against the substrate by moving the SECM probe holder further downwards to reach an $h_P = -35 \mu\text{m}$ (vertical distance of the probe after the probe had contacted the substrate surface). This value or similar ones (h_P generally ranged from $-25 \mu\text{m}$ to $-35 \mu\text{m}$) were applied. They were changed and adjusted according to the needs to guarantee that the soft probe was always in contact with the sample during line scan experiments. **Fig.5.9** shows a photo with the soft probe being translated over the biofilm-coated area. This photo was made for demonstration purposes and does not contain a QRE or CE. Furthermore, the biofilm and the tip of the soft probe were covered with a droplet of the solution rather than immersing the sample completely into the electrolyte solution as it was done for all SECM measurements.

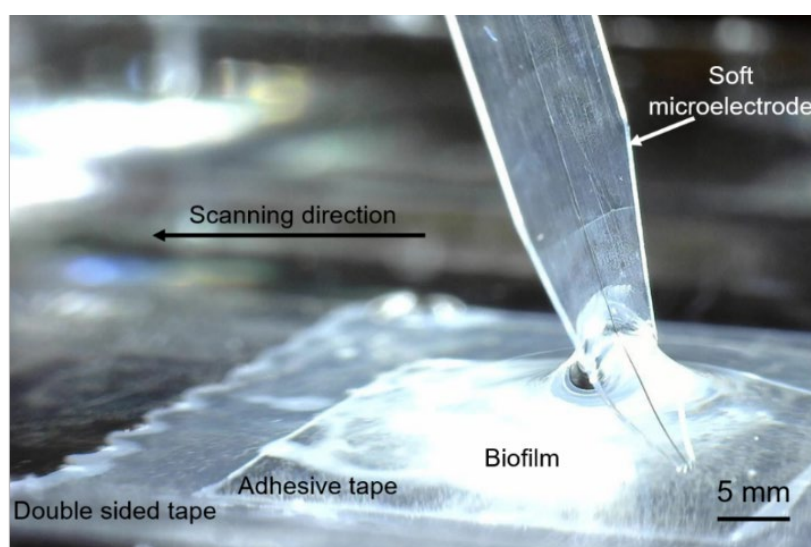


Fig.5.9 Soft-Probe-SECM over tape collected biofilm. Photo for demonstration purposes. Experiments were always carried out in an electrochemical cell with QRE and CE.

The reduction of Fe^{III} -containing species, which can compete with oxygen as terminal electron acceptors within the respiratory electron transport chain in *E. coli* cells, as previously reported [317]. In this work, FcMeOH^+ (Fe^{III}) is generated by electrochemical oxidation of FcMeOH at the soft ME, from where it then diffuses towards the sample (**Fig.5.10**). Compared to a soft probe in solution bulk (probe height $h_P = 1$ mm), the SECM currents are lower when the soft probe is in physical contact ($h_P \leq 0$ μm) with biofilm-free, insulating sample regions. The diffusion of FcMeOH from the solution bulk is physically hindered by the substrate ("negative feedback"). FcMeOH reaches the soft microelectrode only through the tiny gap between microelectrode and sample, leading to the remaining current recorded (**Fig.5.10**).

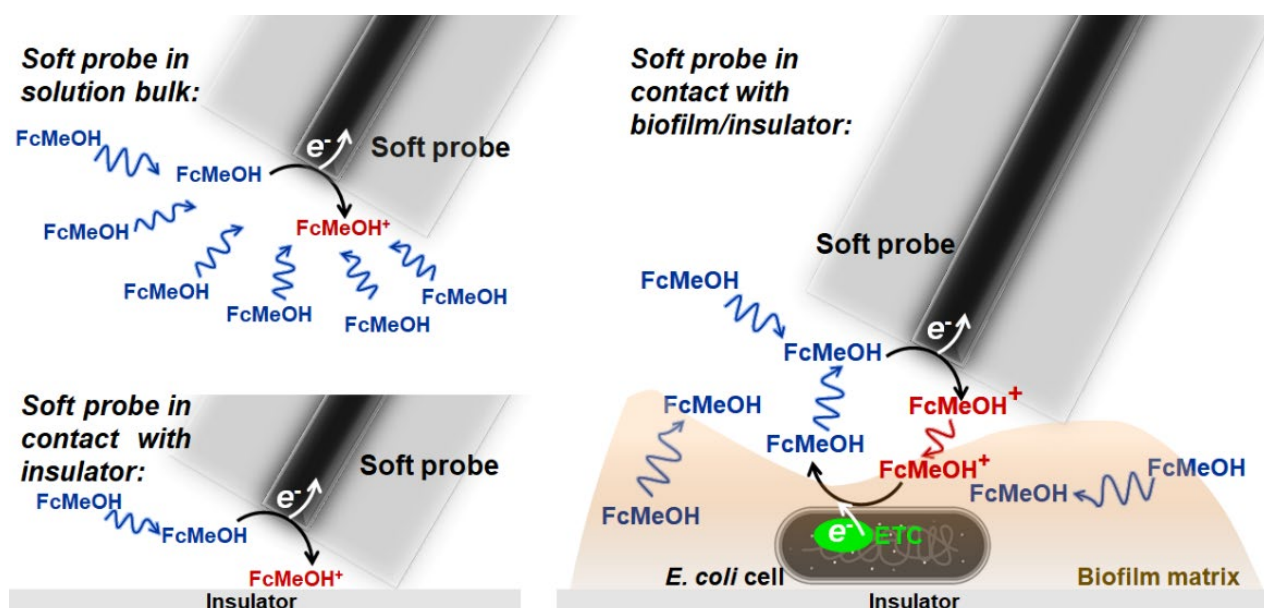


Fig.5.10 SECM feedback mode approach curves over one-day-old-*E. coli* biofilm-coated and biofilm-free glass and adhesive tape substrates. (a) Schematic representation of the "unhindered", nearly hemispherical diffusion of FcMeOH towards the microelectrode with the soft probe in the solution bulk ($I_{\text{Norm,bulk}} = 1$), hindered diffusion when the soft probe is near or in contact with a smooth insulator like glass ($I_{\text{Norm,insulator}} \rightarrow 0$), hindered diffusion with redox mediator regeneration when the soft probe contacts the biofilm ($I_{\text{Norm,insulator}} < I_{\text{Norm,biofilm/insulator}} < I_{\text{Norm,bulk}}$).

When the soft probe touched a glass slide, it started sliding forward with a nearly constant working distance, which becomes clear by the constant SECM current for $h_P < 0$ μm ($I_{\text{Norm,glass}} < 0.20$, black curve in **Fig.5.11a**). For the approach curves in **Fig.5.11**, the SECM currents I were normalized by the current recorded in the solution bulk I_{Bulk} giving in the bulk $I_{\text{Norm,bulk}} = 1$. In contrast, approaching the soft microelectrode towards a one-day-old *E. coli* biofilm on glass resulted in the contact point between soft probe and biofilm in a feedback current significantly larger than over bare glass ($I_{\text{Norm,biofilm/glass}} = 0.88$, **Fig.5.11a,b**). This could be due to the ability of the biofilm to reduce FcMeOH^+ back to FcMeOH , for instance, within the respiratory electron transport chain of metabolically active *E. coli* cells (redox potential of $\text{FcMeOH} = 0.44$ V vs SHE) [318]. The electrochemical reactivity of the biofilm results in an additional flux of FcMeOH from the *E. coli* cells embedded in the biofilm and thus towards the soft microelectrode. The SECM current over the biofilm on glass was up to eight times higher than over bare glass (**Fig.5.11a**) but lower than the steady-state diffusion-controlled current for the oxidation of FcMeOH in the solution bulk ($I_{\text{Norm,bulk}} = 1$). This suggests finite kinetics

for the regeneration reaction in the biofilm and/or limited mass transport within the biofilm matrix and across the bacterial cell membranes. In the literature, similar approach curves with FcMeOH as a redox mediator were reported to locate the surface of *E. coli* biofilms [319]. However, the diffusion of FcMeOH from the solution bulk within the biofilm matrix and reaching the microelectrode as an additional flux from the bottom could principally contribute to the signal (the water content in biofilms can be up to 97%, [156]). It would depend on the thickness of the biofilm and also on the size of available diffusion channels in the three-dimensional biofilm structure. However, as the estimated thickness of one-day-old biofilms on glass was herein generally in the range of 10 μm (**Fig.5.7**), it should not explain alone the higher current compared to bare glass ($I_{\text{Norm,glass,hp}=10\ \mu\text{m}} = \sim 0.5$). Finally, also redox activity of the extracellular matrix and biofilm microenvironment (e.g., by the release of redox-active molecules) could contribute to the signal. Still, the release of compounds, such as quorum-sensing molecules, plays a larger role in other bacterial species than *E. coli* [174, 175, 320, 321]. Approach curves were then performed over three identically grown *E. coli* biofilms on glass ($N_{\text{Sample}} = 3$, **Fig.5.11a**) duplicate and laterally separated by 100 μm (six approach curves in total). The normalized feedback current at the contact point between soft probe and sample for all six approach curves over the biofilm was ~ 0.87 and varied by 2% (**Fig.5.11b**). This suggests repeatability for the biofilm growth protocol, as well as for the feedback mode approach curves. After that, three identically grown biofilms on glass were tape-stripped with adhesive tape ($N_{\text{Sample}} = 3$). This procedure removes a few micrometers (determined as 2.2 ± 1.1) μm , **Fig.5.7**) surface of the biofilm, demonstrating the possibility of collecting biofilm surface layers from any surface of interest for analysis using Soft-Probe-SECM. Notably, the approach curves over the bare adhesive tape and tape-collected biofilm surface layers resulted in very similar feedback mode currents compared to the entire biofilms on glass. The normalized currents at the contact points between the soft probe and the biofilm-free adhesive layer were $I_{\text{Norm,adhesive}} = 0.2$, and with the tape-collected biofilm surface $I_{\text{Norm,biofilm surface/adhesive}} = 0.86$ (**Fig.5.11c**). This was verified for a total of six approach curves on the three different samples (**Fig.5.11d**). These results suggest that the sensitivity of the SECM feedback mode is restricted to the surface layer of the biofilm. Therefore, the SECM approach seems to operate in a surface-confined mode and enables the analysis of biofilm surface layers on entire biofilms and tape-collected biofilm surface layers. The concentration of FcMeOH was quite high. In the future it could be tested how lower concentrations will affect the approach curves. It could result in larger normalized currents.

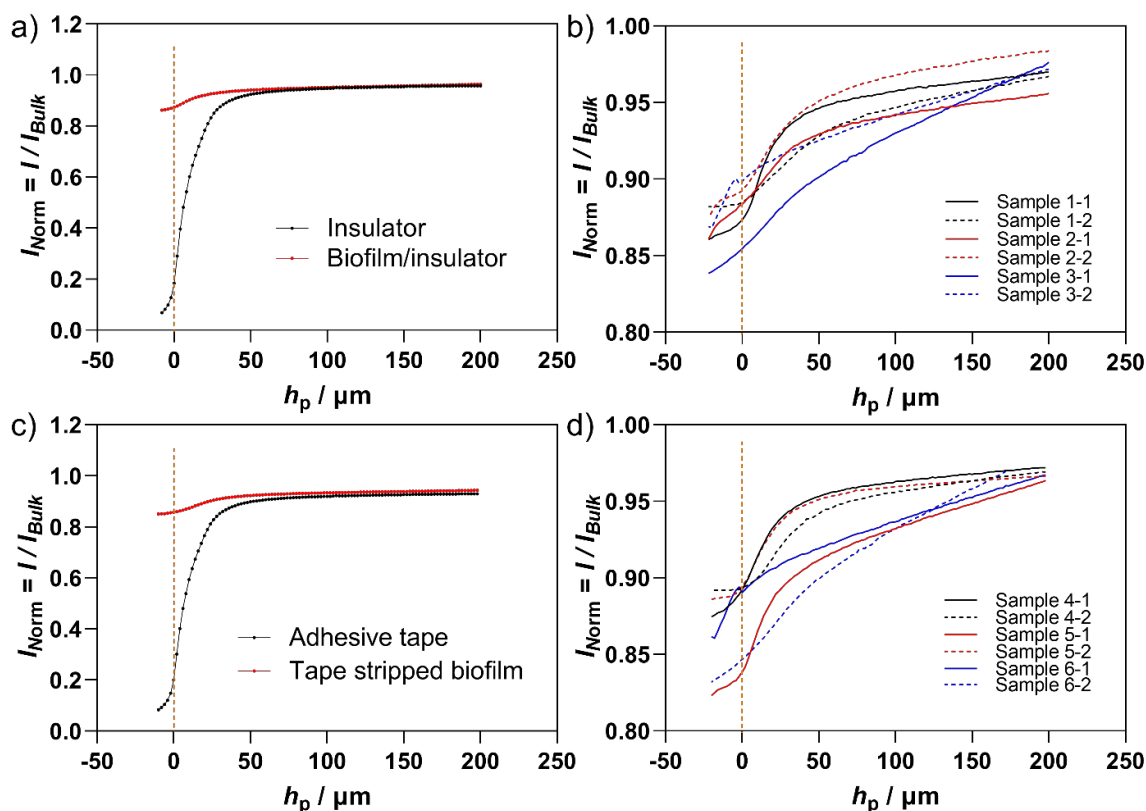


Fig.5.11 (a) Approach curves over glass and biofilm/glass. (b) Two locally separated approach curves over three identically grown biofilms/glass ($N_{\text{Sample}} = 3$). (c) Approach curves over the adhesive tape and tape-stripped biofilm surface layer on adhesive tape. (d) Two locally separated approach curves over each of three identically grown, tape-stripped biofilm surface layers on adhesive tape ($N_{\text{Sample}} = 3$). Experimental details: $E_T = 0.5$ V, probe translation speed = $5 \mu\text{m s}^{-1}$, step size = $2 \mu\text{m}$, 2.5 mM FcMeOH in 100 mM PBS (pH 7.4). Orange dashed lines indicate the contact point between the approaching soft probe and sample.

After that, an *E. coli* biofilm, grown for one day on a glass slide, was partially cleared using a soft wipe wetted with alcohol to create a sample with an almost sharp biofilm-glass border for SECM feedback mode imaging (**Fig.5.12a-b**). The sample was air-dried at room temperature for 15 min before SECM measurement. A soft probe was repeatedly placed with continuous perpendicular displacements onto the glass part and horizontally translated over the biofilm-coated region constructing the SECM feedback mode image in **Fig.5.12c**. As expected, the SECM feedback mode currents over the biofilm were higher than over the glass, suggesting that the biofilm-coated region reduced FcMeOH⁺ (plus the other possible signal generating events discussed *vide supra*). The mean SECM current over the glass was generally (0.09 ± 0.04) nA and (0.70 ± 0.24) nA on the biofilm-coated site. The presence of a few remaining active bacterial cells and biofilm (**Fig.5.12b**) on the cleaned glass side most likely could not contribute to the SECM signal due to the sensitivity limits of the used probe. The integrity of the biofilm and thus the ability to regenerate the redox mediator metabolically could have been influenced by the nearby alcohol treatment. In conclusion, the biofilm during consecutive contact mode line scanning remained adhered. The active part of the soft probe did not get contaminated by biofilm material, as seen by its stable response.

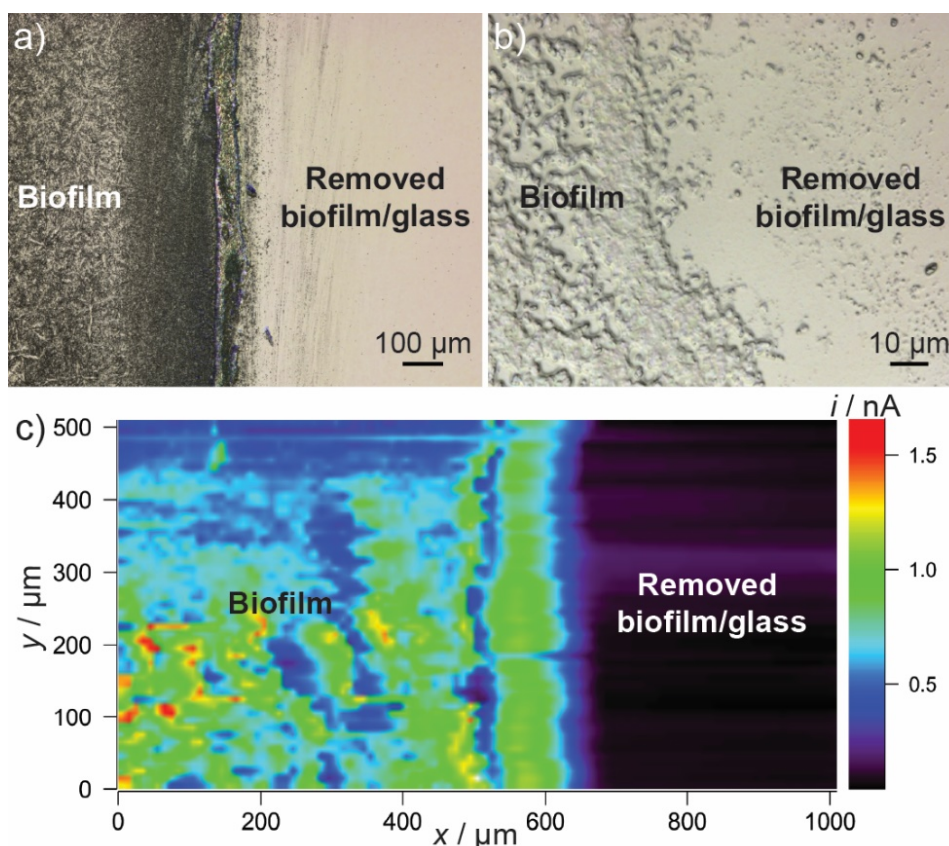


Fig.5.12 Soft-Probe-SECM imaging of *E. coli* biofilm on glass. (a,b) LSMs of the biofilm with two magnifications. (c) Soft-Probe-SECM feedback mode image of an *E. coli* biofilm-glass border, generated with an alcohol-soaked wipe. Considered biofilm area = 0.5 mm². Experimental details: $E_T = 0.5$ V, probe translation speed = 25 $\mu\text{m s}^{-1}$, step size = 10 μm , 2.5 mM FcMeOH in 100 mM PBS (pH 7.4).

5.2.3 Feedback mode imaging of biofilm formation with ampicillin resistant or susceptible DH5 α *E. coli* cells

Biofilm formation is a stepwise process (**Fig.5.13**): (1) attachment of bacterial cells to a substrate surface, (2) maturation of the biofilm (formation of a viable 3D structure), and (3) partial dispersion/detachment of biofilm components (bacterial cells are released from biofilm regions with less nutrient).

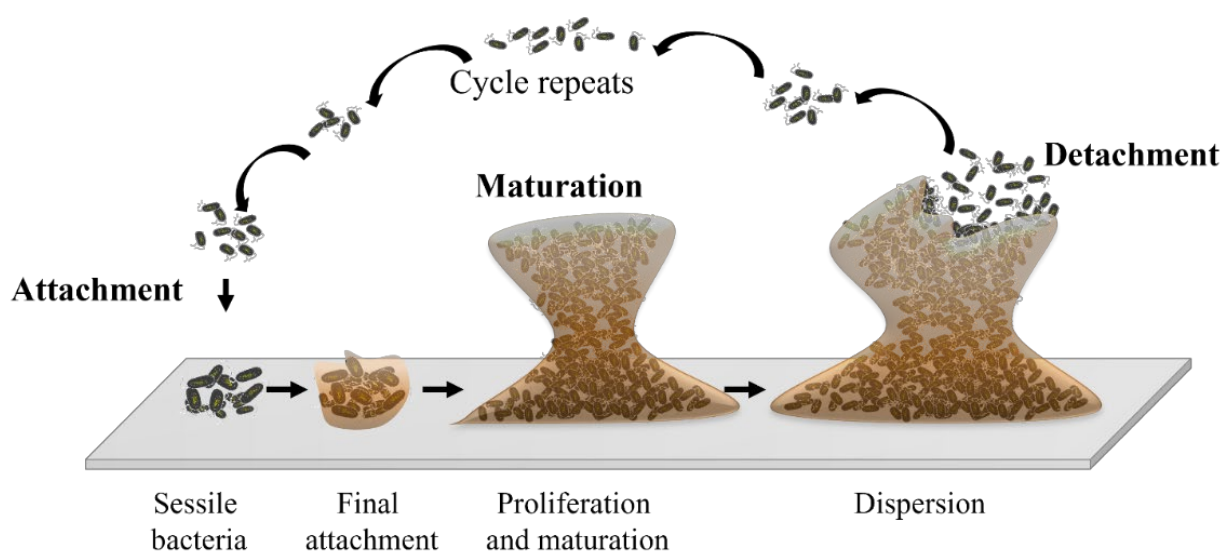


Fig.5.13 Steps of biofilm attachment, maturation, and detachment.

Crystal violet staining was first carried out daily on ten separately grown ampicillin-susceptible *E. coli* biofilms on glass ($N_{\text{sample}} = 10$, **Fig.5.14a**). Ampicillin-susceptible bacterial cells are grown in a solution without ampicillin protection against co-bacterial contamination. An overall increase of the total biofilm mass was detected by the increasing $OD_{630\text{nm}}$ leading to a sigmoidal shape of the $OD_{630\text{nm}}$ value as a function of culturing time, approaching a quasi-plateau at day six (**Fig.5.14b**).

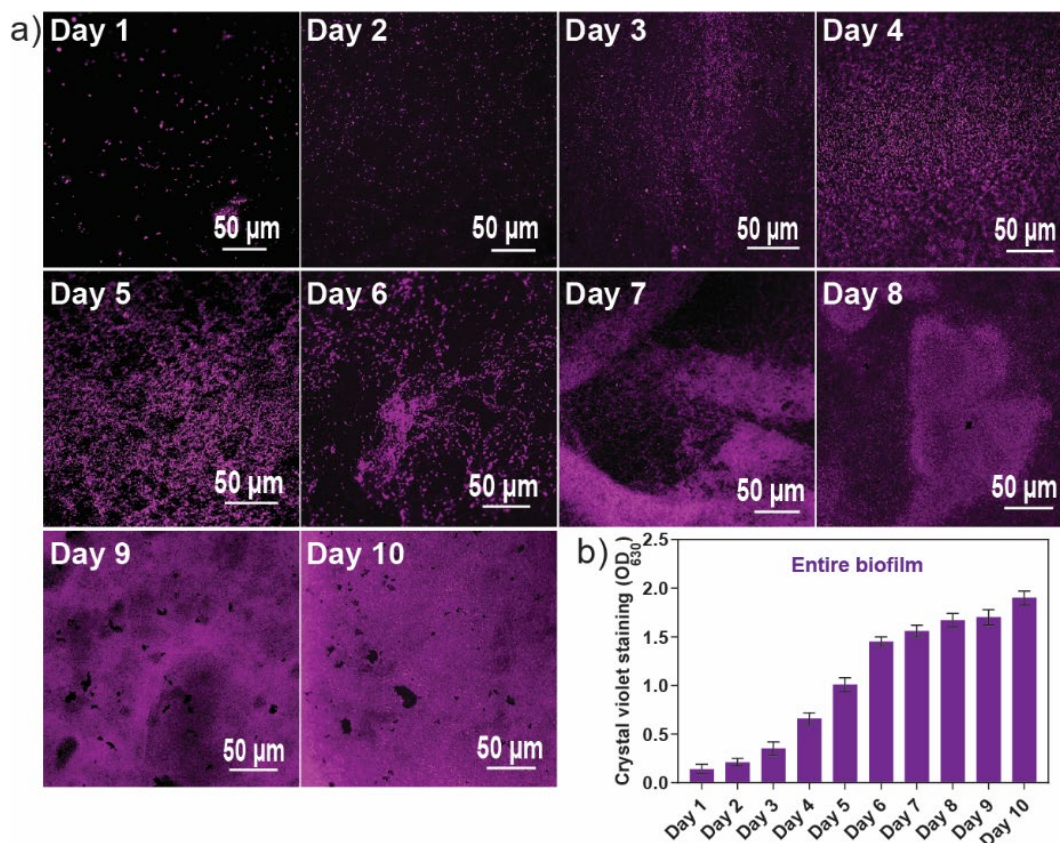


Fig.5.14 (a) Fluorescence images of entire crystal violet stained biofilms on glass. (b) OD_{630} of crystal violet-stained total biomass of *E. coli* biofilms after removal from glass.

This quasi-plateau could indicate a continuous biofilm growth with the constant detachment of similar daily amounts of biofilm material. Based on the conclusions made in the previous section, *i.e.*, tape-stripped biofilm surface layers give similar SECM signals as the direct analysis of the surface layers of entire biofilms, the top layer of one biofilm for each of the ten samples with progressing growth period was collected with an adhesive tape and then analyzed by SECM feedback mode imaging (**Fig.5.15**). The SECM feedback mode images indicate local variations in current over lateral dimensions of about 50 µm to 100 µm.

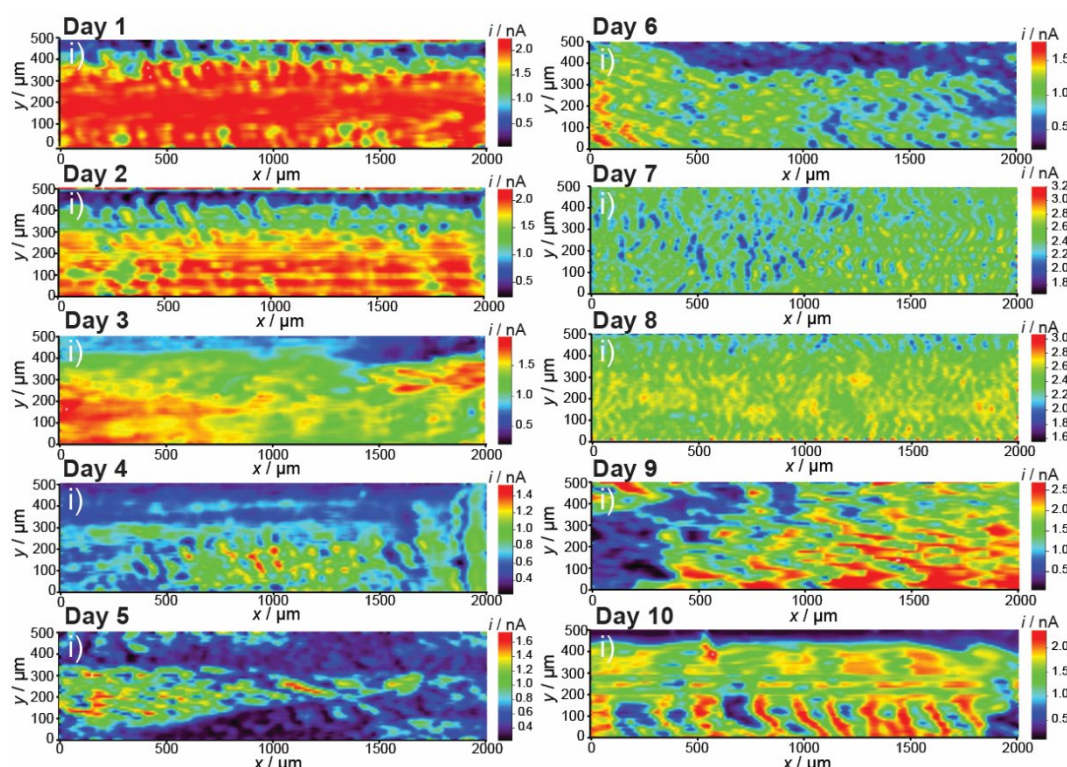


Fig.5.15 Soft-probe-SECM images of native *E. coli* biofilm collected with adhesive tape in 10 days. Experimental details: working potential $E_T = 0.5$ V, probe translation speed = $25 \mu\text{m s}^{-1}$, step size = $10 \mu\text{m}$, 2.5 mM FcMeOH in 100 mM PBS (pH 7.4).

For instance, these features are repeatedly observed, seen by repeatedly recorded SECM line scans (**Fig.5.16**). This could be due to the morphology of the adhesive tape after sample collection and by mounting the tape in the SECM cell. The tape morphology could affect probe sliding and probe angle but was not seen in similar experiments with skin cells in chapter 3 [290].

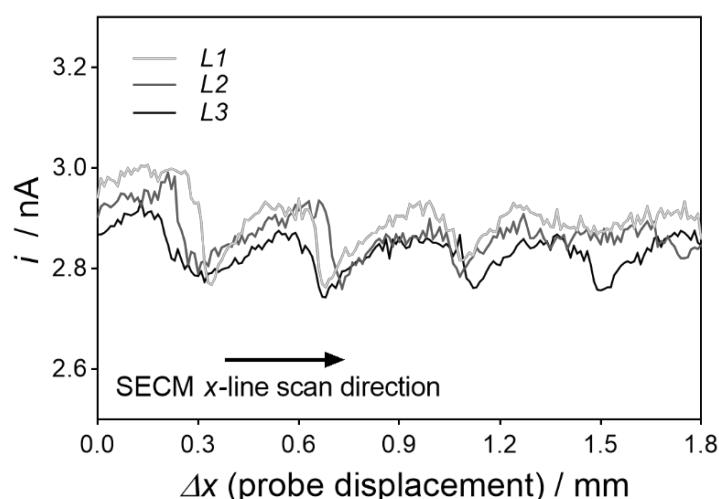


Fig.5.16 Repeatability of Soft-Probe-SECM line scans over one *E. coli* biofilm surface layer, collected with an adhesive tape. Three linescans L1 to L3. Experimental details: $E_T = 0.5$ V, probe translation speed = $25 \mu\text{m s}^{-1}$, step size = $10 \mu\text{m}$, 2.5 mM FcMeOH in 100 mM PBS (pH 7.4).

Further, variations in local biofilm collection efficiency of the adhesive layer could affect the biofilm coverage on the tape. Finally, signal variations could result from a yet to be determined intrinsic heterogeneous metabolic activity of the biofilm. Features of similar dimensions can be seen in the images of crystal violet-stained biofilms from Day 6 to Day 9. The mean feedback mode current was

calculated for each SECM image (1 mm²) using all 10'251 data points per image. To compensate for possible variations between SECM experiments in terms of the exact soft probe dimension after mechanical cutting and the exact probe angle [46, 290], the mean soft probe responses were calibrated by considering the bulk current and negative feedback current over an insulator (Equation 5.1 and Equation 5.2).

$$I_{\text{solution bulk}}^* = I_{\text{solution bulk, AC}} - I_{\text{insulator, AC}} \quad (\text{Equation 5.1})$$

where $I_{\text{solution bulk}}^*$ ($I_{\text{sol. bulk}}^*$) is calculated by subtracting from the current $I_{\text{solution bulk, AC}}$ ($I_{\text{sol. bulk}}$), measured in the solution bulk at the beginning of an approach curve (AC), the negative feedback current with the soft probe in contact with the insulating surface of the substrate ($I_{\text{insulator, AC}}$). For the bar plots, Equation 5.2 is used,

$$I_{\text{cal,mean}} = \left(I_{\text{mean, FB-image}} - I_{\text{insulator, AC}} \right) \cdot \left(I_{\text{solution bulk}}^* \right)^{-1} \quad (\text{Equation 5.2})$$

where $I_{\text{mean, FB-image}}$ is the average current of all SECM image points either over the biofilm, adhesive layer, or insulator. The bulk current then normalizes the mean SECM current $I_{\text{solution bulk}}^*$. In this way, the purely negative feedback current over an insulating surface is nearly zero. The calibrated $I_{\text{cal,mean}}$ would be equal to 1 if the FB current over the biofilm would be the same as in the solution bulk.

Table 5.1 Details about SECM data from **Fig.5.15** and **Fig.5.17a** and its calibration to create **Fig.5.17b**. N = number of data points per SECM image.

Day	$I_{\text{sol. bulk}} / \text{nA}$	$I_{\text{insulator}} / \text{nA}$	$I_{\text{sol. bulk}}^* / \text{nA}$	$I_{\text{mean, FB-image}} / \text{nA}$	$I_{\text{cal,mean}}$
1	3.95	0.02	3.93	$(1.73 \pm 0.54) (N = 10251)$	$(0.43 \pm 0.13) (N = 10251)$
2	3.75	0.02	3.74	$(1.49 \pm 0.54) (N = 10251)$	$(0.39 \pm 0.14) (N = 10251)$
3	3.91	0.08	3.84	$(1.29 \pm 0.35) (N = 10251)$	$(0.32 \pm 0.07) (N = 10251)$
4	3.76	0.02	3.75	$(0.72 \pm 0.24) (N = 10251)$	$(0.19 \pm 0.06) (N = 10251)$
5	3.58	0.01	3.56	$(0.64 \pm 0.37) (N = 10251)$	$(0.18 \pm 0.10) (N = 10251)$
6	4.28	0.02	4.26	$(0.90 \pm 0.38) (N = 10251)$	$(0.21 \pm 0.09) (N = 10251)$
7	4.44	0.05	4.38	$(2.43 \pm 0.33) (N = 10251)$	$(0.54 \pm 0.06) (N = 10251)$
8	4.36	0.03	4.32	$(2.48 \pm 0.25) (N = 10251)$	$(0.57 \pm 0.05) (N = 10251)$
9	4.07	0.13	3.94	$(1.53 \pm 0.78) (N = 10251)$	$(0.36 \pm 0.17) (N = 10251)$
10	3.52	0.09	3.43	$(1.36 \pm 0.62) (N = 10251)$	$(0.37 \pm 0.18) (N = 10251)$

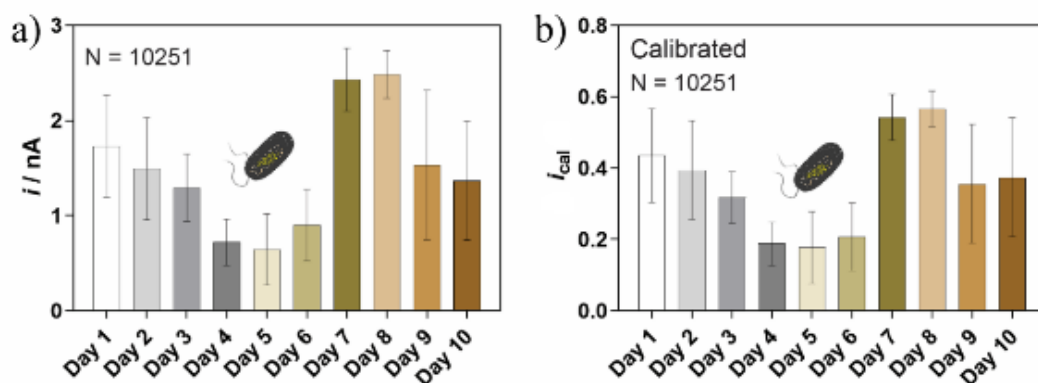


Fig.5.17 Bar plots show the mean currents \pm standard deviation from all data points of ten SECM images of tape-collected *E. coli* biofilm surface layers without (a) and with (b) calibration according to **Table 5.1**. One biofilm per day.

The mean SECM feedback mode current during SECM imaging of the biofilm-coated adhesive layer (one-day biofilm growth) was ten times higher ((1.73 ± 0.54) nA, (**Fig.5.15** and **Table 5.1**) than the current over bare adhesive tape (0.17 ± 0.05) nA (**Fig.5.18** and **Table 5.2**).

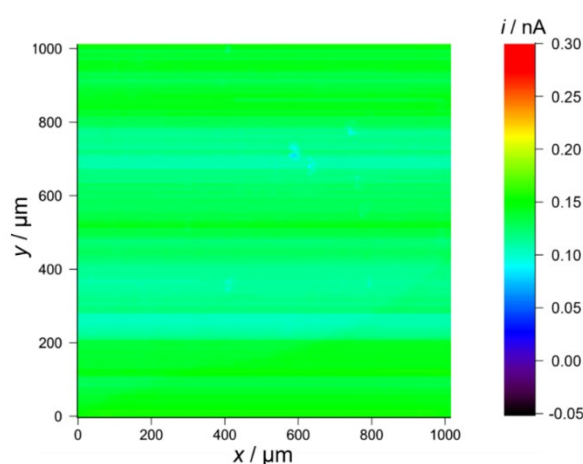


Fig.5.18 Soft-Probe-SECM FB image of bare adhesive tape. Experimental details: $E_T = 0.5$ V, probe translation speed = $25 \mu\text{m s}^{-1}$, step size = $10 \mu\text{m}$, 2.5 mM FcMeOH in 100 mM PBS (pH 7.4).

Table 5.2 Details about SECM data of the calibration of the SECM FB currents from **Fig.5.18**.

$I_{\text{sol. bulk}} / \text{nA}$	$I_{\text{insulator}} / \text{nA}$	$I_{\text{sol. bulk}} / \text{nA}$	$I_{\text{mean,FB-image}} / \text{nA}$	$I_{\text{cal,mean}}$
4.635	0.04	4.59	(0.17 ± 0.05) ($N = 10201$)	0.11 ($N = 10201$)

As the SECM detection sensitivity seems to be surface-confined, the mean currents of the SECM images of the tape-collected top biofilm layer over ten days cannot follow the same trend as the increasing $\text{OD}_{630\text{nm}}$ intensities from the crystal violet stained entire biofilm mass on glass. The mean SECM current of the measurement series with ampicillin-susceptible *E. coli* biofilms was calculated and compared with the mean current of the ten images taken daily during the growth of ten separate ampicillin-resistant *E. coli* biofilms (grown in the presence of ampicillin, (**Fig.5.19** and **Table 5.3**)).

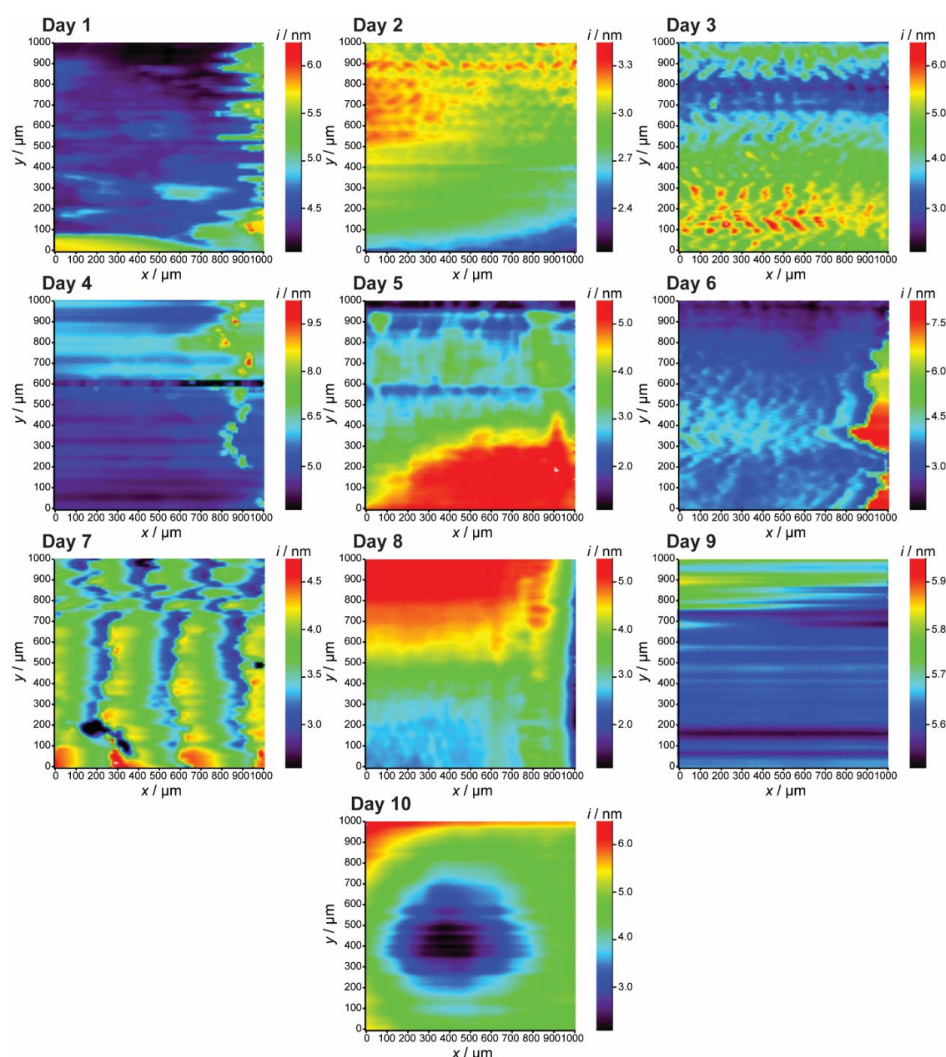


Fig.5.19 Soft-probe-SECM images of resistant *E. coli* biofilm with ampicillin collected with adhesive tape in 10 days. Experimental details: working potential $E_T = 0.5$ V, probe translation speed = $25 \mu\text{m s}^{-1}$, step size = $10 \mu\text{m}$, 2.5 mM FcMeOH in 100 mM PBS (pH 7.4).

Table 5.3 Details about SECM data from **Fig.5.19** and **Fig.5.20a** and its calibration to create **Fig.5.20b**. N = number of data points per SECM image.

Day	$I_{\text{sol. bulk}} / \text{nA}$	$I_{\text{insulator}} / \text{nA}$	$\bar{I}_{\text{sol. bulk}} / \text{nA}$	$I_{\text{mean,FB-image}} / \text{nA}$	$\bar{I}_{\text{cal,mean}}$
1	7.2	0.07	7.14	$(4.61 \pm 0.41) (N = 10201)$	$(0.64 \pm 0.05) (N = 10201)$
2	8.2	0.07	8.13	$(2.83 \pm 0.15) (N = 10201)$	$(0.34 \pm 0.010) (N = 10201)$
3	6.7	0.05	6.65	$(3.80 \pm 0.45) (N = 10201)$	$(0.56 \pm 0.06) (N = 10201)$
4	8.1	0.15	7.95	$(6.43 \pm 0.22) (N = 10201)$	$(0.79 \pm 0.01) (N = 10201)$
5	7.3	0.04	7.26	$(3.55 \pm 0.81) (N = 10201)$	$(0.48 \pm 0.01) (N = 10201)$
6	8.3	0.06	8.24	$(3.97 \pm 0.74) (N = 10201)$	$(0.47 \pm 0.08) (N = 10201)$
7	8.1	0.02	7.86	$(3.24 \pm 0.05) (N = 10201)$	$0.41 (N = 10201)$
8	8.1	0.09	8.01	$(3.45 \pm 0.83) (N = 10201)$	$(0.42 \pm 0.09) (N = 10201)$
9	7.9	0.01	7.89	$(5.65 \pm 0.08) (N = 10201)$	$(0.71 \pm 0.01) (N = 10201)$
10	7.8	0.05	7.75	$(4.35 \pm 0.68) (N = 10201)$	$(0.55 \pm 0.08) (N = 10201)$

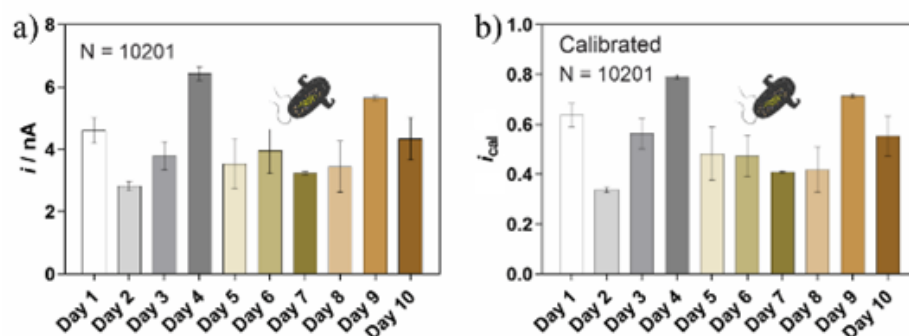


Fig.5.20 Bar plots show mean SECM FB currents \pm standard deviation from all data points of ten SECM images of tape-collected *E. coli* biofilm surface layers with ampicillin-resistant *E. coli* cells without (a) and (b) calibration according to Table S10.

The lower calibrated mean current of 0.36 ± 0.14 versus 0.54 ± 0.14 suggests that the use of ampicillin-resistant *E. coli* resulted in a biofilm with higher metabolic activity (or increased side events increasing the SECM feedback current, *vide infra*) (**Fig.5.21**).

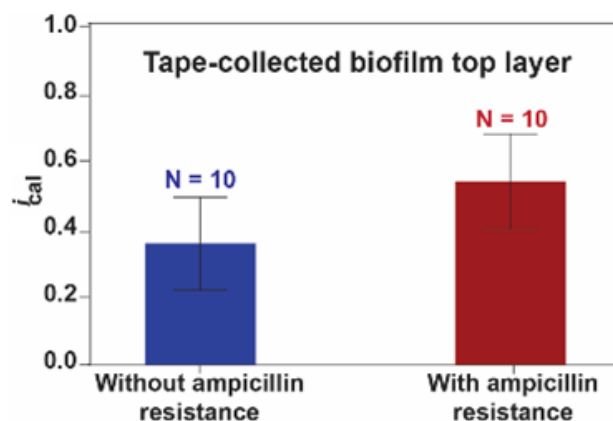


Fig.5.21 Mean currents \pm standard deviation of ten biofilms with *E. coli* without and with ampicillin resistance. Experimental SECM details: $E_T = 0.5$ V, probe translation speed = $25 \mu\text{m s}^{-1}$, step size = $10 \mu\text{m}$, 2.5 mM FcMeOH in 100 mM PBS (pH 7.4). Reported SECM imaging area: 1 mm^2 .

5.2.4 SECM imaging of *E. coli* biofilm during antibiotic treatment

Gentamicin is one of the most effective antibiotics against *E. coli* biofilms [322]. It is an aminoglycoside-based hydrophobic compound that permeates through the outer membrane of *E. coli* cells [323]. The effectiveness of aminoglycosides is based on the inhibition of the synthesis of proteins through binding to the 30S ribosome. A second lethal effect could be the perturbation of the surface of the bacterial cells [322]. Herein, the minimum inhibitory concentration (MIC) of $32 \mu\text{g/mL}$ gentamicin was applied for 1 h (**Fig.5.22a**) and 24 h (**Fig.5.22b**) to two tape-collected *E. coli* biofilms. Thereafter, 20 times the MIC ($20 \text{ MIC} = 640 \mu\text{g/mL}$) was applied for 1 h (**Fig.5.22c**) to a third tape-collected *E. coli* biofilm [324]. SECM imaging of the same areas was carried out in all three cases before and after the antibiotic treatment. The two solutions with FcMeOH and the antibiotics were changed, and the samples were washed. However after antibiotic treatment, the SECM FB currents over the biofilms decreased to a different extent. At the MIC, the mean SECM current decreased by 80% after 1 h and 94% after 24h. Therefore, it can be concluded that only little biofilm activity

remained. After 1 h with 20 MIC, the activity of the biofilms was nearly completely reduced (*i.e.*, 99%). As expected, the antibiotic treatment was more efficient with longer treatment times and higher antibiotic concentrations. LSMs of the biofilm after (**Fig.5.22d,e**) antibiotic treatment with 20 MIC demonstrated the presence of remaining biofilm on the tape.

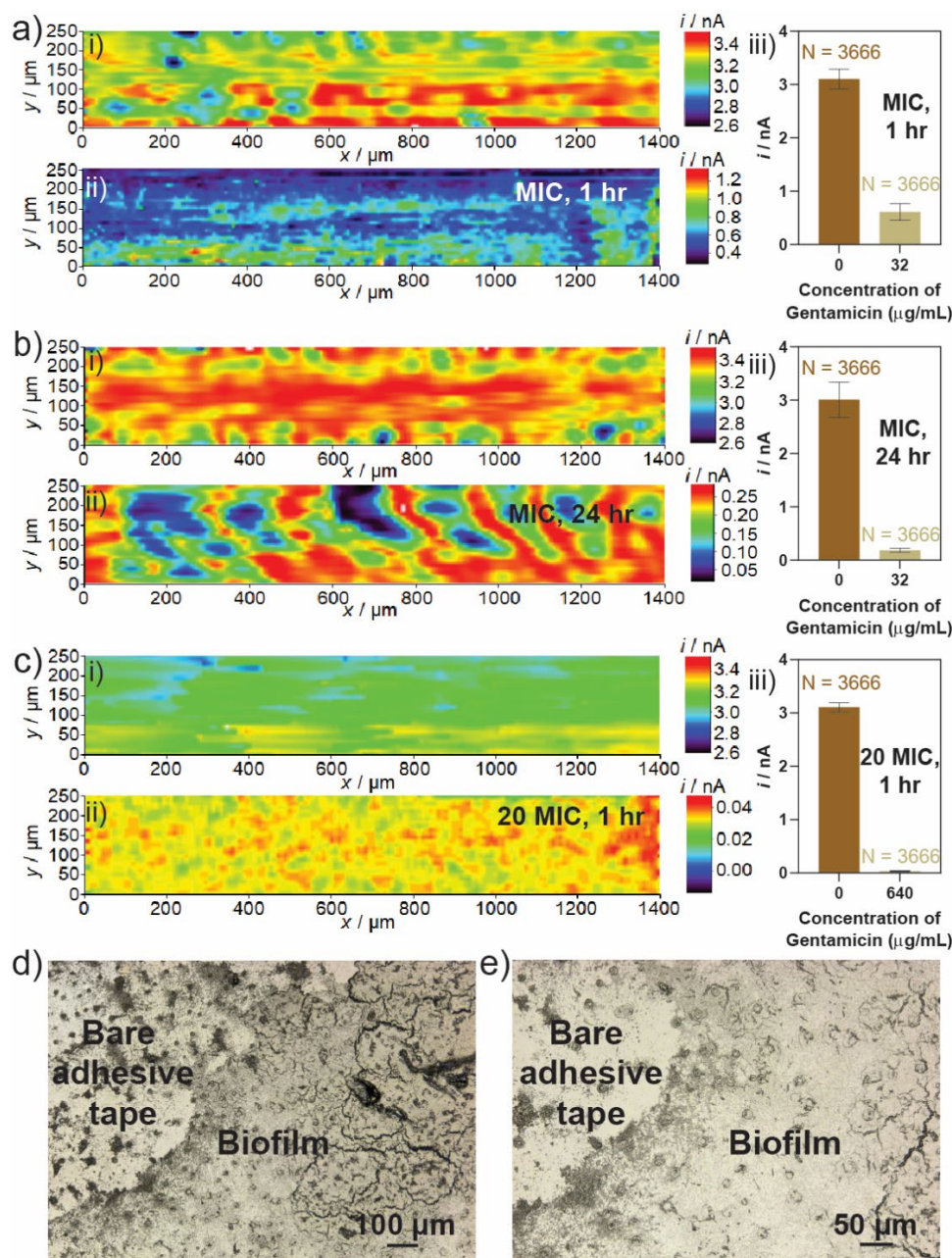


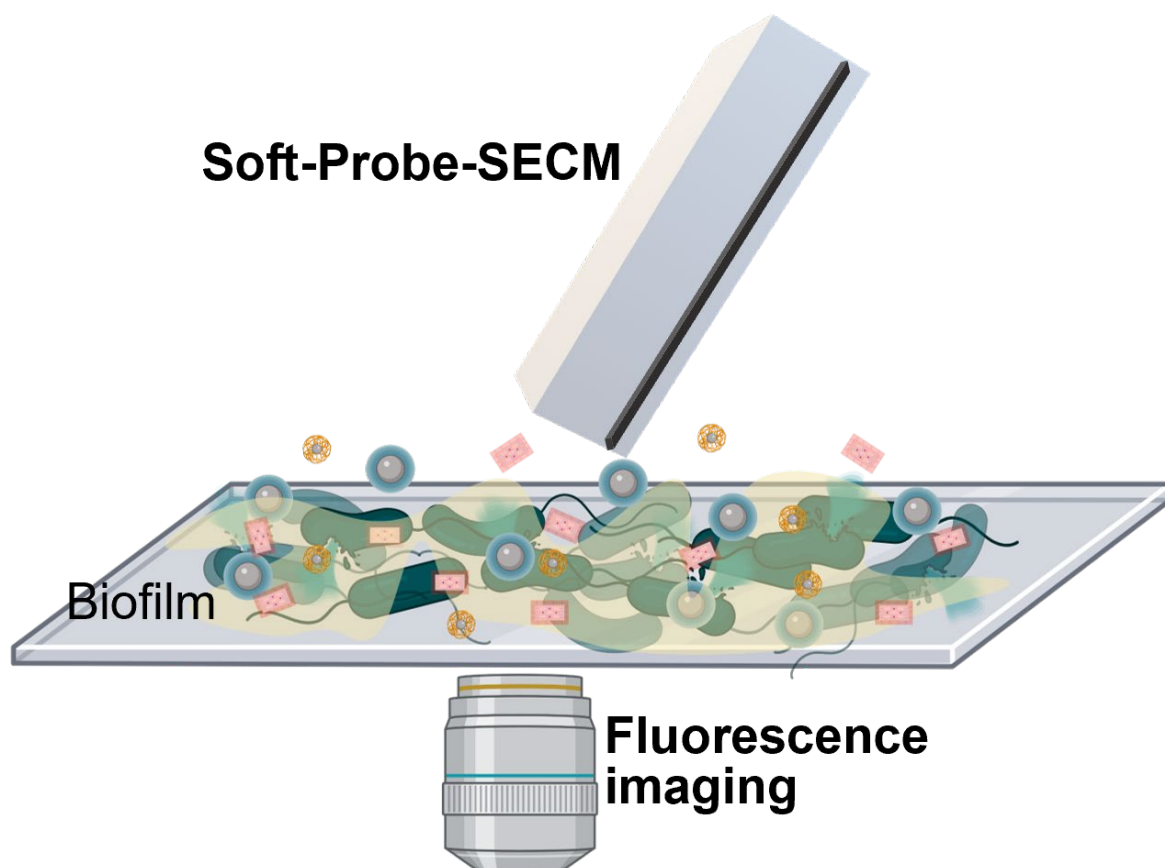
Fig.5.22 Soft-Probe-SECM imaging of tape-collected one day old, ampicillin-resistant *E. coli* biofilm before (i) and after (ii) gentamicin treatment. (a) 32 $\mu\text{g/mL}$ (MIC), incubation time = 1 h. (b) 32 $\mu\text{g/mL}$ (MIC), incubation time = 24 h. (c) 640 $\mu\text{g/mL}$ (20 MIC), incubation time = 1 h. (a-c, iii) Mean SECM FB currents \pm standard deviation. (d) and (e) LSMs of one *E. coli* biofilm after the gentamicin treatment with 20 MIC and an incubation time of 1 h in two magnifications. Experimental SECM details: $E_T = 0.5$ V, probe translation speed = 25 $\mu\text{m s}^{-1}$, step size = 10 μm , 2.5 mM FcMeOH in 100 mM PBS (pH7.4).

5.3 Conclusions

In this chapter, Soft-Probe-SECM imaging of the metabolic activity of *E. coli* biofilms using a redox mediator was presented. First, the formation of *E. coli* biofilms was confirmed using standard microscopic methods. FcMeOH was used as a metabolic activity indicator for visualizing biofilm

metabolic activity electrochemically. The biofilms showed the ability to reduce FcMeOH^+ and enabled SECM feedback mode characterization and imaging. Soft microelectrodes were gently brushed over the biofilm allowing scanning experiments with a nearly constant working distance while keeping the biofilm intact. Biofilms were analyzed on glass slides and their top surface layer of $\sim 2\ \mu\text{m}$ thickness after collection with adhesive tapes. As the responses of both systems appeared very similar, the SECM method seemed sensitive to the surface layer of the biofilms. The micro-electrochemical imaging procedure was repeated during several days of biofilm growth and could distinguish the growth of ampicillin-susceptible and -resistant *E. coli* biofilms. Finally, this work demonstrated that Soft-Probe-SECM imaging is a powerful tool to analyze the degradation of biofilms in the presence of antimicrobial agents such as antibiotics. The work showed that FcMeOH is a suitable redox indicator for general and long-lasting biofilms studies with accessible recording the biofilm metabolic activity. The technique complements microscopic techniques, gene expression analysis, and proteomics and could open the door for further SECM-based biofilm studies.

CHAPTER 6 Revealing the effects of four different antimicrobial agents on *E. coli* biofilms by using Soft-Probe Scanning Electrochemical Microscopy



6.1 Introduction

Bacterial biofilms are thin organic layers composed of more bacterial cells embedded in a matrix containing extracellular polymeric substances (EPS) and water [325]. The EPS-based matrix behaves as a physicochemical barrier limiting the accessibility of nutrient supplements and antimicrobial reagents [326]. The lack of nutrients reduces the metabolism of bacteria deep inside the biofilm, and they adapt to a dormant state, making them less susceptible to antimicrobial agents [327]. The efficiency of antibiotic treatments is evaluated by detecting the viability of bacterial cells in the biofilm when exposed to antimicrobial agents. Several techniques can be applied to assess biofilm viability based on biofilm's culturability, RNA detection, metabolic activity, or the determination of membrane integrity [124]. For instance, counting colony-forming unit (CFU) of bacteria grown in agar plates with artificial nutrients is one such method. It quantifies the number of colonies that are formed by viable cells. Utilizing the CFU method for evaluating biofilm viability may generate potential errors due to the significant merging of adjacent colonies during readout [132, 134]. Molecular methods based on the polymerase chain reaction (PCR) provide genetic information that is correlated to bacterial species and their mutations [136, 138]. Although PCR is very powerful and is being increasingly used, it lacks antimicrobial sensitivity [328]. Flow cytometry (FCM) comprises multiparametric analysis, in which the bacterial cell surface or its components are labeled with one or more fluorescent dyes [329, 330]. FCM shows limitations when distinguishing between small cells and cellular debris due to the small size of bacteria [331]. Static biofilms can be analyzed using fluorescence imaging [332] alone or with staining techniques like crystal violet staining or live/ dead staining [154]. It provides worthy information. However, these methods can suffer from intrinsic defects. Crystal violet indicates the biomass of biofilms (*i.e.*, bacteria and the extracellular matrix), but it does not show biofilm viability. Live/dead staining with microscopic fluorescence imaging is time-consuming (*e.g.*, stacked imaging to investigate the 3D structure) and limited to a small biofilm section. Therefore, it is not suitable for high-throughput quantification.

In situ and *ex situ* methods, metabolic assays detect metabolic compounds produced or consumed by bacteria. This approach evaluates the viability of intact biofilms and can be realized by utilizing metabolic indicator dyes such as resazurin [134, 159], fluorescein diacetate [162], or pH indicators [156]. Metabolic assays often evaluate the free-floating bacteria and the bacteria within the biofilm differently. This could be the main drawback of the metabolic assays for detecting biofilm viability [333]. Alternatively, electrochemical methods can be applied for the *in situ* investigation of the metabolic activity of biofilms. Electrochemical detection is sensitive, can be non-destructive to living biological samples, is operational in small sample volumes, can be applied in portable devices (*e.g.*, sensors), and is generally less prone to interferences than optical methods [290, 334-337]. Electrochemical investigations of biofilms with microelectrodes offer many opportunities, as recently reviewed [177]. In particular, scanning electrochemical microscopy (SECM) is attractive for real-time

detection of redox-active small molecules and a biofilm's metabolic activity with micrometer resolution. SECM has been used for different investigations on biofilms, e.g., the detection of H_2O_2 at biofilms to study glucose metabolism of various biofilms [183, 193], catalase activity of *Vibrio fischeri* biofilms [183], quorum sensing molecules with the aid of the detection of pyocyanin [174, 175, 338]. Also, SECM was proposed to detect the effect of antimicrobial treatments [339-342].

Several chemical and physical methods have demonstrated antimicrobial effects on biofilms, including antibiotics, various materials, heat treatment, light treatment, or filtration [343, 344]. Antimicrobial reagents have been discussed in detail in Chapter 1. Briefly, antimicrobial agents can be divided into different groups based on the mechanism of antimicrobial activity [114, 345], including; i) inhibition of the microbial adherence, ii) inhibition of microbial quorum sensing, iii) degradation of the extracellular matrix, iv) inhibition of bacterial cell wall synthesis, v) depolarizing of the bacteria cell membrane, vi) inhibition of protein and nucleic acid synthesis, and vii) inhibition of metabolic pathways in bacteria [114, 343, 344, 346, 347]. Metal nanoparticles such as gold (AuNPs) and silver nanoparticles (AgNPs) possess an intrinsic antimicrobial activity. This thesis used silver nanoparticles as antimicrobial agents [348, 349]. Furthermore, antimicrobial chemicals including fluoride [350], chlorine [351], and chlorhexidine [352], and sodium azide [353, 354] were used to eradicate biofilms. Among the antimicrobial chemicals, azide has a significant effect as an inhibitory agent on bacteria's metabolic pathways within the biofilm.

In chapter 5, the potential to use Soft-Probe-SECM for the investigation of metabolic activity of biofilms by using the feedback mode of SECM was demonstrated [355]. In this chapter, the objectives were to determine the inherent impacts of antimicrobial reagents on the biofilm of the model bacterium *E. coli* strain DH5 α by recording the electrochemical surface reactivity of biofilm and to determine whether Soft-Probe-SECM is sensitive to the impact of incubation time and concentration of antimicrobial reagents on the biofilms. We present the use of SECM to visualize the response of *E. coli* biofilms to two different antimicrobial agents: sodium azide and silver nanoparticles and flashlight treatment, and the constraints of combining and comparing with data obtained from state-of-the-art biofilm detection methods. Further, since nanoparticle transport in the biofilm are affected by particle size and therefore aggregation state, the treatment effects of using three types of AgNPs with different colloidal stability were compared.

6.2. Results and discussion

6.2.1 Selection of redox mediator for feedback mode imaging of native *E. coli* biofilms

First, two redox mediators were compared to identify a more sensitive redox-active mediator to detect the redox activity of biofilms by SECM. One day old *E. coli* biofilms were grown on glass slides in a culture medium. The successful formation of the biofilm, i.e., viable and intact bacterial cells embedded in EPS were confirmed by laser scanning microscopy, SEM, and live/ dead fluorescence

microscopy. Laser scanning micrographs (LSMs) in **Fig.6.1a,b** show the 3D structure of an *E. coli* biofilm attached to a glass slide in two magnifications. Low magnifications (**Fig.6.1a**) show the compact and homogeneous biofilm grown on the glass slide. The higher magnification (**Fig.6.1b**) shows the bacteria embedded in the EPS. Scanning electron microscopy (SEM) also shows biofilm morphology in **Fig.6.1c,d** and supports the results from LSMs. The fluorescence image of crystal violet, which stained both bacteria and the EPS of the biofilm, is used to visualize the biofilm's formation and biomass (**Fig.6.1d**). The live/dead co-staining of *E. coli* biofilm was investigated by staining with SYTO 9 and propidium iodide (PI). The SYTO 9 stain labels all bacteria green, whereas propidium iodide labels (red color) nonviable bacteria with compromised membranes. **Fig.6.1f** shows the 3D z-stack fluorescence image of the biofilm, which indicates the 3D structure of the *E. coli* biofilm on the glass slide. The fluorescence image (**Fig.6.1f**) shows mostly the green fluorescence emitted by SYTO 9, which indicates that most of the bacteria embedded in the EPS were alive.

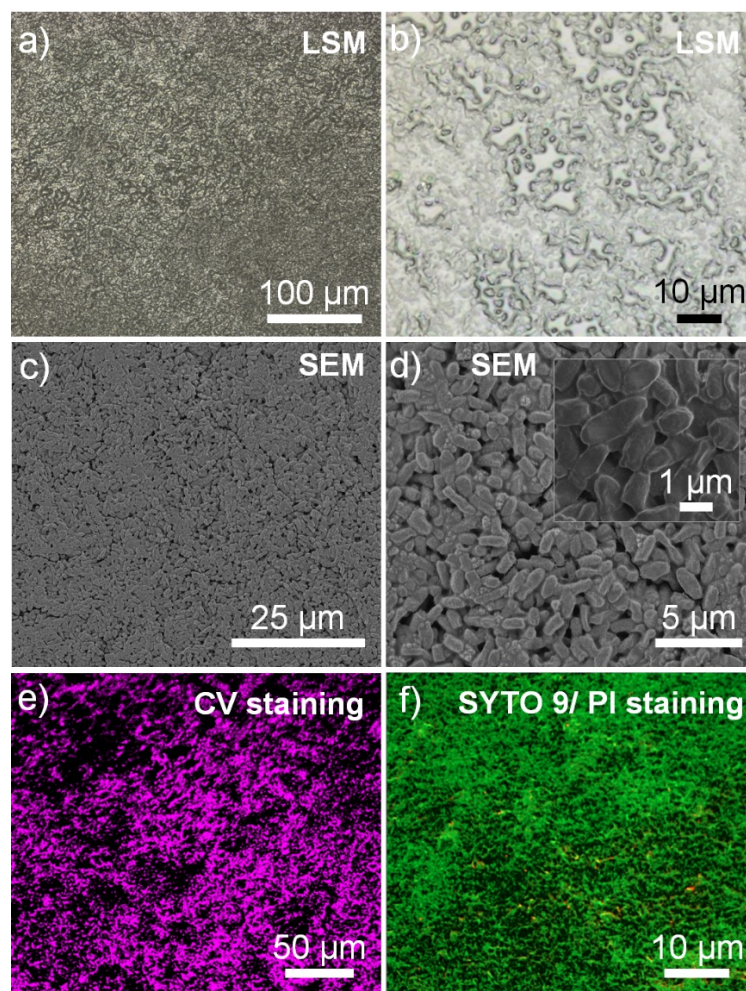


Fig.6.1 Investigate the presence of one-day-old *E. coli* biofilm grown on a coverslip using microscopy: (a-b) laser scanning micrograph in two magnifications. (c-d) SEM images at three different magnifications. e) Fluorescence crystal violet biomass staining. (f) Fluorescence images of SYTO 9/ PI co-staining. SYTO 9 (green color) stained all bacteria, and PI (red color) stained dead bacteria.

Furthermore, the 3D structure of the biofilm was evaluated by z-stack CLSM (**Fig.6.2a**). The biofilm thickness was less than 10 μm , as shown in **Fig 6.2b**.

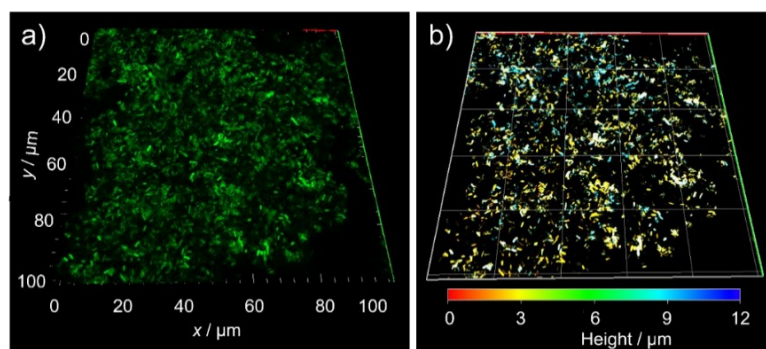


Fig.6.2 (a) 3D structure of one day old *E. coli* biofilm on the coverslip. (b) Height profile of the biofilm. The color bar indicates the height of the biofilm.

In chapter 5, Soft-Probe-SECM in feedback mode was recorded based on ferrocene methanol (FcMeOH) oxidation at the tip of the SECM soft probe. An enhanced SECM current was recorded over the biofilm compared to a biofilm-free surface, most likely due to the transfer of FcMeOH^+ inside the biofilm matrix (biofilms contain channels for nutrient supply and a significant amount of water [113]) and/or the ability of the biofilm to reduce the as-oxidized redox mediator, e.g., as the final electron acceptor in the respiratory electron transport chain (ETC) of the bacterial cells embedded in the biofilm. The reduction might also partially occur outside the bacterial cells, thus by the EPS or redox species released from the biofilms into the microenvironment [174-176, 320, 321]. It is known that generally, there are different species secreted from bacterial cells (**Fig.6.3**). For the *E. coli* biofilm, quinone-derivatives are the electro-active components secreted from *E. coli* and entrapped in the EPS.

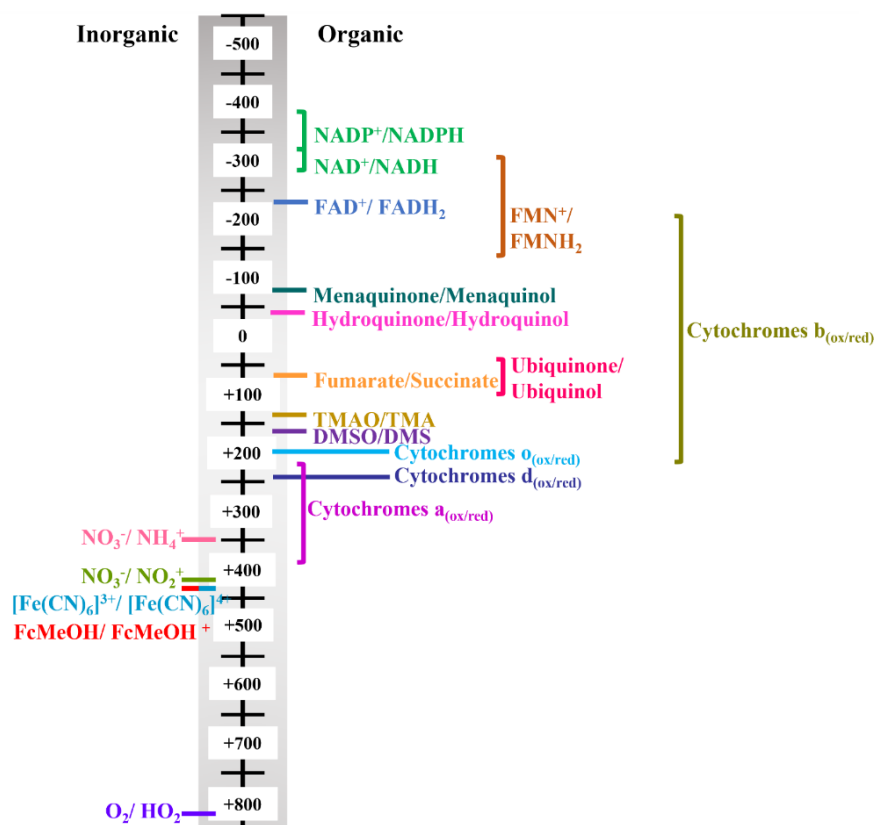


Fig.6.3 Redox potentials of important redox couples in the electron transport chain of *E. coli*. Standard redox potentials (E^0 [mV, 25°C, pH 7]) are indicated. Physiological or environmental conditions are known to shift the potential from the E^0 , redox windows are indicated [320].

Herein, anionic and hydrophilic ferrocenecarboxylic acid (FcCOO^- , pK_a 4.2) [356] (**Fig.6.4a**) and neutral and more lipophilic ferrocene methanol (**Fig.6.4b**) were compared in separate experiments. The biofilm samples were grown on a thin coverslip (the coverslip thickness was 170 μm). The electron transfer chain of bacteria is located on the plasma membrane of the *E. coli* cells (**Fig.6.4a,b**) [357]. Therefore, the redox mediator must permeate through the outer membrane of the *E. coli* cells, reaching terminal metabolic redox enzymes of the electron transfer chain [358]. The outer leaflet of the outer membrane is composed of lipopolysaccharides (LPS), which are highly negatively charged and works as a selective permeability barrier [359]. One possibility for the transfer of the redox mediator is beta-barrel proteins, such as porins located in the outer membrane [360]. Porins are narrow channels that allow selective diffusion, driven by the concentration gradient between the two sides of the membrane. Porins allow, by passive diffusion, the passage of hydrophilic and lipophilic ions and molecules with molecular weights below 600 Da. Furthermore, lipophilic compounds may also cross the membranes directly [361, 362]. The reduced form of the redox mediator must leave the bacterial cells through the outer membrane.

Soft-Probe-SECM in feedback mode was carried out in 100 mM PBS (pH 7.4) using 2.5 mM FcCOOH and FcMeOH separately as a redox mediator to investigate the sensitivity of the redox mediators for reading out the surface reactivity of the *E. coli* biofilm. By applying 0.5 V to the SECM probe, the oxidized forms of the redox mediators, *i.e.*, neutral albeit zwitterionic Fc^+COO^- and positively charged FcMeOH^+ , were continuously generated and diffused towards the nearby biofilm.

Soft microelectrode approach curves were recorded by approaching the soft probe to the substrate from the bulk solution. The SECM currents I were normalized by the current recorded in the solution bulk I_{Bulk} giving in the bulk $I_{\text{Norm, Bulk}} = 1$. When the soft probe touched the coverslip, the current for both redox mediators was close to zero (**Table 6.1, Fig.6.4c,d**). In contrast, approaching the soft microelectrode towards a one-day-old biofilm on the coverslip shows a significantly higher current indicating the ability of the biofilm to reduce both Fc^+COO^- and FcMeOH^+ and back to FcCOO^- and FcMeOH , respectively. Notably, the feedback current recorded for the reduction of FcMeOH was 59% higher than for FcCOOH , which is rather significant (**Table 6.1, Fig.6.4c,d**). Approach curves were then performed over three different but identically grown biofilms on a coverslip in duplicate and laterally separated by 250 μm (**Fig.6.4e,f**). The normalized feedback currents between the soft probe and samples at the contact point are presented in **Table 6.2** and **Table 6.3** for FcCOOH and FcMeOH , respectively. The average normalized feedback current for FcCOOH was 0.18, which varied by 5%, and for FcMeOH , it was 0.48 and varied by 5%. The feedback current recorded over six different samples and in total for 12 measurements by FcMeOH was 63% higher than the normalized feedback currents recorded with FcCOOH as a redox mediator. The oxidized forms of the redox mediators, *i.e.*, Fc^+COO^- and FcMeOH^+ , are hydrophilic. They diffuse through the biofilm matrix and could permeate the outer membrane *via* porins [323]. The reduced forms of the redox mediator FcMeOH and FcCOO^- [363] diffuse through the porins as well with the additional possibility

for FcMeOH to cross the outer membrane due to its slightly higher lipophilicity. This might have contributed to the higher SECM current.

Table 6.1 Details of $I_{\text{Norm, coverslip}}$ and $I_{\text{Norm, biofilm surface/coverslip}}$ of **Fig.6.1c** and **Fig.6.1d**.

Sample	Bare coverslip	Biofilm grown on coverslip
$I_{\text{Norm}} (// I_{\text{Bulk}})$ of FcCOOH	0.08	0.24
$I_{\text{Norm}} (// I_{\text{Bulk}})$ of FcMeOH	0.11	0.58

Table 6.2 Details about $I_{\text{Norm, biofilm surface/coverslip}}$ of **Fig.6.1e** for FcCOOH mediator.

Sample	1-1	1-2	2-1	2-2	3-1	3-2
$I_{\text{Norm}} = // I_{\text{Bulk}}$	0.19	0.10	0.21	0.13	0.20	0.26

Table 6.3 Details about $I_{\text{Norm, biofilm surface/coverslip}}$ of **Fig.6.1f** for FcMeOH mediator.

Sample	4-1	4-2	5-1	5-2	6-1	6-2
$I_{\text{Norm}} = // I_{\text{Bulk}}$	0.53	0.48	0.42	0.42	0.54	0.52

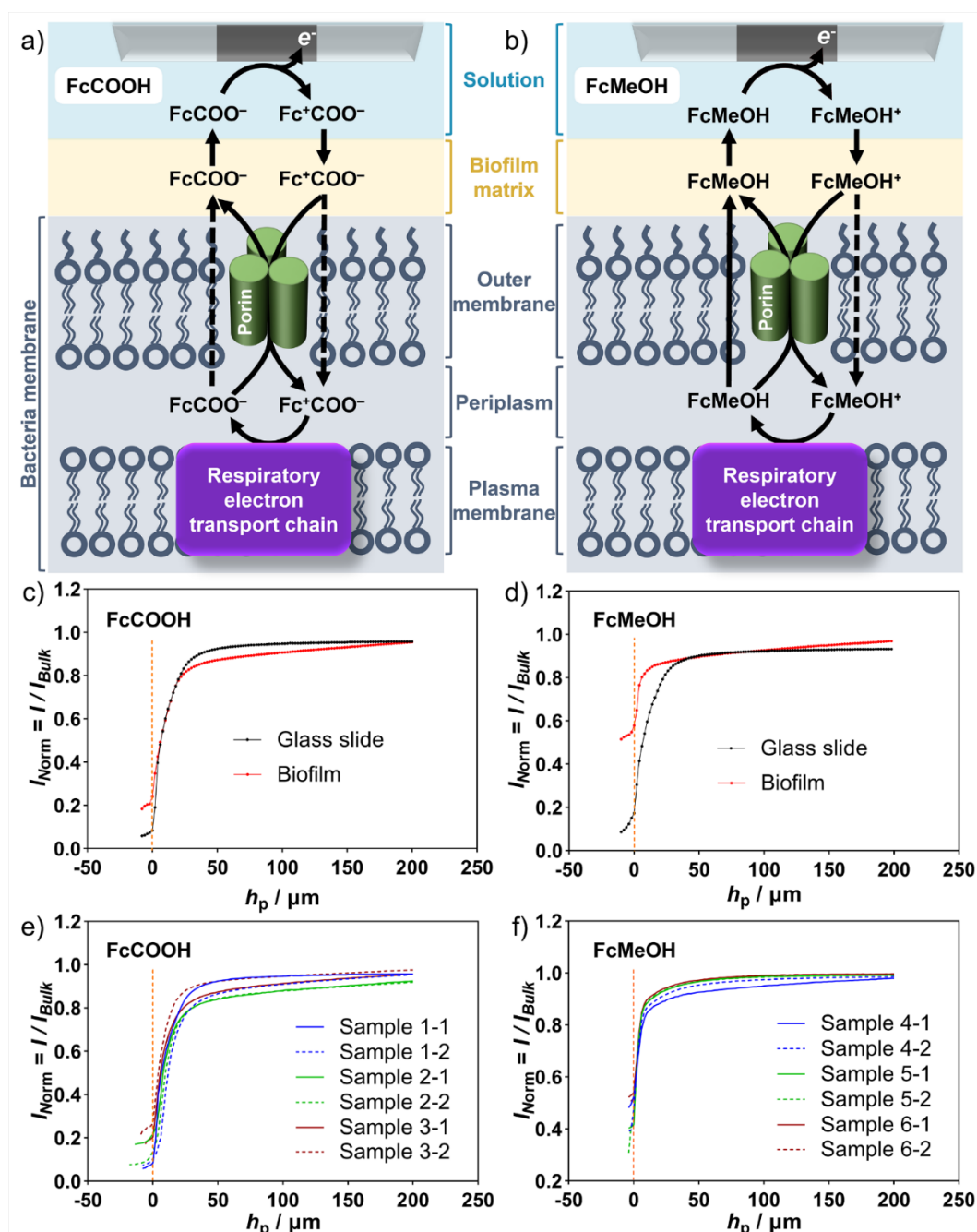


Fig.6.4 Schematic representation of the main possible transport paths of (a) FcMeOH and FcMeOH^+ , (b) FcCOO^- and Fc^+COO^- between the exterior part and periplasmic space of *E. coli*. Solid arrows indicate high permeability, dashed lines low or absent permeability. Approach curves over bare coverslip and biofilm grew on glass in solution with (c) FcCOOH and (d) FcMeOH . Two locally separated approach curves (lateral $\Delta x = 250 \mu\text{m}$) over each of three identically grown biofilm surfaces ($N_{\text{sample}} = 3$) performed in (e) FcCOOH and (f) FcMeOH . Experimental details: $E_T = 0.5 \text{ V}$, probe translation speed $= 5 \mu\text{m s}^{-1}$, step size $= 2 \mu\text{m}$, 2.5 mM FcMeOH in 100 mM PBS ($\text{pH } 7.4$).

Furthermore, $[\text{Ru}(\text{NH}_3)_6]^{3+}$ was a positively charged and hydrophilic redox mediator. FcMeOH and FcCOOH are more hydrophobic than $[\text{Ru}(\text{NH}_3)_6]^{3+}$, which resulted in a higher permeability in the biofilm for the Fc derivatives, influencing the mass transport and improving most likely by this effect the feedback current. $[\text{Ru}(\text{NH}_3)_6]^{3+}$ is a positively-charged mediator that is reduced at the microelectrode, contrary to FcMeOH , like other hydrophilic mediators $[\text{Ru}(\text{NH}_3)_6]^{3+}$ cannot diffuse through the cell membrane, and the cell effectively acts as an insulator [364, 365]. As the microelectrode approaches the cell, the diffusion of $[\text{Ru}(\text{NH}_3)_6]^{3+}$ toward the microelectrode is

hindered, creating negative feedback. Due to the higher feedback current, FcMeOH was selected for all further experiments (**Fig.6.5**).

Table 6.4 Details of $I_{\text{Norm, coverslip}}$ and $I_{\text{Norm, biofilm surface/coverslip}}$ of **Fig.6.2a** and **Fig.6.2b**.

Sample	Bare coverslip	Biofilm grown on coverslip
$I_{\text{Norm}} (// I_{\text{Bulk}})$ of FcMeOH	0.10	0.85
$I_{\text{Norm}} (// I_{\text{Bulk}})$ of $[\text{Ru}(\text{NH}_3)_6]^{3+}$	0.09	0.19

Table 6.5 Details about $I_{\text{Norm, biofilm surface/coverslip}}$ of **Fig.6.2c** for $[\text{Ru}(\text{NH}_3)_6]^{3+}$ mediator.

Sample	1-1	1-2	2-1	2-2	3-1	3-2
$I_{\text{Norm}} = // I_{\text{Bulk}}$	0.17	0.26	0.18	0.21	0.13	0.16

Table 6.6 Details about $I_{\text{Norm, biofilm surface/coverslip}}$ of **Fig.6.2d** for FcMeOH mediator.

Sample	4-1	4-2	5-1	5-2	6-1	6-2
$I_{\text{Norm}} = // I_{\text{Bulk}}$	0.82	0.88	0.81	0.82	0.78	0.86

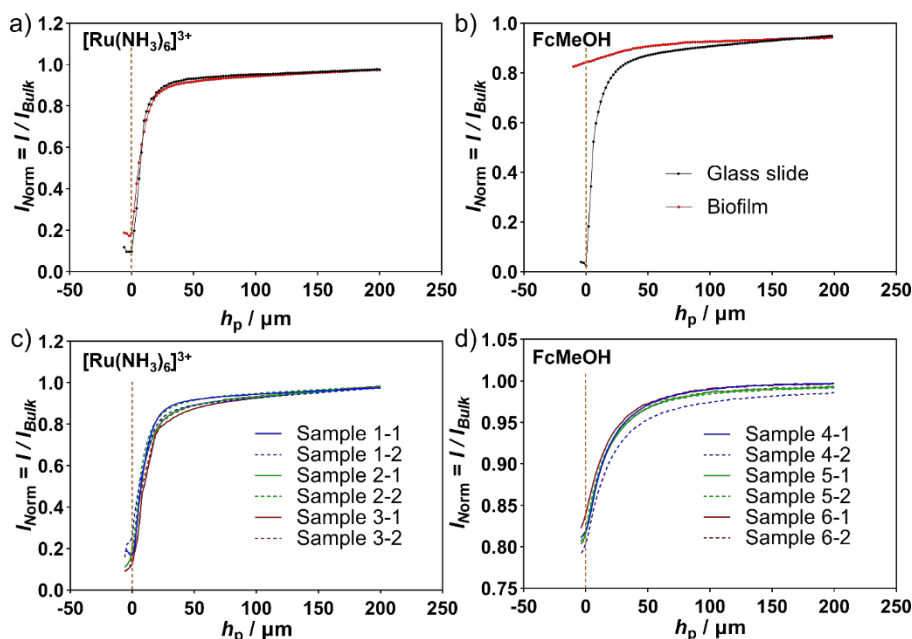


Fig.6.5 Approach curves over bare coverslip and biofilm grown on in two redox active mediators of (a) $[\text{Ru}(\text{NH}_3)_6]^{3+}$ and (b) FcMeOH. Two locally separated approach curves (lateral $\Delta x = 250 \mu\text{m}$) over each of three identically grown biofilm surface ($N_{\text{sample}} = 3$) performed in (c) $[\text{Ru}(\text{NH}_3)_6]^{3+}$ and (d) FcMeOH. Experimental details: $E_T = 0.5 \text{ V}$ for FcMeOH, $E_T = -0.4 \text{ V}$ for $[\text{Ru}(\text{NH}_3)_6]^{3+}$ probe translation speed $= 5 \mu\text{m s}^{-1}$, step size $= 2 \mu\text{m}$, 2.5 mM FcMeOH in 100 mM PBS (pH7.4).

6.2.2 SECM investigation of biofilm degradation induced with azide

First, sodium azide was used to inhibit the metabolic activity of an *E.coli* biofilm. In metabolically active bacteria, ATPase in the plasma membrane catalyzes the synthesis of ATP from ADP (**Fig.6.6a**). This oxidative phosphorylation reaction is coupled to the proton motive force and proton transport from the outside of bacterial cells into the cytoplasm [366]. Electron transfer reactions maintain the proton motive force (and thus the membrane potential). NADH serves as an electron donor. Its oxidation at NADH dehydrogenase pumps protons out of the cytoplasm. Under aerobic conditions, oxygen is the final electron acceptor. This results in the transport of up to eight protons

[320]. The ETC consists of membrane-bound cytochromes (*a*-, *b*-, *d*-, *o*-type), dehydrogenases, quinones, and flavins. The sites of electron transfer of the anodic electron transport are cytochrome *bo*, cytochrome *bd*, Ubiquinone-pool, FAD reduction, and NADH oxidation, according to Equations 6.1-6.3 (**Fig.6.3**, $E^{0'}$ given at 25°C and pH 7 [320]):



Reported potentials (ox/ red) of cytochromes *a*-, *b*-, *d*- and *o*-type are 0.290 V, 0.080 V, 0.024 V, and 0.200 V, respectively [320]. In the aerobic respiration of *E. coli*, oxygen ($E^0 = 0.82 \text{ V}$) acts as electron acceptor [320]. FcMeOH⁺ with the standard redox potential of 0.44 V [367] competes with O₂ as an electron acceptor. Inhibition of the respiratory chain affects the viability of *E. coli* cells through the proton motive force and electron transport chain [353, 354], thus reducing FcMeOH⁺. Biofilms on a coverslip were incubated in solution with 4 mM sodium azide, a potent inhibitor of bacterial growth [368]. Sodium azide inhibits bacterial growth by inhibiting the activity of SecA, an ATPase required for translocation of proteins across the cytoplasmic membrane [369]. The inhibition of the three F1-ATPase catalytic sites was discussed in the literature [370]. Three different biofilms were grown on the coverslip and incubated in a sodium azide-containing solution. The same biofilms were evaluated for the non-treated samples. Three SECM approach curves were performed over the biofilms before incubation in sodium azide and after, each time by changing the solution and washing of the biofilm. SECM measurements were carried out without antimicrobial agents. The details of SECM approach curve signals are presented in **Table 6.7** and shown in **Fig.6.6b**.

Table 6.7 Details of SECM currents at the contact point of the soft probe with the biofilm surface.

Sample	$I_{\text{Norm}} = I/I_{\text{Bulk}}$
Non treated-1	0.62
Non treated-2	0.60
Non treated-3	0.64
5 min-1	0.43
5 min-2	0.46
5 min-3	0.45
15 min-1	0.38
15 min-2	0.30
15 min-3	0.36

The average of the normalized currents over nontreated samples was (0.62 ± 0.02), and after 5 min and 15 min decreased to (0.45 ± 0.01) and (0.34 ± 0.02) for three different samples. The feedback current decreased by 27% and 46%, respectively, after 5 min and 15 min incubation in sodium azide. As the results show, the developed SECM approach is very sensitive to the effect of sodium azide treatment. It can record a significant change of the SECM current after 5 min of azide incubation. This may result from the reduced activity of the electron transport chain to reduce FcMeOH⁺ and a

reduced number of living bacterial cells. Therefore, with the feedback mode of SECM, the effect of ETC inhibitors on biofilms could be recorded fast and with high sensitivity.

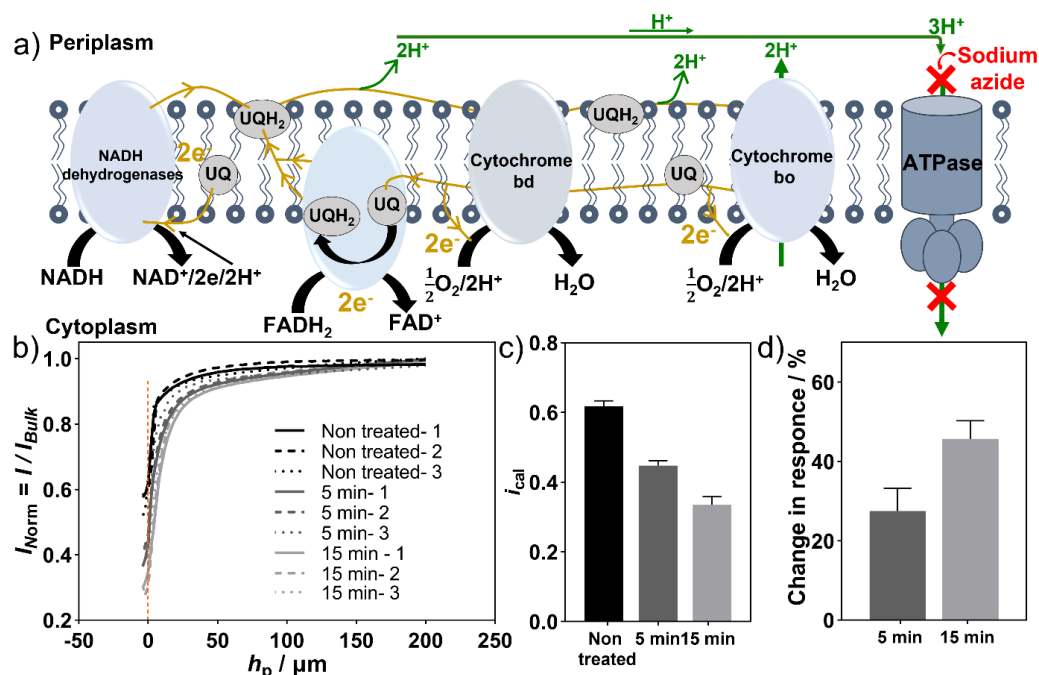


Fig. 6.6 (a) Schematic representation of the respiratory electron transport chain in *E. coli*, including possible sites of electron transfer on plasma membrane (adapted from Ref [320]). Drak yellow lines indicate the transfer paths of electrons and protons within the electron transport chain. (c) Mean \pm standard deviation of current at the touching point on the substrates. (d) Percentage of reduction of feedback current after 5 min and 15 min compared to the non-treated condition. Experimental details for approach curve SECM scans: working potential $E_T = 0.5$ V, probe translation speed = $5 \mu\text{m s}^{-1}$, step size = $2 \mu\text{m}$, 2.5 mM FcMeOH in 100 mM PBS (pH 7.4).

Furthermore, four SECM feedback line scans were performed, with lateral space of $250 \mu\text{m}$ between them, on the same sample (**Table 6.8** and **Fig. 6.7**), and the mean calibrated current values for each line scan are shown in the bar plot in **Fig. 6.7d**. The average of calibrated current over nontreated samples were (0.58 ± 0.004) , and after 5 min and 15 min were (0.41 ± 0.003) and (0.33 ± 0.004) , respectively, for four different locations. The calibrated feedback current decreased about 30% and 44% after 5 min and 15 min incubation in sodium azide-containing solution. Therefore, the biofilm activity to reduce FcMeOH^+ upon inhibition of cellular respiration by sodium azide was reduced.

Table 6.8 Details of SECM x-line scan data of **Fig. 6.7** using Equation 5.1 and Equation 5.2.

Position	Time	$I_{\text{bulk}} / \text{nA}$	$I_{\text{plastic}} / \text{nA}$	$I_{\text{bulk}}^* / \text{nA}$	$I_{\text{mean,FB-image}} / \text{nA}$	I_{mean}^*
Position 1	non	3.74	0.10	3.64	$(2.08 \pm 0.005) (N = 81)$	$0.57 (N = 81)$
	5	3.69	0.09	3.60	$(1.47 \pm 0.006) (N = 81)$	$0.41 (N = 81)$
	15	3.66	0.11	3.55	$(1.06 \pm 0.01) (N = 81)$	$0.26 (N = 81)$
Position 2	non	3.74	0.10	3.64	$(2.09 \pm 0.009) (N = 81)$	$0.58 (N = 81)$
	5	3.68	0.09	3.59	$(1.44 \pm 0.02) (N = 81)$	$0.40 (N = 81)$
	15	3.66	0.11	3.55	$(1.24 \pm 0.19) (N = 81)$	$0.35 (N = 81)$
Position 3	non	3.74	0.10	3.64	$(2.11 \pm 0.007) (N = 81)$	$0.58 (N = 81)$
	5	3.69	0.09	3.59	$(1.47 \pm 0.03) (N = 81)$	$0.41 (N = 81)$
	15	3.66	0.11	3.55	$(1.22 \pm 0.20) (N = 81)$	$0.35 (N = 81)$
Position 4	non	3.74	0.10	3.64	$(2.08 \pm 0.02) (N = 81)$	$0.57 (N = 81)$
	5	3.69	0.09	3.59	$(1.47 \pm 0.03) (N = 81)$	$0.41 (N = 81)$
	15	3.66	0.11	3.55	$(1.21 \pm 0.20) (N = 81)$	$0.34 (N = 81)$

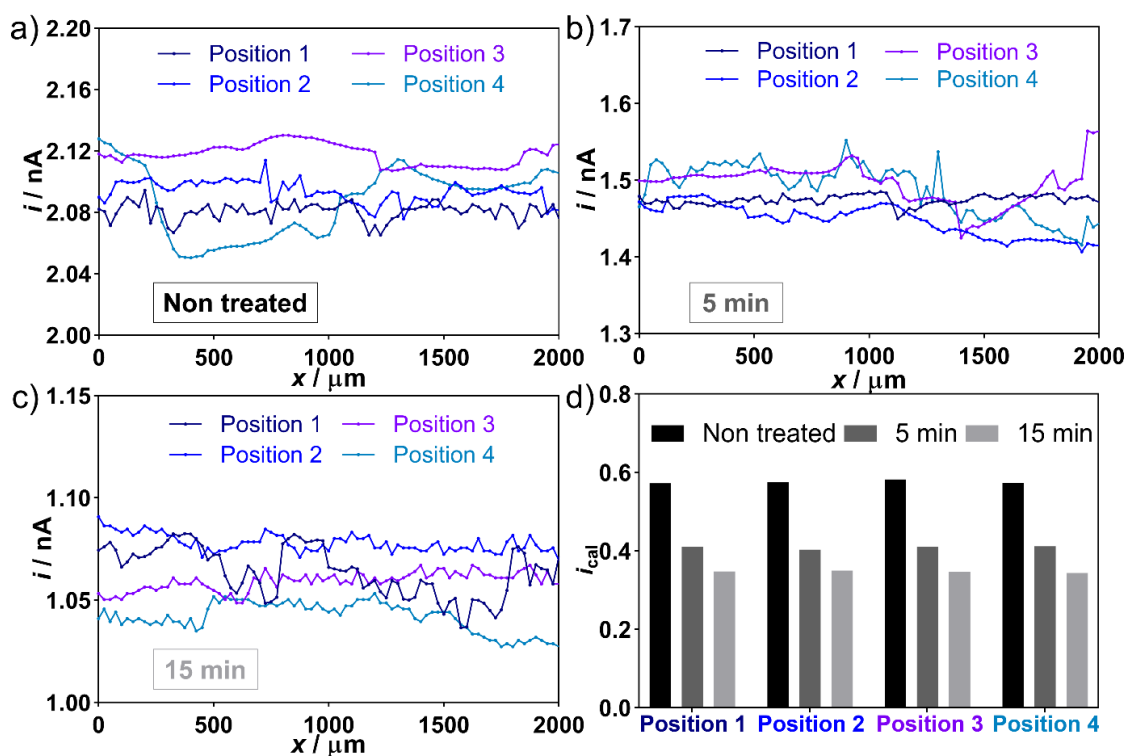


Fig.6.7 X-line scan SECM in four separated positions with a lateral distance of $250\ \mu\text{m}$ before sodium azide treatment (a), after 5 min (b), and after 15 min of sodium azide treatment. (d) Calibrated mean currents \pm standard deviation of three SECM feedback line scans over tape stripped one *E. coli* biofilm before and after 5 min and 15 min incubation of the biofilm in sodium azide containing solution, grouped by (b) line scan position and (c) grouped by treatment time. Experimental details for *x-line* SECM scans: working potential $E_T = 0.5\ \text{V}$, probe translation speed = $25\ \mu\text{m s}^{-1}$, step size = $10\ \mu\text{m}$, $2.5\ \text{mM FcMeOH}$ in $100\ \text{mM PBS}$ (pH 7.4).

Furthermore, the inhibitory effect of sodium azide was evaluated by live/dead staining CLSM. Furthermore, the effect of sodium azide treatment on the intact biomass of the biofilm was investigated by Cristal Violet (CV) staining. Before sodium azide treatment, as it is shown in **Fig.6.8(a-c)(i)**, the biofilm mostly emitted a green colour (both dead and living bacterial cells) and very few red color (dead cells) indicating the bacteria within the biofilm were predominantly alive. **Fig.6.8(d)(i)** shows the biomass of the biofilm before incubation in sodium azide containing solution.

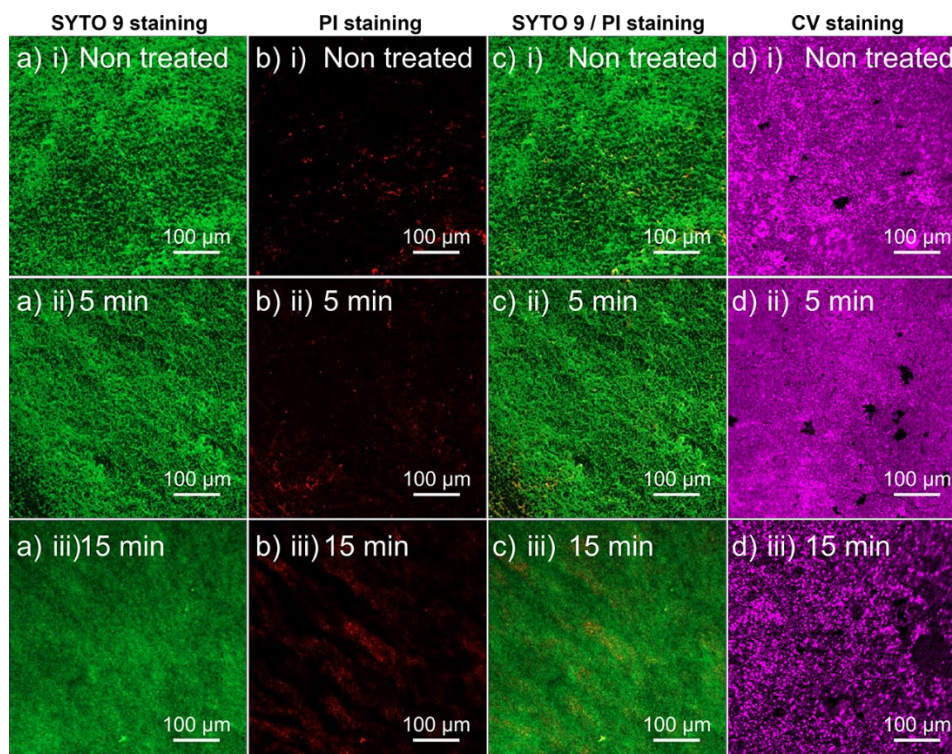


Fig.6.8 Live/dead co-staining of *E. coli* biofilm with (a) SYTO 9/ (b) PI and overlap of staining (c). (d) Biomass staining was performed by crystal violet staining. (i) Fluorescence image of biofilm before azide treatment. Fluorescence image of biofilm after (ii) 5 min and (iii) 15 min incubation in a solution with 10 mM sodium azide.

as calculated by ImageJ calculated the intensity of fluorescence images calculated the intensity of fluorescence images. The intensity values are presented in **Table 6.9** and **Fig.6.9**. The intensity of SYTO 9 staining was similar between the non-treated and azide-treated biofilms for short incubation time, and it decreased by 9% after 5 min incubation. Furthermore, the biomass of the biofilm decreased by 6%. Both few changes in the intensity of SYTO 9 and CV suggest that the biofilm's total biomass was stable after 5 min. The changes in the intensity of SYTO 9 and CV after 15 min was 21% and 21%, respectively. The intensity of the red color emitted by the biofilms increased by 8% and 67% after 5 min and 15 min, indicating an increasing number of dead bacteria within the biofilm, with a particular impact after 15 min. As result suggests, the optical microscopy techniques seem to detect the effect of sodium azide in the longer time with less sensitivity than SECM. Furthermore, the loss of biomass has been observed, which mainly resulted from washing the dyes essential for staining the biofilm. In the other study, Rapp *et al.* [371] used sodium azide as a biocide agent for monitoring biofilm destabilization and deactivation effects in real-time. They have treated *P.aeruginosa* biofilm with 1% v/v sodium azide solution and observed the impact of the treatment *via* continuous amperometric monitoring. They have reported that the biofilm's respiratory activity was significantly impaired, and most of the bacteria within the biofilm were dead.

Table 6.9 Details about quantification intensity data of **Fig.6.9**.

Time of incubation	Stain	Mean	Standard deviation	Area	Mean
Non treated	SYTO 9	47.92	20.40	213904	43.37
	PI	3.51	8.83	217622	6.15
	CV	98.31	29.87	104949	96.01
5 min	SYTO 9	43.37	19.09	218556	-8.59
	PI	6.15	7.79	218089	13.03
	CV	96.01	24.36	104619	-6.02
15 min	SYTO 9	41.66	12.11	221370	-21.20
	PI	8.28	14.92	222312	66.67
	CV	60.48	41.19	104949	-21.03

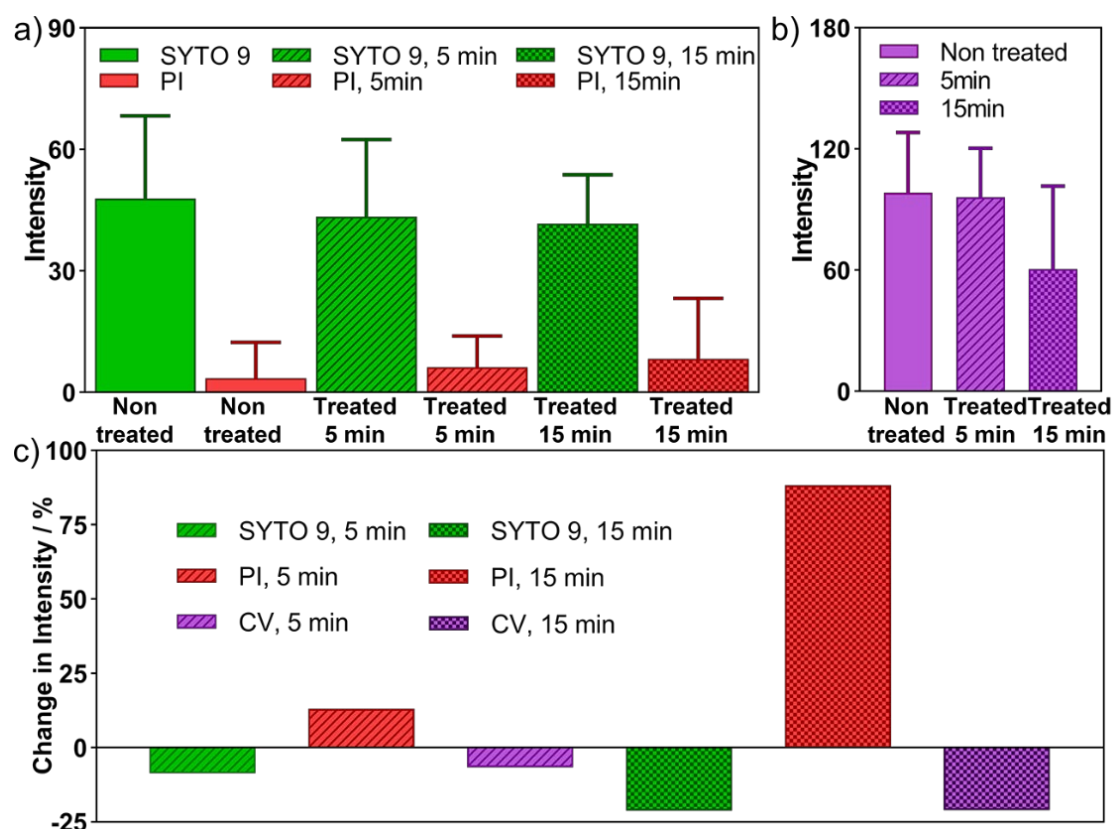


Fig.6.9 Analysis of intensity from live/dead co-staining and biomass staining of *E. coli* biofilm with SYTO 9/ PI and CV. (a) Bar plot of mean \pm standard deviation of the intensity of images in **Fig.6.8a,b** calculated by ImageJ. (b) Bar plot of mean \pm standard deviation of the intensity of images in **Fig.6.8d** calculated by ImageJ. (c) Percentage of intensity changes compared to non-treated samples after different time of sodium azide incubation.

The statistical analysis of the results from live/ dead fluorescence microscopy and SECM shows that the SECM readout is more sensitive for detecting the harsh effect of azide treatment than PI staining, which didn't show a significant impact in a short time. PI is a membrane-impermeable dye generally used to distinguish the intact from damaged cells. Sodium azide has the main inhibitory effect on the respiratory chain, and from the investigations herein, it is more readable by the feedback mode of SECM. Furthermore, as the results in chapter 5 show, Soft-Probe-SECM appears to be sensitive to surface reactivity. Therefore, even though washing the antimicrobial agents has a minor effect on biomass, it does not interfere with the SECM results. Furthermore, washing steps in the staining protocols leads to the removal of biomass, which has prominent external effects on the intensity of the images after treatments. As this result shows, just after 15 min, the biomass decreased about 21% after sodium azide treatment and washing steps. Also, SECM could be recorded right after

treating the biofilm and washing away sodium azide since it does not need any treatment; however, for CLSM, sample preparation and staining steps are required.

6.3.3 SECM investigation of biofilm degradation by silver nanoparticles

Silver nanoparticles (AgNPs) are widely used as antimicrobial agents [372]. The antibacterial activity of AgNPs is mainly associated with the generation of silver ions (**Fig.6.10a**). For instance, Ag(I) ions can interact with Thiol groups on the cell surface, leading to the collapse of proton motive force collapse and eventually cell death [373]. Ag(I) ions (ionic radius of 0.115 nm) [372] pass through porin channels (pore size, 1-3 nm) [372]. They can bind to membrane-bound enzymes and proteins containing thiol groups [374], interfere with DNA replication and deactivate many enzymatic functions [372]. Ag(I) ions further increase the level of reactive oxygen species (ROS) inside the cell [375]. Moreover, AgNPs can mechanically create pores in the outer membrane inducing physical damages to the bacterial cells. The mechanism of action of silver is linked with its interaction with thiol group compounds found in the respiratory enzymes of bacterial cells. Silver binds to the bacterial cell wall, cell membrane and inhibits the respiration process [376]. In the case of *E. coli*, silver acts by inhibiting phosphate uptake and releasing phosphate, mannitol, succinate, proline, and glutamine from *E. coli* cells [377]. The nanoparticles preferably attack the respiratory chain, cell division finally leading to cell death. Our study also suggests a similar mechanism of action in the case of silver nanoparticles as they penetrate the cell wall forming pits and thus causing cell death. Herein, three different silver nanoparticles were synthesized. Citrate capped AgNPs and Ag/PVP nanocomposites capped by PVP in water and ethylene glycol were successfully synthesized using a solution chemistry method (**Fig.6.10b**). UV/Vis absorption spectra of AgNPs are shown in **Fig.6.10(c,d,e)**. The maximum absorption of the studied nanocomposites was found at 438 nm, 435 nm, and 445 nm for citrate capped AgNPs, PVP capped AgNPs in water and, PVP capped AgNPs in EG, respectively [236, 237]. It has been reported that the absorption spectrum of spherical silver nanoparticles shows a maximum between 420 nm and 450 nm with a blue or red shift when particles size diminishes or increases, respectively. Due to this reason, the nanocomposites synthesized in ethylene glycol show a plasmon, which is red shifted. AgNP size distributions determined by dynamic light scattering (DLS) are included in **Fig.6.10(f,g,h)**. AgNPs showed a single peak of hydrodynamic diameter distribution with the average peak in the number weighted distribution at (23 ± 4) nm, (8 ± 2) nm, and (4 ± 1) nm

for citrate capped AgNP, PVP capped AgNP in water and EG. The obtained single peaks indicating the homogeneity of particles size.

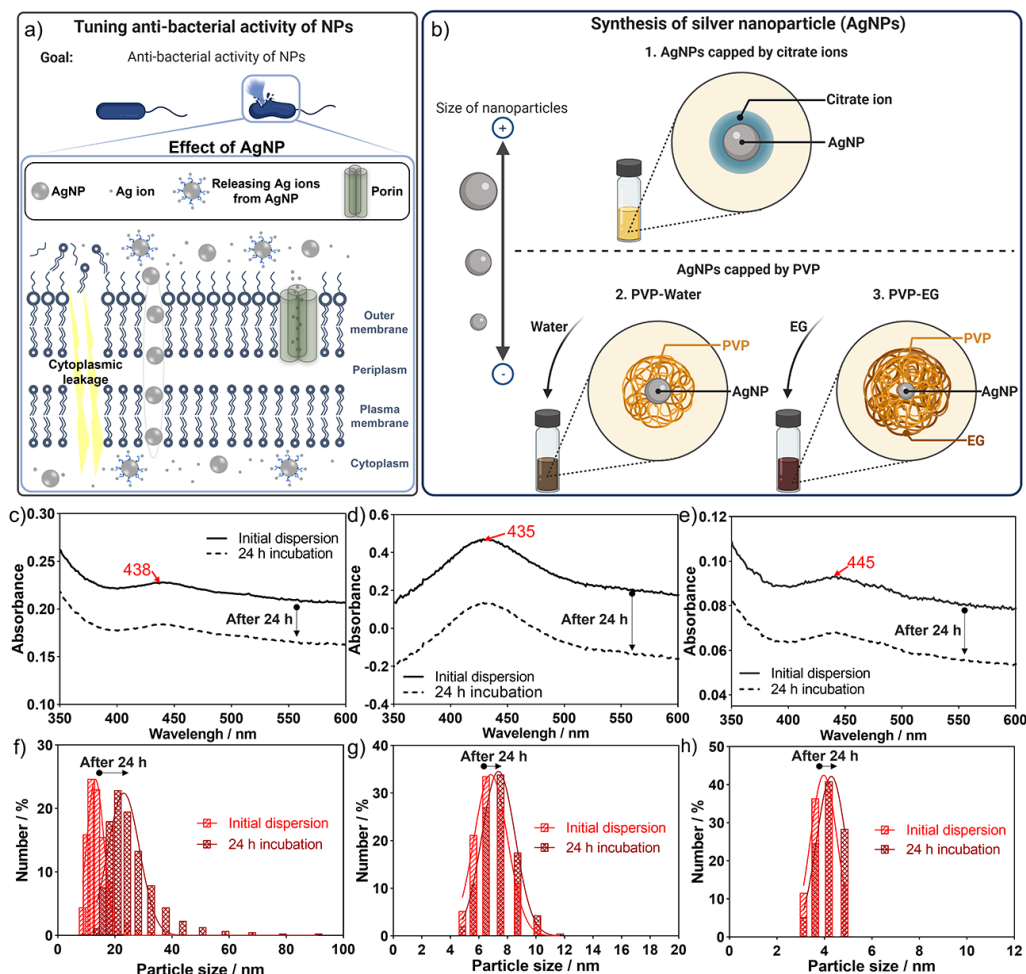


Fig.6.10 Treating biofilm with AgNPs: (a) Schematic representing the effect of AgNPs against *E.coli*. (b) Synthesis of different AgNPs. UV-Vis spectra of (c) AgNPs capped with citrate, PVP capped AgNPs in (d) water, and EG just after and 24 hr after synthesis. Dynamic light scattering results of (f) citrate capped AgNPs, PVP capped AgNPs in water (g), and EG (h) based on the percentage of the count of number distribution.

Further intensity-weighted distributions are shown in **Fig6.11**. The difference between intensity- and number-weighted distribution indicates that the initial suspension contained a fraction of aggregate particles that could not be thoroughly dispersed [378].

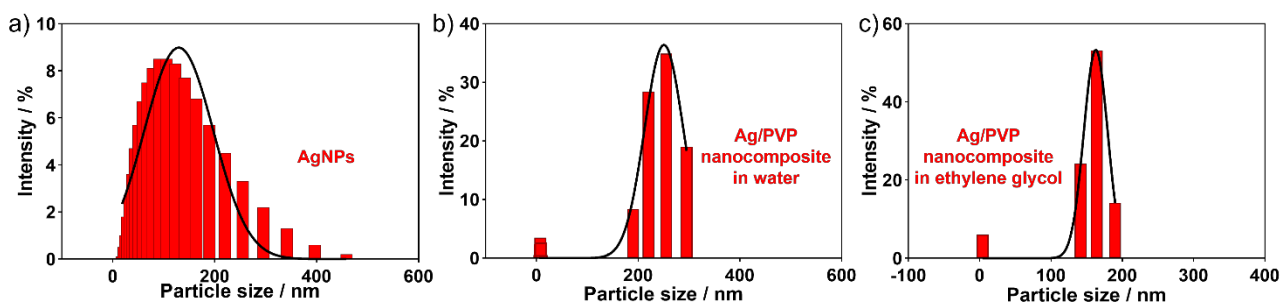


Fig.6.11 Dynamic light scattering results of (a) citrate capped AgNPs, PVP capped AgNPs in water (b), and EG (c) based on the percentage of the count of the intensity distribution.

The biofilm was incubated for 24 hr in AgNP suspension. Therefore, the DLS and UV-Vis were also performed after 24hr (without dispersion and ultrasonication to simulate biofilm incubation over 24 h

in a static environment). The peaks of the UV-Vis spectra of AgNPs after 24 h incubation were shifted to lower absorbance in **Fig.6.10(c-e)**. The absorbance decreases with increasing size for larger particle sizes due to the reduction of particle concentration [379]. The same effect has been shown in the DLS spectra. As shown in **Fig.6.10(f-h)**, after 24 h incubation, the peak of the number weighted hydrodynamic diameter shifted to the larger particle size, indicating substantial aggregation of primary particles. Citrate capped AgNPs had shown a higher shift of the peak, indicating PVP capped AgNPs have aggregated less. The PVP-capped AgNPs maintained their stability when incubated for 24 h, as indicated by stable DLS size distribution. Therefore, the important observation is that in contrast to citrate capped AgNPs, after 24 h, PVP capped AgNPs remain suspended, and these suspended particles are mostly unaggregated.

For SECM analysis, an *E. coli* biofilm was grown for one day on a coverslip and then partially covered with AgNPs for one additional day. Biofilms were exposed for one day to $0.1 \mu\text{g}\cdot\text{mL}^{-1}$ AgNP suspension, the minimum inhibitory concentration of The AgNP suspension for *E.coli* biofilm [380], and $1 \mu\text{g}\cdot\text{mL}^{-1}$ AgNO_3 , 10 fold of MIC. The MIC of The AgNP suspension for biofilm is about 10 times higher than the MIC of planktonic bacteria due to the known enhanced resistance of the biofilm against antimicrobial reagents [380]. The AgNP suspension ($0.1 \mu\text{g}\cdot\text{mL}^{-1}$ and $1 \mu\text{g}\cdot\text{mL}^{-1}$ of AgNPs, 10 μL) was dropped carefully on a small sample region only. This region appeared greyish and was therefore easy to locate by the naked eye. After the treatment, the solution and the AgNPs were gently but thoroughly washed away from the biofilm. Soft-Probe-SECM feedback z-line scanning (approach curves) of the treated and non-treated areas were performed for all three different AgNPs

and for the two concentrations of AgNO_3 (MIC and $10\times\text{MIC}$) in triplicate with $250\text{ }\mu\text{m}$ lateral distance and is shown in **Fig.6.12**.

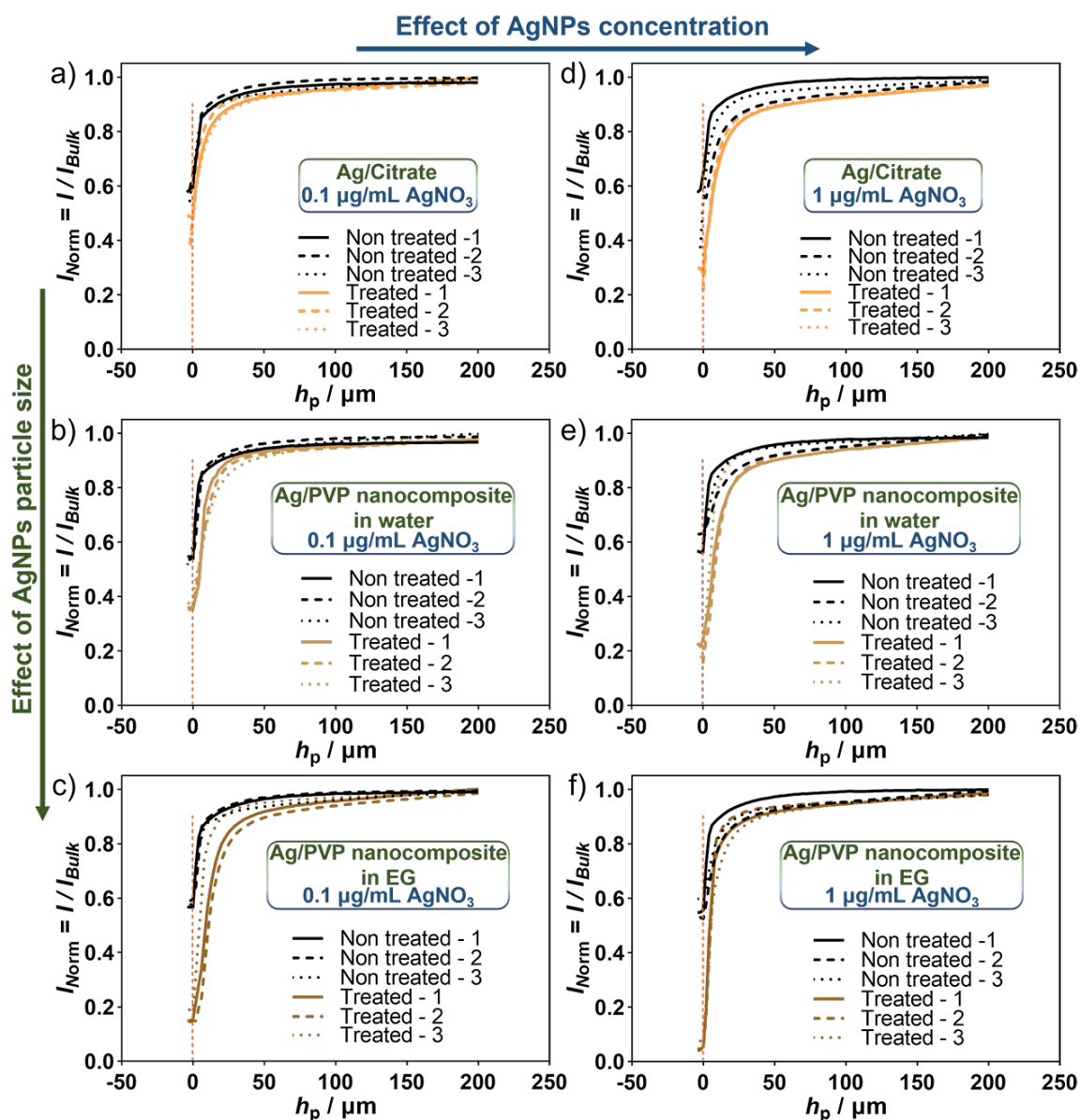


Fig.6.12 Soft-Probe-SECM approach curves for the detection of the effect of AgNP on *E. coli* biofilm on a glass coverslip: Treating one day old *E. coli* biofilm with $0.1\text{ }\mu\text{g/mL}$ AgNO_3 (a, b, c) and $1\text{ }\mu\text{g/mL}$ AgNO_3 (d, e, f). (a) and (d) *E. coli* biofilms were treated with citrate capped AgNPs. (b) and (e) *E. coli* biofilms were treated with PVP capped AgNPs in water. (c) and (f) *E. coli* biofilm were treated with PVP capped AgNPs in EG. For each experiment, three different samples were evaluated. Experimental details for SECM approach curves: working potential $E_T = 0.5\text{ V}$, probe translation speed = $5\text{ }\mu\text{m/s}$, step size = $2\text{ }\mu\text{m}$, 2.5 mM FcMeOH in 100 mM PBS (pH 7.4).

Table 6.10 includes the normalized currents when the soft probe contacted the sample surface. The average of the normalized SECM currents is indicated in **Table 6.11**.

Table 6.10 Details of SECM z-line scan data at the approached point of **Fig.6.12**.

Concentration of AgNO ₃ / μg/mL	Treatment	AgNPs	Repitition	$I_{\text{Norm}} = I/I_{\text{Bulk}}$
0.1	Non treated	AgNPs/Citrate	1	0.59
			2	0.64
			3	0.64
		AgNPs/PVP/Water	1	0.55
			2	0.54
			3	0.59
		AgNPs/PVP/EG	1	0.57
			2	0.60
			3	0.58
	Treated	AgNPs/Citrate	1	0.48
			2	0.48
			3	0.46
		AgNPs/PVP/Water	1	0.36
			2	0.37
			3	0.39
		AgNPs/PVP/EG	1	0.16
			2	0.15
			3	0.19
1	Non treated	AgNPs/Citrate	1	0.65
			2	0.54
			3	0.55
		AgNPs/PVP/Water	1	0.56
			2	0.63
			3	0.59
		AgNPs/PVP/EG	1	0.56
			2	0.52
			3	0.60
	Treated	AgNPs/Citrate	1	0.28
			2	0.22
			3	0.26
		AgNPs/PVP/Water	1	0.24
			2	0.16
			3	0.18
		AgNPs/PVP/EG	1	0.05
			2	0.05
			3	0.06

Table 6.11 Details of the average of SECM z-line scan data at the approached point of **Table 6.7**. *N* = sample number.

Concentration of AgNO ₃ / µg/mL	Treatment	AgNPs	Average of $I_{\text{Norm}} = I/I_{\text{Bulk}}$
0.1	Non treated	AgNPs/Citrate	(0.62 ± 0.02) (<i>N</i> = 3)
		AgNPs/PVP in water	(0.56 ± 0.02) (<i>N</i> = 3)
		AgNPs/PVP in EG	(0.58 ± 0.01) (<i>N</i> = 3)
	Treated	AgNPs/Citrate	(0.47 ± 0.01) (<i>N</i> = 3)
		AgNPs/PVP in water	(0.37 ± 0.01) (<i>N</i> = 3)
		AgNPs/PVP in EG	(0.16 ± 0.01) (<i>N</i> = 3)
1	Non treated	AgNPs/Citrate	(0.58 ± 0.05) (<i>N</i> = 3)
		AgNPs/PVP in water	(0.60 ± 0.02) (<i>N</i> = 3)
		AgNPs/PVP in EG	(0.56 ± 0.03) (<i>N</i> = 3)
	Treated	AgNPs/Citrate	(0.25 ± 0.03) (<i>N</i> = 3)
		AgNPs/PVP in water	(0.19 ± 0.04) (<i>N</i> = 3)
		AgNPs/PVP in EG	(0.06 ± 0.005) (<i>N</i> = 3)

The feedback current decreased about 24 %, 32%, and 72% for 0.1 µg·mL⁻¹ of AgNPs and 55%, 68%, and 90% for 1 µg·mL⁻¹ of AgNPs of citrate capped AgNPs, PVP capped AgNPs in water and EG, respectively (**Fig.6.13**). SECM results show that treated biofilms with Ag⁺ have lower feedback currents. This means that Ag⁺ treatment could damage the respiratory chain. Despite the effect of AgNPs on the electron transport chain, it has different effects, *e.g.*, disruption of the cell membrane, inactivation of proteins/enzymes, *etc.* This leads to reducing biofilm activity, specifically the respiratory of the bacterial cells in the biofilm, which affects the feedback current recorded by SECM. EPS could act as a barrier for antimicrobial transport into the biofilm and play a role in biofilm's extraordinary antimicrobial tolerance [381]. Transport hindrance in hydrogels becomes significant and increasingly severe for several nanometers or larger [382]. The relatively large sizes of AgNPs and especially their aggregates suggest that transport hindrance could play a role in biofilm tolerance. As a result shows, the PVP capped AgNPs in EG show a prominent inhibitory effect with a clear dropping of the feedback SECM current. Compared with PVP capped AgNPs in water, it has almost twice the effect. This could come from two reasons. First, PVP-capped AgNPs in EG is small enough to pass through porin channels and has significant inhibitory effects. Second, the capping agents could decrease the interaction of AgNPs with the outer membrane. Therefore, PVP for the larger AgNPs could behave as a barrier and decrease the interaction while they are located outside of bacteria cells [378]. Hindered nanoparticle diffusion in biofilms has been demonstrated by Peulen and Wilkinson [383]. They observed negligible diffusion of carboxylated polymer nanoparticles with

diameters greater than 50 nm in laboratory grown *P. fluorescens* biofilms with a reported thickness of less than 30 μm .

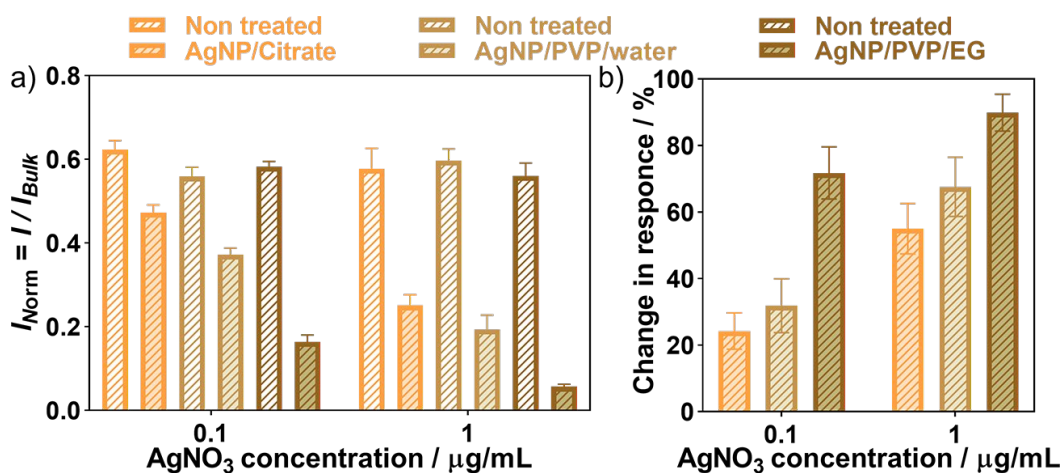


Fig.6.13 (a) Mean \pm standard deviation of the normalized SECM current when the soft probe contacted the biofilm surface during approach curves shown in Fig.6.12. (b) Relative changes of the current response in respect to the non-treated sample.

In another study, Bard and co-workers [339] discussed the interaction of Ag⁺ with the enzymes of the respiratory chain of *E. coli*. The authors suggested an inhibitory effect of Ag⁺ at a low potential point, possibly NADH dehydrogenase. Ferricyanide was used as an alternative electron acceptor to oxygen so that the reduction of ferricyanide to ferrocyanide by the respiration of *E. coli* was electrochemically followed. Ferricyanide is a hydrophilic molecule that doesn't pass the outer membrane to reach the plasma membrane. Therefore, the authors suggested the interaction of ferricyanide with a membrane-spanning protein, such as complex I or III, at some point in the periplasmic space, outside the cytoplasmic membrane [384].

Furthermore, the live/dead and biomass staining have been investigated as complementary detection. PVP capped AgNPs in EG (1 $\mu\text{g}\cdot\text{mL}^{-1}$ of AgNPs) were considered for biofilm treatment. **Fig.6.14** shows the fluorescence images of two-day-old biofilm, including one day of growth in the solution with AgNPs, and details of the intensity of figures, which were measured by ImageJ and were written in **Table 6.12**. The control was one-day-old biofilms (the same biofilm before treatment) without exposure to the AgNPs solution demonstrating the bacterial cells' viability embedded in the non-treated biofilm (**Fig.6.14(a-d)**). As seen from the live/dead stained fluorescence images and biomass staining, most bacteria died and the intensity of PI staining increased by 90%. Furthermore, the biomass also decreased by about 57%, indicating the silver treatments also lead to the biofilm eradication. As reported in chapter 5, the surface reactivity is most likely recorded. The recorded result of SECM and CLSM were quite the same, in contrast to the azide treatment discussed above. SECM showed a 90% reduction of feedback current, and CLSM showed a 90% increase of the PI intensity. However, SECM approach curves are much faster than recording CLSM images. In this

study, each approach curve took 50 sec; however, each CLSM image took more than 45 minutes since the biofilm is about 12 μm thick and z-stacking imaging takes a long time.

Table 6.12 Details about quantification intensity data of Fig.6.14.

Stain	Non treated			AgNPs			Changes / %
	Mean	Standard deviation	Area	Mean	Standard deviation	Area	
SYTO 9	47.69	19.81	212517	39.10	17.45	218085	-15
PI	2.908	1.87	212517	24.70	24.36	218085	90
CV	89.65	15.60	213443	18.51	26.22	213443	-57

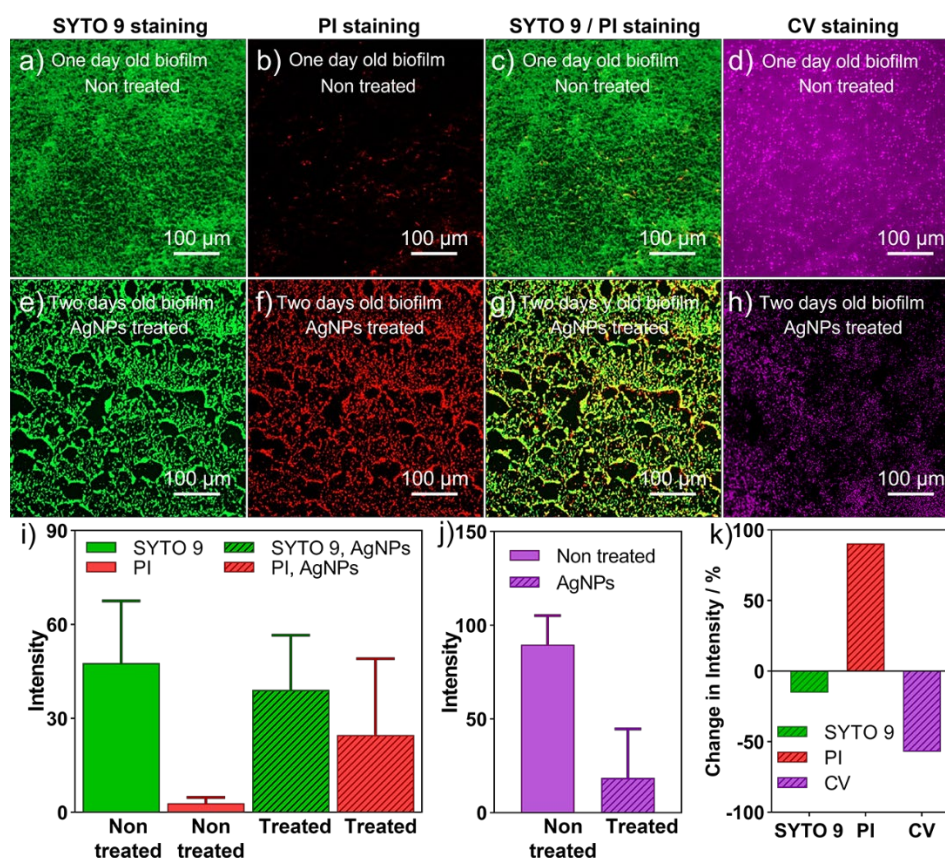


Fig.6.14 Fluorescence images of co-live/dead staining of SYTO 9/PI and biomass staining of biofilm with CV. One day old biofilm was treated for one day with 1 $\mu\text{g/mL}$ AgNO_3 , which was synthesized with PVP capped AgNPs in EG. (a) SYTO 9, (b) PI, (c) overlap of SYTO 9/PI, and (d) CV staining of non-treated sample. (e) SYTO 9, (f) PI, (g) overlap of SYTO 9/PI, and (h) CV staining of a treated sample after one-day incubation of one-day old *E.coli* biofilm in AgNPs. (i) Mean intensity \pm standard deviation of the live/dead fluorescence image intensity was obtained from ImageJ for the non-treated and treated *E.coli* biofilm. (j) Mean intensity \pm standard deviation of the intensity of CV fluorescence images was obtained from ImageJ for the non-treated and treated biofilm. (k) Changes in intensity of the treated sample in comparison to the non-treated sample.

6.3.4 SECM investigation of biofilm treatment by flashlight

Lastly, the *E. coli* biofilm was treated by flashlight irradiation. The method uses a high-intensity Xe flash lamp whose emission contains UV and white light (wavelengths from 200 nm to 1500 nm). As bacterial cells are prone to damage when they are exposed to UV light, rapid flashes might be used to disinfect environmental (water pipes) or clinical surfaces (operation equipment). The intensity of the flashlight is relatively high reaching several J/cm^2 in a single flash. Flashlight is an eco-friendly

method, which has mostly been used in the laboratory of this thesis to synthesize uniformly-sized single and alloyed nanoparticles by photochemical reduction from precursor solutions with good control over precursor composition and particle size/loading. The flashlight irradiation technique is conducted at room temperature and air, thus under ambient conditions [385-387]. Herein, a one-day-old *E. coli* biofilm was treated with flashlight irradiation applying 550 V for charging the lamp driving capacitors for different numbers of shots, *i.e.*, one, three, and five. **Fig.6.15** shows the SECM feedback response of the flash-light treated biofilms. **Table 6.13** and **Table 6.14** indicate the details of the SECM currents at the contact point between the soft probe and the biofilm surface

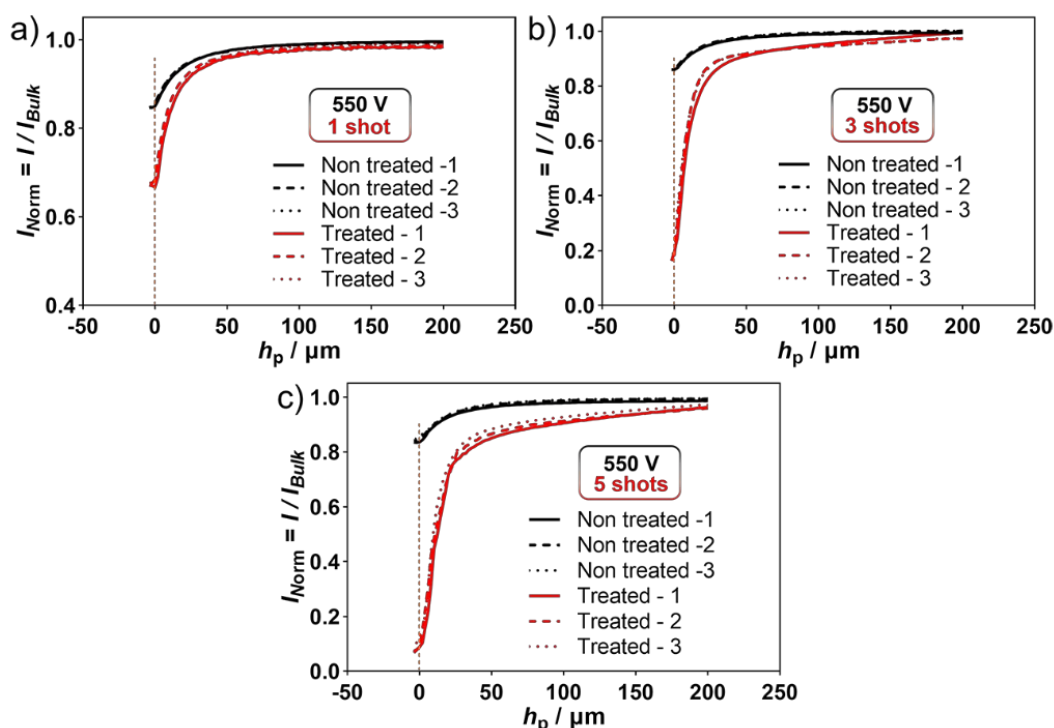


Fig.6.15 Soft-Probe-SECM approach curves of detection of the effect flash light on *E. coli* biofilm on the coverslip: Treating one day old *E. coli* biofilm with (a) 550 V, 1 shot, (a) 550 V, 3 shots, (a) 550 V, 5 shots of the flash light. Experimental details for approach curve SECM scans: working potential $E_T = 0.5$ V, probe translation speed = 5 $\mu\text{m/s}$, step size = 2 μm , 2.5 mM FcMeOH in 100 mM PBS (pH 7.4).

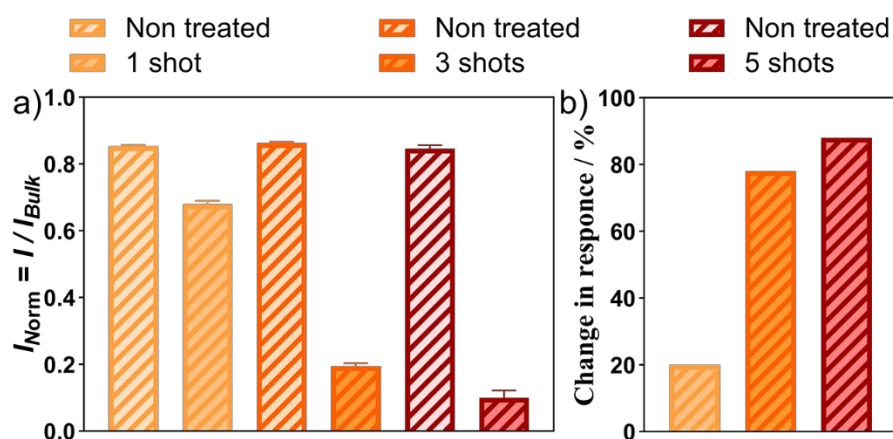
Table 6.13 Details of SECM z-line scan data at the approached point of Fig.6.15.

Treatment	Flashlight	Repetition	$I_{\text{Norm}} = I/I_{\text{Bulk}}$
550 V, 1 shot	Non treated	1	0.85
		2	0.86
		3	0.85
	Treated	1	0.67
		2	0.68
		3	0.68
550 V, 3 shots	Non treated	1	0.86
		2	0.87
		3	0.86
	Treated	1	0.20
		2	0.18
		3	0.21
550 V, 5 shots	Non treated	1	0.84
		2	0.85
		3	0.86
	Treated	1	0.09
		2	0.08
		3	0.12

Table 6.14 Details of the average of SECM z-line scan data at the approached point of Table 6.13.

Treatment	$I_{\text{Norm}} = I/I_{\text{Bulk}}$
550 V, 1 shot	Non treated
	Treated
550 V, 3 shots	Non treated
	Treated
550 V, 5 shots	Non treated
	Treated

As indicated in Fig.6.16 the current decreased by 20%, 78%, and 88% after treating the biofilm with the 550 V flashlight irradiation in one, three, and five shots.

**Fig.6.16** (a) Mean \pm standard deviation of SECM approach curve of Fig.6.15. (b) Changes in response in respect to the non-treated sample.

Complementary detection has been performed based on Co-SYTO 9/ PI staining (**Fig.6.17**). As illustrated, the flash light treatment killed the bacteria, but it also partially removed the biofilm, leading to biofilm eradication. The details of each fluorescence image has each fluorescence image's intensity has been assessed by ImageJ and are indicated in **Table 6.15**.

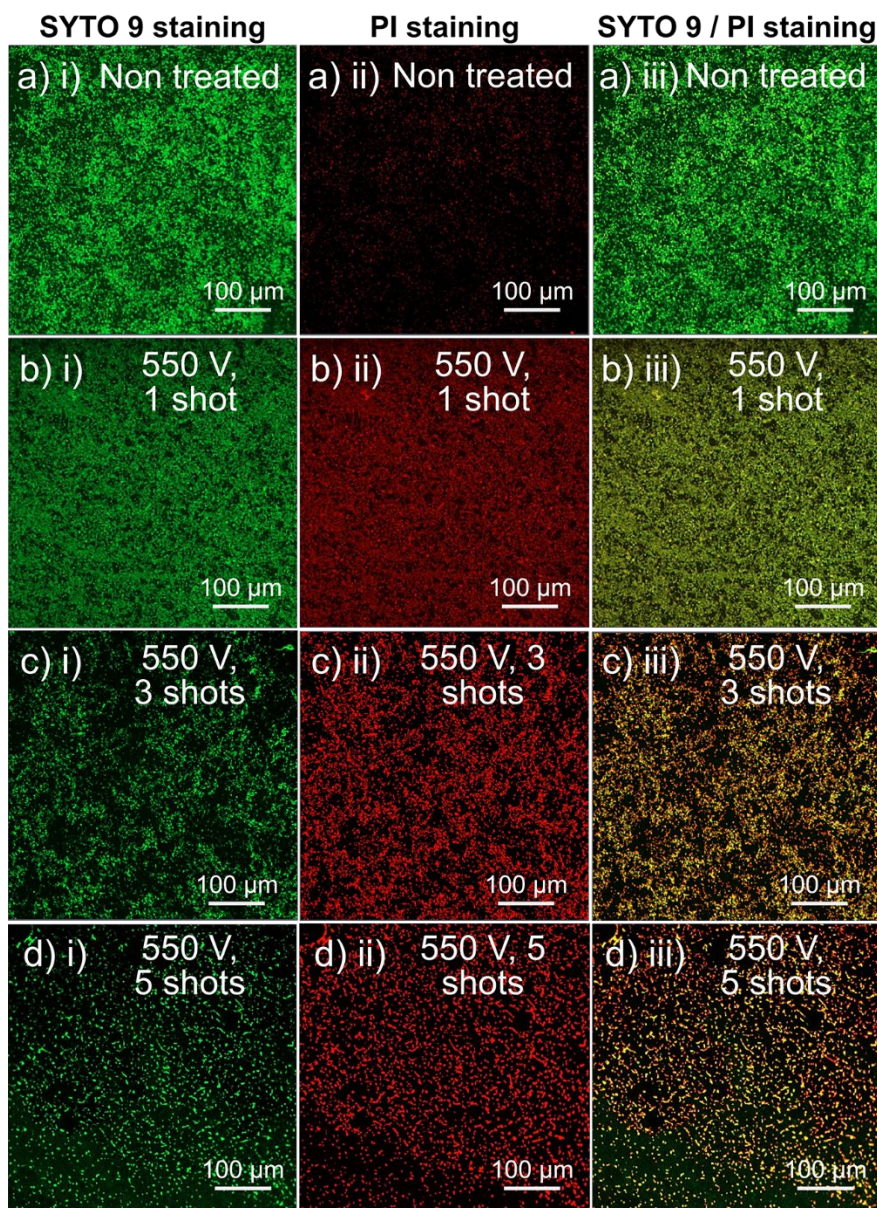


Fig.6.17 Fluorescence images of co-live/dead staining of SYTO 9/PI. (a) Non-treated sample. One day old biofilm was treated by flashlight in 550 V with one (b), three (c), and five shots (d). (i) SYTO 9 staining, (ii) PI staining, and (iii) co SYTO 9/PI staining.

Table 6.15 Details about quantification intensity data of **Fig.6.17**.

Stain	SYTO 9				PI			
	Mean	Standard deviation	Area	Changes / %	Mean	Standard deviation	Area	Changes / %
Non treated	46.52	31.50	429016	-	6.67	11.90	429016	-
1 shot	35.56	17.66	429016	-32	27.58	11.80	429016	+21
3 shots	21.52	19.88	429016	-47	11.90	28.26	429016	+63
5 shots	15.83	23.28	429016	-50	18.83	25.78	429016	+79

The intensity of PI staining increased by 21%, 63%, and 79% by treating of the biofilm by 550 V driven flashlight using one, three, and five shots.

Flashlight irradiation is a quick and clean technique for treating biofilm. In a case *in vivo* applications are envisaged, the large portion of UV with high intensity must be considered, and measures must be applied to enable a safe operation for the organs. However, for environmental applications, flashlight treatments of biofilms could be considered a powerful biofilm eradication technique.

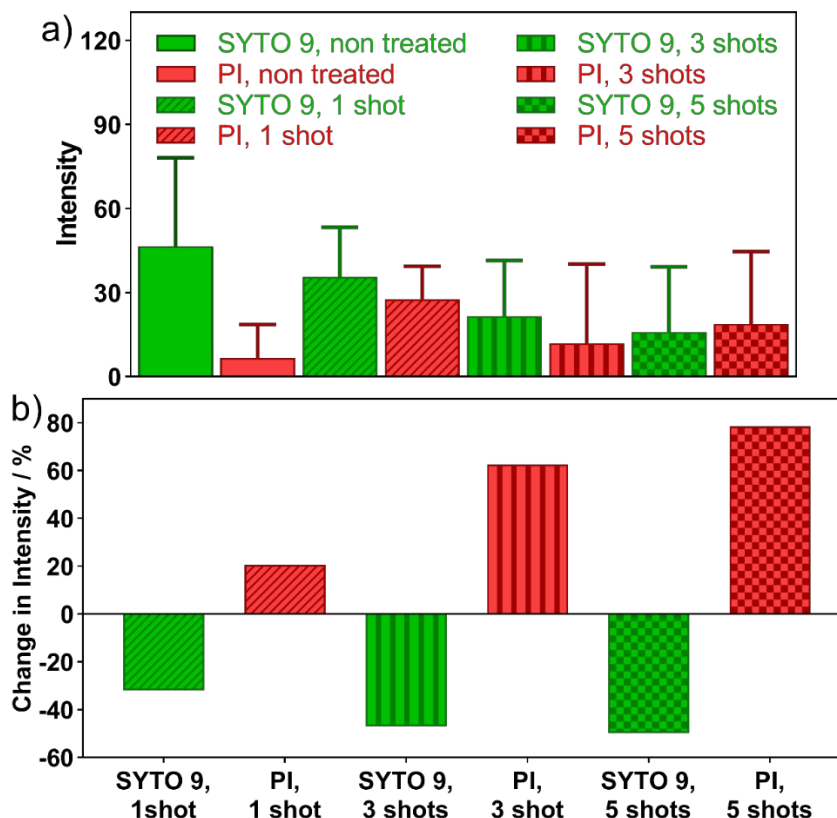


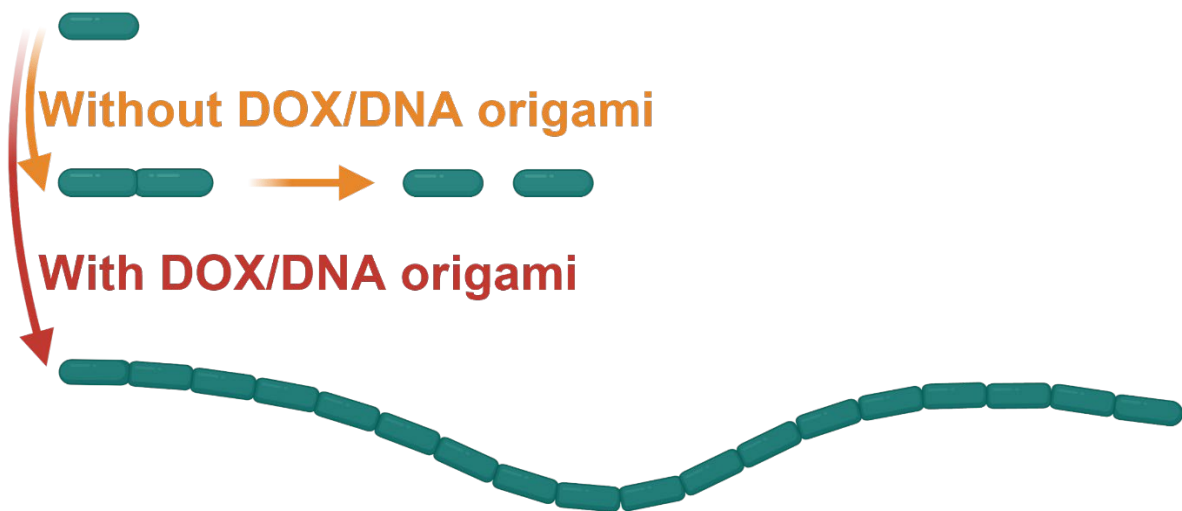
Fig.6.18 (a) Mean intensity \pm standard deviation of the live/dead fluorescence image intensity was obtained from ImageJ for the non-treated and treated *E.coli* biofilm. (b) Changes in intensity of the treated sample in comparison to the non-treated sample.

6.3 Conclusions

To conclude, Soft-Probe-SECM of *E. coli* biofilms treated with different antimicrobial agents and treatments was presented. Antimicrobial agents were sodium azide, which acts as a respiratory chain inhibitor, and silver nanoparticles, disruptive effects on cellular membranes, proteins, and polysaccharides. In addition, biofilms were treated with light flashes generated from a high-intensity Xenon flash lamp. The antimicrobial concentrations were (4 mM sodium azide and $0.1 \mu\text{g}\cdot\text{mL}^{-1}$ AgNO_3 and $1 \mu\text{g}\cdot\text{mL}^{-1}$ AgNO_3), and the change of the biofilm properties was followed depending on the treatment time for sodium azide and size of nanoparticles for silver nanoparticle treatment. The inhibitory effect of these agents on cell viability was confirmed by using live/ dead fluorescence imaging and biomass staining. SYTO 9 intensity indicated that the total number of living and dead bacterial cells remained constant, independent of the applied antimicrobial treatment. PI intensity showed an increasing number of dead bacterial cells with treatment. The SECM feedback mode was

used, and feedback currents decreased after the biofilms were treated with antimicrobial strategies. The feedback current reduction was most likely based on the surface reactivity of treated samples. SECM revealed a change of biofilm activity already after 5 min. Similarly, the feedback SECM current reduction after exposure to AgNPs was significant, suggesting that SECM could record the biocide effects of sodium azide on the electron transfer chain more sensitively than fluorescence at short treatment times. Furthermore, flashlight irradiation was used as a quick technique. The results indicated that this technique is a powerful tool for biofilm eradication. The results demonstrate further that SECM could become a powerful technique for recording various agents' effects with an inhibitory effect at the intracellular level, especially those affecting the respiratory chain. SECM showed to be very sensitive with fast responses compared to the complementary techniques. SECM approach curves were recorded in less than a minute. Furthermore, SECM in the modes applied herein does not acquire any sample pre-treatment as the sensitive marker is a redox mediator in the solution.

CHAPTER 7 Destruction of *E.coli* biofilms with DNA nanostructures loaded Doxorubicin¹



¹ This work has been carried out in collaboration with my Ph.D. group at EPFL and under the supervision of Professor Clemens Kaminski and Dr. Ioanna Mela during my visit to the University of Cambridge in the United Kingdom.

I was awarded a six-month Doc. Mobility Swiss National Science Foundation (SNSF) visiting fellowship for this project at the University of Cambridge.

7.1 Introduction

A first challenge in developing new infection control strategies is developing an antimicrobial or antimicrobial delivery system that allows the antimicrobial to penetrate deeply into a biofilm and kill biofilm-bacteria across the entire biofilm thickness [388, 389]. Many nanotechnology-based drugs and drug-delivery systems have been developed to self-target, penetrate, and eradicate [390-392]. Biofilms and tumors are, on the one hand, very different, yet are both characterized by a low pH environment, allowing self-targeting of pH adaptive, innovative carriers [393]. Also, their clinical treatment poses the same challenges, including preventing resistance and recurrence. Not surprisingly, new strategies for infection control are arising nowadays that are derived from technologies initially designed for tumor treatment. Nanotechnology-derived antimicrobial delivery systems have excellent biocompatibility and can be designed to be environmentally responsive and self-targeting [394-396], provided their diameter is below the limit for reticuloendothelial rejection of around 100–200 nm [397]. However, their antimicrobial efficacy is usually low without suitable functionalizing their outermost surface or drug-loading. The delivery of active compounds to the biofilms is often hindered due to the EPS of biofilm existence and the poor solubility of drugs and antibiotics. A possible strategy to overcome the EPS barrier is incorporating antimicrobial agents into a nanocarrier, penetrating the matrix and delivering the active substance to the cells [398].

As it has been mentioned in Chapters 5 and 6, recently, interest in electrochemical methods for biofilm detection has increased due to the many advantages, such as simplicity, rapidity, label-free, and low-cost detection of biomolecules [399]. It is noteworthy that electrochemical methods can also selectively analyze the electrochemical signals for each target molecule under certain conditions. Among various electrochemical methods, electrochemical impedance spectroscopy (EIS) is appropriate for monitoring bacterial cells since the electrochemical signals caused by the bacterial cells can be collected without damaging the cells or changing the environment. The difference in the electrochemical phenomenon can be measured over a wide frequency range. Targeted signals are also recorded at a fixed frequency [400]. The adoption of microelectrode array (MEA) technology in different fields has played a pivotal role in supporting the biological studies of electrogenic tissues both *in vivo* and *in vitro* [401-405]. Compared to patch-clamp or microwire electrodes, the greater flexibility of MEAs in their design and use has made them the preferred option for studying large cell populations. MEAs can record both low and high-frequency signals arising from the fluctuation of ions across cell membranes. For *in vitro* applications, metal microelectrodes patterned on glass are extensively used to interface with cell cultures and tissue slices for drug screening and toxicology studies [401]. A recent trend in the field involves the use of conducting polymer electrodes. Materials such as poly(3,4-ethylenedioxythiophene) doped with polystyrene sulfonate (PEDOT: PSS) have been successfully employed for the recording of neural activity *in vivo* [406-408] and *in vitro* [409-412]. PEDOT: PSS is a mixed electronic/ionic conductor with a capacitance that depends on the volume rather than the area of the film [413]. Consequently, PEDOT: PSS electrodes have a

significantly lower impedance than Pt and Au electrodes, which are limited by the capacitance of the electrochemical double layer formed at the metal/electrolyte interface. Their lower equivalent resistance in an electrolyte reduces thermal noise, a significant noise source in electrical recordings [414]. As a result, PEDOT: PSS electrodes lead to recordings with a high signal-to-noise ratio (SNR) and to effective neural stimulation [406, 409, 415] while being biocompatible and promoting neuron attachment and growth [416]. Furthermore, they show low impedance in a physiological environment, which derives from high electrical conductivity and high surface-to-volume ratio, consequently reducing their impedance signal [417]. Conducting polymers show several advantages over their inorganic counterparts, most importantly 1) ease of processability by simple wet deposition methods, such as spin-coating and screen printing, at low temperature; and 2) the ability to tune material properties through chemical synthesis and modifications [418-420]. Overall, the integration of these micro- and/or nanofabricated devices with biorecognition elements yields multiplexed, compact, high-throughput analysis allowing simultaneous detection of multiple bacteria or bacterial analytes.

In this chapter, novel antibiofilm agents in the form of antimicrobial carriers have been developed to treat *E.coli* biofilms and analyze electrochemically the treatment effect. The project had, therefore, two main goals. First, antibiofilm agents was to be made with high selectivity and efficiency for attacking the biofilm. The antibiofilm agent can pass through the extracellular polymeric matrix of the biofilm and penetrate through the biofilm. The novel materials were developed based on DNA nanotechnology, in which the drug doxorubicin (DOX) was loaded to DNA origami. Second, an electrochemical device was used for the complementary analysis to follow the impact of the treatment with the newly developed drug carrier (**Fig.7.1**).

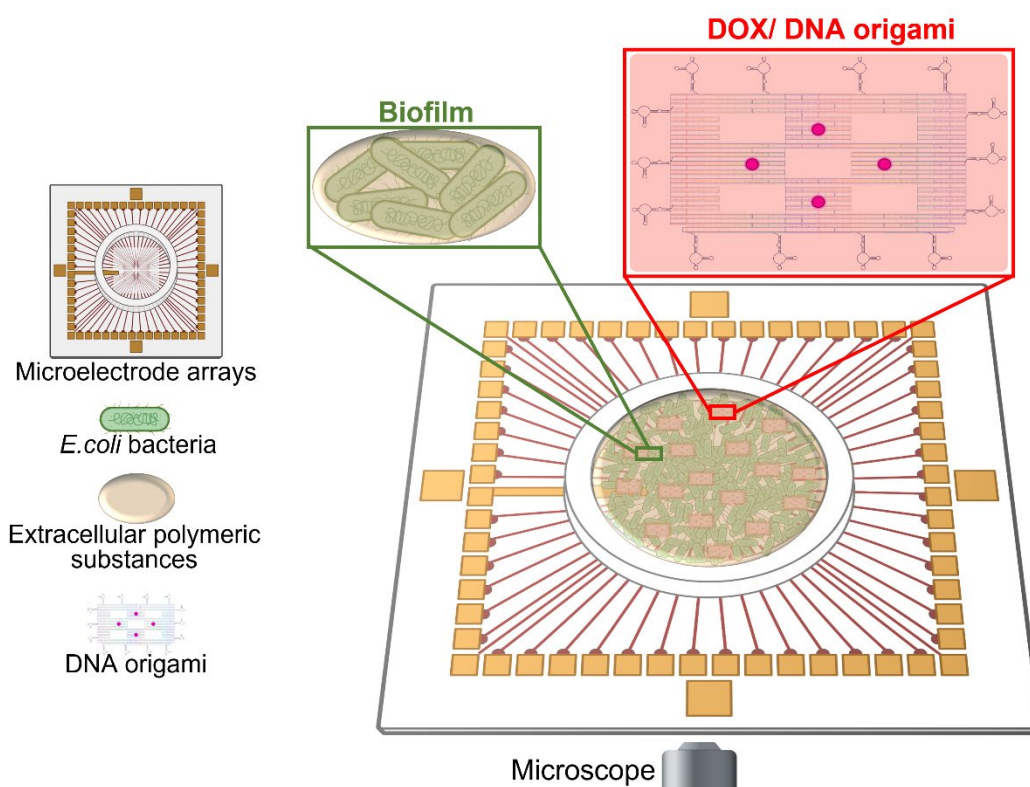


Figure.7.1 Complementary analysis of the effect of antibiofilm treatment based on DNA origami loaded with DOX using confocal laser scanning microscopy and electrochemical readout.

7.2 Results and discussion

7.2.1 Doxorubicin loaded DNA origami

DNA origami design was based on the work of Yoshidome *et al.* [238] and DNA origami functionalities were based on the research of Mela *et al.* [239]. The designs incorporated two functionalities: Alexa-Fluor 647 for fluorescence analysis and aptamers targeting specifically *E. coli* cells [240] (**Fig.7.2**). **Fig.7.2a** shows the structure of DNA origami was used in this study schematically and the AFM image (**Fig.7.2b**) shows the structure of the DNA origami. The DNA origami was 100 nm long and contained four open wells. Due to the DNA origami design, doxorubicin (DOX) was noncovalently intercalated into these nanostructures (**Fig.7.2c**). DOX, one of the most effective cytotoxic drugs, has been widely used in chemotherapy regimens against various cancers [421], but it is also an antimicrobial agent. Previously, it has been reported that two origami shapes were used to load doxorubicin through intercalation [422], and the nanostructural morphology of DNA origami was retained after DOX intercalation [423].

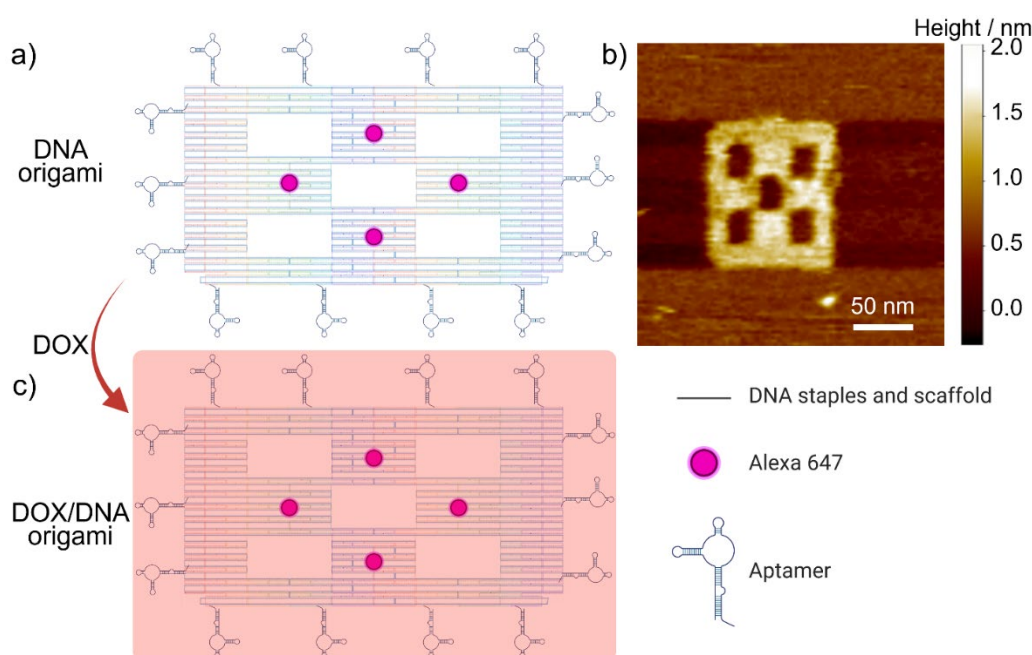


Figure.7.2 DOX/DNA origami: (a) Schematic representation of a DNA origami structure was used in this study. (b) AFM of the DNA origami. (c) Schematic representing DOX loading to the DNA origami structure (DOX/DNA origami).

DOX binds to the bacteria and inhibits FtsZ proteins, a structural protein involved in bacterial cell division. FtsZ assembles into a ring at the future site of bacterial cell division, and when inhibited, cell division does not happen. As a result, DOX-treated *E.coli* cells grow as filaments due to the inability of the daughter cells to separate one from another [424] (**Fig.7.3**).

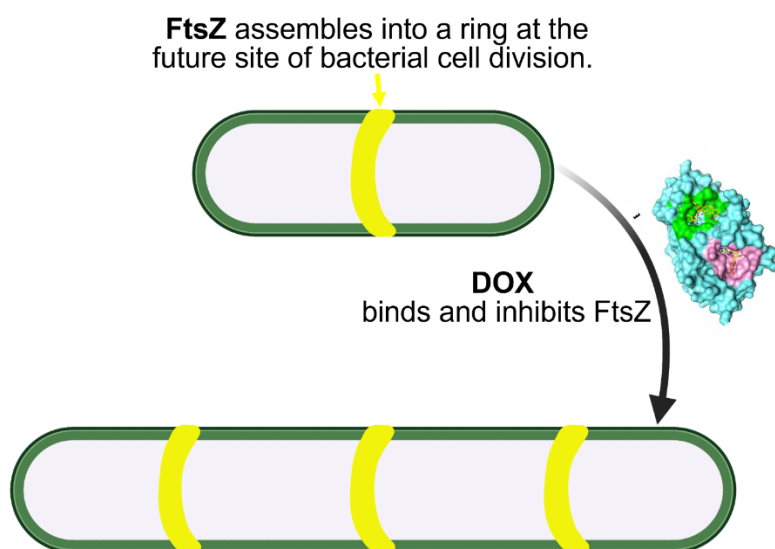


Figure.7.3 Schematic illustration of the inhibitory mechanism of the DOX against *E.coli* bacteria cell division.

The DOX loading process depends on the temperature and concentration of the drug. Therefore, different mixtures of different concentrations of DOX (20 μM , 40 μM , and 60 μM) and DNA origami at two temperatures (23 $^{\circ}\text{C}$ and 37 $^{\circ}\text{C}$) were shaken up to 60 h in 100 rpm to evaluate the drug loading efficiency. Loading efficiency was calculated by measuring the absorption of doxorubicin at 480 nm using UV/Vis spectroscopy. The doxorubicin loading content and efficiency of loading into the DNA nanocarriers were calculated based on Equations 7.1 and 7.2.

Loading content of DOX = Initial content of DOX – Unloaded DOX in the supernatant

(Equation 7. 1)

$$\text{Loading efficiency} = \frac{\text{Loading content of DOX}}{\text{Initial content of DOX}} \times 100$$

(Equation 7. 2)

As depicted in **Fig 7.4a** and **Fig 7.4b**, DNA loading consistently reached a plateau after about a day. Further, loading at 37 °C showed higher loading efficiency of 68%, 77%, and 86% while the 23 °C showed 35%, 48%, and 69% after 24 h incubation in 20 µM, 40 µM, and 60 µM DOX solutions to 10 nM DNA origami (**Fig 7.4c**).

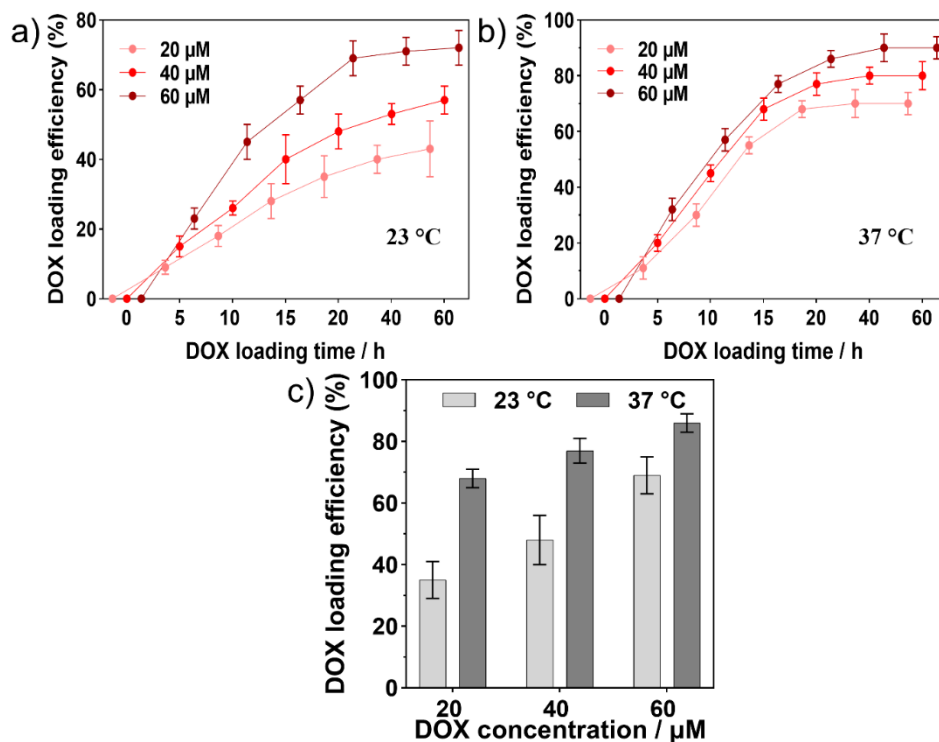


Figure.7.4 Characterization of Doxorubicin (DOX) loading efficiency in DNA origami nanostructures. The drug loading efficiency of DNA origami was analyzed by incubating 10 nM DNA origami with DOX at (a) 25 °C and (b) 37 °C for 5 h, 10 h, 15 h, 20 h, 40 h, and 60 h, respectively, with three different DOX concentrations. The error bar represents the standard deviation of three independent measurements for each group. (c) Bar plot comparison of loading efficiency after 24 h incubation in 25 °C and 37 °C solutions.

The releasing profile of DOX is an important factor since the controlled and efficient release of the antimicrobial agent at a target site is essential for an ideal antimicrobial delivery system. Therefore, the *in vitro* release profiles of DOX-loaded DNA origami was evaluated. Five condition of PBS (pH 7.4), DNA origami (pH 7.2), PBS (pH 5.5), DNase I, and extracellular polymeric matrix were considered with the goal to study conditions that mimic intracellular and physiological conditions. A biofilm has a variable pH based on environmental conditions. DOX-loaded origamis were incubated for 0, 5, 10, 15, 20, 40, and 60 hours at 37 °C and then centrifuged at 10'000 rpm at room temperature for 10 min. After centrifugation, the released doxorubicin in the supernatant was collected and quantified by measuring doxorubicin's absorption (480nm). The results reveal that the DOX release exhibited a one-phase profile based on the Langmuir desorption isotherm (**Fig.7.5**).

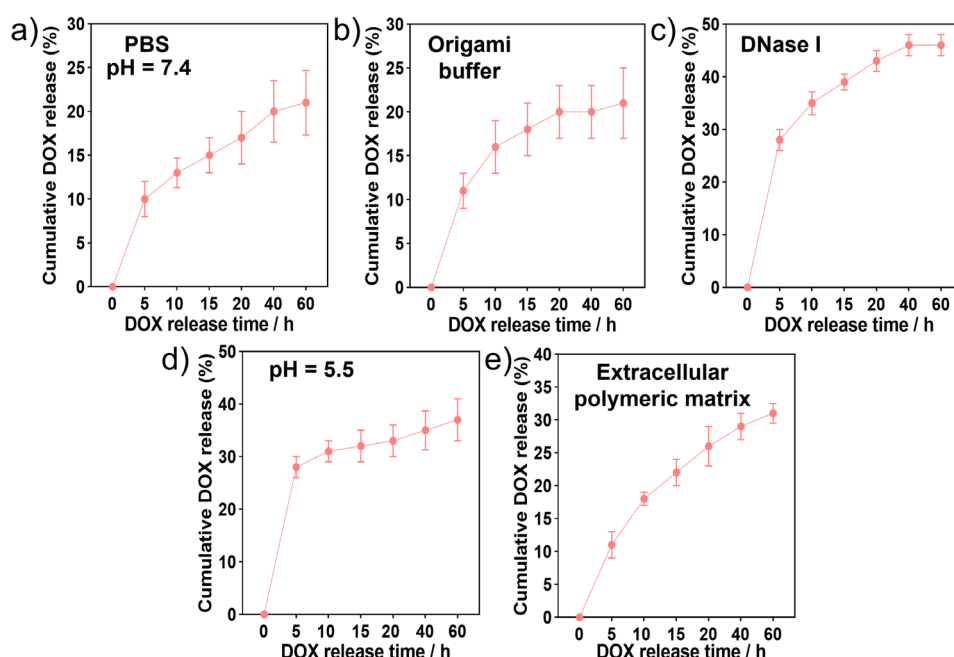


Figure.7.5 *In vitro* release profiles of doxorubicin . DOX release profile from DOX-loaded DNA origami (40 μ M and 24 hr at 37 $^{\circ}$ C) in (a) PBS (pH 7.4), (b) DNA origami, (c) PBS (pH 5.5), (d) DNase I, and (d) extracellular polymeric matrix taking from a one-day old *E. Coli* biofilm.

The experimental data were fitted to the one-phase association equation. This equation describes the pseudo-first-order association kinetics of the interaction between a ligand and its receptor, or a substrate and an enzyme. A certain fraction of the unoccupied receptors could be released during each time interval. But as time advances, fewer receptors are unoccupied, so fewer ligands release and the curve levels off. The model is as in Equation 7.3 and **Fig.7.6**:

$$Y = Y_0 + (\text{Plateau} - Y_0) * (1 - \exp(-K * x)) \quad (\text{Equation 7.3})$$

Y_0 is the Y value when X (time) is zero. It is expressed in the same units as Y,

Plateau is the Y value at infinite times, expressed in the same units as Y.

K is the rate constant, expressed in reciprocal X-axis time units. If X is in minutes, then K is expressed in inverse minutes.

Tau is the time constant, expressed in the same units as the X-axis. It is computed as the reciprocal of K.

Half-time is in the time units of the X-axis. It is computed as $\ln(2)/K$.

Span is the difference between Y_0 and Plateau, expressed in the same units as the Y values.

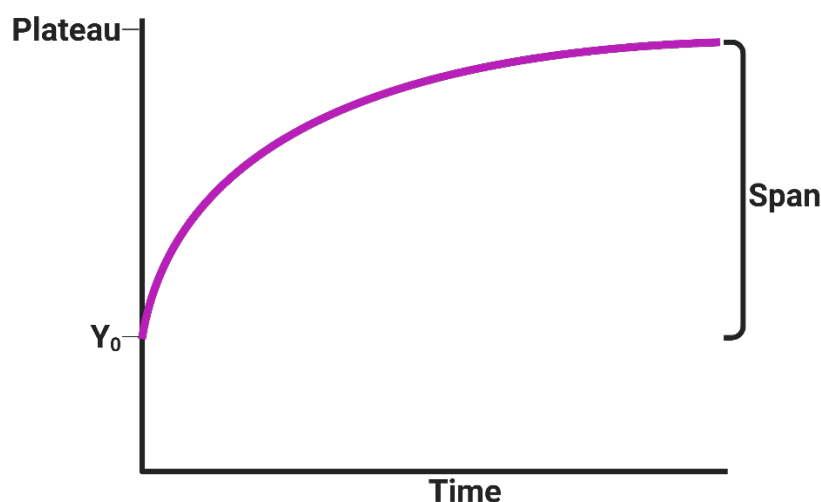


Figure.7.6 The fitting curve of one phase association equation. In the experiments of this study, y-axis is cumulative DOX release percentages.

The experimental data were fitted based on equation 7.3, and the best-fitted data is recorded in **Table 7.1**.

Table 7.1 Best fitted data of **Fig.7.5**. The values after fitting have been reported and have the same values as the main data.

Best-fit values	pH 7.4	Origami buffer	DNase I	pH 5.5	Extracellular polymeric matrix
Y_0 (%)	0.6847	0.03170	0.6746	0.1122	0.03335
Plateau (%)	20.39	20.58	45.04	34.15	30.66
K	0.09878	0.1002	0.1632	0.3129	0.08791
Tau (h)	10.12	6.659	6.129	3.196	11.38
Half-time (h)	7.017	4.615	4.248	2.215	7.885
Span (%)	19.70	20.55	44.36	34.03	30.63
R squared	0.8953	0.8980	0.9805	0.9458	0.9763

An initial burst release that occurred within the first 5 h was followed by a slower release rate for almost all solutions. Comparing the results obtained under-tested pH conditions clearly shows that DOX was released very slowly from the DNA origami in neutral (pH 7.4) and origami buffer (pH 7.2) K values 0.098 and 0.10, respectively. Release efficiencies were about 20% for 60 h. When the pH dropped to 5.5, approximately 34% of DOX was released within 60 h, a higher release than at pH 7.4 and pH 7.2. This observation indicates that the release of DOX from DNA origami carriers is acid-responsive [422]. The drug release from DNA origami carriers was enhanced in buffers containing DNase I, and the K value reached 0.1632. For the initial 5 h, less than 30% of the drug was released, and the release proceeded slowly but continuously for 60 h until the maximum release of above 44% was achieved. Furthermore, DOX released from DOX-loaded DNA origami in EPS is close to 12% after 5 hours and reached a maximum of ~30% after 60 hours.

7.2.2 DOX/DNA origami against *E.coli* planktonic bacteria

Structured Illumination Microscopy (SIM) images were collected using 3-color SIM for optical sectioning [242]. The same lens of the A×60/1.2 NA water immersion lens (UPLSAPO 60XW,

Olympus) focused the structured illumination pattern and captured the fluorescence emission light before imaging onto an sCMOS camera (C11440, Hamamatsu). The wavelengths for excitation were 488 nm (iBEAM-SMART-488, Toptica), 561 nm (OBIS 561, Coherent), and 640 nm (MLD 640, Cobolt). Images were acquired using custom SIM software [243]. To find the minimum inhibitory concentration of DOX, bacteria were incubated in different conditions. **Fig.7.7** shows the incubation of *E.coli* planktonic bacteria in different concentrations of 0 μM , 20 μM , 40 μM , and 60 μM DOX (no DNA origami) for 2 hr, 4 hr, 6 hr, and 8 hr. As illustrated in **Fig.7.7**, DOX is effective against *E.coli* bacteria, and bacteria are formed as a filament.

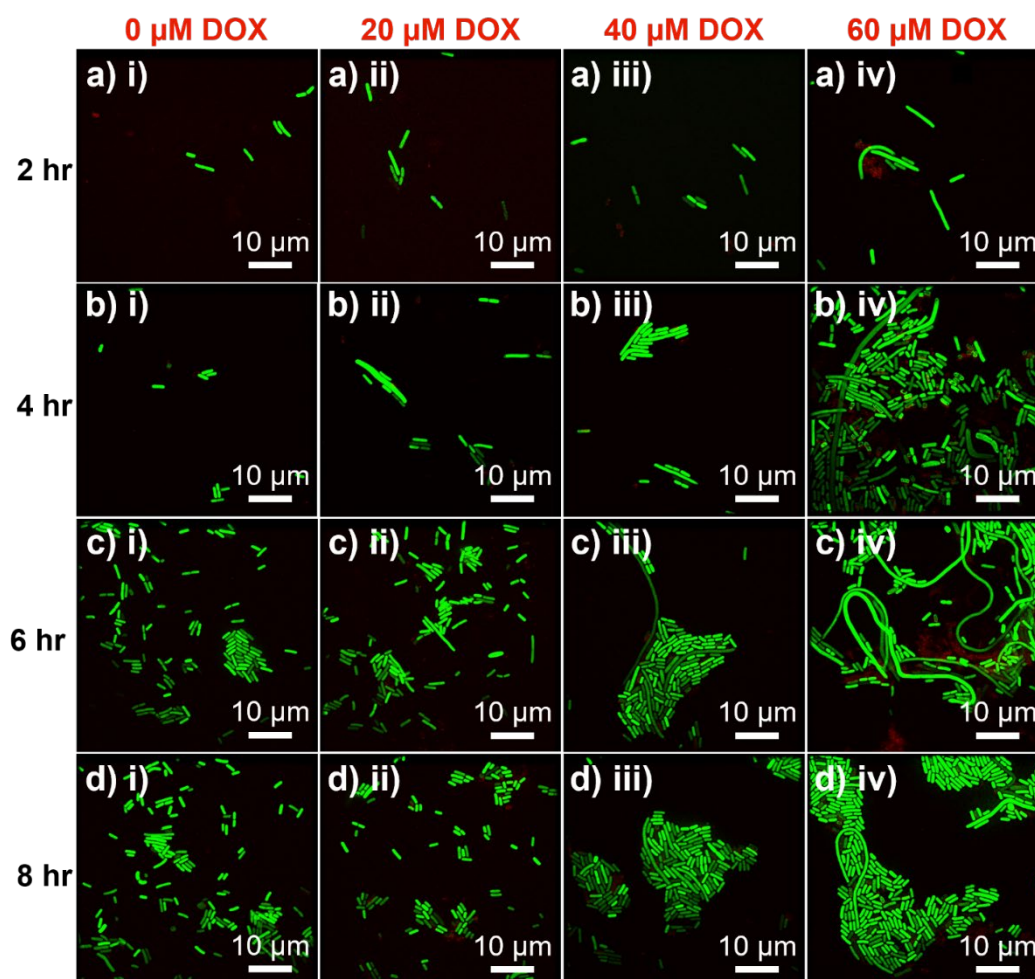


Figure.7.7 SIM images of *E.coli* bacteria after treating by DOX: Incubation of planktonic *E.coli* bacteria in (i) 0 μM DOX, (ii) 20 μM DOX, (iii) 40 μM DOX, and (iv) 60 μM DOX for (a) 2 hr, (b) 4 hr, (c) 6 hr, and (d) 8 hr.

The images were processed with an automated analysis tool, which had been written in MatLab by a colleague in Cambridge. The code defines the length of bacteria. Based on the image processing results, the size of bacteria was calculated and illustrated in **Fig.7.8**. The length of bacteria is increased by increasing the DOX concentration. The most prolonged bacteria appeared at 60 μM after 6 hr of incubation in DOX. The effect of DOX was observed from the concentration of 40 μM . Therefore, this concentration is considered the minimum inhibitory concentration and 6 hr as the maximum effective incubation time.

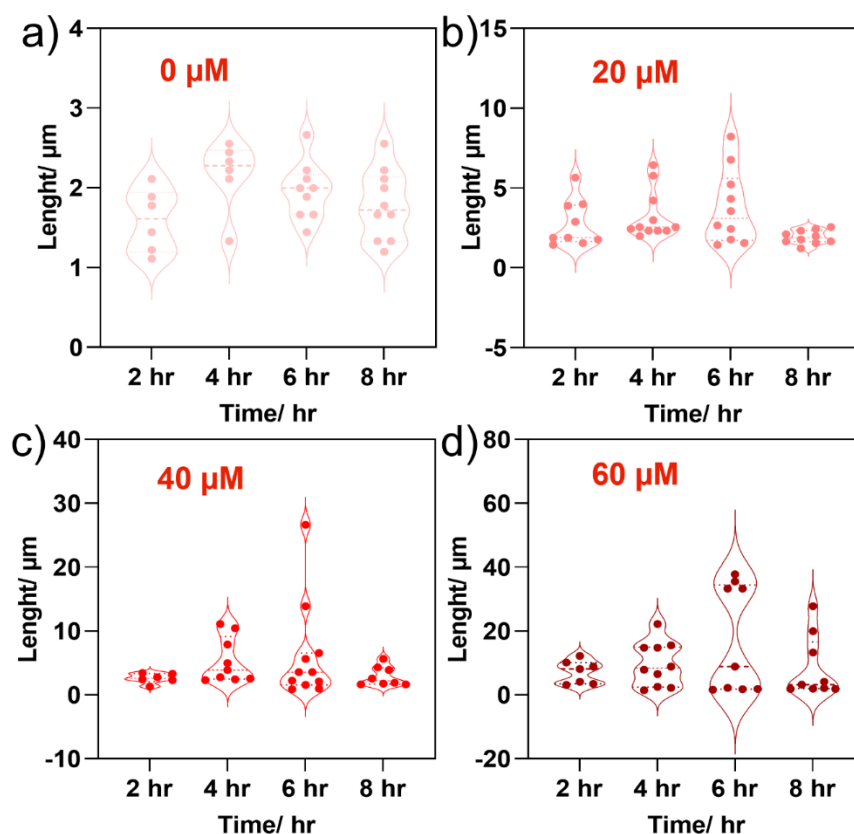


Figure.7.8 Length of *E.coli* bacteria after DOX treatment: (a) 0 μM, (b) 20 μM, (c) 40 μM and (d) 60 μM of DOX.

In the next step, DOX was loaded to the DNA origami. SIM evaluated the effect of DOX/DNA origami. As **Fig 7.9** shows, the DOX/DNA origami has a selective and effective inhibitory effect against planktonic bacteria. The given concentrations give the concentration of DOX in the DOX loading solution. The wavelengths used for excitation were 488 nm (iBEAM-SMART-488, Toptica) for the GFP channel for bacteria detection, 561 nm (OBIS 561, Coherent) for DOX detection, and 640 nm (MLD 640, Cobolt) for observation of DNA origami.

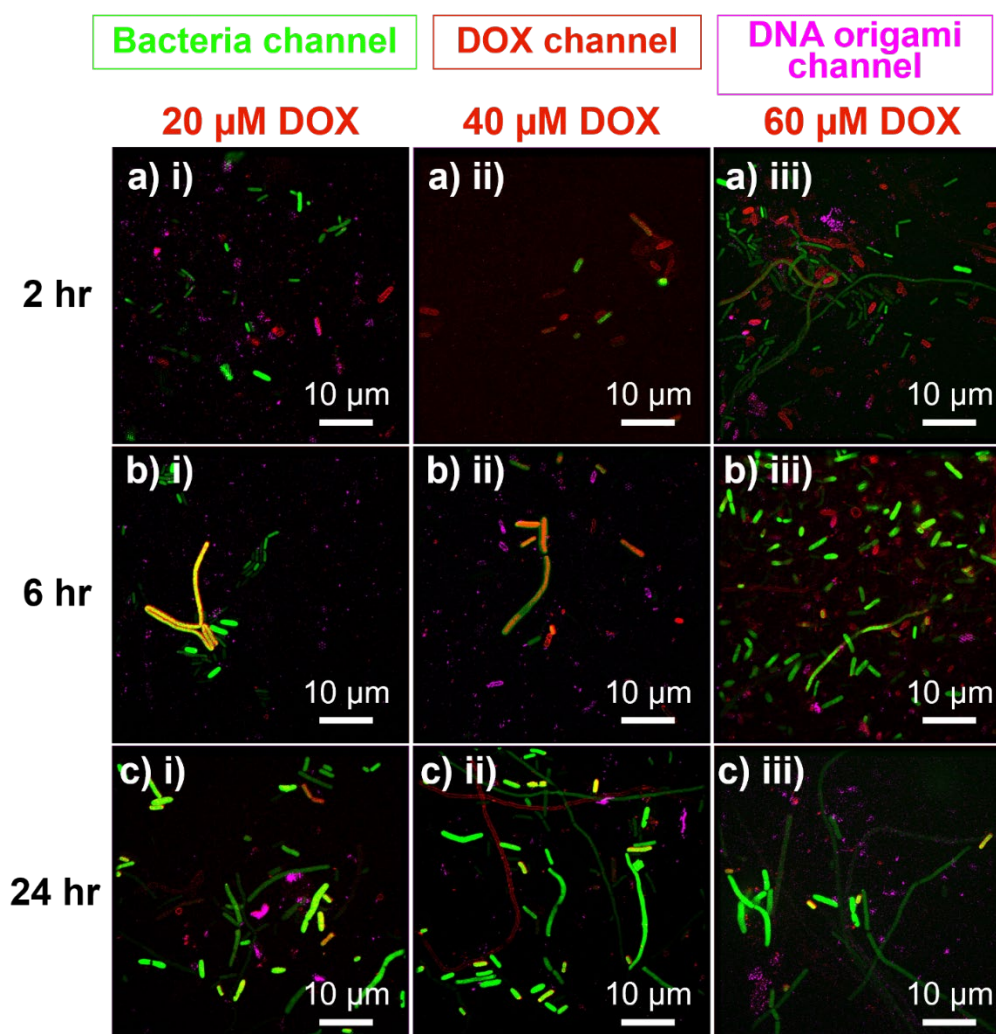


Figure.7.9 SIM images of *E.coli* bacteria after treating by DOX-loaded DNA origami: Incubation of planktonic *E.coli* bacteria in (i) 20 μ M DOX, (ii) 40 μ M DOX, and (iii) 60 μ M DOX for (a) 2 hr, (b) 6 hr, and (c) 24 hr.

As shown in **Fig.7.10**, there is a loss of the green fluorescent protein (GFP) signal in the area where the Z-ring of the bacteria would form, which indicates the harsh local treatment (Red arrows in **Fig.7.10**). It reveals the outer membrane's shrinkage and consequently releases the GFP [425]. This suggests that DOX/DNA origami locally attacked the FtsZ, in other words, the Z ring.

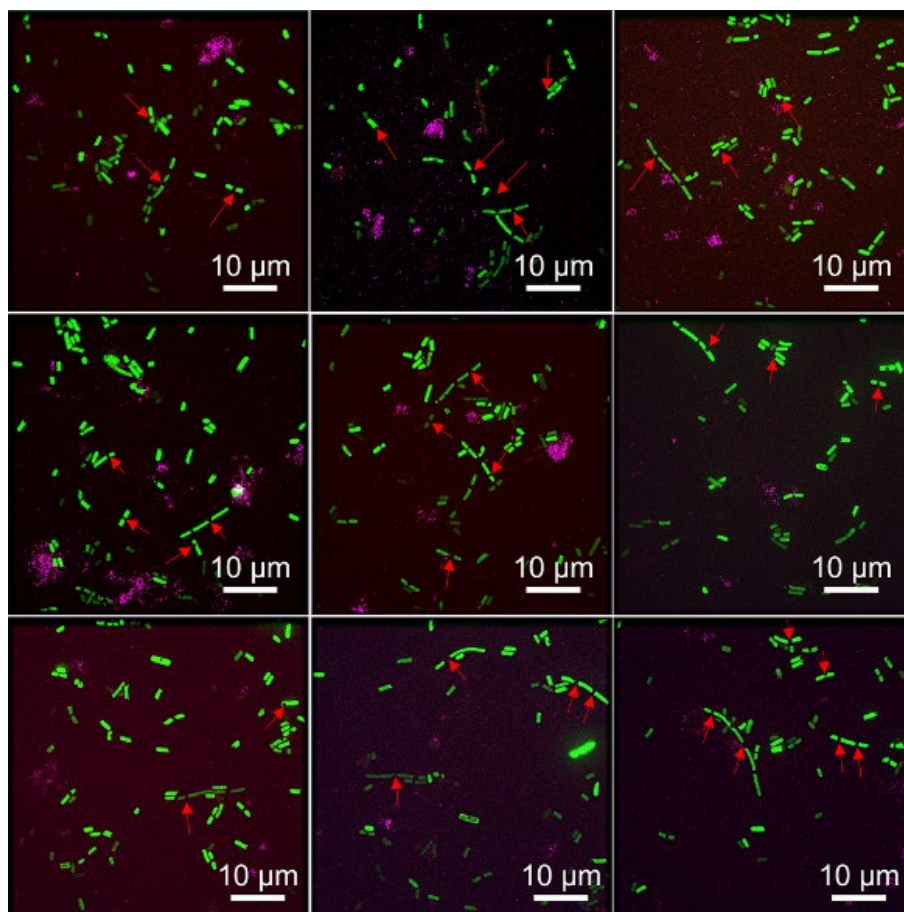


Figure.7.10 SIM images of *E.coli* bacteria after treating by filtered DOX/DNA origami. Red arrows show the local parts that lost the GFP.

7.2.3 DOX/DNA origami against *E.coli* biofilm

Mature biofilms are more tolerant to most disinfectants than the initial state of biofilms [426]. Therefore, monitoring the initial biofilm formation could be a strategy for effective biofilm treatment [427, 428]. In this project, DOX/DNA origami was utilized to prevent biofilm formation and eradicate mature biofilms. First, the DNA origami was incubated from the beginning of biofilm culture. A BL21 *E.coli* biofilm was grown *in vitro* on a coverslip under static conditions in the Petri dish. **Fig.7.11** shows the CLSM image of a one-day-old biofilm that is thoroughly formed on the coverslip.

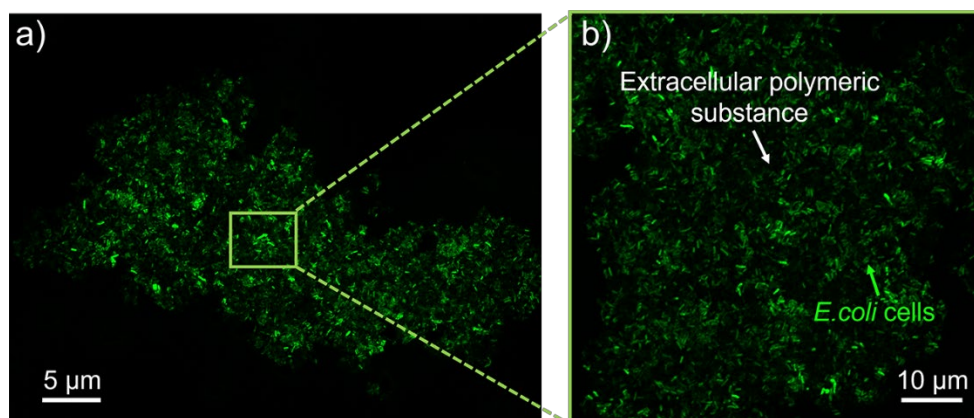


Figure.7.11 BL21 *E.coli* biofilm is grown on the coverslip: (a) and (b) CLSM image of BL21 *E.coli* biofilm in two magnifications.

The DNA origami was incubated from the beginning in the same culture as BL21 *E.coli* planktonic bacteria in order to evaluate the inhibitory effect of DNA origami. **Fig.7.12** shows the CLSM image of one-day-old biofilm which formed in the presence of DNA origami. The green channel is the expression of GFP. The red emission comes from the emission of Alexa 647 located on the DNA origami indicating the DNA origami. As it is illustrated, the biofilm in the presence of DNA origami formed in the colony. This may result due to the electrostatic interactions between DNA origami and the biofilm. A DNA origami is negatively charged. However, in this study, it is synthesized in the presence of Mg^{+2} . It should also be noted that negatively charged unmodified DNA origami nanostructures can be electrostatically adsorbed onto a zwitterionic bilayer in the presence of divalent cations [429-431] such as Mg^{2+} and Ca^{2+} . Therefore, DNA origami is partially positively charged in the presence of Mg^{2+} . Furthermore, the culture medium also has 2.5 mM $MgSO_4$, consequently, has free Mg^{+2} . DNA origami is positively charged, and the biofilm is negatively charged. Therefore, due to electrostatic effects, the biofilm is aggregated in the spherical shape, and DNA origami is covered by the colonies.

Suzuki *et al.* [432] reported that DNA origami nanostructures are strongly adsorbed and immobilized on negatively charged mica surfaces with the aid of buffer-derived Mg^{2+} ions. Furthermore, this electrostatic effect has been reported in other applications mainly to make specific arrangements of nanoparticles. DNA origami has been used to arrange metal nanoparticles into spatially ordered structures based on electrostatic interaction [433]. Julin *et al.* [433] have shown that ordered 3D metal nanoparticle superlattices could be formed by employing electrostatic interactions between particles and DNA nanostructures. They utilized the negatively charged DNA origami surface to assemble 6-helix bundle DNA origami and cationic gold nanoparticles (AuNPs) into well-ordered 3D tetragonal superlattices. In the other study, Shang *et al.* [434] reported a novel method to site-specifically synthesize silica nanostructures with designed patterns on DNA origami templates. The molecular dynamic simulation confirms that the positively charged silica precursors have a strong electrostatic affinity to protruding double-stranded DNA (dsDNA).

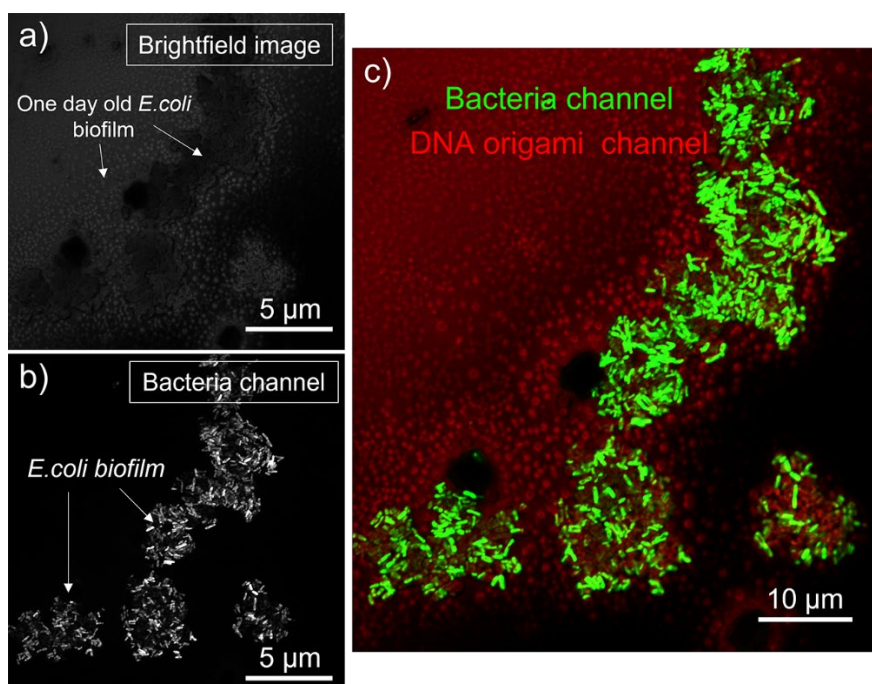


Figure.7.12 Growing BL21 *E.coli* biofilm for one day in the presence of DNA origami: (a) Brightfield image (b) bacteria channel, and (c) bacteria and DNA origami channel

Furthermore, mature biofilm was treated by DNA origami. Mature biofilms, which are much harder to control than initial biofilms, impede the treatment of biofilms [114, 435, 436]. **Fig.7.13** shows a 3-day treatment of a formed biofilm with DNA origami. **Fig.7.13a** shows the biofilm before adding the DNA origami, and **Fig.7.13b** was captured after adding DNA origami. As illustrated, the EPS behaves as a barrier, and the DNA signal is like a halo on the biofilm, indicating that DNA is blocked as the biofilm is treated.

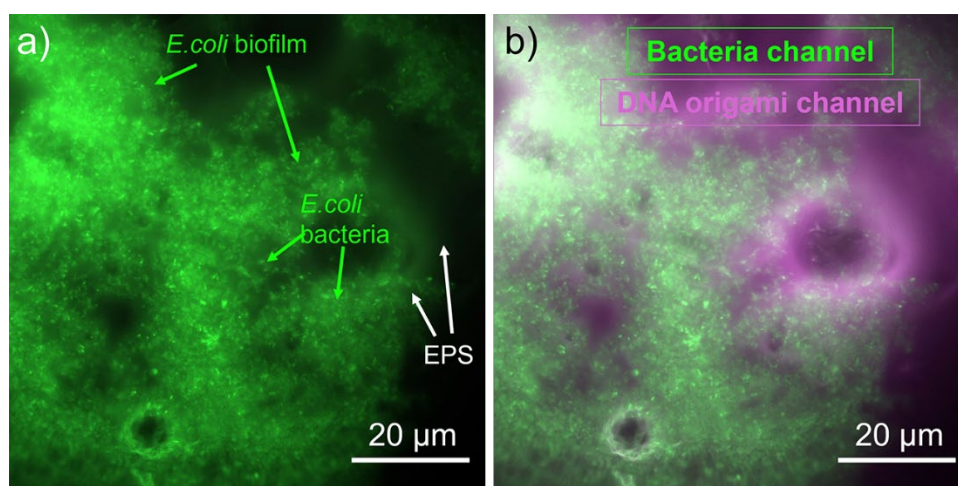


Figure.7.13 Treating the mature three-day-old biofilm with DNA origami: CLSM of 3 days old BL21 *E.coli* biofilm (a) before and (b) after adding DNA origami.

In order to evaluate the penetration of DNA origami through the 3D structure of the biofilm, a 3-day old BL21 *E.coli* biofilm was treated with DNA origami. The biofilm was incubated for 1 hour in a DNA solution. The Z-stack CLSM was recorded to investigate the penetration of DNA origami. Z-stack CLSM images (**Fig.7.14**) indicate that the DNA origami can successfully penetrate through the EPS.

Fig.7.14a shows the 3D view of the penetration of the biofilm. **Fig.7.14b** shows the 2D image with the cross-sections. The green cross-section indicates the X-Z view of the middle of **Fig.7.14a**. However, the red cross-section shows the X-Z view of the middle of **Fig.7.14a**. Also, **Fig.7.14c** is illustrated the X-Z 3D view of penetrating the DNA origami through mature biofilm. These results indicate that DNA origami can penetrate successfully through the biofilm structure. The hydrophobic character of DNA origami in their free form is probably an obstacle for the effective permeation throughout the network of hydrophilic biomolecules (proteins, polysaccharides, eDNA) of EPS [398]. In addition to this effect, the fact that an aptamer is linked to the DNA scaffold makes them prone to prefer to be attached to the bacteria embedded in EPS [239]. Furthermore, the strong electrostatic attraction that we clearly observed with previous results (**Fig.7.12**) could enhance the penetration of DNA origami in the biofilm [437, 438].

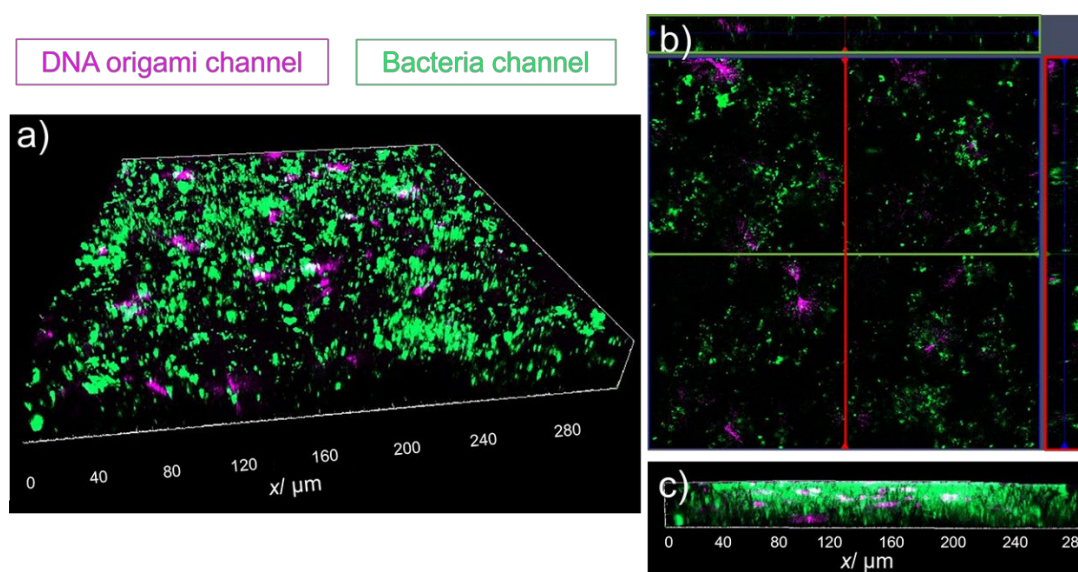


Figure.7.14 Penetration of DNA origami through 3 days old BL21 *E.coli* biofilm: (a) 3D view of the penetration of DNA origami through biofilm structure. (b) 2D view of biofilm with X-Z and Y-Z section in green (top) and red (right) views. (c) X-Z 3D view on the penetration of DNA origami in EPS.

The inhibitory effect of DOX against BL21 *E.coli* biofilm was further evaluated. **Fig.7.15a** shows the CLSM image of one-day-old BL21 *E.coli* biofilm grown in the presence of DOX-loaded DNA origami. One long filament of bacteria remained after most bacteria were killed. The length of bacteria is about 1200 μm which is almost 1000 times longer than the length of *E.coli* bacteria. This is because DOX accumulated in EPS causing an intense effect. Furthermore, the DOX was treated against mature, three days old BL21 *E.coli* biofilm. As indicated in **Fig.7.15b**, There is a low level of GFP signal showing most bacteria were killed when DOX is applied to mature biofilms. Furthermore, the length of bacteria is about 650 μm which is almost 650 times more than normal *E.coli* bacteria. For both **Fig.7.15a** and **Fig.7.15a**, there is just a DOX signal, and there is no signal in the GFP channel indicating that the bacteria is dead [439, 440] and the DOX on the outer membrane could be detected. As observed in planktonic results, some of the treated bacteria with DOX could be observed just in the DOX channel since they are dead and do not express GFP anymore.

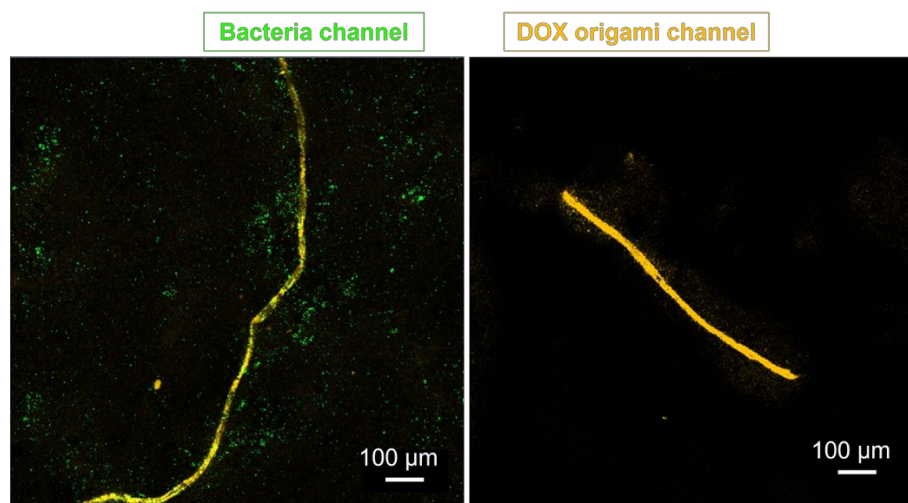


Figure.7.15 Inhibitory effect of DOX against BL21 *E.coli* biofilm: (a) CLSM image of one-day-old BL21 *E.coli* biofilm was grown in the presence of DOX. (b) CLSM image of three-days-old BL21 *E.coli* biofilm was treated with DOX-loaded DNA origami.

Furthermore, electrochemical measurements have been done with microelectrode arrays. This work is preliminary, and more elaboration is needed. However, to complete the project's goal, the preliminary results are presented here. The electrodes were made of the conducting polymer PEDOT: PSS for the electrochemical readout and were patterned by optical lithography, ensuring scalable fabrication with reasonable control over device parameters. A thickness of 380 nm provides low enough impedance and >75% transparency throughout the visible part of the spectrum, making them suitable for artifact-free recording in the presence of laser illumination of CLSM (**Fig.7.16**). Au interconnects were used outside the transparent window to minimize resistive losses. The recording area had 59 recording electrodes which are circular with 30 μm in diameter. The distance between electrodes was 200 μm (**Fig.7.16**).

In previous studies, selective detection has been reported through the change in conductivity and double-layer capacitance of the medium caused by bacterial growth [441-443]. In particular, an impedance biosensor integrated with an interdigitated array (IDA) electrode can generate sensitive electrochemical signals due to its low ohmic drop, rapid reaction kinetics, and high signal-to-noise ratio [444-446]. Using the interdigitated microelectrode impedance sensor has shown changes in electrochemical signals with bacterial growth [447].

Microelectrode arrays for electrochemical readout

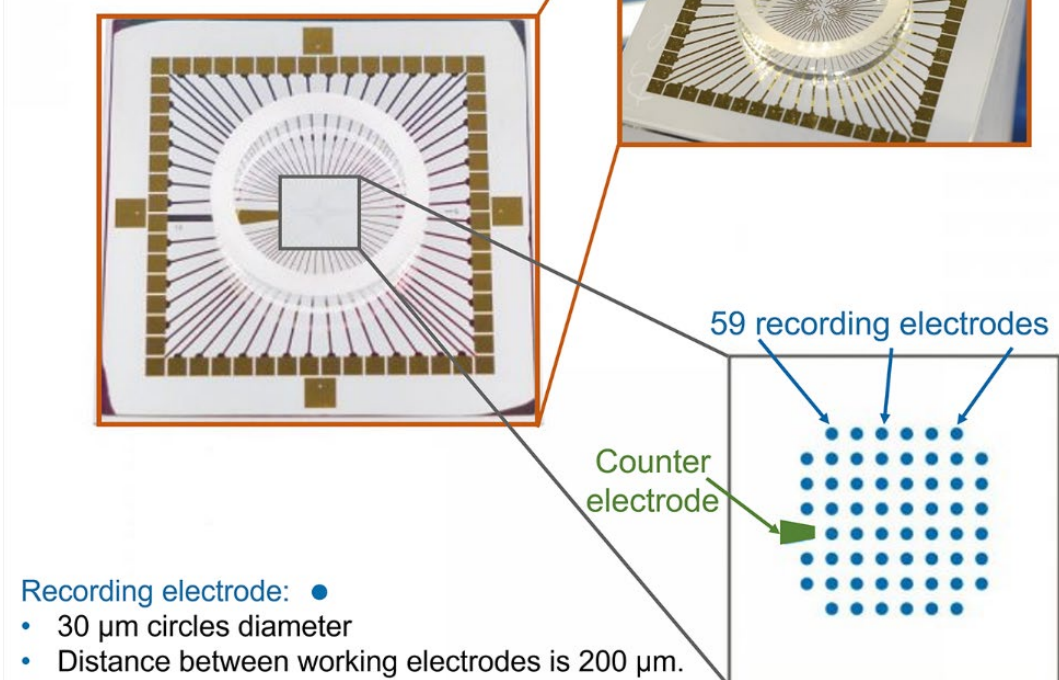


Figure.7.16 Schematic representing the microelectrode arrays: Optical image of the transparent MEA (left), close-up view of the transparent recording region (right, bottom).

Before biofilm culture, a PDMS mold was mounted on the active area. The biofilm was then cultured in the PDMS well (Fig.7.17).

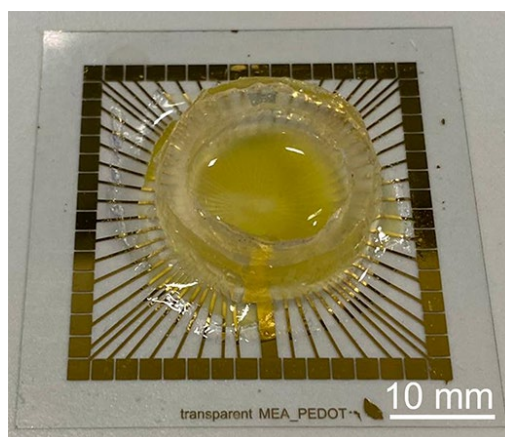


Figure.7.17 Biofilm culture in the PDMS well on the MEA.

To evaluate the effect of biofilm culture on the swelling of PEDOT: PSS, AFM microscopy was done before (Fig.7.18) and after (Fig.7.19) adding the culture medium on the polymer.

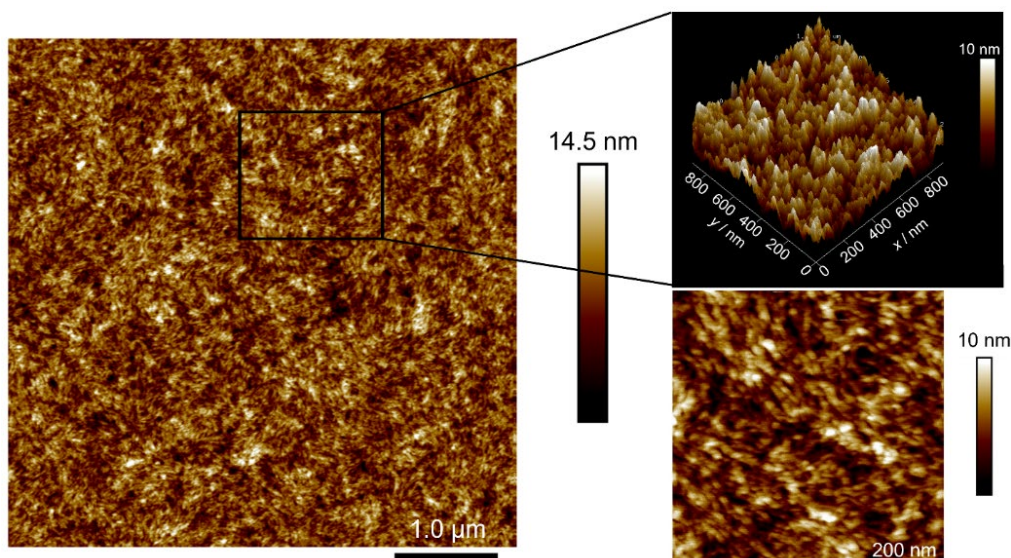


Figure.7.18 AFM image of the dry PEDOT:PSS polymer.

Comparing **Fig.7.18** and **Fig.7.19** indicated that the PEDOT: PSS after introducing the culture medium swell about 11 nm, which is very little to consider the polymer as a scaffold platform for entrapping the *E.coli* cells.

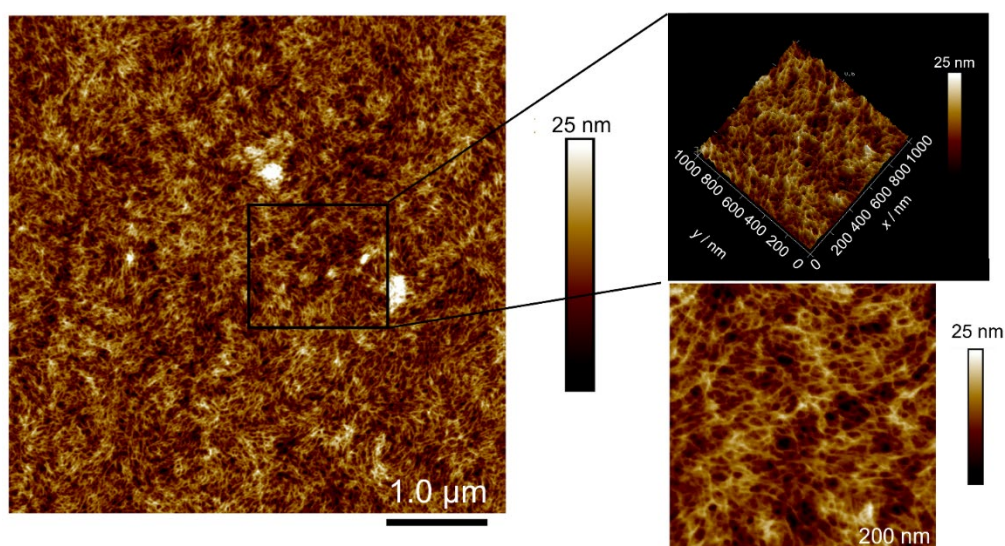


Figure.7.19 AFM image of the wet PEDOT: PSS polymer.

The biofilms were then cultured on MEAs (PEDOT: PSS coated Au microelectrodes), and electrochemical impedance spectroscopy (EIS) was performed. Although EIS of biofilms is well-known and often discussed in the literature, in this thesis, an MEA with 30 μm microelectrodes was used that could provide some localized information by EIS imaging. At each grid point of the MEA, an EIS spectrum can be recorded, which could be very useful for biofilms that contain structural and chemical heterogeneities, such as gradients of nutrients and metabolites. **Fig.7.20** represents Randles equivalent circuit often used for a working electrode-electrolyte solution interface. It consists of a solution resistance R_s , a charge transfer resistance (R_{ct}), a diffusion element (Warburg element, Z_d) to account for the diffusion of species, and a constant phase element (CPE). The CPE represents the double layer capacitance at the electrode-electrolyte solution interface and describes an

imperfect capacitor [448]. Constructing a Randles equivalent circuit for the system under study is more complex. It contains various phases and interfaces, such as Au-PEDOT: PSS, PEDOT: PSS-biofilm biofilm-electrolyte solution. The different contributions of the double layer (pseudo-)capacitances and interface resistances might both play all separate critical roles.

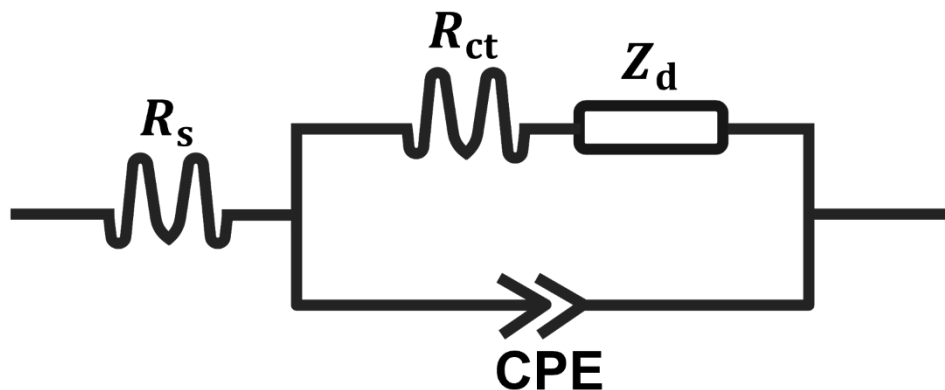


Figure.7.20 Equivalent circuit for describing bacterial attachment with the MEA electrode. R_s refers to the solution resistance; CPE refers to the constant phase element, which represents the double layer capacitance, R_{ct} refers to the charge transfer resistance, which accounts for the leakage current.

Although the simple Randles equivalent circuit shown in **Fig.7.20** is not accurate enough to describe the studied system in detail, a preliminary analysis of EIS spectra and fitting those to the simplified equivalent circuit from **Fig.7.20** was performed. Suitable limits on each of the parameters were selected, and fitting was done using the Python package "Impedance.py". The electrodes where any of the fitted parameters were at the upper or lower frequency limits were not considered for comparison, even if the fitting errors were low.

In order to eliminate possible electrode-to-electrode variations in one MEA, the CPE from each experiment with biofilm was normalized by the CPE of the same electrode of the MEA without biofilm (Eq. 7.4). Measurements without biofilm are indicated below as bare culture medium Super Optimal Broth (SOB):

$$\text{Normalized } CPE = \frac{CPE \text{ in the presence of biofilm } (CPE)}{CPE \text{ in culture medium, SOB (no biofilm)} (CPE_{SOB})} \quad (\text{Equation 7.4})$$

According to previous studies, the double-layer capacitance can be affected by two contrary factors; ionic species generated by bacterial cell growth and accumulated at the biofilm surface could increase the double-layer capacitances of the involved biofilm interfaces, but physically attached bacteria could decrease the double layer capacitance of an electrode by blocking it [447, 449].

In this very preliminary approach, the total apparent CPE value was considered a rough electrochemical reference value to have an indication whether the antibiofilm reagents and treatments affected the biofilm. EIS results were thus compared with fluorescence images. Ideally, the EIS with a microchip could provide a simplified, compact measurement platform in the future. However, it is very clear that a deeper study of the construction of the Randles equivalent circuit and data elaboration of the whole system is needed. Moreover, more measurements have to be done in

order to obtain statistically solid data sets. As this work was done at the end of the internship period at Cambridge, time constraints did not allow a deeper investigation so far. Therefore, the following analysis must be considered as a preliminary investigation. It is assumed that the pseudo-capacitance depends on various factors, such as the concentration of ions in the phases and the surface areas of the electrode [447, 449]. The general procedure was the following, biofilm growth was initiated directly in the presence of reagents, or a three-day-old, more robust biofilm was continued to grow with the reagents.

First, an *E. coli* biofilm was grown on the chip in the presence of free 40 μM DOX, thus without DNA origami (**Fig.7.21**). The CLSM images show the BL21 *E.coli* biofilm growth on the MEA in the presence of DOX for five days. In all CLSM images, the MEs are shown as shadows, and the biofilm can easier be seen in the areas in-between. The GFP signal (= mass of bacteria) decreased by 35% and 57% after three and five days, respectively. **Table 7.2** illustrates the normalized total apparent *CPE* values, and **Table 7.3** shows the average values, considering a set of eight MEs of the MEA. The total apparent *CPE* was higher at day one in comparison to Super Optimal Broth (SOB, blank), which was the bacteria and biofilm-free culture medium being in contact with the PEDOT: PSS-Au electrode. However, the total apparent *CPE* decreased after that by 53% and 50% after three and five days, respectively, but still being higher than the blank. After five days, an accumulation of DOX in the biofilm appears in the CLSM image, and DOX accumulation and affected biofilm material composition might influence the EIS signal. There was no significant difference between day 3 and day 5 when analyzing the electrode mean signals, indicating a stable situation regarding total apparent *CPE*. The total apparent *CPE* might not be a suitable indicator as the GFP decreases.

Table 7.2 $CPE = CPE / CPE_{\text{SOB}}$

Time of DOX treatment / day	Electrod e 1	Electrod e 2	Electrod e 3	Electrod e 4	Electrod e 5	Electrod e 6	Electrod e 7	Electrod e 8
Bare	1	1	1	1	1	1	1	1
One	1.64	19.9	35.0	7.01	8.03	4.41	6.70	6.15
Three	4.73	8.05	15.6	3.26	4.92	2.30	2.29	1.96
Five	5.00	8.78	12.1	2.63	5.21	2.74	3.71	3.75

Table 7.3 $CPE = CPE / CPE_{\text{SOB}}$

Bare	1
One	11.11
Three	5.39
Five	5.49

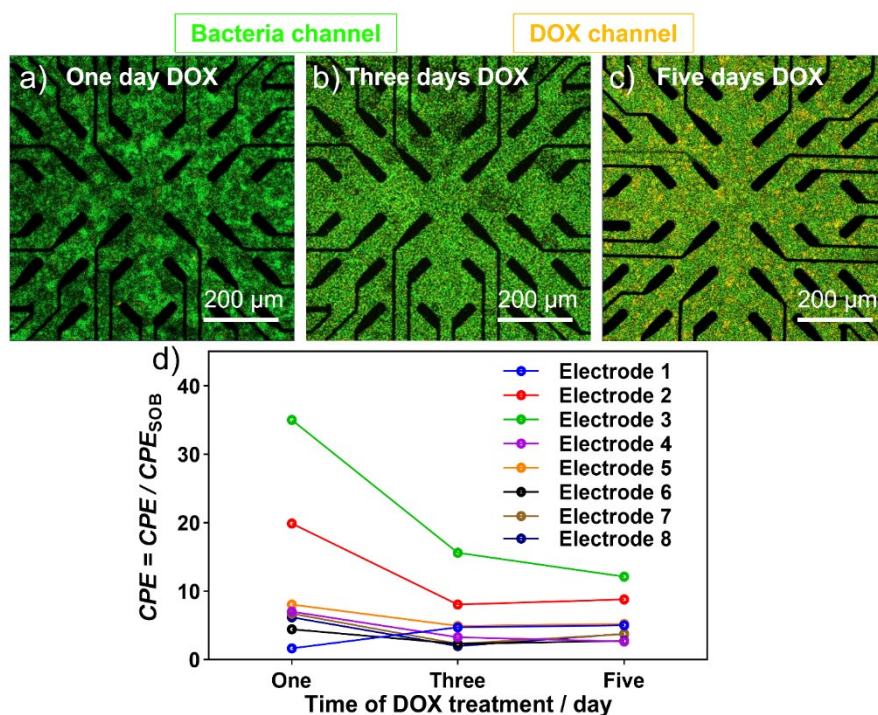


Figure.7.21 Growing a BL21 *E.coli* biofilm in the presence of DOX: (a-c) CLSM images and (d) normalized total apparent CPE. Growth of BL21 *E.coli* biofilm in the presence of free 40 μM DOX for one day (a), three days (b), and five days (c).

In general, all CPE values were higher than SOB (bare) due to different ionic environments after introducing DOX and having a biofilm on the electrode.

After that, a robust and mature three-day-old biofilm was pre-grown and treated with free 40 μM DOX for one day. The CLSM images show the three 3-day old BL21 *E.coli* biofilms before and after DOX treatment (**Fig.7.22**). The GFP signal decreased by 43% after one day of treatment with 40 μM DOX (**Fig.7.21**). **Table 7.3** illustrates the CPE values, and **Table 7.4** shows the average values.

Table 7.4 $\text{CPE} = \text{CPE} / \text{CPE}_{\text{SOB}}$

	Electrod e 1	Electrode 2	Electrode 3	Electrode 4	Electrode 5	Electrode 6	Electrode 7	Electrode 8
Bare	1	1	1	1	1	1	1	1
Before	0.20	0.23	0.20	1.19	0.55	0.73	0.18	0.24
After	0.12	0.36	0.25	1.14	0.42	0.67	0.23	0.51

Table 7.5 $\text{CPE} = \text{CPE} / \text{CPE}_{\text{SOB}}$

Bare	1
Before	0.44
After	0.46

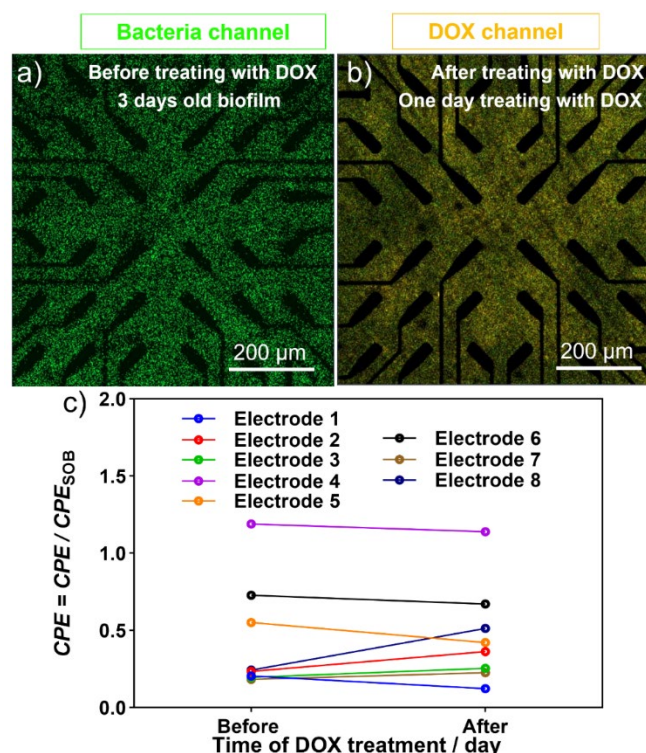


Figure.7.22 Treating mature BL21 *E.coli* biofilm with DOX: CLSM image of a 3-day-old biofilm (a) before and (b) after treating with 40 μM DOX for one day. (c) The fitted CPE was extracted from EIS results.

The biofilm grown for three days shows a lower total apparent CPE compared to the blank (= 1) for almost all the electrodes. The value of the total apparent CPE did not change between day 0 (before) and 1 (after treatment). This result could indicate that the total biofilm mass is stable, and the total apparent CPE is not indicative of the treatment.

An *E. coli* biofilm was then grown in the presence of DOX-free DNA origami on the MEA (**Fig.7.23**). Having DNA origami in the culture let the biofilm grow in clusters (**Fig.7.12 and Fig.7.23b**) due to the electrostatic interactions between DNA origami and the biofilm. The initial total apparent CPE is higher than the blank, as it was observed *vide supra* (**Tab 7.6 and Tab. 7.7**). The mean total apparent CPE increased by 28% after three days compared to day 1. This was different from the DOX-containing solutions and could indicate that the biofilm continues growing without DOX, however, in clusters. Furthermore, the GFP signal is also decreased by about 19%. But as it is shown in **Fig.7.23a,b**, the GFP signal is more local and in the cluster.

Table 7.6 $CPE = CPE / CPE_{SOB}$

	Electrode 1	Electrode 2	Electrode 3	Electrode 4
Bare	1	1	1	1
One	10.8	9.29	7.22	3.99
Three	18.2	11.5	4.88	5.61

Table 7.7 $CPE = CPE / CPE_{SOB}$

Bare	1
One	7.825
Three	10.048

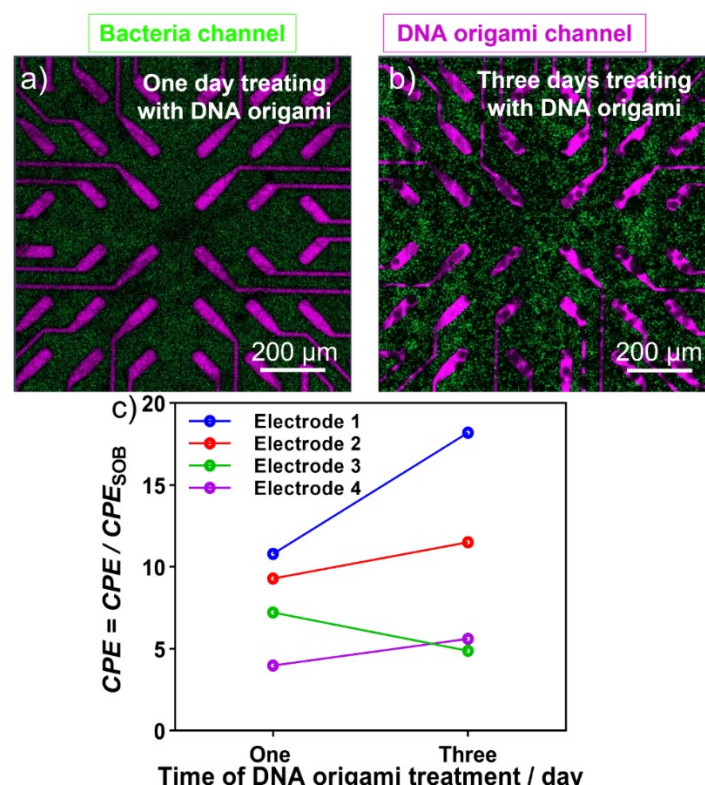


Figure.7.23 Growing BL21 *E.coli* biofilm with DNA origami: (a and b) CLSM images and (c and d) MEAs readout. Growth of BL21 *E.coli* biofilm in the presence of DNA origami for one day (a), three days (b). (c) The fitted CPE was extracted from EIS results.

An *E. coli* biofilm was then grown in the presence of DOX-loaded DNA origami nanostructures (**Fig.7.24**). The GFP signal decreased drastically (83%) and much more than the DOX solutions as expected and discussed *vide supra* (**Fig.7.24a** and **Fig.7.24b**). When the bacteria and DOX-loaded DNA origami nanostructures were cultured together, biofilms did not even form on some electrodes, generating a very heterogeneous biofilm "coating". Therefore, the total apparent CPE for some electrodes was below 1 and for others above 1 at day one (**Table 7.7** and **Table 7.8**), thus much lower than in the previous cases. The heterogeneity can also clearly be seen in CLSM images.

Table 7.8 $CPE = CPE / CPE_{SOB}$

	Electrode 1	Electrode 2	Electrode 3	Electrode 4	Electrode 5	Electrode 6	Electrode 7
Bare	1	1	1	1	1	1	1
One	0.21	1.16	0.36	4.11	0.59	3.45	0.36
Three	0.44	1.20	0.35	3.66	1.68	2.87	0.42

Table 7.9 $CPE = CPE / CPE_{SOB}$

Bare	1
One	1.463
Three	1.517

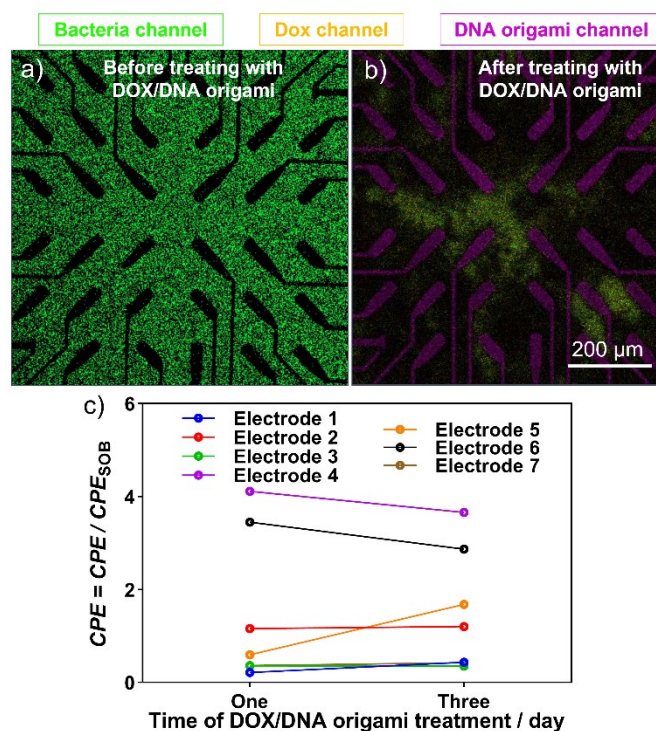


Figure.7.24 Growing BL21 *E.coli* biofilm with DOX/DNA origami: (a and b) CLSM images and (c and d) MEAs readout. Growth of BL21 *E.coli* biofilm in the presence of DOX/DNA origami for one day (a), three days (b). (c) The fitted CPE was extracted from EIS results.

Finally, the three-day-old and thus robust biofilm was treated with DOX-loaded DNA origami nanostructures for one day and three days (**Fig. 7.25**). The CLSM shows that the GFP signals decreased drastically, *i.e.*, by 73% and 91% after one day and three days of treatment, respectively. Furthermore, the electrochemical readout of the three-day biofilm shows an increase of the total apparent CPE over time (**Table 7.9** and **Table 7.10**). The capacitance of each electrode reflects its local environment, and since the biofilm is non-uniform, variations are noticed across different electrodes.

Therefore, while the GFP-based CLSM showed the effect of DOX treatments clearly, the electrochemically obtained total apparent CPE changed partially in a contrary way. This suggests that a better equivalent circuit should be designed, as the species added to the solution and the attacked biofilm might influence the EIS spectra differently.

Table 7.10 $CPE = CPE / CPE_{SOB}$

	Electrode 1	Electrode 2	Electrode 3	Electrode 4	Electrode 5	Electrode 6	Electrode 7
Bare	1	1	1	1	1	1	1
One	5.57	1.20	0.73	1.90	0.69	1.15	0.96
Three	9.70	1.48	3.50	4.91	2.85	3.63	4.37

Table 7.11 $CPE = CPE / CPE_{SOB}$

Bare	1
One	1.743
Three	4.349

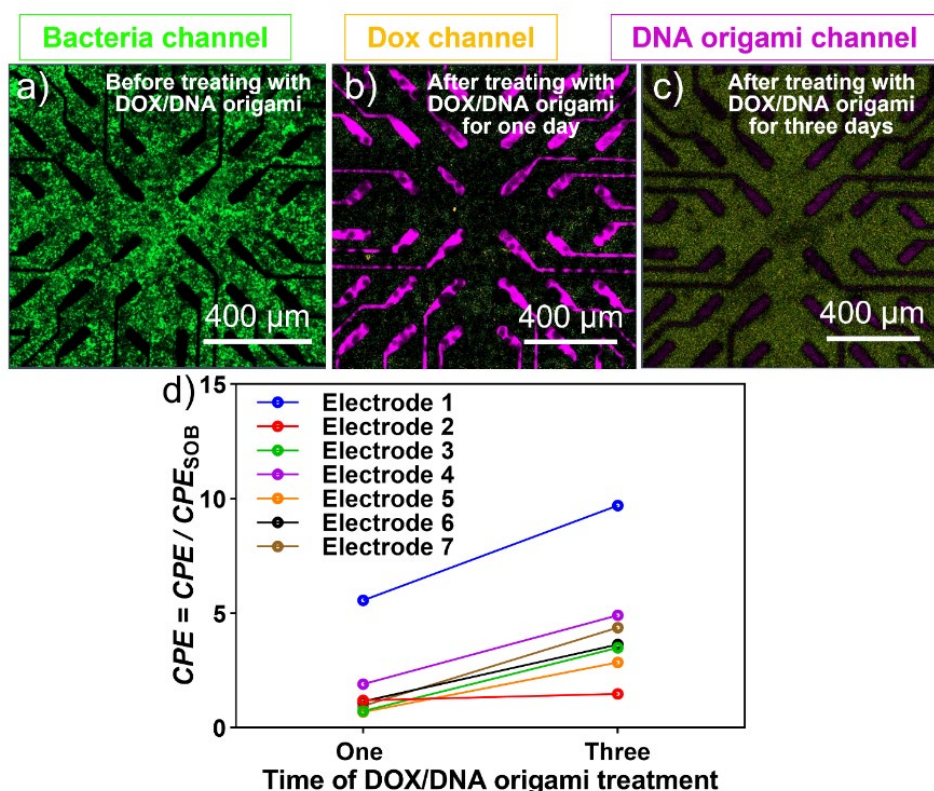


Figure.7.25 Treating mature BL21 *E.coli* biofilm with DOX/DNA origami: CLSM image of 3 days of biofilm (a) before and after treating with DOX/DNA origami for one day (b) and three days (c). (d) The fitted CPE was extracted from EIS results.

7.3 Conclusion

This chapter discusses antibiofilm agents with high selectivity and efficiency for attacking *E. coli* biofilms. The novel materials were developed based on DNA nanotechnology and loading of DNA origami with DOX. The antibiofilm agent can pass through the extracellular polymeric matrix of the biofilm and penetrate through its 3D structure. The results show that DOX/DNA origami are promising antibiofilm reagents for inhibition of biofilm formation as well as biofilm eradication. Complementary detection has been addressed by using CLSM and MEAs. The MEAs were used to record localized EIS spectra. A simplified Randles equivalent circuit was used to fit the experimental EIS spectra. This led to a total apparent CPE that changed with treatments, but was difficult to compare with the CLSM image data. Therefore, the electrochemical detection concept should be optimized in view of the experimental design, hardware, and data elaboration.

CHAPTER 8

General conclusions and future perspectives

In this thesis, complementary detection methods based on electrochemical analysis and fluorescence imaging were investigated to provide new insights and new approaches for electrochemical imaging of complex biological materials. Melanoma and bacterial biofilms were the two main targets of this thesis, and the results were discussed in five results chapters. The measurement of tyrosinase, a melanoma protein marker, was realized non-invasive and semi-invasive (Chapters 3 and 4). Tyrosinase was detected Soft-Probe-SECM by first linking a primary TYR antibody, which was Soft-Probe-SECM by first linking a primary TYR antibody, followed by linking a secondary antibody with a secondary antibody peroxidase label to produce electrochemically detectable species. Soft-Probe-SECM has been used to study bacterial biofilm electrochemical surface reactivity in Chapters 5 and 6 and to investigate the effect of antibiofilm treatment with different reagents and treatments. Finally, in Chapter 7, an antimicrobial-loaded DNA origami has been applied for the selective and efficient treatment of the biofilm. The achievements of each project are summarized below.

In Chapter 3, an adhesive tape collection method for cutaneous cells from a suspicious skin area and subsequent transfer of the tape with collected cells into an SECM was presented. The adhesive tape removed the cells and kept them well attached to the adhesive layer during experiments in an electrolyte solution. An antibody labeled with horseradish peroxidase was applied to visualize by Soft-Probe-SECM the intracellular enzyme tyrosinase (TYR) on the tape-collected cells. Notably, the tape stripping procedure seemed to have damaged the cell membranes sufficiently, not requiring cell lysis or cell membrane permeabilization strategies. First, mouse model melanoma cells were analyzed in different concentrations. Following this, increased TYR levels were observed in melanoma mouse models reflecting three different stages of tumor growth. By analyzing cells from the *stratum corneum* in different depths, *e.g.*, by consecutive tape stripping on the same area, three-dimensional information about melanoma biomarker distributions might be obtainable in the future. This method could develop into a skin screening tool for skin disease diagnosis in a broader range of skin conditions. Although it would require more testing, the method may also be applied to organoids and 3D microtissues to study cancer.

In Chapter 4, the fabrication of a microneedle array electrode was presented as a potentially semi-invasive device for the *in vivo* detection of TYR. Microneedles (MNs) were fabricated with a steel template and a PDMS negative mold. Various polymers were tested to generate a mechanical strong MN base. The polymeric microneedles were then coated with gold by sputtering. A liquid electrolyte layer was deposited on the gold microneedles in the form of an alginate hydrogel loaded with catechol. Catechol is an electroactive species whose oxidation to o-benzoquinone can be catalyzed by TYR. If the MN electrode is immersed in a sample that contained TYR, a negative MN current will be recorded due to the reduction of o-benzoquinone. The sensor showed a high sensitivity for TYR of $7.52 \mu\text{A}\cdot\text{mg}^{-1}\cdot\text{mL}$ in dummy skin. A relative standard deviation (RSD) of 9% ($n=5$ repetitive) confirmed that catechol@alginate: gold microneedle had excellent stability. Moreover, five catechol@alginate: gold microneedle electrodes showed an RSD of 4% ($n=5$). Based on these results, it appears that the electrode fabrication process was reproducible, and catechol@alginate: gold microneedle biosensors are stable for repeated detection of tyrosinase. A further advantage of this sensor is its selectivity over potential interference components.

In Chapters 5 and 6, the electrochemical surface reactivity of biofilms was investigated with Soft-Probe-SECM. The feedback mode of SECM was used to generate *in situ* metabolic activity maps by the on film reduction of ferrocene methanol. Comparing SECM approach curves over entire biofilms on glass and the tape-stripped top surface layer of the biofilm, it can be inferred that SECM-based metabolic activity measurements are surface-confined. Additionally, it was possible to distinguish biofilms containing *E. coli* cells with or without ampicillin resistance.

The reduction of redox mediators based on various redox-active materials has been investigated. Based on the results, hydrophobicity is the critical parameter for the redox mediator to penetrate the extracellular polymeric matrix of biofilms and the outer membrane of *E. coli*. The extracellular polymeric matrix has a network of hydrophilic biomolecules, including proteins, polysaccharides, and extracellular DNA. And also, an outer membrane of *E. coli* has just one type of transport channel opening: porin. A higher reduction current from hydrophobic redox material. These considerations were discussed by recording approach curves over biofilms with different redox mediators.

Furthermore, the effects of different antimicrobial agents based on a chemical treatment (sodium azide), nanotechnology (silver nanoparticles), antibiotics (gentamicin), and flashlight treatment on the *E. coli* biofilms were investigated using Soft-Probe-SECM in feedback mode. SECM showed the possibility of recording the effect of antimicrobial agents, especially those with intracellular effects. The mean feedback currents were reduced the more effective was the antibiotic. Soft-Probe-SECM was used to study the inhibitory effect of sodium azide on the plasma membrane of bacteria. The inhibitory effect of silver nanoparticles in different sizes and concentrations after one-day incubation of *E. coli* biofilms was further analyzed, which was

followed by using flashlight to degrade biofilms with UV and white light irradiation. Soft-Probe-SECM was shown to be a sensitive and fast response technique to quantify the antimicrobial effects on the respiratory chain. It can be used as a complementary readout with other methods for recording the biofilm activity.

In Chapter 7, a novel antibiofilm material, *i.e.*, a DOX-loaded DNA origami, was developed for biofilms' selective and efficient treatment. The DNA origami behaved as a nanocarrier that could penetrate through the 3D structure of biofilm. DNA origamis were loaded with a Doxorubicin (DOX) drug, which inhibits the growth of bacteria, but cannot surpass the EPS of a biofilm alone, making it less effective for treating biofilms. Indeed, the DOX, when loaded on DNA origami nanostructures, was able to penetrate successfully through the biofilm to attack the internal part of the biofilms and to treat it efficiently. Furthermore, complementary detection has been designed in this study. A microelectrode array was designed and fabricated for rapid biofilm analysis. In preliminary experiments and data elaboration approaches, the antibiofilm properties of the DOX/DNA origami were addressed by trials to extract the total apparent constant phase element.

One of the most acute problems associated with biofilms is their formation on wound surfaces. Bacteria in this form impede the healing of 60% of chronic wounds and 6% of acute wounds [450-452]. A wound biofilm is formed when microorganisms, mostly pathogenic bacteria, adhere to the wound surface. The extracellular polymeric matrix, a three-dimensional (3D) matrix, provides protection and cohesion for bacteria growing in wound sites [453, 454]. Bacteria are more likely to attach to wound surfaces when the immune system is dysfunctional or dysregulated. All open wounds contain microorganisms from endogenous or exogenous sources because the innate protective covering of the skin is compromised [455]. The host's immune system controls or destroys pathogenic bacteria early in the development of wounds, leading to a normal wound healing process. However, a biofilm matrix can develop when bacteria successfully attach to the wound surface [456], effectively protecting bacteria from phagocytic attack by neutrophils and macrophages [457]. Detecting wound infections can be challenging, especially in wounds with pathogenic biofilms. Although some clinical symptoms of the formation of pathogenic biofilms, such as yellow exudate, pale wound bed, necrotic tissue, and clear tissue fluid, are distinguishable, the bacterial aggregates in wound biofilms are not discernible by the unaided eye as they usually measure less than 100 μm in size [458]. Therefore, an approach to detect specific bacterial species on the wound site is vital.

Traditionally, chronic wound biofilm detection techniques are categorized into microbiology, molecular and imaging assays. Microbiology culture-based techniques have been used to detect viable culturable bacteria in the wound. However, diagnosis of chronic wound infection using this method lacks accuracy and was demonstrated to considerably underestimate the existence and the variety of bacteria in the wound [458, 459]. Inaccuracies in the detection may arise because many

bacteria do not form colonies in normal culturing conditions (slow-growing variants, dormant persister cells, and anaerobic bacteria) [460, 461].

DNA- and RNA-based analyses of biofilm bacterial species are more precise than culturing methods and can detect unculturable cells and samples with mixed species (anaerobic and aerobic bacteria) [462]. Nevertheless, some limitations are associated with DNA-based technologies. The three primary concerns are the possibility of DNA contamination from the clinical environment or the patient's skin, not communicating cell viability information, and not distinguishing between biofilms and planktonic microbes [463].

A wound biofilm can also be detected and investigated using microscopy. For the identification of biofilms in wounds, confocal laser scanning microscopy (CLSM) and scanning electron microscopy (SEM), which examine biofilms by imaging their polysaccharide matrix and bacterial morphologies, have also been used [464-466]. Nevertheless, these imaging techniques may require time-consuming staining of the biofilm components (bacteria or EPS), special equipment, and highly trained staff. Because of this, they are not applicable in clinical settings [467].

While the methods described above have offered advances in biofilm detection, there is still a need for precise and reproducible biofilm detection on the wound site. This can be achieved through biosensor technologies that exploit specific characteristics of biofilms. Biofilms on wound beds produce quantifiable biomarkers and lend themselves as indicators for a wound's normal or pathological state [468]. They can be a powerful tool in designing personalized treatment options according to the needs of specific patient populations. Apart from specific biomarkers, other indicators of wound biofilm establishment include pH, transepidermal water loss from peri-wound skin, nutritional factors, and temperature [469]. **Fig.8.1** shows the methods for the detection of chronic wound biofilm.

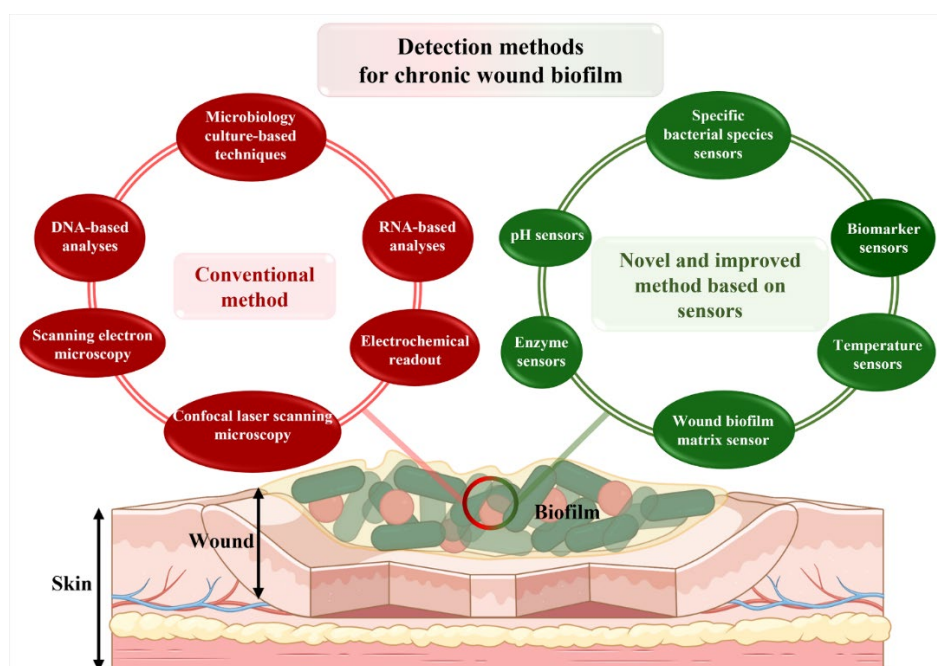


Figure.8.1 Methods for detecting chronic wound biofilm: Methods are separated into conventional and novel methods.

The first category of studies used in wound biofilms indicates whole bacteria in the wound site rather than specific biomarkers. In a recent study, Thet *et al.* [470] describe a sensor for detecting skin pathogenic bacteria at an early stage of biofilm formation. An embedded fluorescent dye is encapsulated within liposomes. Toxins from infecting bacteria cause liposomes to break down, trigger dye activation, and cause the sensor color to turn yellow to green, demonstrating infection. In another study, Jones *et al.* [471] focused on visualizing polymicrobial populations based on porphyrin fluorescence. In this study, 32 bacteria and 4 yeast species were plated on agar and tested for red fluorescence. According to the findings, 28 of 32 bacteria studied and one in four yeast species and monomicrobial biofilms produce red fluorescence when they can produce porphyrin. These sensors offer precise detection for pathogenic bacteria and particularly for chronic nonhealing infected wounds.

Different studies have demonstrated that chronic, acute, and healthy skin pH profiles differ significantly [472]. The pH within the wound milieu is a significant biochemical marker, an important contributing factor throughout the wound healing process [469, 473]. pH of normal skin and healing wounds is between 4–6.5 (*i.e.*, acidic) [474, 475]. However, chronic wounds have an alkaline pH [476]. When an infected wound has a high pH, it inhibits microorganism growth and invasion. These pH changes affect matrix metalloproteinases, fibroblast activity, keratinocyte proliferation, microbial proliferation, and immunologic reactions in the wound [474]. Since pH changes can modulate biological and biochemical processes in wound healing, various pH sensors have been developed to monitor wound status. Electrochemical pH sensors mainly measure the pH-sensitive potential, current, or impedance [477]. In a study by Rahimi *et al.* [478], a potentiometric pH sensor was developed for wound infection detection.

Additionally, wound inflammation and infection are closely linked to wound temperature [479]. As recently demonstrated, it is possible to predict infection by observing any abnormal changes in wound temperature before any secondary symptoms appear [480]. As such, temperature is an essential indicator of wound biofilms. Different innovative wound dressings with integrated temperature sensors have been designed to provide precise real-time information about the wound environment [481]. For instance, Pang *et al.* [482] developed a double-layer structure including polydimethylsiloxane-encapsulated flexible electronics integrated with a temperature sensor and ultraviolet (UV) light-emitting diodes.

Furthermore, various studies have demonstrated the role of enzymes, precisely that of matrix metalloproteinases (MMPs), in the healing process of chronic wounds. Some of these enzymes are excessively released and activated in chronic cutaneous wounds, which leads to long-term healing. For a wound to heal, MMPs should be at an appropriate level, in the correct location, and for a precise duration of time. TIMPs (tissue inhibitors of metalloproteinases) are generally produced in excessive amounts during wound healing, and their levels are concomitantly downregulated, resulting in decreased production of MMPs. In response, the balance between MMP and TIMP is

altered [483-486]. MMPs were chronically elevated in chronic wounds, and TIMPS were reduced, leading to aberrations in their ratios serving as potential diagnostic biomarkers to detect wound biofilms.

Furthermore, the growing aging populations and limited clinical resources have created an enormous demand for wearable health devices and portable medical monitoring. Wearable biosensors now make it possible to monitor human bodies and health without any invasive input for long periods [487, 488]. Through continuous monitoring of an individual's health status, wearable sensors are the key to personalized medicine [489]. While wearable sensor technologies are rapidly growing in popularity, it is crucial to develop flexible devices to collect more insightful information regarding skin infections from the human skin.

As illustrated, there is an increasing interest in developing sensors for the precise detection of different wound biofilm-associated markers and providing reliable information about wound status. Personalized medicine is made possible by wearable sensors. In this way, continuous monitoring of the human body and collecting meaningful health status data can be captured and used for preventive intervention. The epidermal measurement is often prone to errors due to motion artifacts and mechanical mismatches between conventional rigid electronic materials and soft skin. Unique properties of flexible electronics, such as high flexibility and conformability, allow for a natural interface between humans and devices [490-493].

Personalized healthcare has recently significantly improved because of advances in nanotechnology and materials science. Wearable electronics can monitor individuals' movements without interrupting them or limiting their movements while wearing it or mating it with their skin [492-495]. A wearable biosensor could thus be used to continuously monitor an individual's physiological variables in real-time [489, 496, 497]. Currently, commercially available wearable sensors can only track one physical activity and vital signs. They are unable to offer insight into a user's state of health.

The integration of flexible sensors in a bandage or so-called innovative wound dressings has recently attracted much attention. Smart bandages have been engineered to provide precise real-time information about wound conditions, including pH, temperature, moisture, and oxygen, to personalize an individual patient's clinical treatment [481, 498]. Although sensor-integrated wound dressings can provide information about the wound environment, some detectable symptoms may stem from other reactions in the body, leading to an incorrect diagnosis. Multiple sensors must be incorporated simultaneously in wound dressings to provide orthogonal information from various wound parameters to counteract this problem. Integrating more than one sensor can give even more accurate information about the wound environment and biofilm formation status.

Based on my biofilm sensing and treatments expertise, I would suggest having an electroactive hydrogel containing redox-active species on the wearable sensor for continuous detection. Based on my expertise, ferrocenemethanol is a promising option for detecting the metabolic activity of biofilm.

Therefore, for future work, I propose fabricating a wearable electronic sensor on a mechanically flexible polyethylene terephthalate (PET) substrate. The sensor will need two main parts based on sensor arrays and wireless flexible printed circuit board (FPCB) (**Fig.8.2**). Wearable sensors could record different wound biofilm properties through multiple channels. The five main characteristics are temperature, pH, enzyme markers, bacteria, and EPS species. Therefore, the four sensing panels are suggested for being developed: (i) Specific bacterial species and wound biofilm EPS sensors. Sensors to indicate environmental parameters, (ii) pH and (iii) temperature. (iv) Enzymes sensors.

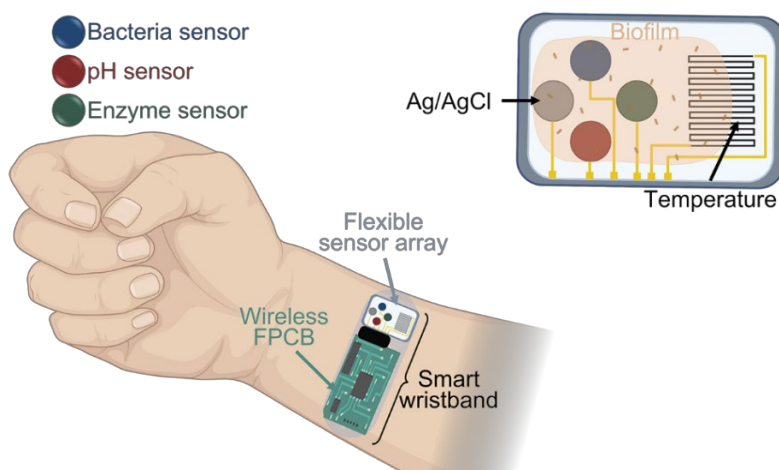


Figure.8.2 Schematic represents the flexible electronic device with various simultaneous readouts for detecting wound chronic biofilm.

The sensor array has several key components, including the substrate, active, and interface. First, the transparent sensor array shall be fabricated (**Fig.8.3**). The sensors could be fabricated on flexible transparent PET to ease the wearable application and microscopy investigations. The electroactive material could be provided by a gold (Au) coating. Before Au coating, a thin layer of chromium (Cr) shall be sputtered to improve the adhesion of Au on PET. A parylene coating shall cover the active area. Ag/AgCl electrodes could be used as reference electrodes for the electrochemical readout.

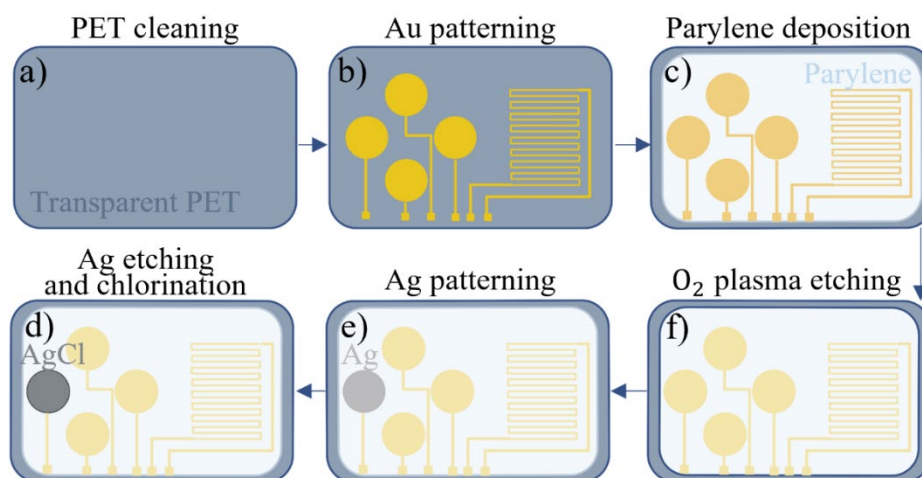


Figure.8.3 Fabrication process of the flexible sensor array: (a) PET cleaning. (b) Patterning of Cr/Au electrodes using photolithography. (c) Parylene insulating layer deposition. (d) Photolithography and O₂ plasma etching of parylene in the electrode areas. (e) Electron-beam deposition of the Ag. (f) Ag etching on the Au working electrode area and Ag chlorination on the reference electrode area.

The next step shall be to fabricate pH sensor, temperature sensor, enzyme sensor, and bacteria sensor on the same base on sensor arrays. This step shall be done in a stepwise process. The sensory characteristics of each sensor, including the limit of detection, sensitivity, selectivity, and long-term performance, shall be developed precisely for each step.

References

- [1] J. Clausmeyer, W. Schuhmann, Nanoelectrodes: Applications in electrocatalysis, single-cell analysis and high-resolution electrochemical imaging, *TrAC Trends in Analytical Chemistry*, 79 (2016) 46-59.
- [2] S. Amemiya, A.J. Bard, F.-R.F. Fan, M.V. Mirkin, P.R. Unwin, Scanning electrochemical microscopy, *Annu. Rev. Anal. Chem.*, 1 (2008) 95-131.
- [3] R.C. Engstrom, M. Weber, D.J. Wunder, R. Burgess, S. Winkquist, Measurements within the diffusion layer using a microelectrode probe, *Analytical Chemistry*, 58 (1986) 844-848.
- [4] H.Y. Liu, F.R.F. Fan, C.W. Lin, A.J. Bard, Scanning electrochemical and tunneling ultramicroelectrode microscope for high-resolution examination of electrode surfaces in solution, *Journal of the American Chemical Society*, 108 (1986) 3838-3839.
- [5] A.J. Bard, F.R.F. Fan, J. Kwak, O. Lev, Scanning electrochemical microscopy. Introduction and principles, *Analytical Chemistry*, 61 (1989) 132-138.
- [6] C. Lee, J. Kwak, A.J. Bard, Application of scanning electrochemical microscopy to biological samples, *Proceedings of the National Academy of Sciences*, 87 (1990) 1740-1743.
- [7] D.T. Pierce, A.J. Bard, Scanning electrochemical microscopy. 23. Retention localization of artificially patterned and tissue-bound enzymes, *Analytical chemistry*, 65 (1993) 3598-3604.
- [8] J. Kwak, A.J. Bard, Scanning electrochemical microscopy. Theory of the feedback mode, *Analytical Chemistry*, 61 (1989) 1221-1227.
- [9] M.A. Edwards, S. Martin, A.L. Whitworth, J.V. Macpherson, P.R. Unwin, Scanning electrochemical microscopy: principles and applications to biophysical systems, *Physiological measurement*, 27 (2006) R63.
- [10] R.J. Forster, Microelectrodes: new dimensions in electrochemistry, *Chemical Society Reviews*, 23 (1994) 289-297.
- [11] C.-C. Chen, Y. Zhou, L.A. Baker, Scanning ion conductance microscopy, *Annual Review of Analytical Chemistry*, 5 (2012) 207-228.
- [12] N. Ebejer, A.G. Güell, S.C. Lai, K. McKelvey, M.E. Snowden, P.R. Unwin, Scanning electrochemical cell microscopy: a versatile technique for nanoscale electrochemistry and functional imaging, *Annual review of analytical chemistry*, 6 (2013) 329-351.
- [13] J.V. Macpherson, P.R. Unwin, Combined scanning electrochemical- atomic force microscopy, *Analytical Chemistry*, 72 (2000) 276-285.
- [14] Y. Takahashi, A.I. Shevchuk, P. Novak, Y. Murakami, H. Shiku, Y.E. Korchev, T. Matsue, Simultaneous noncontact topography and electrochemical imaging by SECM/SICM featuring ion current feedback regulation, *Journal of the American Chemical Society*, 132 (2010) 10118-10126.
- [15] D.J. Comstock, J.W. Elam, M.J. Pellin, M.C. Hersam, Integrated ultramicroelectrode- nanopipet probe for concurrent scanning electrochemical microscopy and scanning ion conductance microscopy, *Analytical chemistry*, 82 (2010) 1270-1276.
- [16] A. Schulte, M. Nebel, W. Schuhmann, Scanning electrochemical microscopy in neuroscience, *Annual Review of Analytical Chemistry*, 3 (2010) 299-318.
- [17] J.L. Fernández, D.A. Walsh, A.J. Bard, Thermodynamic guidelines for the design of bimetallic catalysts for oxygen electroreduction and rapid screening by scanning electrochemical microscopy. M- Co (M: Pd, Ag, Au), *Journal of the American Chemical Society*, 127 (2005) 357-365.
- [18] I. Serebrennikova, S. Lee, H.S. White, Visualization and characterization of electroactive defects in the native oxide film on aluminium, *Faraday discussions*, 121 (2002) 199-210.
- [19] C.-C. Chen, M.A. Derylo, L.A. Baker, Measurement of ion currents through porous membranes with scanning ion conductance microscopy, *Analytical chemistry*, 81 (2009) 4742-4751.
- [20] M.A. O'Connell, A.J. Wain, Mapping electroactivity at individual catalytic nanostructures using high-resolution scanning electrochemical-scanning ion conductance microscopy, *Analytical chemistry*, 86 (2014) 12100-12107.
- [21] Y. Matsumae, Y. Takahashi, K. Ino, H. Shiku, T. Matsue, Electrochemical monitoring of intracellular enzyme activity of single living mammalian cells by using a double-mediator system, *Analytica chimica acta*, 842 (2014) 20-26.
- [22] Y. Takahashi, A.I. Shevchuk, P. Novak, B. Babakinejad, J. Macpherson, P.R. Unwin, H. Shiku, J. Gorelik, D. Klenerman, Y.E. Korchev, Topographical and electrochemical nanoscale imaging of living cells using voltage-switching mode scanning electrochemical microscopy, *Proceedings of the National Academy of Sciences*, 109 (2012) 11540-11545.
- [23] H. Yamada, D. Haraguchi, K. Yasunaga, Fabrication and characterization of a K⁺-selective nanoelectrode and simultaneous imaging of topography and local K⁺ flux using scanning electrochemical microscopy, *Analytical chemistry*, 86 (2014) 8547-8552.
- [24] S.E. Salamifar, R.Y. Lai, Use of combined scanning electrochemical and fluorescence microscopy for detection of reactive oxygen species in prostate cancer cells, *Analytical chemistry*, 85 (2013) 9417-9421.

- [25] S. Darvishi, H. Pick, E. Oveisi, H.H. Girault, A. Lesch, Soft-probe-scanning electrochemical microscopy reveals electrochemical surface reactivity of *E. coli* biofilms, *Sensors and Actuators B: Chemical*, 334 (2021) 129669.
- [26] H. Xiong, J. Guo, S. Amemiya, Probing heterogeneous electron transfer at an unbiased conductor by scanning electrochemical microscopy in the feedback mode, *Analytical chemistry*, 79 (2007) 2735-2744.
- [27] K. Eckhard, X. Chen, F. Turcu, W. Schuhmann, Redox competition mode of scanning electrochemical microscopy (RC-SECM) for visualisation of local catalytic activity, *physical chemistry chemical physics*, 8 (2006) 5359-5365.
- [28] A.O. Okunola, T.C. Nagaiah, X. Chen, K. Eckhard, W. Schuhmann, M. Bron, Visualization of local electrocatalytic activity of metalloporphyrins towards oxygen reduction by means of redox competition scanning electrochemical microscopy (RC-SECM), *Electrochimica Acta*, 54 (2009) 4971-4978.
- [29] L. Guadagnini, A. Maljusch, X. Chen, S. Neugebauer, D. Tonelli, W. Schuhmann, Visualization of electrocatalytic activity of microstructured metal hexacyanoferrates by means of redox competition mode of scanning electrochemical microscopy (RC-SECM), *Electrochimica Acta*, 54 (2009) 3753-3758.
- [30] W.S. Roberts, D.J. Lonsdale, J. Griffiths, S.P. Higson, Advances in the application of scanning electrochemical microscopy to bioanalytical systems, *Biosensors and Bioelectronics*, 23 (2007) 301-318.
- [31] D.J. Stephens, V.J. Allan, Light microscopy techniques for live cell imaging, *Science*, 300 (2003) 82-86.
- [32] K. Ino, T. Nishijo, T. Arai, Y. Kanno, Y. Takahashi, H. Shiku, T. Matsue, Local Redox-Cycling-Based Electrochemical Chip Device with Deep Microwells for Evaluation of Embryoid Bodies, *Angewandte Chemie*, 124 (2012) 6752-6756.
- [33] H. Shiku, T. Shiraishi, H. Ohya, T. Matsue, H. Abe, H. Hoshi, M. Kobayashi, Oxygen consumption of single bovine embryos probed by scanning electrochemical microscopy, *Analytical chemistry*, 73 (2001) 3751-3758.
- [34] Y.-s. Torisawa, N. Ohara, K. Nagamine, S. Kasai, T. Yasukawa, H. Shiku, T. Matsue, Electrochemical monitoring of cellular signal transduction with a secreted alkaline phosphatase reporter system, *Analytical chemistry*, 78 (2006) 7625-7631.
- [35] A.J. Bard, X. Li, W. Zhan, Chemically imaging living cells by scanning electrochemical microscopy, *Biosensors and Bioelectronics*, 22 (2006) 461-472.
- [36] S. Amemiya, J. Guo, H. Xiong, D.A. Gross, Biological applications of scanning electrochemical microscopy: chemical imaging of single living cells and beyond, *Analytical and bioanalytical chemistry*, 386 (2006) 458-471.
- [37] A. Schulte, W. Schuhmann, Single-cell microelectrochemistry, *Angewandte Chemie International Edition*, 46 (2007) 8760-8777.
- [38] G. Wittstock, M. Burchardt, S.E. Pust, Y. Shen, C. Zhao, Scanning electrochemical microscopy for direct imaging of reaction rates, *Angewandte Chemie International Edition*, 46 (2007) 1584-1617.
- [39] T. Kaya, Y.-s. Torisawa, D. Oyamatsu, M. Nishizawa, T. Matsue, Monitoring the cellular activity of a cultured single cell by scanning electrochemical microscopy (SECM). A comparison with fluorescence viability monitoring, *Biosensors and Bioelectronics*, 18 (2003) 1379-1383.
- [40] B. Liu, S.A. Rotenberg, M.V. Mirkin, Scanning electrochemical microscopy of living cells: Different redox activities of nonmetastatic and metastatic human breast cells, *Proceedings of the National Academy of Sciences*, 97 (2000) 9855-9860.
- [41] S. Kuss, D. Polcari, M. Geissler, D. Brassard, J. Mauzeroll, Assessment of multidrug resistance on cell coculture patterns using scanning electrochemical microscopy, *Proceedings of the National Academy of Sciences*, 110 (2013) 9249-9254.
- [42] Y. Matsumae, T. Arai, Y. Takahashi, K. Ino, H. Shiku, T. Matsue, Evaluation of the differentiation status of single embryonic stem cells using scanning electrochemical microscopy, *Chemical Communications*, 49 (2013) 6498-6500.
- [43] R. Obregon, Y. Horiguchi, T. Arai, S. Abe, Y. Zhou, A. Hisada, K. Ino, H. Shiku, T. Matsue, A Pt layer/Pt disk electrode configuration to evaluate respiration and alkaline phosphatase activities of mouse embryoid bodies, *Talanta*, 94 (2012) 30-35.
- [44] F. Conzuelo, A. Schulte, W. Schuhmann, Biological imaging with scanning electrochemical microscopy, *Proceedings of the Royal Society A: Mathematical, Physical and Engineering Sciences*, 474 (2018) 20180409.
- [45] F. Cortés-Salazar, M. Träuble, F. Li, J.-M. Busnel, A.-L. Gassner, M. Hojeij, G. Wittstock, H.H. Girault, Soft stylus probes for scanning electrochemical microscopy, *Analytical chemistry*, 81 (2009) 6889-6896.
- [46] T.E. Lin, Y.J. Lu, C.L. Sun, H. Pick, J.P. Chen, A. Lesch, H.H. Girault, Soft Electrochemical Probes for Mapping the Distribution of Biomarkers and Injected Nanomaterials in Animal and Human Tissues, *Angewandte Chemie International Edition*, 56 (2017) 16498-16502.
- [47] T.-E. Lin, Y.-J. Lu, C.-L. Sun, J.-P. Chen, A. Lesch, H.H. Girault, Soft Probe Scanning Electrochemical Microscopy with Spider Array for Visualizing Biomarkers and Redox Active Proteins in Animal Tissues, *ECS Transactions*, 77 (2017) 85-90.
- [48] A. Lesch, B. Vaske, F. Meiners, D. Momotenko, F. Cortés-Salazar, H.H. Girault, G. Wittstock, Parallel Imaging and Template-Free Patterning of Self-Assembled Monolayers with Soft Linear Microelectrode Arrays, *Angewandte Chemie International Edition*, 51 (2012) 10413-10416.

- [49] F. Cortes-Salazar, D. Momotenko, A. Lesch, G. Wittstock, H.H. Girault, Soft microelectrode linear array for scanning electrochemical microscopy, *Analytical chemistry*, 82 (2010) 10037-10044.
- [50] A. Lesch, D. Momotenko, F. Cortés-Salazar, F. Roelfs, H.H. Girault, G. Wittstock, High-throughput scanning electrochemical microscopy brushing of strongly tilted and curved surfaces, *Electrochimica Acta*, 110 (2013) 30-41.
- [51] T.-E. Lin, *Soft probes for bio-electrochemical imaging*, Springer 2018.
- [52] C. Combellas, M. Fermigier, A. Fuchs, F. Kanoufi, Scanning electrochemical microscopy. Hydrodynamics generated by the motion of a scanning tip and its consequences on the tip current, *Analytical chemistry*, 77 (2005) 7966-7975.
- [53] M. Imisides, R. John, G. Wallace, Microsensors based on conducting polymers, *Chemtech*, 26 (1996) 19-25.
- [54] D. Gunning, C. Adams, W. Cunningham, K. Mathieson, V. O'Shea, K. Smith, E. Chichilnisky, A. Litke, M. Rahman, 30µm spacing 519-electrode arrays for in vitro retinal studies, *Nuclear Instruments and Methods in Physics Research Section A: Accelerators, Spectrometers, Detectors and Associated Equipment*, 546 (2005) 148-153.
- [55] T.J. Davies, R.G. Compton, The cyclic and linear sweep voltammetry of regular and random arrays of microdisc electrodes: Theory, *Journal of Electroanalytical Chemistry*, 585 (2005) 63-82.
- [56] S. Middy, V.F. Curto, A. Fernández-Villegas, M. Robbins, J. Gurke, E.J. Moonen, G.S. Kaminski Schierle, G.G. Malliaras, Microelectrode Arrays for Simultaneous Electrophysiology and Advanced Optical Microscopy, *Advanced Science*, (2021) 2004434.
- [57] E. Månsson-Brahme, H. Johansson, O. Larsson, L.E. Rutqvist, U. Ringborg, Trends in incidence of cutaneous malignant melanoma in a Swedish population 1976-1994, *Acta oncologica*, 41 (2002) 138-146.
- [58] R. Ocaña-Riola, C. Martínez-García, S. Serrano, A. Buendía-Eisman, C. Ruiz-Baena, J. Canela-Soler, Population-based study of cutaneous malignant melanoma in the Granada province (Spain), 1985–1992, *European journal of epidemiology*, 17 (2001) 169-174.
- [59] N. Maddodi, A. Jayanthi, V. Setaluri, Shining light on skin pigmentation: The darker and the brighter side of effects of UV radiation, *Photochemistry and Photobiology*, 88 (2012) 1075-1082.
- [60] S.A.N. D'Mello, G.J. Finlay, B.C. Baguley, M.E. Askarian-Amiri, Signaling pathways in melanogenesis, *International Journal of Molecular Sciences*, 17 (2016).
- [61] E. Houben, K. De Paepe, V. Rogiers, A keratinocyte's course of life, *Skin Pharmacology and Physiology*, 20 (2007) 122-132.
- [62] L.M. Russell, S. Wiedersberg, M. Begoña Delgado-Charro, The determination of stratum corneum thickness An alternative approach, *European Journal of Pharmaceutics and Biopharmaceutics*, 69 (2008) 861-870.
- [63] W.H. Clark, D.E. Elder, D. Guerry, L.E. Braitman, B.J. Trock, D. Schultz, M. Synnestvedt, A.C. Halpern, Model predicting survival in stage I melanoma based on tumor progression, *Journal of the National Cancer Institute*, 81 (1989) 1893-1904.
- [64] D. Guerry IV, M. Synnestvedt, D.E. Elder, D. Schultz, Lessons from tumor progression: the invasive radial growth phase of melanoma is common, incapable of metastasis, and indolent, *Journal of investigative dermatology*, 100 (1993) S342-S345.
- [65] J.E. Mayer, S.M. Swetter, T. Fu, A.C. Geller, Screening, early detection, education, and trends for melanoma: current status (2007-2013) and future directions: Part II. Screening, education, and future directions, *Journal of the American Academy of Dermatology*, 71 (2014) 611. e611-611. e610.
- [66] M. Carrara, A. Bono, C. Bartoli, A. Colombo, M. Lualdi, D. Moglia, N. Santoro, E. Tolomio, S. Tomatis, G. Tragni, Multispectral imaging and artificial neural network: mimicking the management decision of the clinician facing pigmented skin lesions, *Physics in Medicine & Biology*, 52 (2007) 2599.
- [67] D.S. Rigel, M. Roy, J. Yoo, C.J. Cockerell, J.K. Robinson, R. White, Impact of guidance from a computer-aided multispectral digital skin lesion analysis device on decision to biopsy lesions clinically suggestive of melanoma, *Archives of dermatology*, 148 (2012) 541-543.
- [68] I. Quinzán, J.M. Sotoca, P. Latorre-Carmona, F. Pla, P. García-Sevilla, E. Boldó, Band selection in spectral imaging for non-invasive melanoma diagnosis, *Biomedical optics express*, 4 (2013) 514-519.
- [69] I. Tromme, L. Sacré, F. Hammouch, C. Legrand, L. Marot, P. Vereecken, I. Theate, P. van Eeckhout, P. Richez, J.-F. Baurain, Availability of digital dermoscopy in daily practice dramatically reduces the number of excised melanocytic lesions: results from an observational study, *British Journal of Dermatology*, 167 (2012) 778-786.
- [70] A. Saez, C. Serrano, B. Acha, Model-based classification methods of global patterns in dermoscopic images, *IEEE Trans. Med. Imaging*, 33 (2014) 1137-1147.
- [71] G. Pellacani, B. De Pace, C. Reggiani, A.M. Cesinaro, G. Argenziano, I. Zalaudek, H.P. Soyer, C. Longo, Distinct melanoma types based on reflectance confocal microscopy, *Experimental dermatology*, 23 (2014) 414-418.
- [72] A. Dancey, B. Mahon, S. Rayatt, A review of diagnostic imaging in melanoma, *Journal of Plastic, Reconstructive & Aesthetic Surgery*, 61 (2008) 1275-1283.

- [73] R. Kleinerman, T.B. Whang, R.L. Bard, E.S. Marmur, Ultrasound in dermatology: principles and applications, *Journal of the American Academy of Dermatology*, 67 (2012) 478-487.
- [74] R.E. Hunger, R.D. Torre, A. Serov, T. Hunziker, Assessment of melanocytic skin lesions with a high-definition laser Doppler imaging system, *Skin research and technology*, 18 (2012) 207-211.
- [75] Z. Hamdoon, W. Jerjes, T. Upile, C. Hopper, Optical coherence tomography-guided photodynamic therapy for skin cancer: case study, *Photodiagnosis and Photodynamic Therapy*, 8 (2011) 49-52.
- [76] L. Themstrup, C. Banzhaf, M. Mogensen, G. Jemec, Optical coherence tomography imaging of non-melanoma skin cancer undergoing photodynamic therapy reveals subclinical residual lesions, *Photodiagnosis and photodynamic therapy*, 11 (2014) 7-12.
- [77] T.E. Lin, A. Bondarenko, A. Lesch, H. Pick, F. Cortés-Salazar, H.H. Girault, Monitoring Tyrosinase Expression in Non-metastatic and Metastatic Melanoma Tissues by Scanning Electrochemical Microscopy, *Angewandte Chemie International Edition*, 55 (2016) 3813-3816.
- [78] S. Li, L. Mao, Y. Tian, J. Wang, N. Zhou, Spectrophotometric detection of tyrosinase activity based on boronic acid-functionalized gold nanoparticles, *Analyst*, 137 (2012) 823-825.
- [79] T.-I. Kim, J. Park, S. Park, Y. Choi, Y. Kim, Visualization of tyrosinase activity in melanoma cells by a BODIPY-based fluorescent probe, *Chemical Communications*, 47 (2011) 12640-12642.
- [80] T.-S. Chang, An updated review of tyrosinase inhibitors, *International journal of molecular sciences*, 10 (2009) 2440-2475.
- [81] Y. Tomita, T. Suzuki, Genetics of pigmentary disorders, *American Journal of Medical Genetics Part C: Seminars in Medical Genetics*, Wiley Online Library, 2004, pp. 75-81.
- [82] W.S. Oetting, R.A. King, Molecular basis of oculocutaneous albinism, *Journal of investigative dermatology*, 103 (1994).
- [83] C. Angeletti, V. Khomitch, R. Halaban, D.L. Rimm, Novel tyramide-based tyrosinase assay for the detection of melanoma cells in cytological preparations, *Diagnostic cytopathology*, 31 (2004) 33-37.
- [84] S.J. Ohsie, G.P. Sarantopoulos, A.J. Cochran, S.W. Binder, Immunohistochemical characteristics of melanoma, *Journal of cutaneous pathology*, 35 (2008) 433-444.
- [85] J.C. García-Borrón, F. Solano, Molecular anatomy of tyrosinase and its related proteins: beyond the histidine-bound metal catalytic center, *Pigment Cell Research*, 15 (2002) 162-173.
- [86] P.H. Lambert, P.E. Laurent, Intradermal vaccine delivery: will new delivery systems transform vaccine administration?, *Vaccine*, 26 (2008) 3197-3208.
- [87] M. Matteucci, M. Casella, M. Bedoni, E. Donetti, M. Fanetti, F. De Angelis, F. Gramatica, E. Di Fabrizio, A compact and disposable transdermal drug delivery system, *Microelectronic Engineering*, 85 (2008) 1066-1073.
- [88] A.L. Teo, C. Shearwood, K.C. Ng, J. Lu, S. Mochhala, Transdermal microneedles for drug delivery applications, *Materials Science and Engineering: B*, 132 (2006) 151-154.
- [89] R.F. Donnelly, R. Majithiya, T.R.R. Singh, D.I. Morrow, M.J. Garland, Y.K. Demir, K. Migalska, E. Ryan, D. Gillen, C.J. Scott, Design, optimization and characterisation of polymeric microneedle arrays prepared by a novel laser-based micromoulding technique, *Pharmaceutical research*, 28 (2011) 41-57.
- [90] M.S. Gerstel, V.A. Place, Drug delivery device, Google Patents, 1976.
- [91] R.S. Shawgo, A.C.R. Grayson, Y. Li, M.J. Cima, BioMEMS for drug delivery, *Current Opinion in Solid State and Materials Science*, 6 (2002) 329-334.
- [92] Y. Xie, B. Xu, Y. Gao, Controlled transdermal delivery of model drug compounds by MEMS microneedle array, *Nanomedicine: Nanotechnology, Biology and Medicine*, 1 (2005) 184-190.
- [93] S. Hashmi, P. Ling, G. Hashmi, M. Reed, R. Gaugler, W. Trimmer, Genetic transformation of nematodes using arrays of micromechanical piercing structures, *BioTechniques*, 19 (1995) 766-770.
- [94] S. Henry, D.V. McAllister, M.G. Allen, M.R. Prausnitz, Microfabricated microneedles: a novel approach to transdermal drug delivery, *Journal of pharmaceutical sciences*, 87 (1998) 922-925.
- [95] F.J. Verbaan, S. Bal, D. Van den Berg, W. Groenink, H. Verpoorten, R. Lüttge, J.A. Bouwstra, Assembled microneedle arrays enhance the transport of compounds varying over a large range of molecular weight across human dermatomed skin, *Journal of Controlled Release*, 117 (2007) 238-245.
- [96] Y. Ito, E. Hagiwara, A. Saeki, N. Sugioka, K. Takada, Feasibility of microneedles for percutaneous absorption of insulin, *European journal of pharmaceutical sciences*, 29 (2006) 82-88.
- [97] J. Wang, J. Lu, S.Y. Ly, M. Vuki, B. Tian, W.K. Adeniyi, R.A. Armendariz, Lab-on-a-cable for electrochemical monitoring of phenolic contaminants, *Analytical chemistry*, 72 (2000) 2659-2663.
- [98] A. Ovsianikov, B. Chichkov, P. Mente, N. Monteiro-Riviere, A. Doraiswamy, R. Narayan, Two photon polymerization of polymer-ceramic hybrid materials for transdermal drug delivery, *International journal of applied ceramic technology*, 4 (2007) 22-29.
- [99] C.S. Kolli, A.K. Banga, Characterization of solid maltose microneedles and their use for transdermal delivery, *Pharmaceutical research*, 25 (2008) 104-113.
- [100] R.F. Donnelly, D.I. Morrow, T.R. Singh, K. Migalska, P.A. McCarron, C. O'Mahony, A.D. Woolfson, Processing difficulties and instability of carbohydrate microneedle arrays, *Drug development and industrial pharmacy*, 35 (2009) 1242-1254.

- [101] D.V. McAllister, P.M. Wang, S.P. Davis, J.-H. Park, P.J. Canatella, M.G. Allen, M.R. Prausnitz, Microfabricated needles for transdermal delivery of macromolecules and nanoparticles: fabrication methods and transport studies, *Proceedings of the National Academy of Sciences*, 100 (2003) 13755-13760.
- [102] J.-H. Park, M.G. Allen, M.R. Prausnitz, Biodegradable polymer microneedles: fabrication, mechanics and transdermal drug delivery, *Journal of Controlled Release*, 104 (2005) 51-66.
- [103] F. Perennes, B. Marmioli, M. Matteucci, M. Tormen, L. Vaccari, E. Di Fabrizio, Sharp beveled tip hollow microneedle arrays fabricated by LIGA and 3D soft lithography with polyvinyl alcohol, *Journal of Micromechanics and Microengineering*, 16 (2006) 473.
- [104] A.K. Banga, Microporation applications for enhancing drug delivery, *Expert opinion on drug delivery*, 6 (2009) 343-354.
- [105] S. Aoyagi, H. Izumi, Y. Isono, M. Fukuda, H. Ogawa, Laser fabrication of high aspect ratio thin holes on biodegradable polymer and its application to a microneedle, *Sensors and Actuators A: Physical*, 139 (2007) 293-302.
- [106] J.W. Lee, J.-H. Park, M.R. Prausnitz, Dissolving microneedles for transdermal drug delivery, *Biomaterials*, 29 (2008) 2113-2124.
- [107] M. Han, D.-H. Hyun, H.-H. Park, S.S. Lee, C.-H. Kim, C. Kim, A novel fabrication process for out-of-plane microneedle sheets of biocompatible polymer, *Journal of Micromechanics and Microengineering*, 17 (2007) 1184.
- [108] P. Aggarwal, C. Johnston, Geometrical effects in mechanical characterizing of microneedle for biomedical applications, *Sensors and Actuators B: Chemical*, 102 (2004) 226-234.
- [109] S.P. Davis, B.J. Landis, Z.H. Adams, M.G. Allen, M.R. Prausnitz, Insertion of microneedles into skin: measurement and prediction of insertion force and needle fracture force, *Journal of biomechanics*, 37 (2004) 1155-1163.
- [110] B. Ciui, A. Martin, R.K. Mishra, B. Brunetti, T. Nakagawa, T.J. Dawkins, M. Lyu, C. Cristea, R. Sandulescu, J. Wang, *Wearable Wireless Tyrosinase Bandage and Microneedle Sensors: Toward Melanoma Screening*, *Advanced healthcare materials*, (2018).
- [111] M.E. Davey, G.A. O'toole, Microbial biofilms: from ecology to molecular genetics, *Microbiology and molecular biology reviews*, 64 (2000) 847-867.
- [112] P.E. Kolenbrander, R.J. Palmer, S. Periasamy, N.S. Jakubovics, Oral multispecies biofilm development and the key role of cell-cell distance, *Nature Reviews Microbiology*, 8 (2010) 471-480.
- [113] I.W. Sutherland, The biofilm matrix—an immobilized but dynamic microbial environment, *Trends in microbiology*, 9 (2001) 222-227.
- [114] T.-F.C. Mah, G.A. O'Toole, Mechanisms of biofilm resistance to antimicrobial agents, *Trends in microbiology*, 9 (2001) 34-39.
- [115] M.E. Olson, H. Ceri, D.W. Morck, A.G. Buret, R.R. Read, Biofilm bacteria: formation and comparative susceptibility to antibiotics, *Canadian journal of veterinary research*, 66 (2002) 86.
- [116] H.-C. Flemming, J. Wingender, The biofilm matrix, *Nature reviews microbiology*, 8 (2010) 623-633.
- [117] R.M. Donlan, J.W. Costerton, Biofilms: survival mechanisms of clinically relevant microorganisms, *Clinical microbiology reviews*, 15 (2002) 167-193.
- [118] C.A. Fux, J.W. Costerton, P.S. Stewart, P. Stoodley, Survival strategies of infectious biofilms, *Trends in microbiology*, 13 (2005) 34-40.
- [119] A. Ito, A. Taniuchi, T. May, K. Kawata, S. Okabe, Increased antibiotic resistance of *Escherichia coli* in mature biofilms, *Applied and environmental microbiology*, 75 (2009) 4093-4100.
- [120] E. Werner, F. Roe, A. Bugnicourt, M.J. Franklin, A. Heydorn, S. Molin, B. Pitts, P.S. Stewart, Stratified growth in *Pseudomonas aeruginosa* biofilms, *Applied and environmental microbiology*, 70 (2004) 6188-6196.
- [121] P.S. Stewart, J.W. Costerton, Antibiotic resistance of bacteria in biofilms, *The lancet*, 358 (2001) 135-138.
- [122] M.E. Roberts, P.S. Stewart, Modeling antibiotic tolerance in biofilms by accounting for nutrient limitation, *Antimicrobial Agents and Chemotherapy*, 48 (2004) 48-52.
- [123] M. Matsumoto-Nakano, H.K. Kuramitsu, Role of bacteriocin immunity proteins in the antimicrobial sensitivity of *Streptococcus mutans*, *Journal of bacteriology*, 188 (2006) 8095-8102.
- [124] A. Nocker, A.K. Camper, Novel approaches toward preferential detection of viable cells using nucleic acid amplification techniques, *FEMS microbiology letters*, 291 (2009) 137-142.
- [125] P. Breeuwer, T. Abee, Assessment of the membrane potential, intracellular pH and respiration of bacteria employing fluorescence techniques, *Molecular microbial ecology manual*, 8 (2004) 1563-1580.
- [126] T. Le, T. Ruyssen, M. Uyttendaele, P. Van Assche, K. Dewettinck, Assessment with a compact flow cytometer of live, injured and dead probiotic lactobacilli and bifidobacteria after subjecting to osmotic, freeze and heat stress, *Conference on Food Science and Technology—Mekong Delta*, 20th–22nd March, 2008.
- [127] A. Mahdhi, M.Á. Esteban, Z. Hmila, K. Bekir, F. Kamoun, A. Bakhrouf, B. Krifi, Survival and retention of the probiotic properties of *Bacillus* sp. strains under marine stress starvation conditions and their potential use as a probiotic in *Artemia* culture, *Research in veterinary science*, 93 (2012) 1151-1159.

- [128] S. Lahtinen, H. Ahokoski, J.P. Reinikainen, M. Gueimonde, J. Nurmi, A.C. Ouwehand, S. Salminen, Degradation of 16S rRNA and attributes of viability of viable but nonculturable probiotic bacteria, *Letters in applied microbiology*, 46 (2008) 693-698.
- [129] N. Shah, Probiotic bacteria: selective enumeration and survival in dairy foods, *Journal of dairy science*, 83 (2000) 894-907.
- [130] J. Keer, L. Birch, Molecular methods for the assessment of bacterial viability, *Journal of microbiological methods*, 53 (2003) 175-183.
- [131] J. Azeredo, N.F. Azevedo, R. Briandet, N. Cerca, T. Coenye, A.R. Costa, M. Desvaux, G. Di Bonaventura, M. Hébraud, Z. Jaglic, Critical review on biofilm methods, *Critical reviews in microbiology*, 43 (2017) 313-351.
- [132] V. Adetunji, I.A. Odetokun, Assessment of biofilm in *E. coli* O157: H7 and *Salmonella* strains: influence of cultural conditions, *Am. J. Food Technol*, 7 (2012) 582-595.
- [133] T.E. Cloete, V.S. Brözel, A. Von Holy, Practical aspects of biofouling control in industrial water systems, *International biodeterioration & biodegradation*, 29 (1992) 299-341.
- [134] R.K. Pettit, C.A. Weber, M.J. Kean, H. Hoffmann, G.R. Pettit, R. Tan, K.S. Franks, M.L. Horton, Microplate Alamar blue assay for *Staphylococcus epidermidis* biofilm susceptibility testing, *Antimicrobial Agents and Chemotherapy*, 49 (2005) 2612-2617.
- [135] K. Fang, X. Jin, S.H. Hong, Probiotic *Escherichia coli* inhibits biofilm formation of pathogenic *E. coli* via extracellular activity of DegP, *Scientific reports*, 8 (2018) 4939.
- [136] G. Álvarez, M. González, S. Isabal, V. Blanc, R. León, Method to quantify live and dead cells in multi-species oral biofilm by real-time PCR with propidium monoazide, *Amb Express*, 3 (2013) 1.
- [137] M. Sanchez, M. Marin, E. Figuero, A. Llama-Palacios, D. Herrera, M. Sanz, Analysis of viable vs. dead *Aggregatibacter actinomycetemcomitans* and *Porphyromonas gingivalis* using selective quantitative real-time PCR with propidium monoazide, *Journal of Periodontal Research*, 48 (2013) 213-220.
- [138] M. Sanchez, M. Marin, E. Figuero, A. Llama-Palacios, R. Leon, V. Blanc, D. Herrera, M. Sanz, Quantitative real-time PCR combined with propidium monoazide for the selective quantification of viable periodontal pathogens in an in vitro subgingival biofilm model, *Journal of periodontal research*, 49 (2014) 20-28.
- [139] P.D. Ghatak, S.S. Mathew-Steiner, P. Pandey, S. Roy, C.K. Sen, A surfactant polymer dressing potentiates antimicrobial efficacy in biofilm disruption, *Scientific reports*, 8 (2018) 873.
- [140] H.K. Nogva, S.M. Drømtorp, H. Nissen, K. Rudi, Ethidium monoazide for DNA-based differentiation of viable and dead bacteria by 5'-nuclease PCR, *Biotechniques*, 34 (2003) 804-813.
- [141] K. Rudi, B. Moen, S.M. Drømtorp, A.L. Holck, Use of ethidium monoazide and PCR in combination for quantification of viable and dead cells in complex samples, *Applied and environmental microbiology*, 71 (2005) 1018-1024.
- [142] K. Rudi, K. Naterstad, S. Drømtorp, H. Holo, Detection of viable and dead *Listeria monocytogenes* on gouda-like cheeses by real-time PCR, *Letters in Applied Microbiology*, 40 (2005) 301-306.
- [143] E.M. Townsend, L. Sherry, R. Rajendran, D. Hansom, J. Butcher, W.G. Mackay, C. Williams, G. Ramage, Development and characterisation of a novel three-dimensional inter-kingdom wound biofilm model, *Biofouling*, 32 (2016) 1259-1270.
- [144] A. Nocker, C.-Y. Cheung, A.K. Camper, Comparison of propidium monoazide with ethidium monoazide for differentiation of live vs. dead bacteria by selective removal of DNA from dead cells, *Journal of microbiological methods*, 67 (2006) 310-320.
- [145] G. Flekna, P. Štefanič, M. Wagner, F.J. Smulders, S.S. Možina, I. Hein, Insufficient differentiation of live and dead *Campylobacter jejuni* and *Listeria monocytogenes* cells by ethidium monoazide (EMA) compromises EMA/real-time PCR, *Research in Microbiology*, 158 (2007) 405-412.
- [146] D.M. Cawthorn, R. Witthuhn, Selective PCR detection of viable *Enterobacter sakazakii* cells utilizing propidium monoazide or ethidium bromide monoazide, *Journal of Applied Microbiology*, 105 (2008) 1178-1185.
- [147] A. Nocker, K.E. Sossa, A.K. Camper, Molecular monitoring of disinfection efficacy using propidium monoazide in combination with quantitative PCR, *Journal of microbiological methods*, 70 (2007) 252-260.
- [148] A.B. Chan, NASBA and other transcription-based amplification methods for research and diagnostic microbiology, *Rev. Med. Microbiol.*, 10 (1999) 185-196.
- [149] T.J. Hellyer, J.G. Nadeau, Strand displacement amplification: a versatile tool for molecular diagnostics, *Expert review of molecular diagnostics*, 4 (2004) 251-261.
- [150] J.L. McKillip, L.-A. Jaykus, M. Drake, rRNA stability in heat-killed and UV-irradiated enterotoxigenic *Staphylococcus aureus* and *Escherichia coli* O157: H7, *Applied and Environmental Microbiology*, 64 (1998) 4264-4268.
- [151] A.C. Pérez-Osorio, M.J. Franklin, qRT-PCR of microbial biofilms, *Cold Spring Harbor Protocols*, 2008 (2008) pdb. prot5066.

- [152] B.P. Tracy, S.M. Gaida, E.T. Papoutsakis, Flow cytometry for bacteria: enabling metabolic engineering, synthetic biology and the elucidation of complex phenotypes, *Current opinion in biotechnology*, 21 (2010) 85-99.
- [153] S. Chen, Y. Cao, L.R. Ferguson, Q. Shu, S. Garg, Flow cytometric assessment of the protectants for enhanced in vitro survival of probiotic lactic acid bacteria through simulated human gastro-intestinal stresses, *Applied microbiology and biotechnology*, 95 (2012) 345-356.
- [154] M. Berney, F. Hammes, F. Bosshard, H.-U. Weilenmann, T. Egli, Assessment and interpretation of bacterial viability by using the LIVE/DEAD BacLight Kit in combination with flow cytometry, *Applied and environmental microbiology*, 73 (2007) 3283-3290.
- [155] G.D. Christensen, W.A. Simpson, J. Younger, L. Baddour, F. Barrett, D. Melton, E. Beachey, Adherence of coagulase-negative staphylococci to plastic tissue culture plates: a quantitative model for the adherence of staphylococci to medical devices, *Journal of clinical microbiology*, 22 (1985) 996-1006.
- [156] K. Welch, Y. Cai, M. Strømme, A method for quantitative determination of biofilm viability, *Journal of Functional Biomaterials*, 3 (2012) 418-431.
- [157] V. Leriche, P. Sibille, B. Carpentier, Use of an enzyme-linked lectinsorbent assay to monitor the shift in polysaccharide composition in bacterial biofilms, *Applied and environmental microbiology*, 66 (2000) 1851-1856.
- [158] J. O'Brien, I. Wilson, T. Orton, F. Pognan, Investigation of the Alamar Blue (resazurin) fluorescent dye for the assessment of mammalian cell cytotoxicity, *European journal of biochemistry*, 267 (2000) 5421-5426.
- [159] A. Mariscal, R.M. Lopez-Gigosos, M. Carnero-Varo, J. Fernandez-Crehuet, Fluorescent assay based on resazurin for detection of activity of disinfectants against bacterial biofilm, *Applied microbiology and biotechnology*, 82 (2009) 773-783.
- [160] K. Honraet, E. Goetghebeur, H.J. Nelis, Comparison of three assays for the quantification of *Candida* biomass in suspension and CDC reactor grown biofilms, *Journal of microbiological methods*, 63 (2005) 287-295.
- [161] B. Prieto, B. Silva, O. Lantes, Biofilm quantification on stone surfaces: comparison of various methods, *Science of the Total Environment*, 333 (2004) 1-7.
- [162] E. Peeters, H.J. Nelis, T. Coenye, Comparison of multiple methods for quantification of microbial biofilms grown in microtiter plates, *Journal of microbiological methods*, 72 (2008) 157-165.
- [163] F. Berlutti, F. Rosso, P. Bosso, F. Giansanti, M. Ajello, A. De Rosa, E. Farina, G. Antonini, P. Valenti, Quantitative evaluation of bacteria adherent to polyelectrolyte HEMA-based hydrogels, *Journal of Biomedical Materials Research Part A: An Official Journal of The Society for Biomaterials, The Japanese Society for Biomaterials, and The Australian Society for Biomaterials and the Korean Society for Biomaterials*, 67 (2003) 18-25.
- [164] F. Pantanella, P. Valenti, A. Frioni, T. Natalizi, L. Coltella, F. Berlutti, BioTimer Assay, a new method for counting *Staphylococcus* spp. in biofilm without sample manipulation applied to evaluate antibiotic susceptibility of biofilm, *Journal of microbiological methods*, 75 (2008) 478-484.
- [165] R.M. Donlan, Biofilm formation: a clinically relevant microbiological process, *Clinical Infectious Diseases*, 33 (2001) 1387-1392.
- [166] M.E. Sandberg, D. Schellmann, G. Brunhofer, T. Erker, I. Busygin, R. Leino, P.M. Vuorela, A. Fallarero, Pros and cons of using resazurin staining for quantification of viable *Staphylococcus aureus* biofilms in a screening assay, *Journal of microbiological methods*, 78 (2009) 104-106.
- [167] G. Li, Y. Wu, Y. Li, Y. Hong, X. Zhao, P.I. Reyes, Y. Lu, Early stage detection of *Staphylococcus epidermidis* biofilm formation using MgZnO dual-gate TFT biosensor, *Biosensors and Bioelectronics*, 151 (2020) 111993.
- [168] D. Naradasu, A. Guionet, W. Miran, A. Okamoto, Microbial current production from *Streptococcus mutans* correlates with biofilm metabolic activity, *Biosensors and Bioelectronics*, 162 (2020) 112236.
- [169] X. Liu, S. Zhuo, X. Jing, Y. Yuan, C. Rensing, S. Zhou, Flagella act as *Geobacter* biofilm scaffolds to stabilize biofilm and facilitate extracellular electron transfer, *Biosensors and Bioelectronics*, 146 (2019) 111748.
- [170] B. Abada, S. Boumerfeg, A. Haddad, M. Etienne, Electrochemical Investigation of *Thiobacillus Denitrificans* in a Bacterial Composite, *Journal of The Electrochemical Society*, 167 (2020) 135502.
- [171] S. Nara, R. Kandpal, V. Jaiswal, S. Augustine, S. Wahie, J.G. Sharma, R. Takeuchi, S. Takenaka, B.D. Malhotra, Exploring *Providencia rettgeri* for application to eco-friendly paper based microbial fuel cell, *Biosensors and Bioelectronics*, 165 (2020) 112323.
- [172] Y. Zhu, M. Jović, A. Lesch, L. Tissières Lovey, M. Prudent, H. Pick, H.H. Girault, Immuno-affinity Amperometric Detection of Bacterial Infections, *Angewandte Chemie International Edition*, 57 (2018) 14942-14946.
- [173] O. Simoska, K.J. Stevenson, Electrochemical sensors for rapid diagnosis of pathogens in real time, *Analyst*, 144 (2019) 6461-6478.

- [174] J.L. Connell, J. Kim, J.B. Shear, A.J. Bard, M. Whiteley, Real-time monitoring of quorum sensing in 3D-printed bacterial aggregates using scanning electrochemical microscopy, *Proceedings of the National Academy of Sciences*, 111 (2014) 18255-18260.
- [175] D. Koley, M.M. Ramsey, A.J. Bard, M. Whiteley, Discovery of a biofilm electrocline using real-time 3D metabolite analysis, *Proceedings of the National Academy of Sciences*, 108 (2011) 19996-20001.
- [176] D.L. Bellin, H. Sakhtah, Y. Zhang, A. Price-Whelan, L.E. Dietrich, K.L. Shepard, Electrochemical camera chip for simultaneous imaging of multiple metabolites in biofilms, *Nature communications*, 7 (2016) 1-10.
- [177] G. Caniglia, C. Kranz, Scanning electrochemical microscopy and its potential for studying biofilms and antimicrobial coatings, *Analytical and Bioanalytical Chemistry*, (2020) 1-16.
- [178] J. Zhang, T. Zhu, J. Lang, W. Fu, F. Li, Recent advances of scanning electrochemical microscopy and scanning ion conductance microscopy for single cell analysis, *Current Opinion in Electrochemistry*, (2020).
- [179] J. Petroniene, I. Morkvenaite-Vilkonciene, R. Miksiunas, D. Bironaite, A. Ramanaviciene, K. Rucinskas, V. Janusauskas, A. Ramanavicius, Scanning electrochemical microscopy for the investigation of redox potential of human myocardium-derived mesenchymal stem cells grown at 2D and 3D conditions, *Electrochimica Acta*, 360 (2020) 136956.
- [180] A. Valiūnienė, J. Petronienė, M. Dulkys, A. Ramanavičius, Investigation of active and inactivated yeast cells by scanning electrochemical impedance microscopy, *Electroanalysis*, 32 (2020) 367-374.
- [181] R. Borghese, M. Malferrari, M. Brucale, L. Ortolani, M. Franchini, S. Rapino, F. Borsetti, D. Zannoni, Structural and electrochemical characterization of lawsone-dependent production of tellurium-metal nanoprecipitates by photosynthetic cells of *Rhodobacter capsulatus*, *Bioelectrochemistry*, 133 (2020) 107456.
- [182] C.S. Santos, F. Macedo, A.J. Kowaltowski, M. Bertotti, P.R. Unwin, F.M. da Cunha, G.N. Meloni, Unveiling the contribution of the reproductive system of individual *Caenorhabditis elegans* on oxygen consumption by single-point scanning electrochemical microscopy measurements, *Analytica chimica acta*, 1146 (2021) 88-97.
- [183] E. Abucayon, N. Ke, R. Cornut, A. Patelunas, D. Miller, M.K. Nishiguchi, C.G. Zoski, Investigating catalase activity through hydrogen peroxide decomposition by bacteria biofilms in real time using scanning electrochemical microscopy, *Analytical chemistry*, 86 (2014) 498-505.
- [184] D. Rudolph, D. Bates, T.J. DiChristina, B. Mizaiakoff, C. Kranz, Detection of Metal-reducing Enzyme Complexes by Scanning Electrochemical Microscopy, *Electroanalysis*, 28 (2016) 2459-2465.
- [185] S.E. Darch, D. Koley, Quantifying microbial chatter: scanning electrochemical microscopy as a tool to study interactions in biofilms, *Proceedings of the Royal Society A*, 474 (2018) 20180405.
- [186] S. Daboss, J. Lin, M. Godejohann, C. Kranz, Redox Switchable Polydopamine-Modified AFM-SECM Probes: A Probe for Electrochemical Force Spectroscopy, *Analytical chemistry*, 92 (2020) 8404-8413.
- [187] L. Guerret-Legras, J. Audibert, G. Dubacheva, F. Miomandre, Combined scanning electrochemical and fluorescence microscopies using a tetrazine as a single redox and luminescent (electrofluorochromic) probe, *Chemical science*, 9 (2018) 5897-5905.
- [188] L. Guerret-Legras, J. Audibert, I.G. Ojeda, G. Dubacheva, F. Miomandre, Combined SECM-fluorescence microscopy using a water-soluble electrofluorochromic dye as the redox mediator, *Electrochimica Acta*, 305 (2019) 370-377.
- [189] K. Cremin, B.A. Jones, J. Teahan, G.N. Meloni, D. Perry, C. Zerfass, M. Asally, O.S. Soyer, P.R. Unwin, Scanning Ion Conductance Microscopy Reveals Differences in the Ionic Environments of Gram-Positive and Negative Bacteria, *Analytical Chemistry*, 92 (2020) 16024-16032.
- [190] C. Cai, B. Liu, M.V. Mirkin, H.A. Frank, J.F. Rusling, Scanning electrochemical microscopy of living cells. 3. *Rhodobacter sphaeroides*, *Analytical chemistry*, 74 (2002) 114-119.
- [191] T. Kaya, D. Numai, K. Nagamine, S. Aoyagi, H. Shiku, T. Matsue, Respiration activity of *Escherichia coli* entrapped in a cone-shaped microwell and cylindrical micropore monitored by scanning electrochemical microscopy (SECM), *Analyst*, 129 (2004) 529-534.
- [192] G. Gao, D. Wang, R. Brocenschi, J. Zhi, M.V. Mirkin, Toward the detection and identification of single bacteria by electrochemical collision technique, *Analytical chemistry*, 90 (2018) 12123-12130.
- [193] V.S. Joshi, J. Kreth, D. Koley, Pt-decorated MWCNTs-ionic liquid composite-based hydrogen peroxide sensor to study microbial metabolism using scanning electrochemical microscopy, *Analytical chemistry*, 89 (2017) 7709-7718.
- [194] N.M. Jayathilake, D. Koley, Glucose microsensor with covalently immobilized glucose oxidase for probing bacterial glucose uptake by scanning electrochemical microscopy, *Analytical chemistry*, 92 (2020) 3589-3597.
- [195] L. Liu, Y. Xu, F. Cui, Y. Xia, L. Chen, X. Mou, J. Lv, Monitoring of bacteria biofilms forming process by in-situ impedimetric biosensor chip, *Biosensors and Bioelectronics*, 112 (2018) 86-92.
- [196] D. Banerjee, P. Shivapriya, P.K. Gautam, K. Misra, A.K. Sahoo, S.K. Samanta, A review on basic biology of bacterial biofilm infections and their treatments by nanotechnology-based approaches, *Proceedings of the National Academy of Sciences, India Section B: Biological Sciences*, (2019) 1-17.
- [197] M. Ramasamy, J. Lee, Recent nanotechnology approaches for prevention and treatment of biofilm-associated infections on medical devices, *BioMed Research International*, 2016 (2016).

- [198] K. Ganesh, M. Sinha, S.S. Mathew-Steiner, A. Das, S. Roy, C.K. Sen, Chronic wound biofilm model, *Advances in wound care*, 4 (2015) 382-388.
- [199] M.R. Parsek, P.K. Singh, Bacterial biofilms: an emerging link to disease pathogenesis, *Annual Reviews in Microbiology*, 57 (2003) 677-701.
- [200] R. Singh, P. Ray, A. Das, M. Sharma, Penetration of antibiotics through *Staphylococcus aureus* and *Staphylococcus epidermidis* biofilms, *Journal of antimicrobial chemotherapy*, 65 (2010) 1955-1958.
- [201] G. Anderson, G. O'toole, Innate and induced resistance mechanisms of bacterial biofilms, *Bacterial biofilms*, Springer 2008, pp. 85-105.
- [202] E.C. Weiss, A. Zielinska, K.E. Beenken, H.J. Spencer, S.J. Daily, M.S. Smeltzer, Impact of sarA on daptomycin susceptibility of *Staphylococcus aureus* biofilms in vivo, *Antimicrobial agents and chemotherapy*, 53 (2009) 4096-4102.
- [203] V. Tzaneva, I. Mladenova, G. Todorova, D. Petkov, Antibiotic treatment and resistance in chronic wounds of vascular origin, *Clujul medical*, 89 (2016) 365.
- [204] G. Han, R. Ceilleuy, Chronic wound healing: a review of current management and treatments, *Advances in therapy*, 34 (2017) 599-610.
- [205] C.M. Jones, A.T. Rothermel, D.R. Mackay, Evidence-based medicine: wound management, *Plastic and reconstructive surgery*, 140 (2017) 201e-216e.
- [206] Y.-J.R. Chang, J. Perry, K. Cross, Low-frequency ultrasound debridement in chronic wound healing: A systematic review of current evidence, *Plastic Surgery*, 25 (2017) 21-26.
- [207] W.-L. Liu, Y.-L. Jiang, Y.-Q. Wang, Y.-X. Li, Y.-X. Liu, Combined debridement in chronic wounds: A literature review, *Chinese Nursing Research*, 4 (2017) 5-8.
- [208] M. Sareh Amini, M. Abolfazl ShojaeeFard, M. Zohreh Annabestani, M. Mohsen Rezaie Hammami, B. Zahra Shaiganmehr, M. Bagher Larijani, Low-frequency ultrasound debridement in patients with diabetic foot ulcers and osteomyelitis, *Wounds*, 25 (2013) 193-198.
- [209] C.A. Murphy, P. Houghton, T. Brandys, G. Rose, D. Bryant, The effect of 22.5 kHz low-frequency contact ultrasound debridement (LFCUD) on lower extremity wound healing for a vascular surgery population: a randomised controlled trial, *International wound journal*, 15 (2018) 460-472.
- [210] O.M. Alvarez, M.E. Wendelken, M.S. Granick, Debridement of Venous Leg Ulcers With Direct-Contact, Low-Frequency Ultrasound: Results of a Randomized, Prospective, Controlled, Clinical Trial, *Eplasty*, 19 (2019).
- [211] H. Wang, F. Teng, X. Yang, X. Guo, J. Tu, C. Zhang, D. Zhang, Preventing microbial biofilms on catheter tubes using ultrasonic guided waves, *Scientific Reports*, 7 (2017) 1-9.
- [212] G. LuTheryn, P. Glynne-Jones, J.S. Webb, D. Carugo, Ultrasound-mediated therapies for the treatment of biofilms in chronic wounds: a review of present knowledge, *Microbial Biotechnology*, 13 (2020) 613-628.
- [213] M. Lee, E.Y. Lee, D. Lee, B.J. Park, Stabilization and fabrication of microbubbles: applications for medical purposes and functional materials, *Soft matter*, 11 (2015) 2067-2079.
- [214] J. Owen, C. Crake, J.Y. Lee, D. Carugo, E. Beguin, A.A. Khrapitchev, R.J. Browning, N. Sibson, E. Stride, A versatile method for the preparation of particle-loaded microbubbles for multimodality imaging and targeted drug delivery, *Drug delivery and translational research*, 8 (2018) 342-356.
- [215] R.D. Wolcott, K.P. Rumbaugh, G. James, G. Schultz, P. Phillips, Q. Yang, C. Watters, P.S. Stewart, S.E. Dowd, Biofilm maturity studies indicate sharp debridement opens a time-dependent therapeutic window, *Journal of wound care*, 19 (2010) 320-328.
- [216] K. Marion-Ferey, M. Pasmore, P. Stoodley, S. Wilson, G. Husson, J.W. Costerton, Biofilm removal from silicone tubing: an assessment of the efficacy of dialysis machine decontamination procedures using an in vitro model, *Journal of Hospital Infection*, 53 (2003) 64-71.
- [217] S. Finnegan, S.L. Percival, EDTA: an antimicrobial and antibiofilm agent for use in wound care, *Advances in wound care*, 4 (2015) 415-421.
- [218] R. Wolcott, Disrupting the biofilm matrix improves wound healing outcomes, *Journal of wound care*, 24 (2015) 366-371.
- [219] L.-m. Sun, C.-I. Zhang, P. Li, Characterization, antibiofilm, and mechanism of action of novel PEG-stabilized lipid nanoparticles loaded with terpinen-4-ol, *Journal of agricultural and food chemistry*, 60 (2012) 6150-6156.
- [220] E. Taylor, T.J. Webster, Reducing infections through nanotechnology and nanoparticles, *International journal of nanomedicine*, 6 (2011) 1463.
- [221] P.A. Suci, D.L. Berglund, L. Liepold, S. Brumfield, B. Pitts, W. Davison, L. Oltrogge, K.O. Hoyt, S. Codd, P.S. Stewart, High-density targeting of a viral multifunctional nanoplatform to a pathogenic, biofilm-forming bacterium, *Chemistry & biology*, 14 (2007) 387-398.
- [222] N. Beyth, Y. Houri-Haddad, A. Domb, W. Khan, R. Hazan, Alternative antimicrobial approach: nano-antimicrobial materials, *Evidence-based complementary and alternative medicine*, 2015 (2015).
- [223] J.R. Morones, J.L. Elechiguerra, A. Camacho, K. Holt, J.B. Kouri, J.T. Ramírez, M.J. Yacaman, The bactericidal effect of silver nanoparticles, *Nanotechnology*, 16 (2005) 2346.

- [224] A.B. Lansdown, Silver in health care: antimicrobial effects and safety in use, *Biofunctional textiles and the skin*, Karger Publishers 2006, pp. 17-34.
- [225] W.K. Jung, H.C. Koo, K.W. Kim, S. Shin, S.H. Kim, Y.H. Park, Antibacterial activity and mechanism of action of the silver ion in *Staphylococcus aureus* and *Escherichia coli*, *Applied and environmental microbiology*, 74 (2008) 2171-2178.
- [226] A.B. Lansdown, Silver I: its antibacterial properties and mechanism of action, *Journal of wound care*, 11 (2002) 125-130.
- [227] K. Chaw, M. Manimaran, F.E. Tay, Role of silver ions in destabilization of intermolecular adhesion forces measured by atomic force microscopy in *Staphylococcus epidermidis* biofilms, *Antimicrobial agents and chemotherapy*, 49 (2005) 4853-4859.
- [228] U. Klueh, V. Wagner, S. Kelly, A. Johnson, J. Bryers, Efficacy of silver-coated fabric to prevent bacterial colonization and subsequent device-based biofilm formation, *Journal of Biomedical Materials Research: An Official Journal of The Society for Biomaterials, The Japanese Society for Biomaterials, and The Australian Society for Biomaterials and the Korean Society for Biomaterials*, 53 (2000) 621-631.
- [229] C. Baker, A. Pradhan, L. Pakstis, D.J. Pochan, S.I. Shah, Synthesis and antibacterial properties of silver nanoparticles, *Journal of nanoscience and nanotechnology*, 5 (2005) 244-249.
- [230] L. Shkodenko, I. Kassirov, E. Koshel, Metal oxide nanoparticles against bacterial biofilms: perspectives and limitations, *Microorganisms*, 8 (2020) 1545.
- [231] J.A. Lichter, M.F. Rubner, Polyelectrolyte multilayers with intrinsic antimicrobial functionality: the importance of mobile polycations, *Langmuir*, 25 (2009) 7686-7694.
- [232] A.L. Lee, V.W. Ng, W. Wang, J.L. Hedrick, Y.Y. Yang, Block copolymer mixtures as antimicrobial hydrogels for biofilm eradication, *Biomaterials*, 34 (2013) 10278-10286.
- [233] D. Dankort, D.P. Curley, R.A. Cartledge, B. Nelson, A.N. Karnezis, W.E. Damsky Jr, M.J. You, R.A. DePinho, M. McMahon, M. Bosenberg, Braf V600E cooperates with Pten loss to induce metastatic melanoma, *Nature genetics*, 41 (2009) 544.
- [234] B. Song, L.G. Leff, Influence of magnesium ions on biofilm formation by *Pseudomonas fluorescens*, *Microbiological research*, 161 (2006) 355-361.
- [235] V. Körstgens, H.-C. Flemming, J. Wingender, W. Borchard, Influence of calcium ions on the mechanical properties of a model biofilm of mucoid *Pseudomonas aeruginosa*, *Water science and technology*, 43 (2001) 49-57.
- [236] A. Šileikaitė, J. Puišo, I. Prosyčevs, S. Tamulevičius, Investigation of silver nanoparticles formation kinetics during reduction of silver nitrate with sodium citrate, *Materials Science (Medžiagotyra)*, 15 (2009) 21-27.
- [237] N. Arshi, F. Ahmed, S. Kumar, M. Anwar, B.H. Koo, C.G. Lee, Comparative study of the Ag/PVP nanocomposites synthesized in water and in ethylene glycol, *Current Applied Physics*, 11 (2011) S346-S349.
- [238] T. Yoshidome, M. Endo, G. Kashiwazaki, K. Hidaka, T. Bando, H. Sugiyama, Sequence-selective single-molecule alkylation with a pyrrole-imidazole polyamide visualized in a DNA nanoscaffold, *Journal of the American Chemical Society*, 134 (2012) 4654-4660.
- [239] I. Mela, P.P. Vallejo-Ramirez, S. Makarchuk, G. Christie, D. Bailey, R.M. Henderson, H. Sugiyama, M. Endo, C.F. Kaminski, DNA nanostructures for targeted antimicrobial delivery, *Angewandte Chemie*, 132 (2020) 12798-12802.
- [240] M.Y. Song, D. Nguyen, S.W. Hong, B.C. Kim, Broadly reactive aptamers targeting bacteria belonging to different genera using a sequential toggle cell-SELEX, *Scientific reports*, 7 (2017) 1-10.
- [241] B.A. Webb, M. Chimenti, M.P. Jacobson, D.L. Barber, Dysregulated pH: a perfect storm for cancer progression, *Nature Reviews Cancer*, 11 (2011) 671-677.
- [242] F. Ströhl, C.F. Kaminski, A joint Richardson—Lucy deconvolution algorithm for the reconstruction of multifocal structured illumination microscopy data, *Methods and Applications in Fluorescence*, 3 (2015) 014002.
- [243] L.J. Young, F. Ströhl, C.F. Kaminski, A guide to structured illumination TIRF microscopy at high speed with multiple colors, *JoVE (Journal of Visualized Experiments)*, (2016) e53988.
- [244] J.K. Rivers, M.R. Copley, R. Svoboda, D.S. Rigel, Non-Invasive Gene Expression Testing to Rule Out Melanoma, *Skin therapy letter*, 23 (2018) 1-4.
- [245] C. Fink, H.A. Haenssle, Non-invasive tools for the diagnosis of cutaneous melanoma, *Skin Research and Technology*, 23 (2017) 261-271.
- [246] P. Gerami, Z. Yao, D. Polsky, B. Jansen, K. Busam, J. Ho, M. Martini, L.K. Ferris, Development and validation of a noninvasive 2-gene molecular assay for cutaneous melanoma, *Journal of the American Academy of Dermatology*, 76 (2017) 114-120.e112.
- [247] V. Narayanamurthy, P. Padmapriya, A. Noorasafin, B. Pooja, K. Hema, A.Y. Firus Khan, K. Nithyakalyani, F. Samsuri, Skin cancer detection using non-invasive techniques, *RSC Advances*, 8 (2018) 28095-28130.
- [248] M.L. Clausen, H.C. Slotved, K.A. Krogfelt, T. Agner, Tape Stripping Technique for Stratum Corneum Protein Analysis, *Scientific Reports*, 6 (2016).

- [249] O. Forslund, B. Lindelöf, E. Hradil, P. Nordin, B. Stenquist, R. Kirnbauer, K. Slupetzky, J. Dillner, High prevalence of cutaneous human papillomavirus DNA on the top of skin tumors but not in "stripped" biopsies from the same tumors, *Journal of Investigative Dermatology*, 123 (2004) 388-394.
- [250] W. Wachsmann, V. Morhenn, T. Palmer, L. Walls, T. Hata, J. Zalla, R. Scheinberg, H. Sofen, S. Mraz, K. Gross, H. Rabinovitz, D. Polsky, S. Chang, Noninvasive genomic detection of melanoma, *British Journal of Dermatology*, 164 (2011) 797-806.
- [251] S. Hou, L. Zhao, Q. Shen, J. Yu, C. Ng, X. Kong, D. Wu, M. Song, X. Shi, X. Xu, W.H. Ouyang, R. He, X.Z. Zhao, T. Lee, F.C. Brunicardi, M.A. Garcia, A. Ribas, R.S. Lo, H.R. Tseng, Polymer nanofiber-embedded microchips for detection, isolation, and molecular analysis of single circulating melanoma cells, *Angewandte Chemie - International Edition*, 52 (2013) 3379-3383.
- [252] K. Warton, K.L. Mahon, G. Samimi, Methylated circulating tumor DNA in blood: Power in cancer prognosis and response, *Endocrine-Related Cancer*, 23 (2016) R157-R171.
- [253] T.B. Steinbichler, J. Dudás, H. Riechelmann, I.I. Skvortsova, The role of exosomes in cancer metastasis, *Seminars in Cancer Biology*, 44 (2017) 170-181.
- [254] G. Yang, L. Li, R.K. Rana, J.-J. Zhu, Assembled gold nanoparticles on nitrogen-doped graphene for ultrasensitive electrochemical detection of matrix metalloproteinase-2, *Carbon*, 61 (2013) 357-366.
- [255] A. Eftekhari, E. Ahmadian, S. Salatin, S. Sharifi, S.M. Dizaj, R. Khalilov, M. Hasanzadeh, Current analytical approaches in diagnosis of melanoma, *TrAC Trends in Analytical Chemistry*, 116 (2019) 122-135.
- [256] L. Syedmoradi, M. Daneshpour, M. Alvandipour, F.A. Gomez, H. Hajghassem, K. Omidfar, Point of care testing: The impact of nanotechnology, *Biosensors and Bioelectronics*, 87 (2017) 373-387.
- [257] A. Pal, H.E. Cuellar, R. Kuang, H.F.N. Caurin, D. Goswami, R.V. Martinez, Self-Powered, Paper-Based Electrochemical Devices for Sensitive Point-of-Care Testing, *Advanced Materials Technologies*, 2 (2017).
- [258] Y. Zhu, M. Jović, A. Lesch, L. Tissières Lovey, M. Prudent, H. Pick, H.H. Girault, Immuno-affinity Amperometric Detection of Bacterial Infections, *Angewandte Chemie - International Edition*, 57 (2018) 14942-14946.
- [259] M. Mossberg, S. Vernick, R. Ortenberg, G. Markel, Y. Shacham-Diamand, J. Rishpon, A direct electrochemical detection method of melanoma based on melanoma biomarker, *Electroanalysis*, 26 (2014) 1671-1675.
- [260] X. Lai, H.J. Wickers, M. Soler-Lopez, B.W. Dijkstra, Structure and Function of Human Tyrosinase and Tyrosinase-Related Proteins, *Chemistry - A European Journal*, 24 (2018) 47-55.
- [261] D. Weinstein, J. Leininger, C. Hamby, B. Safai, Diagnostic and prognostic biomarkers in melanoma, *Journal of Clinical and Aesthetic Dermatology*, 7 (2014) 13-24.
- [262] T.E. Lin, F. Cortés-Salazar, A. Lesch, L. Qiao, A. Bondarenko, H.H. Girault, Multiple scanning electrochemical microscopy mapping of tyrosinase in micro-contact printed fruit samples on polyvinylidene fluoride membrane, *Electrochimica Acta*, 179 (2015) 57-64.
- [263] T.E. Lin, Y.J. Lu, C.L. Sun, H. Pick, J.P. Chen, A. Lesch, H.H. Girault, Soft Electrochemical Probes for Mapping the Distribution of Biomarkers and Injected Nanomaterials in Animal and Human Tissues, *Angewandte Chemie - International Edition*, 56 (2017) 16498-16502.
- [264] B. Ciui, A. Martin, R.K. Mishra, B. Brunetti, T. Nakagawa, T.J. Dawkins, M. Lyu, C. Cristea, R. Sandulescu, J. Wang, Wearable wireless tyrosinase bandage and microneedle sensors: toward melanoma screening, *Advanced healthcare materials*, 7 (2018) 1701264.
- [265] T.-E. Lin, S. Rapino, H.H. Girault, A. Lesch, Electrochemical Imaging of cells and tissues, *Chemical Science*, 9 (2018) 4546-4554.
- [266] A. Soldà, G. Valenti, M. Marcaccio, M. Giorgio, P.G. Pelicci, F. Paolucci, S. Rapino, Glucose and Lactate Miniaturized Biosensors for SECM-Based High-Spatial Resolution Analysis: A Comparative Study, *ACS Sensors*, 2 (2017) 1310-1318.
- [267] F.P. Filice, Z. Ding, Analysing single live cells by scanning electrochemical microscopy, *Analyst*, 144 (2019) 738-752.
- [268] C. Cai, B. Liu, M.V. Mirkin, H.A. Frank, J.F. Rusling, Scanning electrochemical microscopy of living cells. 3. *Rhodobacter sphaeroides*, *Analytical Chemistry*, 74 (2002) 114-119.
- [269] S. Kuss, D. Polcari, M. Geissler, D. Brassard, J. Mauzeroll, Assessment of multidrug resistance on cell coculture patterns using scanning electrochemical microscopy, *Proceedings of the National Academy of Sciences of the United States of America*, 110 (2013) 9249-9254.
- [270] S. Rapino, R. Marcu, A. Bigi, A. Soldà, M. Marcaccio, F. Paolucci, P.G. Pelicci, M. Giorgio, Scanning electrochemical microscopy reveals cancer cell redox state, *Electrochimica Acta*, 179 (2015) 65-73.
- [271] Y. Matsumae, Y. Takahashi, H. Shiku, T. Matsue, Quantitative Real-Time Monitoring of Antibody-Induced Internalization of Epidermal Growth Factor Receptor on Single Living Mammalian Cells Using Scanning Electrochemical Microscopy, *ChemElectroChem*, 5 (2018) 3096-3101.
- [272] J.D. Henderson, F.P. Filice, M.S.M. Li, Z. Ding, Tracking Live-Cell Response to Hexavalent Chromium Toxicity by using Scanning Electrochemical Microscopy, *ChemElectroChem*, 4 (2017) 856-863.
- [273] P. Actis, S. Tokar, J. Clausmeyer, B. Babakinejad, S. Mikhaleva, R. Cornut, Y. Takahashi, A. López Córdoba, P. Novak, A.I. Shevchuck, J.A. Dougan, S.G. Kazarian, P.V. Gorelkin, A.S. Erofeev, I.V. Yaminsky,

P.R. Unwin, W. Schuhmann, D. Klenerman, D.A. Rusakov, E.V. Sviderskaya, Y.E. Korchev, Electrochemical nanoprobe for single-cell analysis, *ACS Nano*, 8 (2014) 875-884.

[274] J. Clausmeyer, W. Schuhmann, Nanoelectrodes: Applications in electrocatalysis, single-cell analysis and high-resolution electrochemical imaging, *TrAC - Trends in Analytical Chemistry*, 79 (2016) 46-59.

[275] Y. Li, K. Hu, Y. Yu, S.A. Rotenberg, C. Amatore, M.V. Mirkin, Direct Electrochemical Measurements of Reactive Oxygen and Nitrogen Species in Nontransformed and Metastatic Human Breast Cells, *Journal of the American Chemical Society*, 139 (2017) 13055-13062.

[276] S. Ito, M. Okura, Y. Nakanishi, M. Ojika, K. Wakamatsu, T. Yamashita, Tyrosinase-catalyzed metabolism of rhododendrol (RD) in B16 melanoma cells: Production of RD-pheomelanin and covalent binding with thiol proteins, *Pigment Cell and Melanoma Research*, 28 (2015) 295-306.

[277] P.D. Josephy, T. Eling, R.P. Mason, The horseradish peroxidase-catalyzed oxidation of 3,5,3',5'-tetramethylbenzidine. Free radical and charge-transfer complex intermediates, *Journal of Biological Chemistry*, 257 (1982) 3669-3675.

[278] A. Bondarenko, T.-E. Lin, P. Stupar, A. Lesch, F. Cortés-Salazar, H.H. Girault, H. Pick, Fixation and permeabilization approaches for scanning electrochemical microscopy of living cells, *Analytical chemistry*, 88 (2016) 11436-11443.

[279] F. Cortés-Salazar, D. Momotenko, A. Lesch, G. Wittstock, H.H. Girault, Soft microelectrode linear array for scanning electrochemical microscopy, *Analytical Chemistry*, 82 (2010) 10037-10044.

[280] L.K. Ferris, R.L. Moy, P. Gerami, J.E. Sligh, B. Jansen, Z. Yao, C.J. Cockerell, Noninvasive Analysis of High-Risk Driver Mutations and Gene Expression Profiles in Primary Cutaneous Melanoma, *Journal of Investigative Dermatology*, 139 (2019) 1127-1134.

[281] R. Halaban, E. Cheng, Y. Zhang, G. Moellmann, D. Hanlon, M. Michalak, V. Setaluri, D.N. Hebert, Aberrant retention of tyrosinase in the endoplasmic reticulum mediates accelerated degradation of the enzyme and contributes to the dedifferentiated phenotype of amelanotic melanoma cells, *Proceedings of the National Academy of Sciences of the United States of America*, 94 (1997) 6210-6215.

[282] F. Mahmoud, B. Shields, I. Makhoul, N. Avaritt, H.K. Wong, L.F. Hutchins, S. Shalin, A.J. Tackett, Immune surveillance in melanoma: From immune attack to melanoma escape and even counterattack, *Cancer Biology and Therapy*, 18 (2017) 451-469.

[283] Y. Zhu, A. Lesch, X. Li, T.-E. Lin, N. Gasilova, M. Jović, H.M. Pick, P.-C. Ho, H.H. Girault, Rapid Noninvasive Skin Monitoring by Surface Mass Recording and Data Learning, *JACS Au*, 1 (2021) 598-611.

[284] K. Ino, T. Onodera, Y. Kanno, A. Suda, R. Kunikata, T. Matsue, H. Shiku, Electrochemicolor imaging of endogenous alkaline phosphatase and respiratory activities of mesenchymal stem cell aggregates in early-stage osteodifferentiation, *Electrochimica Acta*, 268 (2018) 554-561.

[285] H. Lee, T.K. Choi, Y.B. Lee, H.R. Cho, R. Ghaffari, L. Wang, H.J. Choi, T.D. Chung, N. Lu, T. Hyeon, A graphene-based electrochemical device with thermoresponsive microneedles for diabetes monitoring and therapy, *Nature nanotechnology*, 11 (2016) 566-572.

[286] P.M. Wang, M. Cornwell, M.R. Prausnitz, Minimally invasive extraction of dermal interstitial fluid for glucose monitoring using microneedles, *Diabetes technology & therapeutics*, 7 (2005) 131-141.

[287] P.R. Miller, R.J. Narayan, R. Polsky, Microneedle-based sensors for medical diagnosis, *Journal of Materials Chemistry B*, 4 (2016) 1379-1383.

[288] S.C. Jena, S. Shrivastava, S. Saxena, N. Kumar, S.K. Maiti, B.P. Mishra, R.K. Singh, Surface plasmon resonance immunosensor for label-free detection of BIRC5 biomarker in spontaneously occurring canine mammary tumours, *Scientific reports*, 9 (2019) 1-12.

[289] Y. Niu, T. Kang, G. Jin, Joint detection of tumor markers with imaging ellipsometry biosensor, *Thin solid films*, 571 (2014) 453-462.

[290] S. Darvishi, H. Pick, T.-E. Lin, Y. Zhu, X. Li, P.-C. Ho, H.H. Girault, A. Lesch, Tape-stripping electrochemical detection of melanoma, *Analytical chemistry*, 91 (2019) 12900-12908.

[291] J. Okuno, K. Maehashi, K. Kerman, Y. Takamura, K. Matsumoto, E. Tamiya, Label-free immunosensor for prostate-specific antigen based on single-walled carbon nanotube array-modified microelectrodes, *Biosensors and Bioelectronics*, 22 (2007) 2377-2381.

[292] N.J. Ronkainen, H.B. Halsall, W.R. Heineman, Electrochemical biosensors, *Chemical Society Reviews*, 39 (2010) 1747-1763.

[293] J. Li, S. Li, C.F. Yang, Electrochemical biosensors for cancer biomarker detection, *Electroanalysis*, 24 (2012) 2213-2229.

[294] T.-E. Lin, F. Cortés-Salazar, A. Lesch, L. Qiao, A. Bondarenko, H.H. Girault, Multiple scanning electrochemical microscopy mapping of tyrosinase in micro-contact printed fruit samples on polyvinylidene fluoride membrane, *Electrochimica Acta*, 179 (2015) 57-64.

[295] A.J. Hobro, N.I. Smith, An evaluation of fixation methods: Spatial and compositional cellular changes observed by Raman imaging, *Vibrational Spectroscopy*, 91 (2017) 31-45.

[296] K. Ho, S. Newman, State of the art electrical discharge machining (EDM), *International Journal of Machine Tools and Manufacture*, 43 (2003) 1287-1300.

[297] S. Krishnamurthy, A. Esterle, N.C. Sharma, S.V. Sahi, Yucca-derived synthesis of gold nanomaterial and their catalytic potential, *Nanoscale research letters*, 9 (2014) 627.

- [298] R.B. Groves, S. Coulman, J.C. Birchall, S.L. Evans, Quantifying the mechanical properties of human skin to optimise future microneedle device design, *Computer methods in biomechanics and biomedical engineering*, 15 (2012) 73-82.
- [299] J.J. García-Guzmán, C. Pérez-Ràfols, M. Cuartero, G.A. Crespo, Microneedle based electrochemical (Bio) Sensing: Towards decentralized and continuous health status monitoring, *TrAC Trends in Analytical Chemistry*, (2020) 116148.
- [300] W. Groenendaal, G. Von Basum, K.A. Schmidt, P.A. Hilbers, N.A. van Riel, Quantifying the composition of human skin for glucose sensor development, *SAGE Publications Sage CA: Los Angeles, CA*, 2010.
- [301] S. Ravetti, C. Clemente, S. Brignone, L. Hergert, D. Allemandi, S. Palma, Ascorbic acid in skin health, *Cosmetics*, 6 (2019) 58.
- [302] G.-e. Rhie, M.H. Shin, J.Y. Seo, W.W. Choi, K.H. Cho, K.H. Kim, K.C. Park, H.C. Eun, J.H. Chung, Aging- and photoaging-dependent changes of enzymic and nonenzymic antioxidants in the epidermis and dermis of human skin in vivo, *Journal of investigative dermatology*, 117 (2001) 1212-1217.
- [303] N.K. Gibbs, M. Norval, Urocanic acid in the skin: a mixed blessing?, *Journal of Investigative Dermatology*, 131 (2011) 14-17.
- [304] M. Besouw, L. Van den Heuvel, R. van Eijdsen, I. Bongaers, L. Kluijtmans, M. Dewerchin, E. Levchenko, Increased human dermal microvascular endothelial cell survival induced by cysteamine, *Journal of inherited metabolic disease*, 36 (2013) 1073-1077.
- [305] M. Rinnerthaler, J. Bischof, M.K. Streubel, A. Trost, K. Richter, Oxidative stress in aging human skin, *Biomolecules*, 5 (2015) 545-589.
- [306] T. Bjarnsholt, The role of bacterial biofilms in chronic infections, *Apmis*, 121 (2013) 1-58.
- [307] P. Neopane, H.P. Nepal, R. Shrestha, O. Uehara, Y. Abiko, In vitro biofilm formation by *Staphylococcus aureus* isolated from wounds of hospital-admitted patients and their association with antimicrobial resistance, *International journal of general medicine*, 11 (2018) 25.
- [308] N. Sabir, A. Ikram, G. Zaman, L. Satti, A. Gardezi, A. Ahmed, P. Ahmed, Bacterial biofilm-based catheter-associated urinary tract infections: Causative pathogens and antibiotic resistance, *American journal of infection control*, 45 (2017) 1101-1105.
- [309] C. Vuotto, F. Longo, C. Pascolini, G. Donelli, M. Balice, M. Libori, V. Tiracchia, A. Salvia, P. Varaldo, Biofilm formation and antibiotic resistance in *Klebsiella pneumoniae* urinary strains, *Journal of applied microbiology*, 123 (2017) 1003-1018.
- [310] O. Fysun, H. Kern, B. Wilke, H.-C. Langowski, Evaluation of factors influencing dairy biofilm formation in filling hoses of food-processing equipment, *Food and bioproducts processing*, 113 (2019) 39-48.
- [311] C. Reichhardt, M.R. Parsek, Confocal laser scanning microscopy for analysis of *Pseudomonas aeruginosa* biofilm architecture and matrix localization, *Frontiers in microbiology*, 10 (2019) 677.
- [312] Y. Chao, T. Zhang, Optimization of fixation methods for observation of bacterial cell morphology and surface ultrastructures by atomic force microscopy, *Applied microbiology and biotechnology*, 92 (2011) 381-392.
- [313] J. Maukonen, T. Mattila-Sandholm, G. Wirtanen, Metabolic indicators for assessing bacterial viability in hygiene sampling using cells in suspension and swabbed biofilm, *LWT-Food Science and Technology*, 33 (2000) 225-233.
- [314] N. Doroshenko, B.S. Tseng, R.P. Howlin, J. Deacon, J.A. Wharton, P.J. Thurner, B.F. Gilmore, M.R. Parsek, P. Stoodley, Extracellular DNA impedes the transport of vancomycin in *Staphylococcus epidermidis* biofilms preexposed to subinhibitory concentrations of vancomycin, *Antimicrobial agents and chemotherapy*, 58 (2014) 7273-7282.
- [315] P.Y. Feipeing, G.A. McFeters, Rapid in situ assessment of physiological activities in bacterial biofilms using fluorescent probes, *Journal of Microbiological Methods*, 20 (1994) 1-10.
- [316] C. Guilhen, C. Forestier, D. Balestrino, Biofilm dispersal: multiple elaborate strategies for dissemination of bacteria with unique properties, *Molecular microbiology*, 105 (2017) 188-210.
- [317] B.M. Appenzeller, C. Yañez, F. Jorand, J.-C. Block, Advantage provided by iron for *Escherichia coli* growth and cultivability in drinking water, *Applied and Environmental Microbiology*, 71 (2005) 5621-5623.
- [318] Y. Fan, R. Hao, C. Han, B. Zhang, Counting Single Redox Molecules in a Nanoscale Electrochemical Cell, *Analytical chemistry*, 90 (2018) 13837-13841.
- [319] Z. Hu, J. Jin, H.D. Abruña, P.L. Houston, A.G. Hay, W.C. Ghiorse, M.L. Shuler, G. Hidalgo, L.W. Lion, Spatial distributions of copper in microbial biofilms by scanning electrochemical microscopy, *Environmental science & technology*, 41 (2007) 936-941.
- [320] F. Kracke, I. Vassilev, J.O. Krömer, Microbial electron transport and energy conservation—the foundation for optimizing bioelectrochemical systems, *Frontiers in microbiology*, 6 (2015) 575.
- [321] Y.-F. Wang, S. Tsujimura, S.-S. Cheng, K. Kano, Self-excreted mediator from *Escherichia coli* K-12 for electron transfer to carbon electrodes, *Applied microbiology and biotechnology*, 76 (2007) 1439-1446.
- [322] L. Wang, M. Di Luca, T. Tkhilaishvili, A. Trampuz, M. Gonzalez Moreno, Synergistic activity of fosfomycin, ciprofloxacin, and gentamicin against *Escherichia coli* and *Pseudomonas aeruginosa* biofilms, *Frontiers in microbiology*, 10 (2019) 2522.

- [323] A.H. Delcour, Outer membrane permeability and antibiotic resistance, *Biochimica et Biophysica Acta (BBA)-Proteins and Proteomics*, 1794 (2009) 808-816.
- [324] B.U. Tezel, N. Akçelik, F.N. Yüksel, N.T. Karatuğ, M. Akçelik, Effects of sub-MIC antibiotic concentrations on biofilm production of *Salmonella Infantis*, *Biotechnology & Biotechnological Equipment*, 30 (2016) 1184-1191.
- [325] R.M. Donlan, Biofilms: microbial life on surfaces, *Emerging infectious diseases*, 8 (2002) 881.
- [326] H. Koo, R.N. Allan, R.P. Howlin, P. Stoodley, L. Hall-Stoodley, Targeting microbial biofilms: current and prospective therapeutic strategies, *Nature Reviews Microbiology*, 15 (2017) 740.
- [327] O. Ciofu, T. Tolker-Nielsen, Tolerance and resistance of *Pseudomonas aeruginosa* biofilms to antimicrobial agents—how *P. aeruginosa* can escape antibiotics, *Frontiers in microbiology*, 10 (2019) 913.
- [328] M. Espy, J. Uhl, L. Sloan, S. Buckwalter, M. Jones, E. Vetter, J. Yao, N. Wengenack, J. Rosenblatt, F. Cockerill, Real-time PCR in clinical microbiology: applications for routine laboratory testing, *Clinical microbiology reviews*, 19 (2006) 165-256.
- [329] M. Jahn, J. Seifert, M. von Bergen, A. Schmid, B. Bühler, S. Müller, Subpopulation-proteomics in prokaryotic populations, *Current opinion in biotechnology*, 24 (2013) 79-87.
- [330] T.U. Sørensen, G.J. Gram, S.D. Nielsen, J.E.S. Hansen, Safe sorting of GFP-transduced live cells for subsequent culture using a modified FACS Vantage, *Cytometry: The Journal of the International Society for Analytical Cytology*, 37 (1999) 284-290.
- [331] V. Ambriz-Aviña, J.A. Contreras-Garduño, M. Pedraza-Reyes, Applications of flow cytometry to characterize bacterial physiological responses, *BioMed research international*, 2014 (2014).
- [332] G. Gebreyohannes, A. Nyerere, C. Bii, D.B. Sbhata, Challenges of intervention, treatment, and antibiotic resistance of biofilm-forming microorganisms, *Heliyon*, 5 (2019) e02192.
- [333] O. Braissant, M. Astasov-Frauenhoffer, T. Waltimo, G. Bonkat, A review of methods to determine viability, vitality, and metabolic rates in microbiology, *Frontiers in Microbiology*, 11 (2020).
- [334] E. Cesewski, B.N. Johnson, Electrochemical biosensors for pathogen detection, *Biosensors and Bioelectronics*, (2020) 112214.
- [335] S. Darvishi, M. Souissi, F. Karimzadeh, M. Kharaziha, R. Sahara, S. Ahadian, Ni nanoparticle-decorated reduced graphene oxide for non-enzymatic glucose sensing: an experimental and modeling study, *Electrochimica Acta*, 240 (2017) 388-398.
- [336] S. Darvishi, M. Souissi, M. Kharaziha, F. Karimzadeh, R. Sahara, S. Ahadian, Gelatin methacryloyl hydrogel for glucose biosensing using Ni nanoparticles-reduced graphene oxide: an experimental and modeling study, *Electrochimica Acta*, 261 (2018) 275-283.
- [337] S. Darvishi, F. Karmizadeh, M. Kharaziha, A facile one-step electrochemical synthesis of nickel nanoparticle/Graphene composites for non-enzymatic biosensor applications, *Procedia Materials Science*, 11 (2015) 142-146.
- [338] L.A. Meirelles, D.K. Newman, Both toxic and beneficial effects of pyocyanin contribute to the lifecycle of *Pseudomonas aeruginosa*, *Molecular microbiology*, 110 (2018) 995-1010.
- [339] K.B. Holt, A.J. Bard, Interaction of silver (I) ions with the respiratory chain of *Escherichia coli*: an electrochemical and scanning electrochemical microscopy study of the antimicrobial mechanism of micromolar Ag⁺, *Biochemistry*, 44 (2005) 13214-13223.
- [340] G. Pecchiola, D. Battistel, S. Daniele, Scanning Electrochemical Microscopy and Voltammetric Investigation of Silver Nanoparticles Embedded within a Nafion Membrane, *ChemElectroChem*, 3 (2016) 2297-2304.
- [341] F.-R.F. Fan, A.J. Bard, Chemical, electrochemical, gravimetric, and microscopic studies on antimicrobial silver films, *The Journal of Physical Chemistry B*, 106 (2002) 279-287.
- [342] S. Aponso, J.G. Ummadi, H. Davis, J. Ferracane, D. Koley, A chemical approach to optimizing bioactive glass dental composites, *Journal of dental research*, 98 (2019) 194-199.
- [343] M.L.P. Vidallon, B.M. Teo, Recent developments in biomolecule-based nanoencapsulation systems for antimicrobial delivery and biofilm disruption, *Chemical Communications*, 56 (2020) 13907-13917.
- [344] X. Li, B. Wu, H. Chen, K. Nan, Y. Jin, L. Sun, B. Wang, Recent developments in smart antibacterial surfaces to inhibit biofilm formation and bacterial infections, *Journal of Materials Chemistry B*, 6 (2018) 4274-4292.
- [345] F.C. Tenover, Mechanisms of antimicrobial resistance in bacteria, *The American journal of medicine*, 119 (2006) S3-S10.
- [346] R. Patel, Biofilms and antimicrobial resistance, *Clinical Orthopaedics and Related Research®*, 437 (2005) 41-47.
- [347] S. Singh, S.K. Singh, I. Chowdhury, R. Singh, Understanding the mechanism of bacterial biofilms resistance to antimicrobial agents, *The open microbiology journal*, 11 (2017) 53.
- [348] Y.K. Mohanta, K. Biswas, S.K. Jena, A. Hashem, E.F. Abd Allah, T.K. Mohanta, Anti-biofilm and antibacterial activities of silver nanoparticles synthesized by the reducing activity of phytoconstituents present in the Indian medicinal plants, *Frontiers in Microbiology*, 11 (2020).

- [349] K. Markowska, A.M. Grudniak, K.I. Wolska, Silver nanoparticles as an alternative strategy against bacterial biofilms, *Acta Biochimica Polonica*, 60 (2013).
- [350] X. Xu, Y. Wang, S. Liao, Z.T. Wen, Y. Fan, Synthesis and characterization of antibacterial dental monomers and composites, *Journal of Biomedical Materials Research Part B: Applied Biomaterials*, 100 (2012) 1151-1162.
- [351] W.H. Lee, J.G. Pressman, D.G. Wahman, Three-dimensional free chlorine and monochloramine biofilm penetration: correlating penetration with biofilm activity and viability, *Environmental science & technology*, 52 (2018) 1889-1898.
- [352] D. Leung, D.A. Spratt, J. Pratten, K. Gulabivala, N.J. Mordan, A.M. Young, Chlorhexidine-releasing methacrylate dental composite materials, *Biomaterials*, 26 (2005) 7145-7153.
- [353] L. Cabrol, M. Quemeneur, B. Misson, Inhibitory effects of sodium azide on microbial growth in experimental resuspension of marine sediment, *Journal of microbiological methods*, 133 (2017) 62-65.
- [354] H.C. Lichstein, M.H. Soule, Studies of the effect of sodium azide on microbic growth and respiration: II. The action of sodium azide on bacterial catalase, *Journal of bacteriology*, 47 (1944) 231.
- [355] Sorour Darvishi, Horst Pick, Emad Oveisi, Hubert H. Girault, a.A. Lesch, Electrochemical imaging of *E. coli* biofilms using Soft-Probe-Scanning Electrochemical Microscopy (under review), *Sensors and Actuators B: Chemical*, (2021).
- [356] T. Skeika, C.R. Zuconelli, S.T. Fujiwara, C.A. Pessoa, Preparation and electrochemical characterization of a carbon ceramic electrode modified with ferrocenecarboxylic acid, *Sensors*, 11 (2011) 1361-1374.
- [357] T.J. Silhavy, D. Kahne, S. Walker, The bacterial cell envelope, *Cold Spring Harbor perspectives in biology*, 2 (2010) a000414.
- [358] K. Chotinantakul, W. Suginta, A. Schulte, Advanced amperometric respiration assay for antimicrobial susceptibility testing, *Analytical chemistry*, 86 (2014) 10315-10322.
- [359] H. Nikaido, Molecular basis of bacterial outer membrane permeability revisited, *Microbiology and molecular biology reviews*, 67 (2003) 593-656.
- [360] N. Ruiz, D. Kahne, T.J. Silhavy, Advances in understanding bacterial outer-membrane biogenesis, *Nature Reviews Microbiology*, 4 (2006) 57-66.
- [361] C. Muheim, H. Götzke, A.U. Eriksson, S. Lindberg, I. Lauritsen, M.H. Nørholm, D.O. Daley, Increasing the permeability of *Escherichia coli* using MAC13243, *Scientific reports*, 7 (2017) 1-11.
- [362] N.A. Amro, L.P. Kotra, K. Wadu-Mesthrige, A. Bulychev, S. Mobashery, G.-y. Liu, High-resolution atomic force microscopy studies of the *Escherichia coli* outer membrane: structural basis for permeability, *Langmuir*, 16 (2000) 2789-2796.
- [363] H. Deng, P. Peljo, T.J. Stockmann, L. Qiao, T. Vainikka, K. Kontturi, M. Opallo, H.H. Girault, Surprising acidity of hydrated lithium cations in organic solvents, *Chemical Communications*, 50 (2014) 5554-5557.
- [364] D. Polcari, J.A. Hernández-Castro, K. Li, M. Geissler, J. Mauzeroll, Determination of the relationship between expression and functional activity of multidrug resistance-associated protein 1 using scanning electrochemical microscopy, *Analytical chemistry*, 89 (2017) 8988-8994.
- [365] X. Li, A.J. Bard, Scanning electrochemical microscopy of HeLa cells—Effects of ferrocene methanol and silver ion, *Journal of Electroanalytical Chemistry*, 628 (2009) 35-42.
- [366] S.I. Miller, N.R. Salama, The gram-negative bacterial periplasm: Size matters, *PLoS biology*, 16 (2018) e2004935.
- [367] M.V.M. Allen J. Bard, *Scanning Electrochemical Microscopy*, 2nd Edition ed., CRC Press Copyright Year 2012.
- [368] M.B. Hamed, E. Burchacka, L. Angus, A. Marchand, J. De Geyter, M.S. Loos, J. Anné, H. Klaassen, P. Chaltin, S. Karamanou, Effective Small Molecule Antibacterials from a Novel Anti-Protein Secretion Screen, *Microorganisms*, 9 (2021) 592.
- [369] M. Jamshad, R. Chandler, M. Jeeves, A. Robinson, F. Alam, T.C. Smith, A. Shah, O.J. Daubney, K.A. Dunne, N. Nabi, A genetic screen suggests an alternative mechanism for inhibition of SecA by azide, *bioRxiv*, (2017) 173039.
- [370] J. Weber, A.E. Senior, Effects of the inhibitors azide, dicyclohexylcarbodiimide, and aurovertin on nucleotide binding to the three F1-ATPase catalytic sites measured using specific tryptophan probes, *Journal of Biological Chemistry*, 273 (1998) 33210-33215.
- [371] L. Pires, K. Sachsenheimer, T. Kleintschek, A. Waldbaur, T. Schwartz, B.E. Rapp, Online monitoring of biofilm growth and activity using a combined multi-channel impedimetric and amperometric sensor, *Biosensors and Bioelectronics*, 47 (2013) 157-163.
- [372] L.M. Stabryla, K.A. Johnston, J.E. Millstone, L.M. Gilbertson, Emerging investigator series: it's not all about the ion: support for particle-specific contributions to silver nanoparticle antimicrobial activity, *Environmental Science: Nano*, 5 (2018) 2047-2068.
- [373] G. Arya, N. Sharma, R. Mankamna, S. Nimesh, Antimicrobial silver nanoparticles: future of nanomaterials, *Microbial Nanobionics*, Springer 2019, pp. 89-119.
- [374] L. Zeiri, B. Bronk, Y. Shabtai, J. Eichler, S. Efrima, Surface-enhanced Raman spectroscopy as a tool for probing specific biochemical components in bacteria, *Applied Spectroscopy*, 58 (2004) 33-40.

- [375] K. Mijndonckx, N. Leys, J. Mahillon, S. Silver, R. Van Houdt, Antimicrobial silver: uses, toxicity and potential for resistance, *Biometals*, 26 (2013) 609-621.
- [376] T.C. Dakal, A. Kumar, R.S. Majumdar, V. Yadav, Mechanistic basis of antimicrobial actions of silver nanoparticles, *Frontiers in microbiology*, 7 (2016) 1831.
- [377] M. Yamanaka, K. Hara, J. Kudo, Bactericidal actions of a silver ion solution on *Escherichia coli*, studied by energy-filtering transmission electron microscopy and proteomic analysis, *Applied and environmental microbiology*, 71 (2005) 7589-7593.
- [378] S.M. Wirth, G.V. Lowry, R.D. Tilton, Natural organic matter alters biofilm tolerance to silver nanoparticles and dissolved silver, *Environmental science & technology*, 46 (2012) 12687-12696.
- [379] E. Goh, X. Xu, P. McCormick, Effect of particle size on the UV absorbance of zinc oxide nanoparticles, *Scripta Materialia*, 78 (2014) 49-52.
- [380] M. Radzig, V. Nadtochenko, O. Koksharova, J. Kiwi, V. Lipasova, I. Khmel, Antibacterial effects of silver nanoparticles on gram-negative bacteria: influence on the growth and biofilms formation, mechanisms of action, *Colloids and Surfaces B: Biointerfaces*, 102 (2013) 300-306.
- [381] Y. Li, P. Xiao, Y. Wang, Y. Hao, Mechanisms and control measures of mature biofilm resistance to antimicrobial agents in the clinical context, *ACS omega*, 5 (2020) 22684-22690.
- [382] J. Tong, J.L. Anderson, Partitioning and diffusion of proteins and linear polymers in polyacrylamide gels, *Biophysical journal*, 70 (1996) 1505-1513.
- [383] T.-O. Peulen, K.J. Wilkinson, Diffusion of nanoparticles in a biofilm, *Environmental science & technology*, 45 (2011) 3367-3373.
- [384] L.P. Hadjipetrou, T. Gray-Young, M. Lilly, Effect of ferricyanide on energy production by *Escherichia coli*, *Microbiology*, 45 (1966) 479-488.
- [385] S.-H. Park, H.-S. Kim, Flash light-assisted facile and eco-friendly synthesis of platinum-based alloy nanoparticle/carbon nano-tube catalysts for a direct methanol fuel cell, *Journal of The Electrochemical Society*, 162 (2014) F204.
- [386] V. Costa Bassetto, M. Mensi, E. Oveisi, H.H. Girault, A. Lesch, Print-Light-Synthesis of Ni and NiFe-nanoscale catalysts for oxygen evolution, *ACS Applied Energy Materials*, 2 (2019) 6322-6331.
- [387] A. Lesch, Print-Light-Synthesis of Platinum Nanostructured Indium-Tin-Oxide Electrodes for Energy Research, *Advanced Materials Technologies*, 3 (2018) 1700201.
- [388] J. Drbohlavova, J. Chomoucka, V. Adam, M. Ryvolova, T. Eckschlager, J. Hubalek, R. Kizek, Nanocarriers for anticancer drugs-new trends in nanomedicine, *Current drug metabolism*, 14 (2013) 547-564.
- [389] Y. Liu, L. Shi, L. Su, H.C. van der Mei, P.C. Jutte, Y. Ren, H.J. Busscher, Nanotechnology-based antimicrobials and delivery systems for biofilm-infection control, *Chemical Society Reviews*, 48 (2019) 428-446.
- [390] X. Kong, Y. Liu, X. Huang, S. Huang, F. Gao, P. Rong, S. Zhang, K. Zhang, W. Zeng, Cancer therapy based on smart drug delivery with advanced nanoparticles, *Anti-Cancer Agents in Medicinal Chemistry (Formerly Current Medicinal Chemistry-Anti-Cancer Agents)*, 19 (2019) 720-730.
- [391] N.J. Vickers, Animal communication: when i'm calling you, will you answer too?, *Current biology*, 27 (2017) R713-R715.
- [392] K. Paunovska, D. Loughrey, C.D. Sago, R. Langer, J.E. Dahlman, Using large datasets to understand nanotechnology, *Advanced Materials*, 31 (2019) 1902798.
- [393] Y. Liu, H.J. Busscher, B. Zhao, Y. Li, Z. Zhang, H.C. van der Mei, Y. Ren, L. Shi, Surface-adaptive, antimicrobially loaded, micellar nanocarriers with enhanced penetration and killing efficiency in staphylococcal biofilms, *ACS nano*, 10 (2016) 4779-4789.
- [394] N.A. Lopes, A. Brandelli, Nanostructures for delivery of natural antimicrobials in food, *Critical reviews in food science and nutrition*, 58 (2018) 2202-2212.
- [395] H. Wolfmeier, D. Pletzer, S.C. Mansour, R.E. Hancock, New perspectives in biofilm eradication, *ACS infectious diseases*, 4 (2018) 93-106.
- [396] D. Zhao, S. Yu, B. Sun, S. Gao, S. Guo, K. Zhao, Biomedical applications of chitosan and its derivative nanoparticles, *Polymers*, 10 (2018) 462.
- [397] F.P. Melchels, J. Feijen, D.W. Grijpma, A review on stereolithography and its applications in biomedical engineering, *Biomaterials*, 31 (2010) 6121-6130.
- [398] C.H. Barros, H. Devlin, D.W. Hiebner, S. Vitale, L. Quinn, E. Casey, Enhancing curcumin's solubility and antibiofilm activity via silica surface modification, *Nanoscale Advances*, 2 (2020) 1694-1708.
- [399] J.S. Daniels, N. Pourmand, Label-free impedance biosensors: Opportunities and challenges, *Electroanalysis: An International Journal Devoted to Fundamental and Practical Aspects of Electroanalysis*, 19 (2007) 1239-1257.
- [400] J.R. Macdonald, *Impedance Spectroscopy--Emphasizing Solid Materials and Systems*, Wiley-Interscience, John Wiley and Sons, (1987) 1-346.
- [401] M.E. Spira, A. Hai, Multi-electrode array technologies for neuroscience and cardiology, *Nature nanotechnology*, 8 (2013) 83-94.

- [402] G. Hong, C.M. Lieber, Novel electrode technologies for neural recordings, *Nature Reviews Neuroscience*, 20 (2019) 330-345.
- [403] K. Niitsu, S. Ota, K. Gamo, H. Kondo, M. Hori, K. Nakazato, Development of microelectrode arrays using electroless plating for CMOS-based direct counting of bacterial and HeLa cells, *IEEE transactions on biomedical circuits and systems*, 9 (2015) 607-619.
- [404] E. Baldrich, F.X. Muñoz, C. García-Aljaro, Electrochemical detection of quorum sensing signaling molecules by dual signal confirmation at microelectrode arrays, *Analytical chemistry*, 83 (2011) 2097-2103.
- [405] J. Ren, Y. Zhou, Y. Zhou, C. Zhou, Z. Li, Q. Lin, H. Huang, A piezoelectric microelectrode arrays system for real-time monitoring of bacterial contamination in fresh milk, *Food and bioprocess technology*, 8 (2015) 228-237.
- [406] D. Khodagholy, T. Doublet, M. Gurfinkel, P. Quilichini, E. Ismailova, P. Leleux, T. Herve, S. Sanaur, C. Bernard, G.G. Malliaras, Highly conformable conducting polymer electrodes for in vivo recordings, *Advanced Materials*, 23 (2011) H268-H272.
- [407] K.A. Ludwig, N.B. Langhals, M.D. Joseph, S.M. Richardson-Burns, J.L. Hendricks, D.R. Kipke, Poly (3, 4-ethylenedioxythiophene)(PEDOT) polymer coatings facilitate smaller neural recording electrodes, *Journal of neural engineering*, 8 (2011) 014001.
- [408] D. Khodagholy, J.N. Gelinas, T. Thesen, W. Doyle, O. Devinsky, G.G. Malliaras, G. Buzsáki, NeuroGrid: recording action potentials from the surface of the brain, *Nature neuroscience*, 18 (2015) 310-315.
- [409] M. Sessolo, D. Khodagholy, J. Rivnay, F. Maddalena, M. Gleyzes, E. Steidl, B. Buisson, G.G. Malliaras, Easy-to-fabricate conducting polymer microelectrode arrays, *Advanced Materials*, 25 (2013) 2135-2139.
- [410] D.A. Koutsouras, A. Hama, J. Pas, P. Gkoupidenis, B. Hivert, C. Faivre-Sarrailh, E. Di Pasquale, R.M. Owens, G.G. Malliaras, PEDOT: PSS microelectrode arrays for hippocampal cell culture electrophysiological recordings, *MRS Communications*, 7 (2017) 259-265.
- [411] J. Pas, C. Pitsalidis, D.A. Koutsouras, P.P. Quilichini, F. Santoro, B. Cui, L. Gallais, R.P. O'Connor, G.G. Malliaras, R.M. Owens, Neurospheres on patterned PEDOT: PSS microelectrode arrays enhance electrophysiology recordings, *Advanced Biosystems*, 2 (2018) 1700164.
- [412] T.J. Zajdel, M. Baruch, G. Méhes, E. Stavrinidou, M. Berggren, M.M. Maharbiz, D.T. Simon, C.M. Ajo-Franklin, PEDOT: PSS-based multilayer bacterial-composite films for bioelectronics, *Scientific reports*, 8 (2018) 1-12.
- [413] D.A. Koutsouras, P. Gkoupidenis, C. Stolz, V. Subramanian, G.G. Malliaras, D.C. Martin, Impedance Spectroscopy of Spin-Cast and Electrochemically Deposited PEDOT: PSS Films on Microfabricated Electrodes with Various Areas, *ChemElectroChem*, 4 (2017) 2321-2327.
- [414] M. Mierzejewski, H. Steins, P. Kshirsagar, P.D. Jones, The noise and impedance of microelectrodes, *Journal of Neural Engineering*, 17 (2020) 052001.
- [415] G. Dijk, H.J. Ruigrok, R.P. O'Connor, Influence of PEDOT: PSS Coating Thickness on the Performance of Stimulation Electrodes, *Advanced Materials Interfaces*, 7 (2020) 2000675.
- [416] M.R. Abidian, J.M. Corey, D.R. Kipke, D.C. Martin, Conducting-polymer nanotubes improve electrical properties, mechanical adhesion, neural attachment, and neurite outgrowth of neural electrodes, *small*, 6 (2010) 421-429.
- [417] S. Kuss, H.M. Amin, R.G. Compton, Electrochemical detection of pathogenic bacteria—recent strategies, advances and challenges, *Chemistry—An Asian Journal*, 13 (2018) 2758-2769.
- [418] M. Mecklenburg, A. Schuchardt, Y.K. Mishra, S. Kaps, R. Adelung, A. Lotnyk, L. Kienle, K. Schulte, Aerographite: ultra lightweight, flexible nanowall, carbon microtube material with outstanding mechanical performance, *Advanced Materials*, 24 (2012) 3486-3490.
- [419] X. Huang, Z. Zeng, Z. Fan, J. Liu, H. Zhang, Graphene-based electrodes, *Advanced Materials*, 24 (2012) 5979-6004.
- [420] S. Löffler, K. Melican, K. Nilsson, A. Richter-Dahlfors, Organic bioelectronics in medicine, *Journal of internal medicine*, 282 (2017) 24-36.
- [421] Y. Zeng, J. Liu, S. Yang, W. Liu, L. Xu, R. Wang, Time-lapse live cell imaging to monitor doxorubicin release from DNA origami nanostructures, *Journal of Materials Chemistry B*, 6 (2018) 1605-1612.
- [422] Q. Jiang, C. Song, J. Nangreave, X. Liu, L. Lin, D. Qiu, Z.-G. Wang, G. Zou, X. Liang, H. Yan, DNA origami as a carrier for circumvention of drug resistance, *Journal of the American Chemical Society*, 134 (2012) 13396-13403.
- [423] Q. Zhang, Q. Jiang, N. Li, L. Dai, Q. Liu, L. Song, J. Wang, Y. Li, J. Tian, B. Ding, DNA origami as an in vivo drug delivery vehicle for cancer therapy, *ACS nano*, 8 (2014) 6633-6643.
- [424] P. Panda, A.C. Tavit, S. Satpati, M.M. Kar, A. Dixit, T.K. Beuria, Doxorubicin inhibits E. coli division by interacting at a novel site in FtsZ, *Biochemical Journal*, 471 (2015) 335-346.
- [425] H. Shi, C.S. Westfall, J. Kao, P.D. Odermatt, S.E. Anderson, S. Cesar, M. Sievert, J. Moore, C.G. Gonzalez, L. Zhang, Starvation induces shrinkage of the bacterial cytoplasm, *Proceedings of the National Academy of Sciences*, 118 (2021).

- [426] S. Stojicic, Y. Shen, M. Haapasalo, Effect of the source of biofilm bacteria, level of biofilm maturation, and type of disinfecting agent on the susceptibility of biofilm bacteria to antibacterial agents, *Journal of endodontics*, 39 (2013) 473-477.
- [427] R. Roy, M. Tiwari, G. Donelli, V. Tiwari, Strategies for combating bacterial biofilms: A focus on anti-biofilm agents and their mechanisms of action, *Virulence*, 9 (2018) 522-554.
- [428] A. Di Somma, A. Moretta, C. Canè, A. Cirillo, A. Duilio, Inhibition of bacterial biofilm formation, *Bacterial Biofilms*, IntechOpen2020.
- [429] J.J. McManus, J.O. Rädler, K.A. Dawson, Does calcium turn a zwitterionic lipid cationic?, *The Journal of Physical Chemistry B*, 107 (2003) 9869-9875.
- [430] S. Gromelski, G. Brezesinski, DNA condensation and interaction with zwitterionic phospholipids mediated by divalent cations, *Langmuir*, 22 (2006) 6293-6301.
- [431] M. Langecker, V. Arnaut, J. List, F.C. Simmel, DNA nanostructures interacting with lipid bilayer membranes, *Accounts of chemical research*, 47 (2014) 1807-1815.
- [432] Y. Suzuki, M. Endo, H. Sugiyama, Lipid-bilayer-assisted two-dimensional self-assembly of DNA origami nanostructures, *Nature communications*, 6 (2015) 1-9.
- [433] S. Julin, A. Korpi, B. Shen, V. Liljeström, O. Ikkala, A. Keller, V. Linko, M.A. Kostianen, DNA origami directed 3D nanoparticle superlattice via electrostatic assembly, *Nanoscale*, 11 (2019) 4546-4551.
- [434] Y. Shang, N. Li, S. Liu, L. Wang, Z.G. Wang, Z. Zhang, B. Ding, Site-Specific Synthesis of Silica Nanostructures on DNA Origami Templates, *Advanced Materials*, 32 (2020) 2000294.
- [435] L. Hall-Stoodley, J.W. Costerton, P. Stoodley, Bacterial biofilms: from the natural environment to infectious diseases, *Nature reviews microbiology*, 2 (2004) 95-108.
- [436] I.B. Beech, J. Sunner, Biocorrosion: towards understanding interactions between biofilms and metals, *Current opinion in Biotechnology*, 15 (2004) 181-186.
- [437] P. Li, X. Yang, X. Zhang, J. Pan, W. Tang, W. Cao, J. Zhou, X. Gong, X. Xing, Surface chemistry-dependent antibacterial and antibiofilm activities of polyamine-functionalized carbon quantum dots, *Journal of Materials Science*, 55 (2020) 16744-16757.
- [438] J. Cao, Y. Zhao, Y. Liu, S. Tian, C. Zheng, C. Liu, Y. Zhai, Y. An, H.J. Busscher, L. Shi, Phosphorylcholine-based polymer encapsulated chitosan nanoparticles enhance the penetration of antimicrobials in a staphylococcal biofilm, *ACS Macro Letters*, 8 (2019) 651-657.
- [439] M. Varshney, Y. Li, Interdigitated array microelectrode based impedance biosensor coupled with magnetic nanoparticle-antibody conjugates for detection of *Escherichia coli* O157: H7 in food samples, *Biosensors and Bioelectronics*, 22 (2007) 2408-2414.
- [440] L. Yang, C. Ruan, Y. Li, Detection of viable *Salmonella typhimurium* by impedance measurement of electrode capacitance and medium resistance, *Biosensors and Bioelectronics*, 19 (2003) 495-502.
- [441] R. Gómez, R. Bashir, A.K. Bhunia, Microscale electronic detection of bacterial metabolism, *Sensors and Actuators B: Chemical*, 86 (2002) 198-208.
- [442] R. Gomez-Sjoberg, D.T. Morissette, R. Bashir, Impedance microbiology-on-a-chip: Microfluidic bioprocessor for rapid detection of bacterial metabolism, *Journal of Microelectromechanical Systems*, 14 (2005) 829-838.
- [443] S. Kim, G. Yu, T. Kim, K. Shin, J. Yoon, Rapid bacterial detection with an interdigitated array electrode by electrochemical impedance spectroscopy, *Electrochimica Acta*, 82 (2012) 126-131.
- [444] C. Amatore, J. Saveant, D. Tessier, Kinetics of electron transfer to organic molecules at solid electrodes in organic media, *Journal of Electroanalytical Chemistry and Interfacial Electrochemistry*, 146 (1983) 37-45.
- [445] M. Ciszowska, Z. Stojek, Voltammetry in solutions of low ionic strength. Electrochemical and analytical aspects, *Journal of Electroanalytical Chemistry*, 466 (1999) 129-143.
- [446] K. Maruyama, H. Ohkawa, S. Ogawa, A. Ueda, O. Niwa, K. Suzuki, Fabrication and characterization of a nanometer-sized optical fiber electrode based on selective chemical etching for scanning electrochemical/optical microscopy, *Analytical chemistry*, 78 (2006) 1904-1912.
- [447] L. Yang, Y. Li, C.L. Griffis, M.G. Johnson, Interdigitated microelectrode (IME) impedance sensor for the detection of viable *Salmonella typhimurium*, *Biosensors and bioelectronics*, 19 (2004) 1139-1147.
- [448] G. Brug, A.L. van den Eeden, M. Sluyters-Rehbach, J.H. Sluyters, The analysis of electrode impedances complicated by the presence of a constant phase element, *Journal of electroanalytical chemistry and interfacial electrochemistry*, 176 (1984) 275-295.
- [449] T. Kim, J. Kang, J.-H. Lee, J. Yoon, Influence of attached bacteria and biofilm on double-layer capacitance during biofilm monitoring by electrochemical impedance spectroscopy, *Water research*, 45 (2011) 4615-4622.
- [450] G.A. James, E. Swogger, R. Wolcott, E.d. Pulcini, P. Secor, J. Sestrich, J.W. Costerton, P.S. Stewart, Biofilms in chronic wounds, *Wound Repair and regeneration*, 16 (2008) 37-44.
- [451] S.L. Percival, Biofilms and their potential role in wound healing, *Wounds*, 16 (2004) 234-240.
- [452] S.G. Jones, R. Edwards, D.W. Thomas, Inflammation and wound healing: the role of bacteria in the immuno-regulation of wound healing, *The International Journal of Lower Extremity Wounds*, 3 (2004) 201-208.

- [453] S.L. Percival, S.M. McCarty, B. Lipsky, Biofilms and wounds: an overview of the evidence, *Advances in wound care*, 4 (2015) 373-381.
- [454] L. Karygianni, Z. Ren, H. Koo, T. Thurnheer, Biofilm Matrixome: Extracellular Components in Structured Microbial Communities, *Trends in Microbiology*, (2020).
- [455] D.G. Metcalf, P.G. Bowler, Biofilm delays wound healing: a review of the evidence, *Burns & Trauma*, 1 (2013) 2321-3868.113329.
- [456] A. Persat, C.D. Nadell, M.K. Kim, F. Ingremeau, A. Siryaporn, K. Drescher, N.S. Wingreen, B.L. Bassler, Z. Gitai, H.A. Stone, The mechanical world of bacteria, *Cell*, 161 (2015) 988-997.
- [457] T. Bjarnsholt, K. Kirketerp-Møller, P.Ø. Jensen, K.G. Madsen, R. Phipps, K. Krogfelt, N. Høiby, M. Givskov, Why chronic wounds will not heal: a novel hypothesis, *Wound repair and regeneration*, 16 (2008) 2-10.
- [458] X.-M.Z. Di Wei, Y.-Y. Chen, X.-Y. Li, Y.-P. Chen, H.-Y. Liu, M. Zhang, Chronic wound biofilms: diagnosis and therapeutic strategies, *Chinese Medical Journal*, 132 (2019) 2737.
- [459] J.M. Martin, J.M. Zenilman, G.S. Lazarus, Molecular microbiology: new dimensions for cutaneous biology and wound healing, *Journal of Investigative Dermatology*, 130 (2010) 38-48.
- [460] R.A. Fisher, B. Gollan, S. Helaine, Persistent bacterial infections and persister cells, *Nature Reviews Microbiology*, 15 (2017) 453.
- [461] Y. Shen, S. Stojicic, M. Haapasalo, Bacterial viability in starved and revitalized biofilms: comparison of viability staining and direct culture, *Journal of endodontics*, 36 (2010) 1820-1823.
- [462] Y. Liu, J. Zhang, Y. Ji, Suppl-1, M2: PCR-based Approaches for the Detection of Clinical Methicillin-resistant *Staphylococcus aureus*, *The open microbiology journal*, 10 (2016) 45.
- [463] Y. Xu, Y. Dhaouadi, P. Stoodley, D. Ren, Sensing the unreachable: challenges and opportunities in biofilm detection, *Current opinion in biotechnology*, 64 (2020) 79-84.
- [464] J. Lawrence, D. Korber, B. Hoyle, J.W. Costerton, D. Caldwell, Optical sectioning of microbial biofilms, *Journal of bacteriology*, 173 (1991) 6558-6567.
- [465] S.C. Davis, C. Ricotti, A. Cazzaniga, E. Welsh, W.H. Eaglstein, P.M. Mertz, Microscopic and physiologic evidence for biofilm-associated wound colonization in vivo, *Wound repair and Regeneration*, 16 (2008) 23-29.
- [466] K.S. Vyas, L.K. Wong, Detection of biofilm in wounds as an early indicator for risk for tissue infection and wound chronicity, *Annals of plastic surgery*, 76 (2016) 127-131.
- [467] Y.-K. Wu, N.-C. Cheng, C.-M. Cheng, Biofilms in chronic wounds: pathogenesis and diagnosis, *Trends in biotechnology*, 37 (2019) 505-517.
- [468] L.E. Lindley, O. Stojadinovic, I. Pastar, M. Tomic-Canic, Biology and biomarkers for wound healing, *Plastic and reconstructive surgery*, 138 (2016) 18S.
- [469] T.R. Dargaville, B.L. Farrugia, J.A. Broadbent, S. Pace, Z. Upton, N.H. Voelcker, Sensors and imaging for wound healing: a review, *Biosensors and Bioelectronics*, 41 (2013) 30-42.
- [470] N.T. Thet, J. Mercer-Chalmers, R.J. Greenwood, A.E. Young, K. Coy, S. Booth, A. Sack, A.T. Jenkins, SPaCE Swab: Point-of-Care Sensor for Simple and Rapid Detection of Acute Wound Infection, *ACS sensors*, 5 (2020) 2652-2657.
- [471] L.M. Jones, D. Dunham, M.Y. Rennie, J. Kirman, A.J. Lopez, K.C. Keim, W. Little, A. Gomez, J. Bourke, H. Ng, In vitro detection of porphyrin-producing wound bacteria with real-time fluorescence imaging, *Future Microbiology*, 15 (2020) 319-332.
- [472] E.M. Jones, C.A. Cochrane, S.L. Percival, The effect of pH on the extracellular matrix and biofilms, *Advances in wound care*, 4 (2015) 431-439.
- [473] L.A. Schneider, A. Korber, S. Grabbe, J. Dissemond, Influence of pH on wound-healing: a new perspective for wound-therapy?, *Archives of dermatological research*, 298 (2007) 413-420.
- [474] S.L. Percival, S. McCarty, J.A. Hunt, E.J. Woods, The effects of pH on wound healing, biofilms, and antimicrobial efficacy, *Wound Repair and Regeneration*, 22 (2014) 174-186.
- [475] R. Rahimi, M. Ochoa, A. Tamayol, S. Khalili, A. Khademhosseini, B. Ziaie, Highly stretchable potentiometric pH sensor fabricated via laser carbonization and machining of Carbon- Polyaniline composite, *ACS applied materials & interfaces*, 9 (2017) 9015-9023.
- [476] H.H. Leveen, G. Falk, B. Borek, C. Diaz, Y. Lynfield, B.J. Wynkoop, G.A. Mabunda, J.L. Rubricius, G.C. Christoudias, Chemical acidification of wounds. An adjuvant to healing and the unfavorable action of alkalinity and ammonia, *Annals of surgery*, 178 (1973) 745.
- [477] A.U. Alam, Y. Qin, S. Nambiar, J.T. Yeow, M.M. Howlader, N.-X. Hu, M.J. Deen, Polymers and organic materials-based pH sensors for healthcare applications, *Progress in Materials Science*, 96 (2018) 174-216.
- [478] R. Rahimi, U. Brener, S. Chittiboyina, T. Soleimani, D.A. Detwiler, S.A. Lelièvre, B. Ziaie, Laser-enabled fabrication of flexible and transparent pH sensor with near-field communication for in-situ monitoring of wound infection, *Sensors and Actuators B: Chemical*, 267 (2018) 198-207.
- [479] H. Jin, Y.S. Abu-Raya, H. Haick, Advanced materials for health monitoring with skin-based wearable devices, *Advanced healthcare materials*, 6 (2017) 1700024.

- [480] R. Feiner, L. Wertheim, D. Gazit, O. Kalish, G. Mishal, A. Shapira, T. Dvir, A stretchable and flexible cardiac tissue–electronics hybrid enabling multiple drug release, sensing, and stimulation, *Small*, 15 (2019) 1805526.
- [481] S. Tavakoli, A.S. Klar, Advanced Hydrogels as Wound Dressings, *Biomolecules*, 10 (2020) 1169.
- [482] Q. Pang, D. Lou, S. Li, G. Wang, B. Qiao, S. Dong, L. Ma, C. Gao, Z. Wu, Smart Flexible Electronics-Integrated Wound Dressing for Real-Time Monitoring and On-Demand Treatment of Infected Wounds, *Advanced Science*, 7 (2020) 1902673.
- [483] R.B. Karim, B.L. Brito, R.P. Dutrieux, F.P. Lassance, J.J. Hage, MMP-2 assessment as an indicator of wound healing: a feasibility study, *Advances in skin & wound care*, 19 (2006) 324-327.
- [484] A. Veves, P. Sheehan, H.T. Pham, A randomized, controlled trial of Promogran (a collagen/oxidized regenerated cellulose dressing) vs standard treatment in the management of diabetic foot ulcers, *Archives of Surgery*, 137 (2002) 822-827.
- [485] A.B. Wysocki, L. Staiano-Coico, F. Grinnell, Wound fluid from chronic leg ulcers contains elevated levels of metalloproteinases MMP-2 and MMP-9, *Journal of Investigative Dermatology*, 101 (1993).
- [486] Y. Liu, D. Min, T. Bolton, V. Nubé, S.M. Twigg, D.K. Yue, S.V. McLennan, Increased matrix metalloproteinase-9 predicts poor wound healing in diabetic foot ulcers, *Diabetes care*, 32 (2009) 117-119.
- [487] M. Bariya, H.Y.Y. Nyein, A. Javey, Wearable sweat sensors, *Nature Electronics*, 1 (2018) 160-171.
- [488] W. Gao, H. Ota, D. Kiriya, K. Takei, A. Javey, Flexible electronics toward wearable sensing, *Accounts of chemical research*, 52 (2019) 523-533.
- [489] W. Gao, S. Emaminejad, H.Y.Y. Nyein, S. Challa, K. Chen, A. Peck, H.M. Fahad, H. Ota, H. Shiraki, D. Kiriya, Fully integrated wearable sensor arrays for multiplexed in situ perspiration analysis, *Nature*, 529 (2016) 509-514.
- [490] J.A. Rogers, T. Someya, Y. Huang, Materials and mechanics for stretchable electronics, *science*, 327 (2010) 1603-1607.
- [491] T. Someya, Z. Bao, G.G. Malliaras, The rise of plastic bioelectronics, *Nature*, 540 (2016) 379-385.
- [492] D.-H. Kim, N. Lu, R. Ma, Y.-S. Kim, R.-H. Kim, S. Wang, J. Wu, S.M. Won, H. Tao, A. Islam, Epidermal electronics, *science*, 333 (2011) 838-843.
- [493] D.J. Lipomi, M. Vosgueritchian, B.C. Tee, S.L. Hellstrom, J.A. Lee, C.H. Fox, Z. Bao, Skin-like pressure and strain sensors based on transparent elastic films of carbon nanotubes, *Nature nanotechnology*, 6 (2011) 788-792.
- [494] M. Kaltenbrunner, T. Sekitani, J. Reeder, T. Yokota, K. Kuribara, T. Tokuhara, M. Drack, R. Schwödiauer, I. Graz, S. Bauer-Gogonea, An ultra-lightweight design for imperceptible plastic electronics, *Nature*, 499 (2013) 458-463.
- [495] S. Xu, Y. Zhang, L. Jia, K.E. Mathewson, K.-I. Jang, J. Kim, H. Fu, X. Huang, P. Chava, R. Wang, Soft microfluidic assemblies of sensors, circuits, and radios for the skin, *Science*, 344 (2014) 70-74.
- [496] D.R. Seshadri, R.T. Li, J.E. Voos, J.R. Rowbottom, C.M. Alfes, C.A. Zorman, C.K. Drummond, Wearable sensors for monitoring the physiological and biochemical profile of the athlete, *NPJ digital medicine*, 2 (2019) 1-16.
- [497] Y. Lin, M. Bariya, A. Javey, Wearable biosensors for body computing, *Advanced Functional Materials*, (2020) 2008087.
- [498] H. Derakhshandeh, S.S. Kashaf, F. Aghabaglou, I.O. Ghanavati, A. Tamayol, Smart bandages: the future of wound care, *Trends in biotechnology*, 36 (2018) 1259-1274.

Curriculum vitae: Sorour Darvishi

1. PERSONAL INFORMATION

Mobiles: +41 (0)78 735 4897

Emails: sorour.darvishi@epfl.ch
sorourdarvishi@gmail.com

Born: 10. December 1991

Switzerland residence, Permit B

ORCID ID: 0000-0002-3156-1789

Google Scholar ID: [Google Scholar](#)

Academic information page: [My EPFL webpage](#)

2. EDUCATION

- Nov. 2017 – Dec. 2021** **Ph.D. in Chemistry and Chemical Engineering**
Swiss Federal Institute of Technology Lausanne (EPFL), Switzerland
Tentative thesis title: "*Electrochemical imaging of metabolic activity in tissue and biofilms*" under the supervision of Prof. Hubert H. Girault and Dr. Andreas Lesch.
- Mar. 2021 – Aug. 2021** **SNSF Doctoral Mobility Fellow at Chemical Engineering and Biotechnology**
University of Cambridge, United Kingdom
Research project: "*The lifetime of skin biofilms and their destruction with DNA nanostructures: A quantitative study*" under supervision of Prof. Clemens Kaminski and Dr. Ioanna Mela.
- Aug. 2014 - Aug. 2016** **M.Sc. in Material engineering, Materials Characterization & Selection**
Isfahan University of Technology, Iran
Thesis title: "*Development of Non-enzymatic Glucose Sensor Based on Nickel Nanoparticles: Graphene/ Gelatin Methacrylate (GelMa)*" under the supervision of Prof. Fathallah Karimzadeh and Prof. Mahshid Kharaziha.
- Aug. 2010- Aug. 2014** **B.Sc. in Material Engineering**
Isfahan University of Technology, Iran
Thesis title: "*The Effect of Thermomechanical Processing and Grain Size of TiNiCo and TiNi Alloys on Corrosion Behavior in Simulated Body Fluids*" under the supervision of Prof. Fathallah Karimzadeh.

3. EMPLOYMENT HISTORY

- Nov. 2017 – Nov. 2021** Doctoral assistant, Laboratory of Physical and Analytical Electrochemistry (LEPA) - Swiss Federal Institute of Technology Lausanne (EPFL), Switzerland. under the supervision of Prof. Hubert H. Girault and Dr. Andreas Lesch.
- Summer 2015** Participation in translating of the book "Inclusion in steel casting". (Under edition) under the supervision of Prof. Hossein Edris.
- Fall 2015** Research Assistant, Heat Treatment Laboratory, under the supervision of Morteza Safari.
- 2012-2014** Member of Dental group held in common with Biomaterial group of Isfahan University of Technology and Dental group of Isfahan Medical University under the supervision of Prof. Mohammadhossein Fathi.

4. INSTITUTIONAL RESPONSIBILITIES

- Nov. 2017- Present** Responsible for the Scanning Electrochemical Microscopy, LEPA, EPFL

5. RESEARCH PROJECTS

Research projects during the Ph.D. study:

Mar. 2021 - Present	The lifetime of skin biofilms and their destruction with DNA nanostructures: A quantitative study.
Aug. 2020 - Mar. 2021	Revealing effects of antimicrobial agents on biofilm by using soft-probe scanning electrochemical microscopy
Dec. 2018 - Aug. 2020	Soft-probe scanning electrochemical microscopy of biofilm.
Jan. 2020 - July 2020	Soft-probe scanning electrochemical microscopy (SECM) of oral cancer.
Dec. 2018 - Present	Transdermal biosensor for the distribution of melanoma biomarkers in the skin.
Nov. 2017 – Nov. 2018	Soft-probe scanning electrochemical microscopy of melanoma.

Research projects during the Master's study:

Nov. 2014 - Aug. 2017	Development of non-enzymatic electrochemical glucose biosensor.
Sept. 2015 - July 2017	Development of bio-implants based on polymer-ceramic coating biomaterial.

Research project during the Bachelor's study:

Oct. 2013 - Sept. 2014	Electrochemical characterization of bio-implants based on titanium shape memory alloys
-------------------------------	--

6. SUPERVISION OF STUDENTS

Oct. 2020 – Dec. 2020	Joël Racine, live/dead biofilms imaging, Master's thesis, Swiss Federal Institute of Technology in Lausanne (EPFL), Switzerland.
Sept. 2016 – Sept. 2017	Mehdi Jokar, Corrosion of biomaterial, Bachelor thesis, Isfahan University of Technology, Iran
Sept. 2015 – Sept. 2016	Reza Torkaman, Corrosion of biomaterial, Bachelor thesis, Isfahan University of Technology, Iran

7. TEACHING ACTIVITIES

Swiss Federal Institute of Technology in Lausanne (EPFL), Switzerland

Spring 2021	Teaching assistant for the course of "Advanced general chemistry".
Spring 2020 – Fall 2020	Teaching assistant for practical B.Sc. course "Experimental physical chemistry", the general concept of amperometry.
Fall 2018 – Fall 2019	Teaching assistant for practical B.Sc. course "Experimental analytical chemistry", the general concept of gas chromatography (GC).
Spring 2018	Supervision for the project of the M.Sc. course "Advanced project in analytical chemistry". I was leading a project on the detection of pesticides in orange's skin.

Isfahan University of Technology, Iran

Fall 2014 – Spring 2015	Material selection and characterization, B.Sc. course.
Fall 2015	Research Assistant in the heat treatment laboratory, B.Sc. course

8. MEMBERSHIPS

2019 – Present	Reviewer for <i>ChemElectroChem</i> journal.
2012 – 2014	Member of the biomaterial group in the Isfahan University of Technology.

9. ACTIVE MEMBERSHIP IN SCIENTIFIC SOCIETIES

Mar. 2021 – Aug. 2021	Doc. Mobility fellowship, Swiss National Science Foundation.
------------------------------	--

10. ORGANISATION OF CONFERENCES

N/A

11. PRIZES, AWARDS, FELLOWSHIPS

Dec. 2021	PostDoc.Mobility fellowship, Swiss National Science Foundation. (116k CHF)
Nov. 2020	Doc. Mobility fellowship, Swiss National Science Foundation. (~25k CHF)
Sept. 2018	Best poster presentation at the 69 th annual meeting of the International Society of Electrochemistry (ISE), Bologna, Italy.
Sept. 2016	The best Master graduated student, Isfahan University of Technology, Iran.
Sept. 2016	Award of the best presentation during master defense with the perfect score (100).
Sept. 2011 – Sept. 2014	An elite bachelor student of the Isfahan University of Technology, Isfahan, Iran.
Sept. 2014	Award of the entrance to graduate studies at the Isfahan University of Technology (recognizing excellent academic performance).
Sept. 2010- Sept. 2014	Ranked 1% of 86 undergraduate students in Material Science and Engineering, Isfahan University of Technology, Iran.

12. PERSONAL SKILLS

LANGUAGES

- English Fluent
- French Intermediate
- Farsi Mother tongue

GENERAL LAB SKILLS (Independently measurement and analysis)

- Electrochemical methods (CV, EIS, SECM, etc.)
- Scanning electron microscopy
- Confocal laser scanning microscopy
- Structured illumination microscopy
- Widefield fluorescence microscopy
- X-ray diffraction
- Fourier-transform infrared spectroscopy
- Raman spectroscopy
- Atomic force microscopy

LAB BIOLOGICAL SKILLS

- Cell culture
- Bacterial culture
- Biofilm culturing
- Gram staining of bacteria
- Live/ dead staining of bacteria and mammalian cells
- Immunoassays

STATISTICAL ANALYSIS

- ANOVA
- t-test

12. CAREER BREAKS

N/A

1. PUBLICATIONS IN PEER-REVIEWED SCIENTIFIC JOURNALS

1. **Darvishi, S.**, Tavakoli, Sh., Kharaziha, M., Girault H.H., Kaminski, C., Mela, I., "Advances in sensing and treating wound biofilms", *Angewandte Chemie International Edition*, Accepted (In press). [Link](#)
2. **Darvishi, S.**, Pick, H.M., Oveisi, E., Girault, H.H. and Lesch, A., "Soft-Probe-Scanning Electrochemical Microscopy reveals electrochemical surface reactivity of *E. coli* biofilms" *Sensors and Actuators: B. Chemical* 334 (2021): 129669. [Link](#)
3. Lin, Y.T., Preet, A., Chiu, Y.P., Yip, B.S., Girault, H.H., **Darvishi, S.**, Wang, L., Lin, T.E. "Communication—Scanning Electrochemical Microscopy Analysis of Interleukin-6 in Oral Cancer" *ECS Journal of Solid State Science and Technology* 9 (2020): 11. [Link](#)
4. **Darvishi, S.**, Lin, Y.T., Preet, A., Huang, T.Y., Lin, S.H., Girault, H.H., Wang, L., and Lin, T.E. "A Review: Electrochemical Biosensors for Oral Cancer." *Chemosensors* 8 (2020): 54. [Link](#)
5. **Darvishi, S.**, Pick, H.M., Lin, T.E., Zhu, Y., Li, X., Ho, P.C., Girault, H.H. and Lesch, A., "Tape-Stripping Electrochemical Detection of Melanoma", *Analytical chemistry* 91 (2019): 12900-12908. [Link](#)
6. Souissi, M., Sahara, R., **Darvishi, S.** and Ahadian, S., "Responses to comments on "Ni nanoparticle-decorated reduced graphene oxide for non-enzymatic glucose sensing: An experimental and modeling study [Electrochim. Acta 240 (2017) 388–398]". *Electrochimica Acta* 300 (2019): 145-149. [Link](#)
7. **Darvishi, S.**, Souissi, M., Kharaziha, M., Karimzadeh, F., Sahara, R. and Ahadian, S., "Gelatin methacryloyl hydrogel for glucose biosensing using Ni nanoparticles-reduced graphene oxide: An experimental and modeling study." *Electrochimica Acta* 261 (2018): 275-283. [Link](#)
8. **Darvishi, S.**, Nemati, S., Kharaziha, M., 2018. "Preparation and Characterization of PDMS-SiO₂-CuO Nanocomposite Coating on Stainless Steel and Its Super-hydrophobicity Property. " *Journal of Advanced Materials in Engineering (Esteghlal)* 37, no. 3 (2018): 1-12. [Link](#)
9. Ahadian, S., Naito, U., Surya, V.J., **Darvishi, S.**, Estili, M., Liang, X., Nakajima, K., Shiku, H., Kawazoe, Y. and Matsue, T., "Fabrication of poly (ethylene glycol) hydrogels containing vertically and horizontally aligned graphene using dielectrophoresis: an experimental and modeling study." *Carbon* 123 (2017): 460-470. [Link](#)
10. **Darvishi, S.**, Souissi, M., Karimzadeh, F., Kharaziha, M., Sahara, R. and Ahadian, S., "Ni nanoparticle-decorated reduced graphene oxide for non-enzymatic glucose sensing: an experimental and modeling study." *Electrochimica Acta* 240 (2017): 388-398. [Link](#)
11. Torkaman, R., **Darvishi, S.**, Jokar, M., Kharaziha, M. and Karbasi, M., "Electrochemical and *in vitro* bioactivity of nanocomposite gelatin-forsterite coatings on AISI 316 L stainless steel." *Progress in Organic Coatings* 103 (2017): 40-47. (*has same contribution and both are first author). [Link](#)
12. Jokar, M., **Darvishi, S.**, Torkaman, R., Kharaziha, M. and Karbasi, M., "Corrosion and bioactivity evaluation of nanocomposite PCL-forsterite coating applied on 316L stainless steel." *Surface and Coatings Technology* 307 (2016): 324-331. [Link](#)
13. **Darvishi, S.**, Karmizadeh, F. and Kharaziha, M., "A facile one-step electrochemical synthesis of nickel nanoparticle/graphene composites for non-enzymatic biosensor applications." *Procedia Materials Science* 11 (2015): 142-146. [Link](#)

2. PEER-REVIEWED BOOKS/MONOGRAPHS

1. **Darvishi, S.**, Ahadian, S., Savoji, H., "Graphene-Based Nanomaterials in Tissue Engineering and Regenerative Medicine." *Handbook of Graphene* 1 (2019): 637-658. [Link](#)
2. Please see Section 11 for the unpublished publication, doctoral thesis.

3. PEER-REVIEWED CONFERENCE PAPERS AND ABSTRACTS IN CONFERENCES

1. Lin, T.E., **Darvishi, S.**, Lesch, A. and Girault, H.H., "Detection of Cancer Biomarkers By Scanning Electrochemical Microscopy" .237th *ECS Meeting with the 18th International Meeting on Chemical Sensors (IMCS 2020)*, May 2020. [Link](#)

2. Zhu, Y., **Darvishi, S.**, Jović, M., Lesch, A. and Girault, H.H., "Scanning electrochemical microscopy of biological tissues and amperometric bacteria detection". *XXII Simpósio Brasileiro de Eletroquímica e Eletroanalítica*, September 2019. **Link:** not available.
3. Tavakoli, Sh., Kharaziha M., Nemati, Sh., **Darvishi, S.**, "Synthesis and characterization of High hydrophobic coating of MS-SiO₂-CuO on the 316L", *17th National seminar of surface coating*, February 2017. **Link:** not available.
4. Nemati, Sh., Kharaziha, M., Tavakoli, Sh., **Darvishi, S.**, "Synthesis of double layer coating of Silika-polydemethy-TiO₂ with sol-gel method on 316L", *17th National seminar of surface coating*, February 2017. **Link:** not available.
5. Safavipoor, M., Ghasemi, Z., **Darvishi, S.**, Karimzadeh, F., Kharaziha, M., "Corrosion evaluation of TiO₂-Chitosan-Bioglass coating on Ti", *17th National seminar of surface coating*, February 2017. **Link:** not available.
6. **Darvishi, S.**, Karimzadeh, F., Kharaziha, M., "New Method for Synthesis of Nickel Nanoparticle/Graphene Composites for Non-enzymatic Biosensor Applications", *UFGNSM 2015*, November 2015. **Link:** not available.
7. **Darvishi, S.**, Karimzadeh, F., Kharaziha, M., "Development of Non-enzymatic Glucose Sensor Based on Nickel Nanoparticle: Graphene /Gelatin methacrylate (GelMA)", *6th International Conference on Nanostructures (ICNS6)*, February 2015. **Link:** not available.
8. **Darvishi, S.**, Karimzadeh, F., "Effect of grain size on the corrosion behavior of NiTi nanocrystalline", *3rd International Engineering Materials & Metallurgy Conference (iMat)*, November 2014. **Link:** not available.
9. **Darvishi, S.**, Karimzadeh, F., "Comparison Corrosion Behavior of NiTi and NiTiCO as metallic Biomaterial", *Iranian Corrosion Association (ICA), 15th National Corrosion Congress*, October 2014. **Link:** not available.
10. **Darvishi, S.**, Karimzadeh, F., "Review corrosion behavior of NiTiCo in simulated body fluid", *Expert Workshop of Nanotechnology*, October 2014. **Link:** not available.

4. CONTRIBUTION TO BOOK AND BOOK CHAPTER

1. **Darvishi, S.**, Ahadian, S., Savoji, H., "Graphene-Based Nanomaterials in Tissue Engineering and Regenerative Medicine." *Handbook of Graphene 1* (2019): 637-658. [Link](#)

5. PATENTS AND LICENSES

N/A

6. CONTRIBUTION TO INTERNATIONAL CONFERENCES, SEMINARS, AND SCHOOLS

Oral presentations

1. Invited speaker, Virtual conference focusing on the SECM work, Montreal, Canada, September 2021. **Link:** not available yet.
2. 72st annual meeting of the International Society of Electrochemistry (ISE), Jeju Island, Korea, September 2021. [Link](#)
3. European Biosensor Symposium (EBS) 2021, Wildau Online, March 2021. [Link](#)
4. 71st annual meeting of the International Society of Electrochemistry (ISE), Belgrade Online, September 2020. [Link](#)
5. 5th International biennial conferences on Ultrafine Grained and Nanostructured Materials, Iran, November 2015. **Link:** not available
6. 3rd International Engineering Materials & Metallurgy Conference (iMat), Iran, November 2014. **Link:** not available.

Poster presentations

1. 10th Workshop on SECM, Paris, France, October 2019. **Link:** not available.
2. 69th annual meeting of the International Society of Electrochemistry (ISE), Bologna, Italy, September 2018. **Link:** not available.
3. Swiss Summer School in Chemical Biology, Villars sur Ollon, Switzerland, August 2018. **Link:** not available.
4. 6th International Conference on Nanostructures (ICNS6), Kish Island, Iran, February 2015. **Link:** not available.

7. OUTREACH ACTIVITIES

- News interview at Chemical & Engineering news (C&EN). [Link](#)
- [Reviewing activities for ChemElectroChem journal, 2019 – Now.](#)
- Member of the biomaterial group in the Isfahan University of Technology, 2012 – 2014.

8. GENERAL CONTRIBUTION TO SCIENCE

- Presenting new science to school students at Scientastic events in EPFL, EPFL, Sion, Switzerland, May 2019. [Link](#)

9. OTHER ARTEFACTS WITH DOCUMENTED USE

1. **Darvishi, S.** and Girault, H.H., “Ex vivo performance evaluation of a transdermal gold injectable microneedle for tyrosinase sensing” *ChemRxiv* (2021). [Link](#)

10. UNPUBLISHED WORK

- 1.1. **Darvishi, S.**, Pick, H.M., Oveisi, E., Lesch, A., Girault, H.H., “Revealing the effects of different antimicrobial agents on *E. coli* biofilm by using Soft-Probe Scanning Electrochemical Microscopy”, *In preparation for publication on arXiv.*
- 1.2. **Darvishi, S.**, Pick, H.M., Oveisi, E., Lesch, A., Girault, H.H., “Revealing the effects of different antimicrobial agents on *E. coli* biofilm by using Soft-Probe Scanning Electrochemical Microscopy”, *In preparation.*
- 2.1. **Darvishi, S.**, Mela, I., Kaminski, C., Girault H.H., “Methods to study the viability of biofilms: Review”, *In preparation for publication on arXiv.*
- 2.2. **Darvishi, S.**, Mela, I., Kaminski, C., Girault H.H., “Methods to study the viability of biofilms: Review”, *In preparation.*
- 3.1. **Darvishi, S.**, Mela, I., Kaminski, C., Girault H.H., “The lifetime of *E.coli* biofilms and their destruction with DNA nanostructures loaded by Doxorubicin”, *In preparation for publication on arXiv.*
- 3.2. **Darvishi, S.**, Mela, I., Kaminski, C., Girault H.H., “The lifetime of *E.coli* biofilms and their destruction with DNA nanostructures loaded by Doxorubicin”, *In preparation.*